



University
of Glasgow

Graham, David Robert (2014) *Extreme ultraviolet spectroscopy of impulsive phase solar flare footpoints*. PhD thesis.

<http://theses.gla.ac.uk/5017/>

Copyright and moral rights for this thesis are retained by the author

A copy can be downloaded for personal non-commercial research or study, without prior permission or charge

This thesis cannot be reproduced or quoted extensively from without first obtaining permission in writing from the Author

The content must not be changed in any way or sold commercially in any format or medium without the formal permission of the Author

When referring to this work, full bibliographic details including the author, title, awarding institution and date of the thesis must be given

Extreme Ultraviolet Spectroscopy of Impulsive Phase Solar Flare Footpoints

David Robert Graham, M.Sci

Astronomy and Astrophysics Group
SUPA School of Physics and Astronomy
Kelvin Building
University of Glasgow
Glasgow, G12 8QQ
Scotland, U.K.



University
of Glasgow

Presented for the degree of
Doctor of Philosophy
The University of Glasgow
September 2013

This thesis is my own composition except where indicated in the text.
No part of this thesis has been submitted elsewhere for any other degree
or qualification.

Copyright © 2013 by David R. Graham

30th September 2013

Acknowledgements

Four years suddenly does not seem like such a long time, but it certainly would have felt far longer without the help of many fantastic people. First of all I owe a huge thanks to my parents for getting me into this astronomy business so many years ago with a passing trip to Jodrell Bank, and for all of the help and support over the years, even putting up with the odd ‘project’ in the kitchen or on the driveway.

A massive thanks to my supervisor Lyndsay Fletcher for the continuous encouragement, inspiration, and always helping with a question or idea, especially when two hours later it meant running back to the office to frantically scribble down another 20 ideas. Thanks also to everyone who has helped along the way, especially Iain Hannah, Hugh Hudson, Nic Labrosse, Ryan Milligan, Helen Mason, Giulio Del Zanna, Peter Young, David Williams, and everyone on the EIS team.

I must also thank Scott McIntosh for introducing me to the mysterious world of spectroscopy and Genetic Algorithms, and agreeing to work with me whilst both times expecting a baby! And of course Jørgen, Hazel, and everyone at HAO for helping me survive in Boulder.

Thanks to everyone in the fantastic Glasgow astronomy group, past and present, and everyone who has made a home in Room 604 (and 614!), in particular for realising that 4 pm coffee and 6 pm pub are matters of religion, and of course Rachael McLauchlan for always being able to help with so many last minute travel bookings.

I also owe many thanks to the Glasgow University Mountaineering Club, for meeting some great friends and the countless adventures in the Scottish highlands which have kept me (in)sane. Finally, thanks to all my friends and family for reminding me that there is a world outside of physics, and for all the support in the form of a walk, pint, or quick escape down the nearest singletrack.

“It was precisely for that reason, to have a bit of a quieter life, that my grandfather came and settled here — Qfwfq said — after the last supernova explosion had flung them once more into space: grandfather, grandmother, their children, grandchildren and great-grandchildren. The Sun was just at that stage condensing, a roundish, yellowish shape, along one arm of the galaxy, and it made a good impression on him, amidst all the other stars that were going around. ‘Let’s try a yellow one this time,’ he said to his wife.”

‘As Long as the Sun Lasts — World Memory and Other Cosmicomic Stories’ (1968)
— by Italo Calvino.

FOR DANNY

Abstract

This thesis is primarily concerned with the atmospheric structure of footpoints during the impulsive phase of a solar flare. Through spectroscopic diagnostics in Extreme-Ultraviolet wavelengths we have made significant progress in understanding the depth of flare heating within the atmosphere, and the energy transport processes within the footpoint.

Chapter 1 introduces the Sun and its outer atmosphere, forming the necessary background to understand the mechanisms behind a solar flare and their observational characteristics. The standard flare model is presented which explains the energy source behind a flare, through to the creation of the EUV and X-ray emission.

In Chapter 2 the basics of atomic emission line spectroscopy are introduced, covering the processes driving electron excitation and de-excitation, the formation of Gaussian line profiles, and the formation of density sensitive line ratios. The concept of a *differential emission measure* is also derived from first principles, followed by a description of all of the instruments used throughout this thesis.

Chapter 3 presents measurements of electron density enhancements in solar flare footpoints using diagnostics from *Hinode*/EIS. Using RHESSI imaging and spectroscopy, the density enhancements are found at the location of hard X-ray footpoints and are interpreted as the heating of layers of increasing depth in the chromosphere to coronal temperatures.

Chapter 4 shows the first footpoint emission measure distributions (EMD) obtained from *Hinode*/EIS data. A regularised inversion method was used to obtain the EMD from emission line intensities. The gradient of the EMDs were found to be compatible

with a model where the flare energy input is deposited in an upper layer of the flare chromosphere. This top layer then cools by a conductive flux to the denser plasma below which then radiates to balance the conductive input. The EUV footpoints are found to be not heated directly by the injected flare energy.

In Chapter 5 electron densities of over 10^{13} cm^{-3} were found using a diagnostic at transition region temperatures. It was shown to be difficult to heat plasma at these depths with a thick-target flare model and several suggestions are made to explain this; including optical depth effects, non-ionisation equilibrium, and model inaccuracies.

Finally, Chapter 6 gathered together both the density diagnostic and EMD results to attempt to forward fit model atmospheres to observations using a Genetic Algorithm. The results are preliminary, but progress has been made to obtain information about the $T(z)$ and $n(z)$ profiles of the atmosphere via observation.

Contents

| | |
|---|-----------|
| List of Figures | xi |
| 1 Introduction | 1 |
| 1.1 The Sun | 2 |
| 1.2 The Solar Atmosphere | 3 |
| 1.3 Solar Flares | 8 |
| 1.3.1 Observations Characteristics | 8 |
| 1.3.2 The Standard Flare Model | 11 |
| 2 Observational Diagnostics and Imaging Spectroscopy | 15 |
| 2.1 Line Formation | 16 |
| 2.2 Density Diagnostics | 20 |
| 2.3 Differential Emission Measure in Temperature | 24 |
| 2.4 Instrumentation | 28 |
| 2.4.1 Hinode EIS | 28 |
| 2.4.2 Hinode XRT | 30 |
| 2.4.3 Hinode SOT | 31 |
| 2.4.4 TRACE | 31 |
| 2.4.5 RHESSI | 32 |
| 2.4.6 IRIS | 33 |
| 3 Density and Velocity Measurements of a Solar Flare Footpoint | 35 |
| 3.1 Flare Observations with Hinode EIS | 36 |

| | | |
|----------|---|-----------|
| 3.1.1 | The June 5th 2007 Event | 37 |
| 3.1.2 | GOES and RHESSI | 39 |
| 3.1.3 | TRACE and SOT | 40 |
| 3.1.4 | XRT | 44 |
| 3.2 | Hinode EIS data | 46 |
| 3.2.1 | Data Preparation and Uncertainties | 47 |
| 3.2.2 | Wavelength Calibration | 48 |
| 3.2.3 | Line Analysis | 51 |
| 3.3 | Hinode EIS plasma diagnostics | 54 |
| 3.3.1 | Intensity, Density and Velocities across the region | 55 |
| 3.3.2 | Footpoint Selection | 61 |
| 3.3.3 | High Velocity Flows | 61 |
| 3.4 | Time Evolution of Selected Footpoints | 69 |
| 3.5 | RHESSI data analysis | 73 |
| 3.6 | Processes taking place at the flare footpoints | 81 |
| 3.6.1 | Electron Stopping Depth | 83 |
| 3.6.2 | Electron Beam Power | 85 |
| 3.6.3 | Flow Speeds | 86 |
| 3.6.4 | Electron Beam Heating | 87 |
| 3.6.5 | Thermal Heating | 88 |
| 3.7 | Conclusions | 89 |
| 4 | Impulsive Phase Flare Footpoint Emission Measure Distributions | 91 |
| 4.1 | Secrets of the EMD | 93 |
| 4.1.1 | DEM to EMD | 93 |
| 4.1.2 | EMD Gradients | 94 |
| 4.1.3 | Early Skylab Observations | 98 |
| 4.2 | EIS Data Preparation | 100 |
| 4.2.1 | Line Selection | 102 |
| 4.2.2 | Line Flux | 106 |

| | | |
|----------|---|------------|
| 4.2.3 | Line Blending | 108 |
| 4.3 | Flare Observations and Footpoint Selection | 110 |
| 4.4 | DEM Technique | 113 |
| 4.4.1 | DEM Inputs and Uncertainties | 118 |
| 4.5 | Flare EMDs | 120 |
| 4.5.1 | Measured Footpoint EMD Profiles | 122 |
| 4.5.2 | EMDs for Different Solar Plasmas | 123 |
| 4.5.3 | Examination of the Assumptions Used | 126 |
| 4.5.4 | Varying the Abundance and Ionisation Equilibrium | 131 |
| 4.5.5 | Electron Densities and Emitting Region Thickness | 132 |
| 4.6 | Discussion | 135 |
| 4.7 | Conclusions | 139 |
| 5 | Measurements of High Densities in Flare Footpoints | 141 |
| 5.1 | Oxygen Diagnostics | 143 |
| 5.2 | Fitting | 145 |
| 5.3 | Fitting Results | 149 |
| 5.4 | Footpoint Densities | 151 |
| 5.5 | Interpretation | 155 |
| 5.5.1 | A Collisional Thick Target Approach | 158 |
| 5.5.2 | Testing for Ionisation Equilibrium | 161 |
| 5.5.3 | Electron-Ion Equilibration Time | 163 |
| 5.5.4 | Testing for Optical Depth Effects | 165 |
| 5.6 | Discussion | 171 |
| 5.7 | Conclusion | 173 |
| 6 | Determining Density and Temperature Profiles Through $\xi(T)$ and $\zeta(n)$ | 174 |
| 6.1 | A Differential Emission Measure in Density - Defining the Problem | 175 |
| 6.2 | Finding $n(T)$ | 178 |

| | | |
|----------|---|------------|
| 6.3 | Forward Fitting with PIKAIA - A Genetic Algorithm | 179 |
| 6.3.1 | Trial Models for $n(h)$ and $n(T)$ | 181 |
| 6.3.2 | Test Event $\xi(T)$ and Line Intensities | 184 |
| 6.3.3 | Density-Sensitive Emission Lines | 184 |
| 6.3.4 | Contribution Functions | 185 |
| 6.3.5 | The Integral | 187 |
| 6.3.6 | Fitness and Residuals | 188 |
| 6.4 | First Results | 188 |
| 6.5 | Multiple GA Realisations | 191 |
| 6.6 | Conclusions and Future Plans | 192 |
| 7 | Conclusions and Future Work | 194 |
| | Bibliography | 203 |

List of Figures

| | | |
|------|---|----|
| 1.1 | Temperatures and densities in the solar atmosphere | 5 |
| 1.2 | The chromosphere in $H\alpha$ | 6 |
| 1.3 | CSHKP flare model | 12 |
| 1.4 | CHIANTI radiative loss curve | 13 |
| 2.1 | Term diagram for Fe XIV | 23 |
| 2.2 | Fe XIV 264/274Å diagnostic ratio | 24 |
| 2.3 | EIS detector schematic | 29 |
| 3.1 | X-ray light curves for the 5th June 2007 flare | 39 |
| 3.2 | TRACE 171 Å for flaring region. | 42 |
| 3.3 | TRACE and XRT imaging for the 5th June 2007 flare | 43 |
| 3.4 | Ca II emission in the northern footpoint | 43 |
| 3.5 | XRT Ti-Poly response and image at second 12-25 keV peak | 45 |
| 3.6 | Intensities, velocities, and densities — Fe XII | 57 |
| 3.7 | Intensities, velocities, and densities — Fe XIII | 58 |
| 3.8 | Intensities, velocities, and densities — Fe XIV | 59 |
| 3.9 | Density diagnostic curves for Fe XII, Fe XIII, and Fe XIV | 60 |
| 3.10 | Footpoint pixels | 62 |
| 3.11 | High temperature velocity shifts at the first 12-25 keV peak | 63 |
| 3.12 | High velocity components in Fe XVI - 15:55:47 UT | 64 |
| 3.13 | High velocity components in Fe XVI - 16:01:05 UT | 64 |
| 3.14 | Double component fits using the R-B asymmetry constraint for Fe XVI | 68 |

| | | |
|------|--|-----|
| 3.15 | Time evolution of Position 0 | 70 |
| 3.16 | Intensity variation of allowed transition | 71 |
| 3.17 | Time evolution of Position 1 | 73 |
| 3.18 | Time evolution of Position 2 | 73 |
| 3.19 | RHESSI Imaging and TRACE | 74 |
| 3.20 | RHESSI HXR Spectra | 78 |
| 3.21 | VAL-C and VAL-E stopping column depth for injected electrons | 84 |
| 4.1 | Line contributions varying in temperature, $G(T)$ | 106 |
| 4.2 | Line contributions varying in density, $G(n)$ | 107 |
| 4.3 | GOES light curves for EMD events | 112 |
| 4.4 | EIS rasters for EMD events | 114 |
| 4.5 | Test EMD solutions for $\alpha = 5.0$ & $\alpha = 5.0$ | 118 |
| 4.6 | Inverted footpoint EMDs from EIS data | 121 |
| 4.7 | Footpoint, active region, and loop EMD comparison | 125 |
| 4.8 | Inverted footpoint EMDs removing optically thick lines | 130 |
| 4.9 | EMDs varying abundances and ionisation equilibrium | 131 |
| 5.1 | Term diagram for O v | 144 |
| 5.2 | Spectrum of the 192Å region from CHIANTI v7.1. | 148 |
| 5.3 | Fitted spectra for the 192Å complex | 150 |
| 5.4 | EMDs for both footpoints in Event (a). | 152 |
| 5.5 | Diagnostic curves for ratios found in Table 5.2. | 153 |
| 5.6 | O v electron density maps | 154 |
| 5.7 | Hydrogen density, electron density, and temperatures from the VAL-E model | 156 |
| 5.8 | Allred flare model parameters for F10 input | 157 |
| 5.9 | Heating rate per particle in the VAL-E atmosphere | 160 |
| 5.10 | I_{192}/I_{248} ratios for multiple temperatures | 162 |
| 5.11 | O v 192Å optical depth | 168 |

| | | |
|-----|--|-----|
| 6.1 | Test model atmosphere | 182 |
| 6.2 | G(n) functions for diagnostics lines | 187 |
| 6.3 | First GA forward model results | 189 |
| 6.4 | Residuals for test GA forward model | 190 |
| 6.5 | 1000 realisations of the GA fitting | 192 |

Chapter 1

Introduction

People often ask me “Why study the Sun?” It rises every morning, and as far as we know it will do the same again tomorrow. On a good day I can normally think of at least a handful of reasons why we should be more aware of our parent star. Starting from the fact its vast output of energy has been the source of heat and light for life to thrive on Earth, to understanding the many aspects of our modern life that are directly influenced by solar activity, such as the communication satellites that guide our mobile phones and Sat Navs, to the national power grids that light our homes, and now, controversially, to the link between solar activity and the extreme winters of recent years. Usually this is met with a nod or a slightly unconvinced acknowledgement. I suppose this is understandable, most of us probably can’t recall the last time a solar flare damaged their iPhone, so it is easy to take for granted something so seemingly unchanging. So for a long time I went without meeting anyone outside of this field who had first hand experience of solar activity affecting their day-to-day life. It seemed I would be stuck in trying to convince people that what happens on the Sun can really influence us here on Earth. At least this was the case up until a few weeks ago, after talking to an ex-submariner. On telling them what I worked on they replied, “oh, solar flares! We had charts to work out how to adjust the radio for them”. Apparently, the very low frequency radio waves used to communicate with submarines at shallow depths are disturbed by changes in the Earth’s ionosphere, a layer which solar flare

X-rays easily ionise. Being able to predict the disturbance from solar activity that day is obviously very important to be able to communicate with the crew. Of course, this is one of many such examples. So whilst it may not be immediately apparent, the Sun has a huge influence on our lives on many scales. Even if it simply means the GPS takes a little longer to connect one day, or that the lights occasionally flicker in the house. It is therefore crucial to understand what drives phenomena like solar flares as we become more dependent on technology. So while we sip on our coffee and contemplate the latest solar data in the comfort of an air conditioned office, we should spare a thought for those worrying about the same, somewhere beneath the sea!

1.1 The Sun

If you are lucky enough to step outside on a clear autumn night, far from any street lights, houses, and shops, you can marvel at the billions of stars that illuminate the night sky. Their light makes a journey of thousands of light years across our galaxy to reach us, by which time they are a glittering point in the sky. To be visible to us across such vast distances means they must be immensely bright. The power behind this luminosity is nuclear fusion in the dense core of a star, where hydrogen is fused together releasing energy in the form of radiation.

The Sun is one of these billions of stars and is found at centre of our solar system. It is a G-type main sequence star with a surface temperature of around 5800 degrees Kelvin. Being within such close proximity, the Earth is intimately linked with the physical processes governing the Sun. Over the course of a year parts of the Earth receive slightly more or less radiation which gives rise to the seasons. For us, the differences between summer and winter are stark, but the change in radiation received is marginal. Should the Sun have been any one of the other classes of star, life would have been very different indeed, if at all possible.

The Solar Interior — In the Sun fusion powers a radiating core with a temperature of around 15 MK and an extremely high electron density of 10^{34} cm^{-3} . In the core of a

solar-like star the opacity is high enough that energetic photons released by fusion are partially absorbed, keeping the plasma hot enough to maintain fusion, but low enough to allow energy to eventually escape. The energy from fusion is transported by photons which interact with the background ions and electrons taking approximately 100,000 years to reach the surface. However, as the temperature drops towards the exterior of the star the opacity increases towards a peak. At this point radiation can no longer transport energy efficiently and for the star to remain in hydrostatic equilibrium it must transport energy by a new means. Since the energy transport rate has slowed the temperature gradient becomes very steep, and at critical gradient, defined by the Schwarzschild criterion, convection will take over from radiative transport. Areas with a plasma density lower than the background will now continue to rise to the surface much like hot air circulating in a heated room. Once at the surface the opacity drops again and the plasma can radiate into open space and cool before beginning a journey back towards the inner edge of the convective zone where the cycle is repeated. In high resolution imaging the surface of the Sun looks somewhat like a pan of boiling water. Granulation cells of around 1000 km in diameter appear bright in the centre, surrounded by cooler (darker) material that is flowing back towards the core.

The solar convective zone is also observed to experience differential rotation, where the equatorial regions of the Sun have a rotation period several days faster than at the poles. The effect of this is to create a large shearing of the plasma at the boundary between the radiative and convective zones known as the *tachocline*. The shearing motion in this region is now accepted as a possible explanation for the generation of large scale solar magnetic fields through a dynamo processes.

1.2 The Solar Atmosphere

The Photosphere — The photosphere is often described as the ‘surface’ of the Sun. As there is no solid surface a definition is often made at the height where the optical depth becomes less than $\tau = 1$ for wavelengths in the green part of the optical spectrum at 5000\AA ($1\text{\AA} = 0.1\text{ nm}$). The density above the outer edge of the convection zone drops

off quickly with height, causing the rate of absorption of photons by negative hydrogen ions to also fall. Photons emitted from this layer can therefore travel freely into space without being reabsorbed. Since the photosphere is significantly brighter than the atmosphere above, it is the layer that we see from Earth. The photosphere emits like an almost perfect black body at a temperature of around 5700 K, radiating around 3.8×10^{26} W of energy into space (Stix 2004) where on average around 1300 Wm^{-2} of this is received at the Earth's surface.

The most prominent observational feature of the photosphere are dark patches known as sunspots, which are easily observed by projecting the solar disc onto a white surface. It is now well established by observation and modelling that sunspots are the locations of strong magnetic fields of several thousand Gauss originating from below the photosphere. The plasma beta, $\beta = 8\pi p/B^2$ where p is the gas pressure and B is the magnetic field strength, is a ratio of the gas to magnetic pressure in a plasma. Below the photosphere $\beta > 1$ and the gas pressure will dictate the motion of the magnetic field. Here convective motions will 'stir' the magnetic field, and in places a collection of magnetic *flux tubes* may emerge from below the surface and rise into the solar atmosphere. Sunspots appear at the locations of this flux emergence, where the magnetic field suppresses the conductive cycle and stops the flow of heat into the photosphere (Chandrasekhar 1961). The result is that the surface temperature drops which appears as a darker area on the solar disc.

The Chromosphere — When we talk of the solar atmosphere, we refer to the plasma between the photosphere and the outer edge of the corona where the tenuous boundary between interplanetary space lies. At the photosphere the hydrogen density is around 10^{17} cm^{-3} but in moving radially outward the density drops rapidly to 10^9 cm^{-3} at the edge of the atmosphere. The atmospheric temperature and density as a function of height has been modelled by Vernazza et al. (1981) and we show these parameters from their quiet sun model (VAL-C) for reference in Figure 1.1. Due to the lower density the solar atmosphere is much fainter than the photosphere. However, the chromosphere can be viewed from Earth by optical instruments using filters at carefully

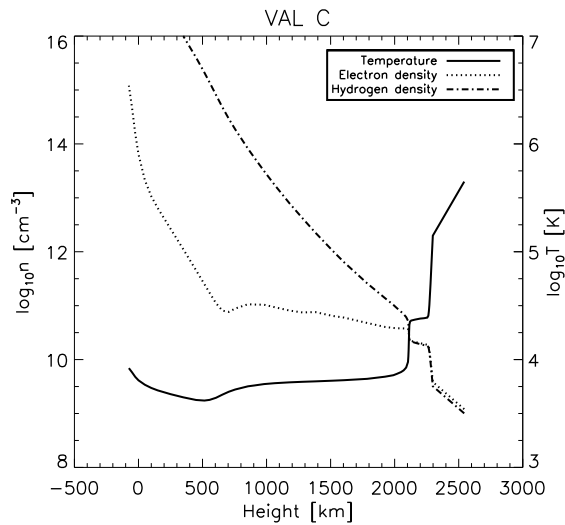


Figure 1.1: Temperature, electron density, and neutral hydrogen density as functions of height above the photosphere — plotted from parameters modelled by Vernazza et al. (1981).

selected wavelengths that remove the bright contribution from the photosphere. The absorption lines of Ca II (singly ionised) H and K lines at 3968Å and 3933Å show features close to the temperature minimum at around 500 km. The chromosphere can also be viewed in emission during a total solar eclipse. During totality the disc occults the photosphere and the chromosphere appears as a red ring around the dark disc with narrow fiery structures seen extending into space known as *spicules*. The plasma beta drops in favour of the magnetic field above the photosphere, and this allows structures like spicules, extending out to 10,000 km, and cool material trapped in magnetic loops (prominences) to form. The solar atmosphere above the photosphere is very non-uniform as a result. Large scale super-granulation cells are also visible as the *chromospheric network* which may be linked by dynamic processes with the corona. An image in H- α of the chromosphere from the Dutch Open Telescope is found in Figure 1.2 showing the chromosphere above a sunspot where dark chromospheric *fibrils* trace magnetic structures above the photosphere.

In Figure 1.1 we see that the temperature above the photosphere drops slightly to a minimum around 500 km as would be expected for an atmosphere continuing to lose

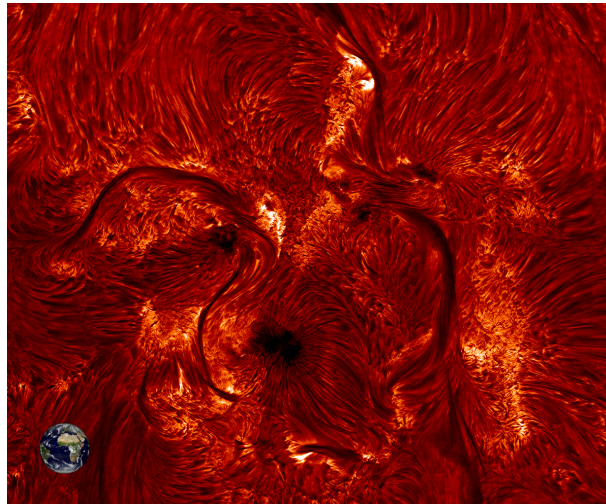


Figure 1.2: The chromosphere in H- α emission taken by the Dutch Open Telescope. Image courtesy of the University of Utrecht and Rob Rutten.

energy from radiation and conduction. However, the presence of dynamic motions and the magnetic field (Mariska 1992) increase the temperature again with height. Above the minimum the temperature rises gradually to around 6000 K at a height of 1000-2000 km. In the model by Gabriel (1976) radiative losses in the hydrogen Lyman- α line causes another small temperature plateau at around 20,000 K and 2000 km. The region between 500-2000 km (4000 - 20,000 K) commonly defines the chromosphere.

The Transition Region — A description of the transition region is often left to a mere sentence in many texts, yet it is extremely important in balancing the energy transport between the chromosphere and corona. The excellent book by John Mariska (Mariska 1992) defines the transition region as the plasma above the temperature plateau at 20,000 K and the lower edge of the corona at 10^6 K. The temperature gradient in this region is extremely steep and in these models represents a height of only a few km. Emission in this region is dominated by atomic lines such as C IV, O IV, and Si VI. As with the chromosphere, imaging in these lines reveals that the transition region is not a uniform layer and may be filled with funnels of plasma rising into the corona and small loops linked to the chromospheric network (Peter 2001). The process that

is heating the corona to over 1 MK must transfer its energy through the transition region, and in reverse the chromosphere will also be heated through it by conduction from hot corona. The same is true for any mass that leaves the chromosphere into the solar wind, or returns back to the solar surface.

The Corona — Prior to the invention of the coronagraph, a telescope with an occulting disc in the centre, the corona was only visible during total eclipses as white diffuse structures extending out into space. The hot structures appear white in optical wavelengths as the emission is predominantly photons from the photosphere scattered by free electrons in the corona. Alongside optical observations the corona is also visible at infrared wavelengths. The magnetic field dominates the morphology of the low density corona. The plasma can be described as *frozen-in-field* as the magnetic field prevents plasma crossing between field lines. Magnetic fields originating from below the photosphere trap hot plasma in loops reaching out to around 3 solar radii with temperatures of 1-3 MK. The discovery of the true coronal temperature was an interesting test for atomic spectroscopy. In the early 1900's a green emission line was observed at 5303Å which could not be identified as being emitted from any known element and was assumed to originate from a hypothetical element named *coronium*. After some years of improved measurement and atomic theory it was later identified in the 1930's to originate from highly ionised iron, which could only be formed at the extreme temperatures in the corona.

The processes that gives rise to the extremely high temperatures in the corona have been a problem in solar physics for many years. One would expect the temperature to fall off with increasing distance from the photosphere, however, some energy source continues to heat the corona. Various models have be proposed, from the release of magnetic energy stored in fields stressed by the motion of the photosphere, plasma wave oscillations leaking from the photosphere and carried into the corona by structures like spicules, and continuous eruptive events such as *nano-flares* (Walsh & Ireland 2003; Hannah et al. 2011).

1.3 Solar Flares

1.3.1 Observations Characteristics

One of the earliest documented observations of a solar flare was by R.C. Carrington and R. Hodgson in the 19th century [Carrington \(1859\)](#). While projecting and drawing a large group of sunspots Carrington witnessed extremely bright white spots growing quickly over the sunspots. The *Carrington flare* was the first recorded example of a white light flare and is regarded as being the largest flare since geomagnetic events have been recorded. Flares of this nature are exceptionally rare, although numerous flares of lower energy output may occur daily during periods of high solar activity. The frequency of flares is closely correlated to the solar cycle, a roughly 11 year rise and fall in the number of sunspots. As mentioned earlier these sunspots are formed in regions of strong, complex magnetic fields and plasma in atmosphere above them is confined and heated by the behaviour of these fields. An *active region* such as this can be observed from UV up to soft X-Ray and extend high into the corona. During solar minimum it is possible to observe almost no sunspots on the disc for days, or even months in the case of the latest deep 2009-2010 minimum, and flares and eruptive events will be rare. At solar maximum there can be several large sunspots on the disc at one time, and their associated active regions will harbour enough energy to release frequent flares.

A solar flare is a rapid, explosive release of colossal amounts of energy stored in the solar atmosphere. Up to 10^{33} ergs of magnetic energy can be released in the space of a few minutes to an hour with the cooling of superheated plasma visible for many hours after. The flare is often accompanied by a readjustment of the coronal magnetic field which can result in a coronal mass ejection (CME), an eruption of charged particles into space, and emission across the entire electromagnetic spectrum from radio bursts to γ -rays.

Generally, a flare can be characterised by a fast rise in soft X-ray (SXR) flux, the *impulsive phase*, followed by a slower decay. The total SXR flux between 1-8 Å is

measured by the Geostationary Operational Environmental Satellites (GOES) and is used as a classification for the size of a flare. The flare classes start at A for peak fluxes above 10^{-8} W m^{-2} , B for 10^{-7} W m^{-2} , and follow the same pattern for C, M, and X class flares. X-class flares are rare, with only a handful occurring in a year, but are extremely energetic and are often followed by geomagnetic storms. The Halloween storms of 2003 were the result of several X-class flares, triggering aurora as far south as Florida and causing power outages in Sweden.

X-rays — The photon spectra of the SXR regime, around 1-10 keV, is primarily the result of thermal bremsstrahlung radiation emitted by electrons undergoing Coulomb collisions with ions (mostly ionised hydrogen) in a Maxwellian plasma distribution. In this ‘free-free’ process, the electron is deflected by the ion, losing a part of its kinetic energy by emitting an X-ray photon. The bulk of the flare X-ray emission is emitted by this thermal process. It is mostly emitted by hot plasma which rises and expands into hot *flare loops* in the corona, but can sometimes be found in compact areas during the impulsive phase of the flare (Mrozek & Tomczak 2004). Also important in flare spectra are the high energy bound-bound transitions emitted by ions in high ionisation states with filled outer shells such as Fe xvii, Ne ix, and O viii. At peak flare temperatures of 20-30 MK ionisation states as high as Fe xxv are observed. Although these are highly energetic transitions, with photon energies greater than 5 keV, the free-free and free-bound processes begin to contribute more to the overall emission above 10 MK.

In the hard X-ray (HXR) energy range, 10-100 keV, the photon spectra can be characterised by a high energy power-law tail. The primary emission process here is non-thermal bremsstrahlung, again mostly through electron-ion interactions. As with thermal bremsstrahlung, a photon is emitted from an electron losing energy as it is deflected. However, when the incoming electrons have been accelerated, and are far more energetic than the background plasma, the resulting photon spectra deviates from the thermal case and takes the form of a power-law. In solar flares, an observed non-thermal tail in the HXR photon spectra is a good indication of the presence of accelerated, or beamed, electrons. In the *thin-target* approximation, the target density is low, and the

electron beam is relatively unchanged by the few collisions (suitable in the corona). In the *thick-target* case, the ambient density is high such as in the chromosphere. The kinetic energy of the rest ion is relatively unchanged by the bremsstrahlung interaction, and only a very small fraction ($\sim 10^{-5}$) of the energy from the fast electron is lost to bremsstrahlung emission. However, in a dense plasma, collisions with other electrons via Coulomb collisions are much more effective at sharing the kinetic energy due to their equal mass. Most of the beam energy in a thick-target is therefore lost in heating the ambient plasma through electron-electron collisions. During the flare impulsive phase, HXR emission can often be observed in compact areas deep in chromosphere. These regions are commonly found at the base of flaring loops and are known as the *flare footpoints*.

Following the work by [Neupert \(1968\)](#) it was shown that the rate of change of the SXR emission is often similar to the evolution in HXR emission. We can arrive at this conceptually if we consider that the HXR emission is proportional to the power emitted by the flaring mechanism. If we assume that the corona stores this energy, i.e. any losses are slow compared to the rate of energy input, then the SXR emission found in the corona should be the integral of the HXR emission in time. For flare observations, it is sometimes convenient to estimate the HXR evolution by taking the time derivative of the SXR emission.

Ultraviolet & Extreme-Ultraviolet — We have discussed that the HXR footpoints could be a location of flare heating through the interaction of non-thermal electrons with the ambient plasma. At lower photon energies, Ultraviolet (UV) and Extreme-Ultraviolet (EUV) line emission is also often observed at similar locations to the HXR emission. Above the photosphere the higher temperatures and relatively low densities change the dominantly observed spectral features from approximately a black-body with absorption lines to emission lines and continua. The formation temperature of these lines ranges from around 10,000 K to over 10 MK. In the flare footpoints they are enhanced significantly with respect to the background transition region and corona. The location of the enhancements varies during the flare evolution, and in the impulsive

phase UV emission normally associated with the chromosphere is found to be enhanced in bright *ribbons* suggesting that the emission originates from low in the solar atmosphere. Along these narrow ribbons, brighter compact sources in UV and EUV may be also found which correspond to the location of the HXR footpoints. The bulk of the rise phase emission is therefore confined to the lower solar atmosphere. As the flare reaches its peak, EUV emission will start to be found in loops extending from the ribbon areas into the corona. These loops brighten significantly across the flare peak and decay slowly during the gradual phase.

Optical — For white light emission to be viewed by projection as easily as the Carrington event is exceptional. However, optical emission is also observed for a wide range of lower energy flares. Even in small events for white light to be viewed against the photospheric background requires a large amount of energy, and it is found that a large part of the total flare emission is in optical and UV wavelengths (Woods et al. 2006). The mechanism behind white light emission is still not well understood as it requires the flare energy deposition to penetrate to below the chromosphere. Heating from the chromosphere and proton beams have been suggested as possible solutions (Fletcher et al. 2011).

1.3.2 The Standard Flare Model

It is generally accepted that the energy source for a flare lies in the coronal magnetic field. The emergence of twisted flux from below the photosphere, and motions in the photosphere can introduce energy into coronal loops which is stored over a period of hours or even days. The system eventually becomes energetically unstable and will release the stored energy, either spontaneously or from a perturbation in the field. To produce the observed heating and non-thermal electron signatures requires a mechanism that can release the coronal magnetic energy and raise electrons to non-thermal velocities. In most current flare models, magnetic reconnection is proposed as a solution that allows the reconfiguration of the magnetic field to a lower energy state.

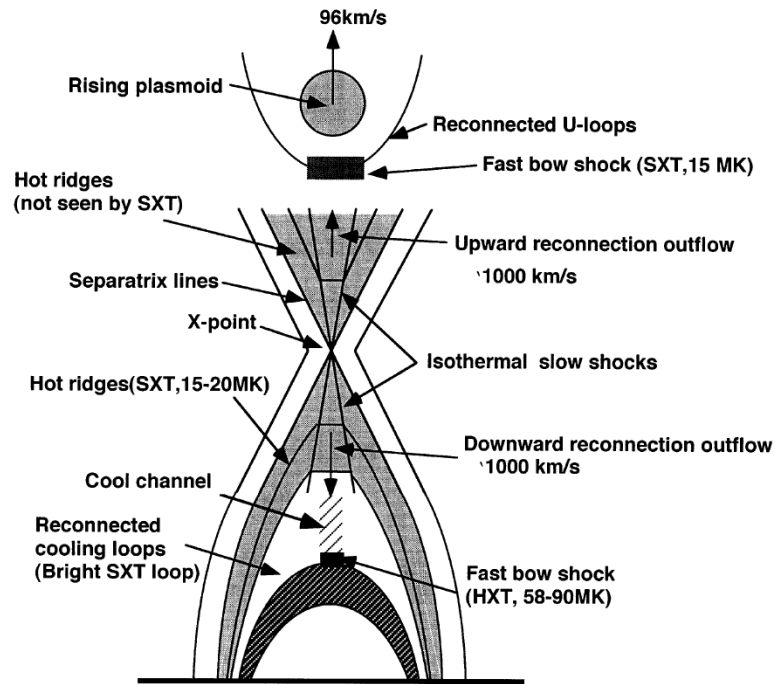


Figure 1.3: Schematic of the CSHKP flare model from [Tsuneta \(1997\)](#).

Over the past 30 years a relatively consistent picture has emerged for the evolution of a solar flare. The CSHKP model has been widely used as a standard model for solar flares based on the 2D reconnection of a single loop ([Carmichael 1964](#); [Sturrock 1966](#); [Hirayama 1974](#); [Kopp & Pneuman 1976](#)). A cartoon of the model and magnetic field layout can be seen in [Figure 1.3](#). The rising plasmoid is a magnetic loop or structure which is moving and stretches the field below. As the two sides of the loop are drawn together, the field on the inside of the loop reconnects near the ‘X-point’ (or ‘X-line’ in 2.5D), resulting in a new closed loop forming inside the original loop. Magnetic energy is released at or near the X-point region and is directed down the loop field lines into the footpoints. The method of energy transport is still unknown but may take the form of plasma waves or beams of accelerated electrons.

The collisional thick-target model ([Brown 1971](#)) uses a beam of accelerated electrons injected from the corona into the chromosphere to generate bremsstrahlung emission and plasma heating, both of which are routinely observed in HXR and EUV spectra. A secondary effect of the plasma heating is to drive motions in the chromospheric plasma.

If the footpoint plasma is heated beyond the peak of the radiative loss curve (Figure 1.4) then the plasma will not be able to balance the energy input and will begin to expand, rising back into the loop. The process is known as chromospheric evaporation, and is observed by the Doppler shift of hot EUV lines (Doschek et al. 1980) and leads to the hot SXR emission found in flare loops. The modelling by Fisher et al. (1985) suggests that two types of evaporation exist, gentle and explosive. If the heating time-scale is less than the local hydrodynamic expansion time-scale (the plasma sound speed) then the evaporation is *gentle*. The evaporation is considered to be *explosive* when the heating time-scale is faster than the plasma can compensate for and the flow speeds can be above the plasma sound speed. The cut-off flare input energy between these scenarios is around $3 \times 10^{10} \text{ ergs s}^{-1} \text{ cm}^{-2}$.

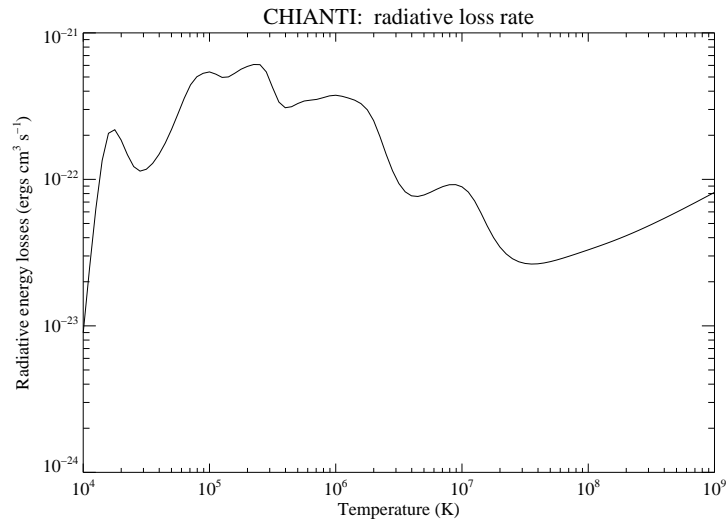


Figure 1.4: The radiative loss curve calculated by CHIANTI v7.0 (Landi et al. 2012) for a density of 10^{11} cm^{-3} and coronal abundances.

In the standard flare model the electrons are assumed to be accelerated in the X-point region and precipitate down the magnetic field lines into the chromosphere. This combination of magnetic reconnection and the thick-target model has been the cornerstone of flare research for decades, primarily due to its ability to explain footpoint HXR emission, plasma heating, and chromospheric evaporation. However, there

is still no single agreed method in which the electrons are accelerated in the corona. Problems also exist in transporting charged electrons from the corona to the chromosphere without the ‘return current’ that exists to balance the charge and current of this beam becoming unstable and halting or significantly redistributing the energy of the beam electrons. Also, heating deep layers of the atmosphere to create white light emission is challenging without very high energy electron beams. Models involving the acceleration of electrons *locally* in the footpoints from the transport of plasma waves have been proposed to solve these issues (see [Russell & Fletcher \(2013\)](#)).

Chapter 2

Observational Diagnostics and Imaging Spectroscopy

This thesis is primarily concerned with diagnosing the thermodynamic properties of solar flare footpoint plasma. Fortunately for solar physicists, much of the energy lost by the footpoints during a flare is in the form of optically-thin line radiation, which in UV and EUV wavelengths is rich in diagnostics of temperature, density, and plasma dynamics. The goal of this chapter is to present the reader with sufficient background in the atomic physics leading to these diagnostics, and the necessary assumptions in their interpretation. We begin with an overview of the formation of optically thin emission lines.

Observationally, an emission line can be characterised by a Gaussian line profile and is a function of wavelength. As the next section will explain, the line emission is the result of electrons undergoing transitions between states of quantised energies, where photons are emitted at a wavelength inversely proportional to the difference in energy of the two states ($\lambda_0 = hc/(E_2 - E_1)$). For a plasma in thermal equilibrium, the random particle velocities Doppler broaden the emission, resulting in a Gaussian line profile centred on the *rest wavelength* λ_0 . In all fields of astronomy the most basic of techniques is to fit a Gaussian profile of three parameters, height, centroid position, and width, to the observed profile of a spectral line. From these three values

we can find the line intensity, velocity of the plasma relative to us, the thermal width and therefore ion temperature, and if present, estimate the component of non-thermal particle motions. From these relatively simple measurements, astronomers have been able to learn an enormous amount from incredibly distance sources.

2.1 Line Formation

Line emission in plasmas and the solar atmosphere is associated with the transitions of electrons moving between energy states of an ion or neutral atom. A variety of different physical processes can initiate these transitions and also lead to ionisation or recombination, for example; collisional excitation and de-excitation, spontaneous radiative decay, or collisional ionisation and dielectronic recombination. The characteristic time scale of these depends on the ion density, electron density, and the respective collision cross sections. In the case of a quiet transition region, where the rate of absorption of background photons is low, collisions between ions and free electrons drive the majority of upward transitions, with radiative decay being responsible for most transitions to lower levels. We also note that while in the transition region and corona the spectra is dominated by emission from ions, emission lines from molecules are also found in cooler regions of the Sun. Spectral lines from fundamental vibration-rotation transitions of CO are seen in the μm wavelength range corresponding to temperatures of ~ 4100 K or even as low as 3800 K. From the work by [Avrett \(2003\)](#) it is apparent that these lines are formed in the temperature minimum at around 500 km above the surface.

The balance of ionisation and recombination processes is extremely important in understanding the observed line emission. The fractional abundance — the proportion of a plasma in each ionisation stage — depends on this balance between the rate of electrons leaving an ion and those recombining. The brightness of an emission line from an ion then depends on this abundance, therefore, accurate rate calculations and careful assumptions must be made to ensure that any diagnostics are correct. In most cases the ionisation and recombination time scales are far longer than the collisional excitation time scales and can be treated separately. This is the assumption

of ionisation equilibrium, and the effect of relaxing the assumption in flaring situations will be discussed throughout this thesis.

In the case of the hot, relatively low density, corona and transition region, the atmosphere can generally be assumed to be *optically thin*. The photons emitted along the line of sight will therefore travel freely through any material between the source and observer. At lower temperatures, and higher densities, the plasma can become *optically thick*, where the emitted photons may be absorbed, scattered, or re-emitted before reaching the observer. As mentioned, in most circumstances the optically thin assumption is valid, although later in the thesis we have discussed circumstances where the assumption may not hold.

The final assumption we make before calculating line intensities is to assume that the plasma is in local thermal equilibrium. Defining the exact temperature of a plasma can be difficult when the very nature of a plasma lends itself to be influenced by magnetic fields and ionisation processes, this is especially true in the dynamic solar atmosphere. Yet in the regions of the atmosphere we are concerned with, the electron-electron collision times are very short, therefore the plasma will equilibrate quickly to temperature changes. We can then assume that the temperature can be described by a Maxwell-Boltzmann distribution.

The emissivity in a transition from an upper level j , to lower level i , emitted by a volume element dV can be expressed as

$$d\epsilon_{ji} = n_j A_{ji} h\nu_{ji} dV \text{ erg s}^{-1}, \quad (2.1)$$

where A_{ji} is the Einstein coefficient of the transition for spontaneous emission, n_j , the number density of ions in the excited state j , and ν_{ji} is the emitted frequency.

In an optically thin plasma the total flux received by an observer is found by integrating each volume element along the line of the sight, and at a distance R is given by

$$F_{ji} = \frac{1}{4\pi R^2} \int_V n_j A_{ji} h\nu_{ji} dV \text{ erg cm}^{-2} \text{ s}^{-1}. \quad (2.2)$$

Commonly in observational studies this is reduced to an integral over the line of sight depth; where the spatial resolution of the instrument defines the minimum area that can be observed.

The number density of ions in the excited state n_j depends on a combination of the excitation processes mentioned above and the plasma temperature and electron density. For many calculations it is easier to express n_j as a number of ratios which can be individually determined. We then have

$$n_j = \frac{n_j}{n_{ion}} \frac{n_{ion}}{n_{el}} \frac{n_{el}}{n_H} \frac{n_H}{n_e} n_e, \quad (2.3)$$

where n_j/n_{ion} is the relative number population of ions in the excited state compared to all other levels, n_{ion}/n_{el} is the abundance of the ionisation stage, n_{el}/n_H is the elemental abundance relative to Hydrogen, and n_H/n_e is the ratio of the number density of Hydrogen to the electron density.

In this thesis we will often refer to these quantities for deriving physical parameters from spectra, for example, in density diagnostic ratios, differential emission measures, and finding optical depths. We obtain these from various sources. The elemental abundances for different parts of the solar atmosphere continue to be measured by many authors, for example [Grevesse & Sauval \(1998\)](#) and [Feldman et al. \(1992\)](#), and are chosen to best suit the solar plasma in question. The number density of electrons can be measured spectroscopically or by volume estimates, and the ionisation level in the atmosphere can be obtained through semi-empirical modelling. Theoretical atomic physics calculations are required for each ion to find the abundance of the ionisation level as a function of temperature, for example the percentage of Oxygen v compared to neutral Oxygen at $\log T = 5.4$ is 54% from [Mazzotta et al. \(1998\)](#). This is also true for the relative number population n_j/n_{ion} , which must be calculated by solving a system of equations that describe the balance of all excitations and de-excitations for every possible transition within the ion which is also sensitive to the plasma temperature and density.

Thanks to a large and ongoing collaborative effort, the CHIANTI atomic physics

database (Dere et al. 1997) provides the most up to date calculations and atomic data that are essential for solar and stellar spectroscopy, for which we are eternally grateful. Compiled from theoretical work and sources such as the National Institute of Standards and Technology (NIST), it is available for use in the Interactive Data Language (IDL). Results of complex calculations which require many weeks of work are therefore always available.

Moving back to describing the line emission in terms of the plasma properties, we can group all of the terms involving the atomic physics of the line formation into a function of temperature and density called the line *contribution function*, $G(T, n_e)$, where

$$G(T, n_e) = \frac{n_j}{n_{ion}} \frac{n_{ion}}{n_{el}} \frac{n_{el}}{n_H} \frac{n_H}{n_e} \frac{A_{ji}}{n_e} h\nu_{ji} \text{ erg cm}^3 \text{ s}^{-1}. \quad (2.4)$$

The contribution functions for each line are calculated from theory for a range of temperatures and densities, and are often peaked strongly in temperature — this peak temperature is often referred to as the formation temperature of the line. The observed line flux from Equation 2.2 can now be written as

$$F = \frac{1}{4\pi R^2} \int_V G(T, n_e) n_e^2 dV, \quad (2.5)$$

separating the atomic physics contained in the contribution functions from information about the emitting plasma environment. The remaining term $n_e^2 dV$ is a combination of the number of free electrons and the electron density n_e within a volume element dV , and is referred to as the emission measure. The total emission measure, defined as

$$EM = \int_V n_e^2 dV \text{ cm}^{-3}, \quad (2.6)$$

is the first step in learning about the properties of the emitting plasma; as it can be directly recovered from the measured flux of a spectral line with a known contribution

function.

A very simple temperature diagnostic can be made by studying an image obtained in one emission line. For the majority of strong lines in the EUV range the contribution functions are strongly peaked, and an image of the emission around the line centre will reveal bright features emitting at the formation temperature of the line. This technique is the basis of many narrow-band imaging instruments such as TRACE and SDO/AIA. However, the filter bandpass often includes a number of lines at different temperatures complicating the analysis, and as we will show later, features in the solar atmosphere are not necessarily isothermal.

2.2 Density Diagnostics

As was shown towards the end of Section 2.1 the plasma emission measure is proportional to the volume of the emitting region and the square of the electron density. As the depth along the line of sight of a footpoint is hidden to us, the volume can not be explicitly measured from our instruments, hence the density inferred remains an upper or lower limit derived from estimates of the emitting region height. However, we can amend this through the use of density sensitive line ratios using the excellent spectral coverage available on instruments such as *Hinode*/EIS, allowing us to make density measurements independently of the emitting volume and other plasma properties.

Large differences in the spontaneous decay rates of allowed transitions and those from metastable levels lead to varying density sensitivity between emission lines of the same ion. Allowed lines follow the rules for electric dipole transitions and have large transition probabilities. Electrons in metastable levels on the other hand must decay either via *forbidden* transitions, a magnetic dipole transition which breaks the L-S coupling selection rules, or *intercombination* transitions, where the electron moves to a state with different spin. These effects greatly reduce the probability of spontaneous decays and the emitted flux. As the electron density rises, collisional excitation and de-excitation rates will contribute more to the level populations and the flux ratio of the two emitted lines becomes sensitive to electron density.

Three Level Case — This is best explained through an example of a simple three level diagnostic. A ground state, Level 1, is accompanied by two upper levels where Level 3 is metastable. At low densities collisional excitation populates both upper levels and one can assume the two level approximation; where collisional excitations are balanced by an almost immediate decay from the upper level, and only the ground level and excited levels are included, i.e no intermediate levels are considered. This case where only the ground level is significantly populated is known as the *coronal approximation*. The excitation and de-excitation balance for each transition can be written as

$$n_e n_1 C_{12} = n_2 A_{21}, \quad (2.7)$$

and

$$n_e n_1 C_{13} = n_3 A_{31}, \quad (2.8)$$

where n_1 , n_2 , and n_3 are the level populations, C_{12} and C_{13} the collision excitation rate coefficients, and A_{21} and A_{31} are the decay rates. The terms on the left hand side give the number of transitions into the excited state while the number of decays is given on the right — corresponding to the emitted flux in that transition. The flux ratio in this case is simply proportional to the ratio of the collision rates, i.e

$$\frac{F_{31}}{F_{21}} \propto \frac{C_{13}}{C_{12}} \quad (2.9)$$

As the density increases collisional excitation rates increase for both lines, and collisional de-excitations become the increasingly preferred method of de-exciting the metastable level since A_{31} and A_{32} are small. Level 2 will also be de-excited by collisions but the contribution from spontaneous de-excitation A_{21} is far larger and C_{21} can be ignored. The flux F_{21} now rises faster than F_{31} for two reasons. More collisional

excitation results in more transitions from Level 2 to 1, but excited electrons in Level 3 may not always spontaneously decay, and collisional de-excitations from Level 3 to 2 will quickly decay, further increasing F_{21} compared to F_{31} . Eventually the collisional de-excitation rate in both lines becomes greater than the radiative decays and the flux ratio returns to approximately the ratio of the spontaneous decay rates A_{31}/A_{21} . Since the flux ratio depends on electron density and can be calculated, measurements of the flux in both lines can be used to directly measure the electron density. However, uncertainties will arise in the inferred density from errors in obtaining the line flux, such as blends and fitting errors, and where the assumptions are not suitable for the plasma conditions.

Four Level Case — The density diagnostics used throughout this thesis (see Table 2.1) can all be described by a 4 level system which is common to many EUV diagnostics in solar and stellar atmospheres. This arises from similarities in the ions atomic structure, leading to a pair of transitions sensitive to density, where one of the upper levels is populated by collisional excitations from a metastable level. The Fe XIV diagnostic is perhaps the simplest configuration here, arising from the Aluminium isoelectronic sequence with 3 electrons in the $n = 3$ outer shell. In this case the flux ratio of the $\lambda 274$ transition, excited from the $3s^2 3p \ ^2P_{1/2}$ ground state, to the $\lambda 264$ transition, excited from the $3s^2 3p \ ^2P_{3/2}$ metastable level, is density sensitive. A term diagram for the Fe XIV diagnostic can be found in Figure 2.1.

Levels 2, 3, and 4 are all excited via collisions from Level 1. At low densities only Level 1 has a significant population and spontaneous decays from Level 2 to Level 1 are rare due to A_{21} being very small. Of the two allowed lines, the $3 \rightarrow 1$ transition is brighter than $4 \rightarrow 2$ by around a factor of 2; this is due to the change in angular momentum required in exciting electrons from the Level 1 $\ ^2P_{1/2}$ state to the Level 4 $\ ^2P_{3/2}$ state - hence $C_{13} \gg C_{14}$.

As the electron density increases, further collisional excitation boosts the population in Level 2 as electrons can not easily decay back to Level 1 — this is seen clearly in Figure 2.2. As there is no change in angular momentum between Levels 2 and 4, the

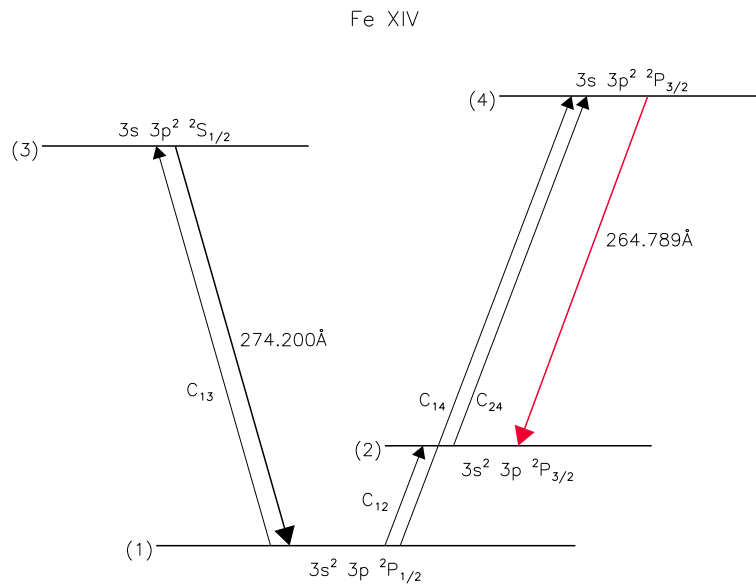


Figure 2.1: Term diagram for Fe XIV showing the four levels involved in the density diagnostic. Level 2 is metastable and has a very low spontaneous decay rate to Level 1 but may be populated at high densities by collisional excitations from Level 1. The red line shows the 264 Å transition which is excited from the metastable state. The ratio of this line to the 274 Å transition excited from the ground state forms the density diagnostic.

collision rate $C_{13} \approx C_{24}$, therefore a second route is available in populating Level 4 and the ratio F_{42}/F_{31} rises with density.

At very high densities, both the metastable level and ground state populations become balanced by collisional excitation and de-excitation, and flux ratio loses any density sensitivity — this is shown on the left of Figure 2.2 as the ratio levels off above 10^{12} cm^{-3} at a value of 2.9.

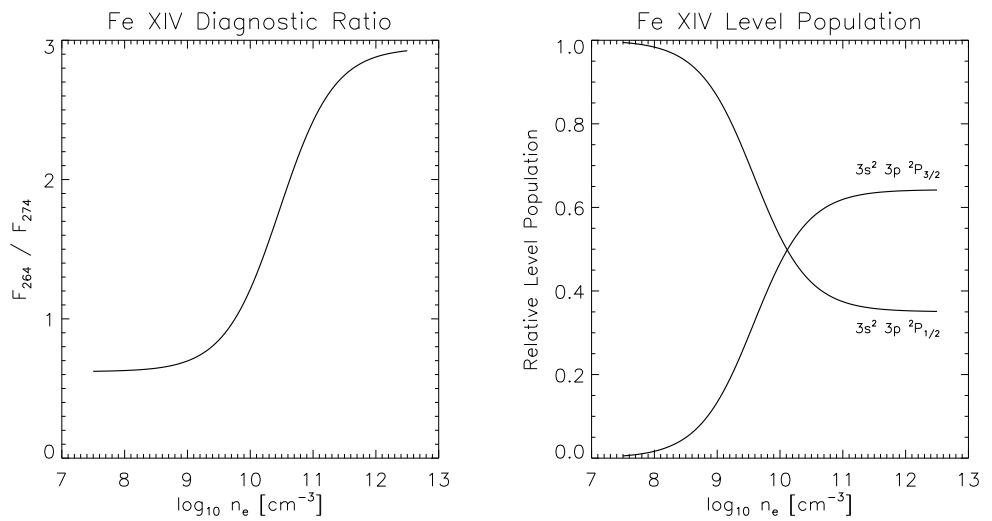


Figure 2.2: Diagnostic flux ratio for the Fe XIV 264/274 diagnostic. In the left panel the flux ratio is shown across the diagnostic density range. On the right panel the electron population in the lower level of the transitions is shown. The population in the metastable level $3s^2 3p \ ^2P_{3/2}$ can be seen increasing with density as collisional excitations fill the level.

2.3 Differential Emission Measure in Temperature

Many features in the solar atmosphere contain plasma at a range of temperatures, from large scale coronal loops to more compact footpoint sources. Even in cases where a plasma may be described as iso-thermal, the temperature distribution is often Gaussian in profile. Finding the temperature distribution is of great importance for understanding heating and energy transfer in the solar atmosphere. As sources at different temperatures in close proximity are never completely isolated when viewed with current multi-band or spectral imagers, or when viewing optically thin features along the line of sight, we require a method of recovering the temperature distribution within an unresolved volume. Finding the differential emission measure (DEM) in temperature is a technique used extensively throughout solar and astrophysics, returning the temperature distribution of the emitting plasma by combining narrowband filter or emission line intensity measurements sensitive to a range of temperatures.

Table 2.1: Density sensitive line pairs used in this thesis. The left hand wavelength in the second column denotes the transition with a metastable lower level. For reference the isoelectronic sequence of the ion is shown and in parenthesis the lowest similar shell configuration. The usable density range is shown in cm^{-3} .

| Ion | Wavelength (\AA) | $\log T_{\text{max}}(K)$ | Electron Configuration | $\log n_e$ range |
|---------|-----------------------------|--------------------------|------------------------|------------------|
| O v | 192.904 / 248.460 | 5.4 | Be-like | 10.5 - 13.5 |
| Mg VII | 280.742 / 278.404 | 5.8 | C-like | 8.5 - 11.0 |
| Si x | 258.374 / 261.057 | 6.2 | B-like | 8.0 - 10.0 |
| Fe XII | 186.854+186.887 / 195.120 | 6.2 | P-like (N-like) | 9.0 - 11.5 |
| Fe XII | 196.640 / 195.120 | 6.2 | P-like (N-like) | 9.0 - 11.5 |
| Fe XIII | 203.797+203.828 / 202.044 | 6.2 | Si-like (C-like) | 8.5 - 10.5 |
| Fe XIV | 264.789 / 274.200 | 6.3 | Al-Like (B-like) | 9.0 - 11.0 |

Recovering the DEM from observation is an inverse problem by nature. The observed intensity is a convolution of the filter or emission lines sensitivity to temperature, and the physical properties of the source itself. Given enough sampling across the temperature range, it is in theory possible to gather information about the source by inversion of the data. One of the earliest and most complete definitions of the problem is found in [Craig & Brown \(1976\)](#) for the application to optically thin X-Ray spectra. We reproduce the derivation here but modified to include the contribution function $G(n, T)$ for EUV emission lines.

In the previous section we saw the flux from a given emission line could be described in terms of the plasma density and contribution function of the line (Equation 2.1). If we define the intensity emitted by the source for an emission line α as

$$I_\alpha = \int_V G(n_e(\mathbf{r}), T) n_e^2(\mathbf{r}) d^3\mathbf{r} \quad (2.10)$$

where $n_e(\mathbf{r})$ is the density at position \mathbf{r} within a source volume V .

The integral over volume can be transformed into one in terms of temperature by first

expressing the volume element $d^3\mathbf{r}$ as a surface dS at position \mathbf{r} , hence

$$d^3\mathbf{r} = dS \, d\mathbf{r}. \quad (2.11)$$

We then divide the emitting region into surfaces of constant temperature, dS_T , this can be expressed as

$$d^3\mathbf{r} = dS \left(\frac{d\mathbf{r}}{dT} \right) dT = |\nabla T|^{-1} dS_T dT, \quad (2.12)$$

where $|\nabla T|^{-1}$ is the inverse of the temperature gradient magnitude. The volume of plasma contained within a range of temperatures between T and $T + dT$ is found by integrating over the surface S_T , such that

$$dV_i = \left(\int_{S_T} |\nabla T|^{-1} dS \right)_i dT \quad (2.13)$$

where we have used i to denote each volume of a particular temperature within the source. At this point it is helpful to think of a map of a mountainous area with contours drawn at set height intervals. We have so far divided the plasma into contours of temperature and we wish to find out how much ‘mountain’ there is at each height. Since many separate hills may share contours of the same height, but not the same location, we must sum over these disjoint surfaces before integrating. We therefore find the total volume between temperatures T and dT to be

$$dV = \phi(T) dT \quad (2.14)$$

where the sum over the N disjoint surfaces is given by

$$\phi(T) = \sum_{i=1}^N \left(\int_{S_T} |\nabla T|^{-1} dS \right)_i. \quad (2.15)$$

If we combine the new volume element with the original expression for line intensity (Equation 2.10), the line intensity can then be described by

$$I_\alpha = \sum_{i=1}^N \int_T \left\{ \int_{S_T} G(n_e(\mathbf{r}), T) n_e^2(\mathbf{r}) |\nabla T|^{-1} dS \right\}_i dT \quad (2.16)$$

and we can define the quantity within the sum as the differential emission measure (DEM)

$$\xi(T) = \sum_{i=1}^N \left(\int_{S_T} n_e^2(\mathbf{r}) |\nabla T|^{-1} dS \right)_i. \quad (2.17)$$

The abstract looking quantity $\xi(T)$ arises from the change from using a volume integral to one where the plasma is treated as regions of temperature. The DEM is essentially the amount of emitting material at a particular temperature weighted by the local plasma density.

In this general case the density depends on the position within the temperature surface S_T . We can simplify our expression for the intensity by first defining a mean square density, weighted by the temperature gradient over the N surfaces.

$$n_o^2(T) = \frac{\xi(T)}{\phi(T)} = \frac{\sum_{i=1}^N \left(\int_{S_T} n_e^2(\mathbf{r}) |\nabla T|^{-1} dS \right)_i}{\sum_{i=1}^N \left(\int_{S_T} |\nabla T|^{-1} dS \right)_i} \quad (2.18)$$

In doing this we note that when the density is constant across each surface of constant T the expression reduces to $n_o^2(T) = n_e^2(T)$, i.e the electron density of the plasma at a temperature T . Where observations are limited by spatial resolution the density is normally assumed to be coupled to the temperature in this manner.

Finally, if we then use the earlier expression for dV (Equation 2.14) the DEM can be rewritten as

$$\xi(T) = n_e^2 \frac{dV}{dT} \quad (2.19)$$

for the case of constant surfaces of density, where $n_o^2 = n_e^2$, and the contribution function can be brought outside the surface integral to give the commonly used form of Equation 2.16,

$$I_\alpha = \int_T G(n_e, T) \xi(T) dT. \quad (2.20)$$

We now have an expression for the intensity emitted by a single spectral line from within a plasma of temperature profile $\xi(T)$. The atomic physics $G(n_e, T)$ is known

for the emission line to within some uncertainty, and the density n_e can be assumed to be constant in T , however, $\xi(T)$ is convolved with the contribution function and can not be immediately recovered from a single filter or emission line intensity. As the temperature range where $G(T)$ is significant is small in comparison to the range of $\xi(T)$ we are interested in, we can make multiple measurements of I_α for many lines and invert the resulting matrix equation to find solutions for $\xi(T)$. The inversion of Equation 2.20 is made non-trivial by uncertainties in the intensity and contribution functions. The problem is therefore ill-posed since errors are amplified in the solution. Techniques to minimise these problems and invert $\xi(T)$ are discussed later in Section 4.4.

2.4 Instrumentation

As the Earth's atmosphere is opaque to almost all radiation with the exception of visible light and radio, the high energy Ultraviolet and X-ray photons emitted by energetic solar phenomena are invisible to ground based instruments. It was only with the advent of space exploration and instruments flown on test rockets after the Second World War that the solar spectrum could be viewed in full. The primary goal of this thesis is to gather information about footpoint plasmas using various diagnostics in the EUV wavelength range. These diagnostics require an instrument capable of resolving the profile of multiple EUV emission lines, of thermal widths less than 0.5\AA , and from sources of only a few arc seconds across ($1'' \sim 725 \text{ km}$ on the solar disc). All of the observations used in this thesis were made using space-borne instrumentation to collect images and spectra of solar features. We discuss the key instruments in the following.

2.4.1 Hinode EIS

Almost the entirety of the work in this thesis has been based on observations from the Extreme Ultraviolet Imaging spectrometer (EIS, [Culhane et al. \(2007\)](#)) on board the *Hinode* (Solar-B) mission ([Kosugi et al. 2007](#)). Launched in 2006, the primary scien-

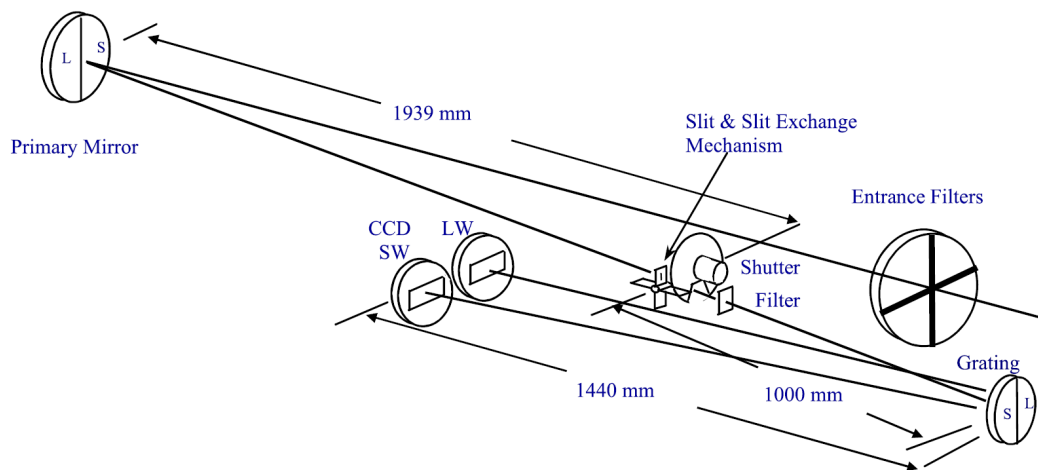


Figure 2.3: Schematic of the EIS light path — reproduced from [Culhane et al. \(2007\)](#). Important parts to note are the entrance slit between the mirror and grating, and the two CCDs for both short wavelength (SW) and long wavelength (LW) emission lines.

tific objectives of *Hinode* were to study the transfer of energy from the photosphere to the corona to help explain the heating of the corona, investigate the generation of the solar magnetic field, and understand the physics behind flares and coronal mass ejections. *Hinode*/EIS is currently the most advanced EUV spectrometer in flight available for flare studies and is a spiritual successor to the Coronal Diagnostic Spectrometer (CDS) ([Harrison et al. 1995](#)) on the Solar and Heliospheric Observatory (SOHO) ([Domingo et al. 1995](#)).

The EIS instrument is a normal incidence scanning slit spectrometer, operating in the EUV with a maximum spatial resolution of $2''$ ($1''$ pixel size), and $22 \text{ m}\text{\AA}$ spectral resolution ($47 \text{ m}\text{\AA}$ FWHM). A schematic of the spectrometer layout is shown in [Figure 2.3](#). Light enters through a primary filter, removing any optical radiation, before being focused by the primary mirror onto the slit. On each half of the mirror are two different coatings, labelled L and S in the figure, and the same is found on the dispersion grating. These two coatings allow the transmission of photons in two wavelength ranges between $170\text{-}210\text{\AA}$ and $250\text{-}290\text{\AA}$ which are dispersed by the grating onto two short and long wavelength CCDs, (SW) and (LW).

The 1'' pixel size applies along the slit which has a maximum usable length of the 510''. A 2'' slit width can also be used or 40'' and 266'' slots. The rastering, or scanning, ability of the spectrometer is achieved by a mechanism that rotates the primary mirror along the slit axis. The slit position on the Sun can be moved in less than a second to scan across a region, building up *raster* images. In each position the CCDs record the dispersed spectrum where the y axis on the CCD is the spatial height on the Sun, while the x axis represents the wavelength. A raster ‘image’ is therefore a data cube, where each spatial pixel contains also the spectral information.

Exposure times in each position are normally on the order of 2-10 seconds, depending on the study, and cover a small flaring region in under two minutes. The slit positioning does not need to be contiguous and can be programmed to jump in steps. In this case the raster is built up far quicker but at the expense of the spatial information between the slit positions. These ‘picket-fence’ or ‘sparse’ raster modes are sometimes desirable for flares and other quickly evolving targets.

The instrument is extremely flexible and can be programmed with a study up to 3 days in advance, where each study is designed with a specific target in mind with exposure times, slit sizes, slit timing all adjusted to suit. The selection of pixels read out by the CCD is important to mention here as this determines the data size of the raster. In March 2008 *Hinode* developed a problem with its X-band (microwave) down-link to Earth and has since used a backup S-band transmitter, reducing the down-link rate from 4 Mbps to 256 Kbps. Now that the spacecraft is limited in telemetry, which is shared with the XRT and SOT instruments (see the next two Sections), the size of the raster and choice of spectral lines must be carefully optimised.

2.4.2 *Hinode* XRT

The X-Ray Telescope (XRT, [Golub et al. \(2007\)](#)) on board *Hinode* is a high spatial and temporal resolution instrument imaging soft X-Ray emission from 6-60Å. XRT employs a grazing-incidence design which focuses X-Rays onto a back-illuminated CCD by using very shallow angles of reflection. The high photon energies of X-Rays mean

that in traditional normal-incidence designs (such as EIS), where the mirror is approximately perpendicular to the normal of a material, they will penetrate and scatter without significant reflection. The use of a grazing-incidence design avoids this while still allowing continuous wavelength coverage. The large field-of-view, $>30'$, can image entire active regions with a cadence of up to 2 seconds between exposures and by using combinations of 9 different filters of varying material and thickness provides a temperature response between $\log T = 6.0 - 7.5$. In our analysis we have frequently used it for context imaging of flaring regions, highlighting loops and brightenings at temperatures above what EIS nominally observes.

2.4.3 Hinode SOT

For low temperature observations, *Hinode* has the Solar Optical Telescope (SOT, [Tsuneta et al. \(2008\)](#)). SOT was arguably the most media publicised of the three instruments, revealing spectacular high resolution movies of spicule motions in the chromosphere. Its 50 cm telescope has a spatial resolution of $0.2''$ and images in many broadband and narrowband filters, observing emission in the photospheric continuum to chromospheric absorption lines. A spectro-polarimeter is also present which allows high precision measurements of the magnetic field in the photosphere.

2.4.4 TRACE

The Transition Region And Coronal Explorer (TRACE, [Handy et al. \(1999\)](#)) was one of the first NASA Small Explorer Missions (SMEX), and was launched in 1998. The SMEX was a program that started to fund small focused missions which have often been extremely successful; TRACE for example only stopped taking data in 2010. TRACE imaged the photosphere, transition region, and corona with excellent spatial and temporal resolution. Images with a pixel size of $2''$ and a $4''$ spatial resolution were possible and could be taken every 20 seconds. Various filters covered wavelengths from white light, UV, and EUV with responses typically less than 10\AA wide in the EUV. The field of view was much smaller than its modern counterpart, the Atmospheric Imaging

Assembly (AIA) on board the Solar Dynamics Observatory (SDO), but provided extremely high detail narrow passband images of the transition region plasma in active regions, moss, and flare footpoints. Among the earliest discoveries with TRACE was the detailed observation of “moss” (Fletcher & de Pontieu 1999) which can be seen as a bright, diffuse, emission in the vicinity of coronal loops within an active region. This hot upper transition region emission, thought to be heated plasma in the tops of small loops, is ubiquitous in most TRACE active region images.

2.4.5 RHESSI

The Reuven Ramaty High Energy Solar Spectroscopic Imager (RHESSI) (Lin et al. 2002), launched in February 2010 was a NASA SMEX mission dedicated to the investigation of energy release and deposition, and particle acceleration in solar flares. 9 cooled germanium detectors detect X-ray photons with an energy resolution of 1-10 keV, ranging from soft X-rays at 3 keV, up to 17 MeV gamma rays. This encompasses photons emitted from the hottest flare thermal sources, around 10-30 MK, to γ -ray emission from highly energetic processes such as the 0.511 MeV electron-positron annihilation line.

Unlike optical and ultraviolet photons, the hard X-rays collected by RHESSI are energetic enough to scatter in, or penetrate through, a reflective coating or grazing incidence mirror. As a result they are difficult to focus onto a pixel based detector. Instead RHESSI makes use of a Fourier transform method to reconstruct images (Hurford et al. 2002). Spatial information is obtained through 9 parallel grid collimators placed in front of each detector. Each collimator uses a different grid pitch, corresponding to angular resolutions ranging between 2-180". RHESSI rotates on its axis every 4 seconds, which moves the grids across a bright X-ray source. The detectors record the energy of photon, and the flux modulated by the passage of the grid over the source. From the temporal modulations in each detector, and knowledge of the spin timing and grid spacings, an image can be constructed from a Fourier transform to recover the spatial information. Different combinations of detectors and grids can

be used to optimise the reconstruction depending on the source size.

Various Fourier imaging algorithms are available but are complex and do not require detailed discussion here. An algorithm called CLEAN is used in Chapter 3 to determine the HXR source sizes. CLEAN was developed for radio interferometry (Högbom 1974) where a similar lack of spatial resolution is encountered. Through selection of the detectors, features with a spatial size of $\sim 2''$ can be recovered.

The high energy resolution of the detectors allow for detailed X-ray spectroscopy. The software package OSPEX written by R. Schwartz (Schwartz et al. 2002) contains fitting routines suitable for thermal and non-thermal emission analysis. Corrections are implemented to account for the absorption of photons in the collimators, scattering in the Earth's atmosphere, and solar background counts. OSPEX collects all of these effects in a time dependent matrix to convert the detected photon count back to the original source counts. Forward fitting routines are included to determine parameters for models predicting bremsstrahlung emission from various electron distributions. Models for thermal Maxwellian distributions can be fitted with parameters for the temperature and total emission measure, while models of accelerated non-thermal electrons interacting with a thin-target, or thick-target, can be fitted using forms of power laws with a spectral index δ . OSPEX was used in Chapter 3 to determine the energy flux in the non-thermal electrons.

2.4.6 IRIS

Though it is not used in this thesis, we briefly discuss the next solar spectroscopic mission which can be used for flare science. The Interface Region Imaging Spectrograph (IRIS), a NASA SMEX mission, was successfully launched on June 27th 2013. IRIS is the next generation of imaging spectrometer, and with a spatial resolution of $0.3''$ and between $40\text{-}80\text{m}\text{\AA}$ spectral resolution will reveal features on scales never before observed in the chromosphere. The high data rate allows for 1s cadence to quickly raster small regions to study their temporal evolution. Flare studies with IRIS will be of particular interest, as the spectral ranges, $1332\text{-}1358\text{\AA}$ and $1390\text{-}1406\text{\AA}$ in the

far-UV, and 2796-2831Å in the near-UV, will include many diagnostics of flare heating in the deep chromosphere.

Chapter 3

Density and Velocity Measurements of a Solar Flare Footpoint

This chapter begins an exploration into the atmospheric structure of impulsive phase footpoints in solar flares using data from the Extreme-ultraviolet Imaging Spectrometer (EIS) on board *Hinode*, a theme that is continued throughout this thesis. The impulsive phase of a solar flare can be characterised by sudden increases in the hard X-ray (HXR) light curve, the formation of compact flare footpoints in the lower atmosphere, and strong emission in UV and EUV wavelengths. As discussed in Section 1.3, magnetic energy stored in the corona is released by the flare mechanism, and is deposited in the lower atmosphere during the impulsive phase, manifesting itself as plasma heating and ionisation. The injected energy is then lost in the dense chromosphere through several processes; by expansion of the footpoint plasma (chromospheric evaporation), radiative losses, and conductive losses to cooler plasma. The standard interpretation of flares suggests that most of the UV emission originates in the chromosphere while the hotter EUV emission is found in post-flare coronal loops. However, recent work suggests that emission in lines of highly ionised iron and calcium (Milligan & Dennis 2009), and thermal soft X-Ray (SXR) continuum emission (Mrozek & Tomczak 2004), is clearly seen in impulsive phase footpoints. The EIS instrument is particularly sensitive to lines in the EUV wavelength range, and given its excellent spatial and temporal resolution,

is well suited to such observations.

In the present chapter, we focus on measuring the electron density of the plasma found in bright footpoints using EUV observations. The electron density is a critical parameter in understanding the nature of heated plasmas. The solar atmosphere is strongly stratified in temperature and density, dropping in electron density from 10^{13} to 10^9 cm^{-3} between the chromosphere and corona, and increasing in temperature rapidly from 10^4 to 10^6 K. The EIS data in this chapter allows us to make diagnostics of the electron density using line ratios for plasma temperatures which are nominally coronal (1-3 MK). By using the diagnostics to obtain values of the electron density in a footpoint at a specified temperature, we may be able to pinpoint the depth in the atmosphere at which the hot emission originates. The depth will be determined by the flare energy deposition, and knowing this is extremely important for placing limits on the form of plasma heating in the footpoint.

3.1 Flare Observations with Hinode EIS

Line emission at these footpoint temperatures — between 50,000 MK and 10 MK — is readily observed by the *Hinode*/EIS instrument. The work described in this chapter began as an exploratory test of the diagnostic capabilities of EIS to capture, in high spectral and spatial detail, a flare footpoint during the impulsive energy deposition phase. More specifically, EIS rasters were selected running a “fast raster” mode that covered the footpoint area multiple times; and which contained a range of density sensitive line pairs (see Section 2.2 for more detail on the various modes and diagnostics available with EIS).

The bulk of the content in this chapter was published in [Graham et al. \(2011\)](#). We describe the analysis of footpoint emission from a medium sized solar flare on 5th June 2007. With coverage from *Hinode*/EIS fast rasters, RHESSI HXR spectra during the impulsive phase, and EUV imaging from TRACE (see Section 2.4 for an overview of these instruments), the range of data available made this a perfect event to investigate the footpoint heating response. Enhanced electron densities, evaporative

flow velocities, and the power deposited by non-thermal electrons were all estimated, and evidence for footpoint densities increasing at a given plasma temperature during the impulsive phase was found. RHESSI HXR spectra allowed us to show that there was a component of non-thermal electrons in the footpoint, and from this the flare energy input flux was estimated. We find that the enhanced densities are consistent with a thick-target electron beam model heating progressively deeper layers of the atmosphere. The flare energy input flux was approximately equal to the theoretical cut-off between explosive and gentle evaporation, yet, given the uncertainties in the HXR spectrum there is no clear case for either scenario. In the next section we present an overview of the event as seen from multiple instruments, verifying that the enhanced emission seen during the flare is indeed originating from the footpoints, and proceed to explore the implications of the results.

3.1.1 The June 5th 2007 Event

To begin with, a set of EIS rasters were required that captured the impulsive phase evolution of a footpoint and contained at least one pair of lines that were density sensitive. Furthermore, as the field of view in most flare-specific EIS rasters is small, we wished to view the overall morphology of the flaring region at similar wavelengths. TRACE imaging in either the 171Å or 195Å filters was ideal for this purpose and was added to the search criteria. Finally, flares with RHESSI HXR coverage were essential if the total energy deposition in the flare was to be calculated.

A search revealed a set of raster observations using the HH_AR+FLR_RAS_H01 study centred on NOAA active region 10960. Analysis of time variation in the EUV emission of the active region was made using EIS data by [Brooks & Warren \(2009\)](#). The authors found that the region was especially flare productive and many C and M class flares were observed. A single C6.6 class flare which took place on June 5th 2007 was found to meet our requirements and was selected for further investigation. The flare was observed by TRACE and RHESSI, and with several EIS rasters, during the impulsive phase and part of the decay phase. While not part of our requirements,

observations by the Solar Optical Telescope (SOT) and X-Ray Telescope (XRT), also on board *Hinode*, proved to be very useful.

SXR light curves represent the overall evolution of a flare and we show the GOES 1-8Å X-ray data for the flare in the upper panel of Figure 3.1. We see that the flare begins at 15:50 UT, peaks at 16:13 UT, and ends at 17:00 UT. The impulsive phase is defined as the period between the start and peak of a flare, and is relatively gradual in this example. The benefit of this is that it was well observed by EIS, and a total of 12 EIS rasters were completed during the rise phase. TRACE and RHESSI observations were equally well timed, although RHESSI missed the pre-flare stage and very early evolution. Unfortunately all of instruments have missing data across the GOES peak, which continues for around 30 minutes into the decay phase due to the nature of their orbits.

Both *Hinode* and TRACE are in sun-synchronous polar orbits which are inclined in such a way that they follow the day-night terminator above the Earth's surface. This allows continuous observing of the Sun for up to 9 months of the year. For the rest of the year, the spacecraft enter an *eclipse season*, in which their orbits take them behind the Earth; these eclipses account for a short fraction of the orbit not long after launch, but as the orbit precesses this fraction can grow in time. RHESSI on the other hand was launched into a low Earth equatorial orbit and experiences an eclipse every orbit and it must also pass through a region of space called the South Atlantic Anomaly (SAA, Sherrill (1991)). The Earth's inner Van Allen radiation belt lies at a lower altitude here, and the local energetic particle flux is much higher, thus during passage through it RHESSI does not make observations. Unfortunately there is no way of avoiding these occultations, which when studying transient events such as flares, can occur with alarming synchronicity! Because of these factors, during the soft X-ray peak of this event EIS, TRACE, and RHESSI were all obscured because of either SAA or night-time passage and no data was taken — we have marked this on the bottom panel of Figure 3.1. However, the majority of the impulsive phase that we are interested in *was* observed, and as we will see, most of the flare energy deposition occurred during the observed times.

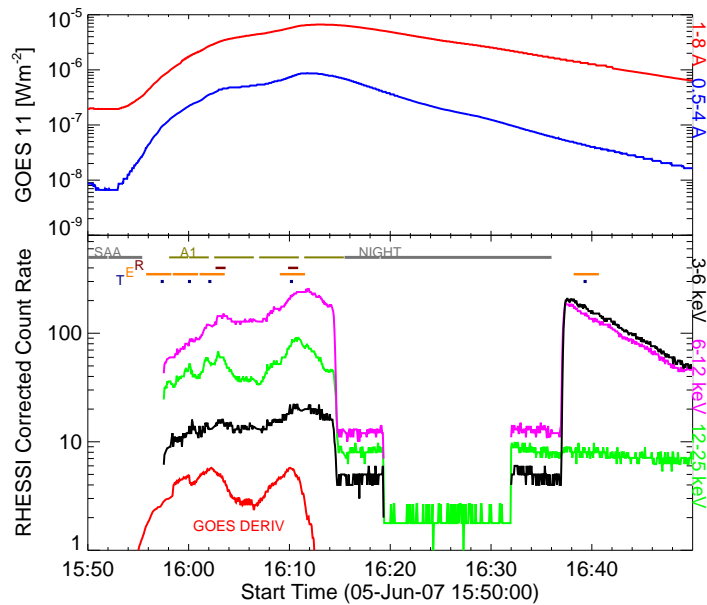


Figure 3.1: X-ray light curves of the flare from GOES and RHESSI, top and bottom panels respectively. The time derivative of the GOES 1 – 8 Å channel can be seen in red line and has been scaled to match the RHESSI light curves. The times of the EIS rasters, TRACE images, and RHESSI images/spectra are shown by the coloured horizontal bars at the top of the bottom panel. Also, the RHESSI eclipse and SAA times are shown in grey with times for when the attenuating shutters were deployed in yellow (A1) (this figure was created for [Graham et al. \(2011\)](#) by I.G. Hannah).

3.1.2 GOES and RHESSI

RHESSI light curves of the X-ray count rate in 3-6 keV, 6-12 keV, and 12-25 keV energy bands are plotted in the bottom panel of [Figure 3.1](#). The RHESSI plots were generated using the HESSI software package for SolarSoft. Throughout this thesis any data analysis or calculation has been performed with the Interactive Data Language (IDL) along with the additional SolarSoft analysis package ([Freeland & Handy 2012](#)). The counts were background subtracted and corrected for attenuating shutter positions (see [Section 3.5](#)) by I.G. Hannah for the work in [Graham et al. \(2011\)](#), and are shown in the bottom panel of [Figure 3.1](#). Significant rises in X-ray flux above 25 keV were

not observed in this relatively small event, which initially suggested that the non-thermal component of the spectra would be small, however, the full spectral analysis performed later in Section 3.5 does show evidence for a non-thermal component in the electron spectra. Two early impulsive phase bursts are seen in the 12-25 keV light curve (green line), occurring at 16:02 UT and 16:12 UT, which are followed by smoother rises in the 6-12 keV (magenta), and 3-6 keV (black) curves. As discussed in Section 1.3, the time derivative of the GOES SXR flux can often be used as a proxy for the temporal evolution of non-thermal electron deposition (Neupert 1968; Dennis & Zarro 1993). The SXR derivative, normalised to the size of the other curves, is plotted on the bottom panel of Figure 3.1 in red, and does show two peaks coincident with the 12-25 keV emission. The fact that the harder X-ray emission is coincident with the SXR derivative is suggestive of two distinct periods of flare heating occurring during the event. As we do not have RHESSI observations during the GOES peak, and that we see no third peak in the SXR derivative, we can assume that there was no additional heating period during the data gap.

EIS rasters were available throughout the impulsive phase up to the data break and in the decay phase. The orange coloured bars on the bottom panel of Figure 3.1 show the times of EIS rasters which were chosen to correspond with the RHESSI 12-25 keV peaks and the optimum times for RHESSI spectral analysis used later. However, plasma velocities and densities were derived for every raster during the impulsive phase.

3.1.3 TRACE and SOT

TRACE imaging in the 171 Å passband was available throughout the impulsive phase to, coincidentally, the same point where the EIS rastering broke off. Fe IX and Fe X contribute to most of the line emission within the 171 Å passband, making it sensitive to plasmas between 160,000 K and 2 MK, i.e. transition region to quiet coronal temperatures (Handy et al. 1999; Raftery et al. 2013). TRACE images at these wavelengths are excellent at highlighting the overarching coronal loops (~ 2 MK plasma) in an active region, while cooler transition region ‘moss’ is visible as patchy background

emission within the region (Fletcher & de Pontieu 1999). TRACE 171 Å images were prepared for this event using the standard SolarSoft TRACE_PREP software. This reads the raw FITS files, performs a dark current and pedestal subtraction, flat field correction and replaces saturated pixels, although the images used in this chapter are for context only and we are not concerned about any absolute intensity calibration.

We show an example image, capturing the flare at the second peak in 12-25 keV X-rays, in Figure 3.2. The overall morphology of the region is clear in this image. Two concentrations of magnetic field are seen at either side of the region, where bright coronal loops fan out; these loops remain stable throughout the event. Underneath the loops, a large patch of moss emission is seen in centre of the image. It is in this moss area that two flare footpoint/ribbon areas are found, shown by the intense ‘U’ and inverted ‘L’ shaped ribbons. Finally, between the two footpoints, the region is bisected by a short dark filament running diagonally from the lower-right towards the upper-left of the image. A filament — prominence when seen in emission on the limb — is a concentration of cool, dense, chromospheric material suspended high in the solar atmosphere by magnetic fields. These filaments may remain stable for weeks; either dissipating back into the atmosphere, or spontaneously erupting into the solar wind, which we are now learning through SDO observations can be triggered by nearby flaring activity (Kumar & Manoharan 2013). The filament in this event does not change during the event and neither do the overlying large TRACE loops, suggesting that this was not an eruptive flare, with no associated coronal mass ejection.

If we look at the TRACE images in sequence we see how the flare footpoints and ribbon patterns evolve. Figure 3.3 shows a series of TRACE images which we have cropped to the same field of view as the EIS rasters. TRACE recorded images at a 40 second cadence throughout the impulsive phase, but we have only shown the times corresponding to the mid-point of the 5 selected EIS rasters in Figure 3.1. We have chosen these times to best represent the evolution of the flare based on the following considerations: (1) a frame showing the earliest signs of footpoint brightening in the EIS rasters; (2) as the enhancements develop into more extended ribbons; (3) the closest EIS raster corresponding to the first peak of the 12-25 keV light curve and

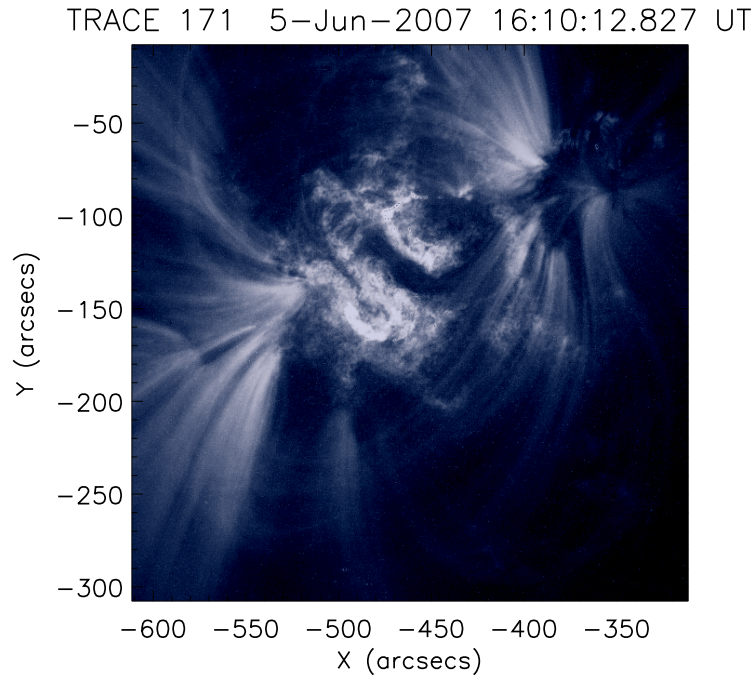


Figure 3.2: TRACE 171 Å image from the time of peak flare heating, showing the active region coronal loops, and moss emission. The flare ribbons take the form of bright ‘U’ and inverted ‘L’ shaped features in the centre of the frame.

GOES SXR derivative; (4) the same but for the larger second peak; and (5) the first raster available in the decay phase after the data gap.

In the first panel of Figure 3.3, small, localised brightenings become apparent on either side of the filament at the ends of the moss region. These footpoints begin to spread into elongated ribbons in the second and third images. In the fourth image, during the second 12-25 keV peak, the flare ribbons have evolved into a distinctive ‘U’ shape in the southern region and an inverted ‘L’ shape in the north, though they are not uniformly bright. The ‘L’ shaped region remains with two small footpoints at either end, and a brighter region is seen to the southern of the ‘U’. The final TRACE exposure shows the flare mid-way through the decay phase. Post-flare loops now become visible, crossing the filament joining the northern and southern regions, but remain brighter

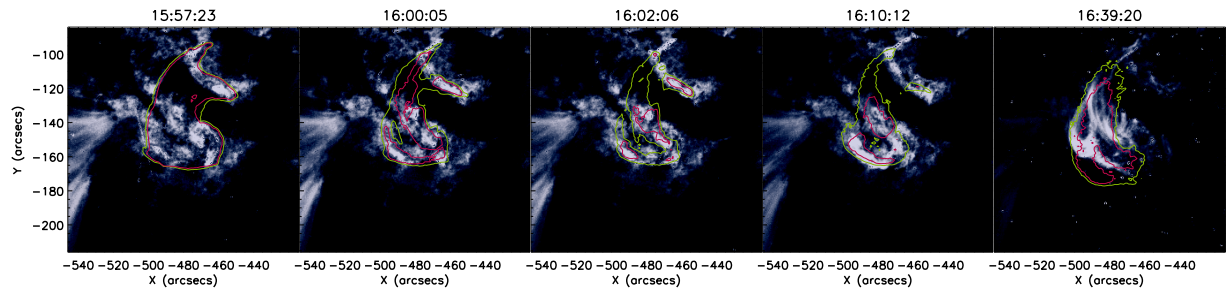


Figure 3.3: TRACE at 171 Å images of the flaring region over several stages during its evolution. Contours for *Hinode*/XRT intensities of 60% and 80% of the maximum are shown in green and magenta. The global XRT intensity for all images peaks around the time of the 16:10 frame, however the maximum extent of the loop structure shown does not vary greatly.

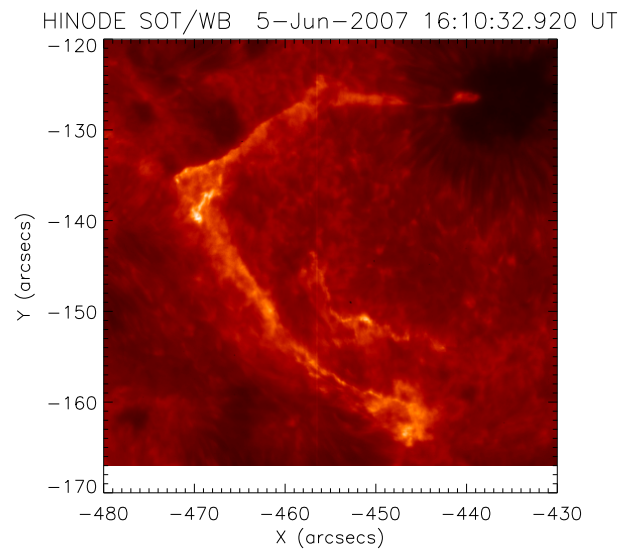


Figure 3.4: Ca II H emission observed by *Hinode*/SOT during the flare impulsive phase taken close to the second 12-25 keV peak.

where the southern flare ribbons were located earlier. This is expected in the standard flare model, as material evaporated from the flare footpoints (see Section 1.3.2) fills these loops after the impulsive phase.

We can verify that the bright areas we are referring to as *footpoints* and *ribbons* are in fact heating in the chromosphere by inspecting the *Hinode*/SOT data. SOT makes observations of the photosphere and chromosphere across a range of narrowband and continuum filters. Narrowband images of the Ca II H 3969.5 Å line, formed around 10,000 K, were available throughout the impulsive phase, and one example is shown in Figure 3.4. The field of view in SOT is much smaller than TRACE, however, the upper ribbon is clear, having the same ‘L’ shape as seen in TRACE. Though the TRACE emission at 171 Å is nominally at coronal temperatures of around 1-2 MK, here we find co-spatial intensity enhancements in a wavelength band which at non-flaring times shows features in the chromosphere. A fundamental problem exists in line-of-sight observations of optically thin plasmas in the solar atmosphere. As without inferring a temperature model, or seeing a distinctive change in the structure of the region with temperature, we can not directly measure the height of sources. In the case above we can either interpret the ribbon as being a coronal height source with a strong component of cooler material (10,000 K), or chromospheric material being heated to 1-2 MK. The first situation seems extremely unlikely as cool material would have to be transported into the corona without being heated during the impulsive phase. The second option fits conceptually with our understanding of the flare standard model. Given the very similar shapes of the sources it is clear that in this instance it is being emitted from chromospheric heights.

3.1.4 XRT

High temperature SXR observations, approximately coincident with the TRACE exposures, were also available from *Hinode*/XRT using the Ti-Poly filter. The XRT instrument uses a range of filters varying in opacity and temperature sensitivity to the SXR emission. As with TRACE, a SolarSoft routine XRT_PREP was run to prepare the data, performing dark frame and flat field subtractions, along with cosmic ray and radiation belt noise removal. An example unsaturated XRT image taken during the impulsive phase with the Ti-Poly filter is shown on the right of Figure 3.5. Plasma

around 8 MK is visible in this image, assuming that most of the observed emission is near the peak of the filter response (plotted on the left of Figure 3.5), and highlights hot loop structures above the transition region which connect 3 more concentrated points of bright emission.

During observations, XRT exposures are adjusted using an automatic exposure control to avoid saturation, however, during flares the lower opacity filters can still often saturate even for low exposure times, limiting the selection of images. With this in mind, images that best matched the TRACE exposure times were selected but could not always be exactly coincident. The XRT emission was plotted over the TRACE images in Figure 3.3 using contours of 60% (green) and 80% (magenta) of the maximum image intensity. We found that the visible edges of the loops found in Figure 3.5 were well defined by a 60% contour, while 80% highlighted the smaller bright areas, hence using the same contours over the TRACE images.

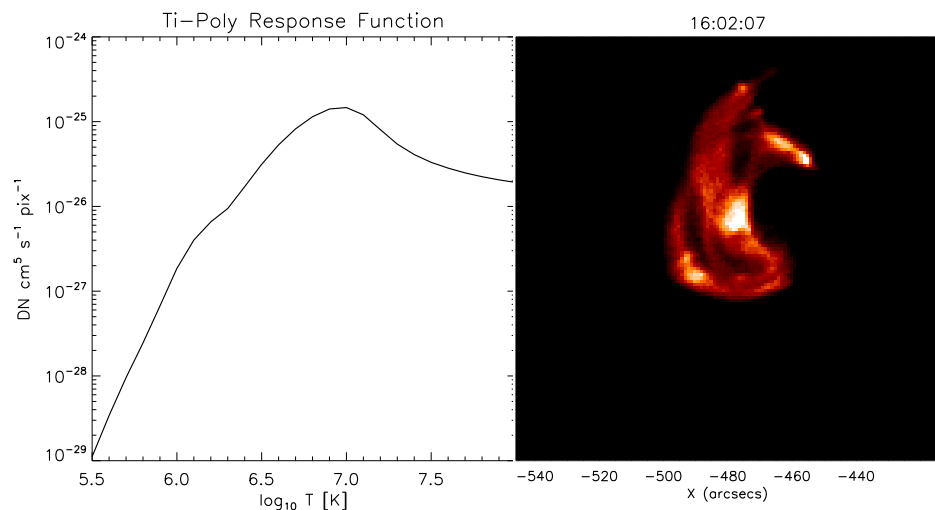


Figure 3.5: The Ti-Poly filter temperature response is shown in the left hand plot peaking at $\log T = 6.9$ K. On the right is a Ti-Poly image from XRT taken at the same time as the centre TRACE image in Figure 3.3. Hot loop structures are visible in addition to compact enhancements near the loop footpoints and in the centre of the moss region.

In the first panel the XRT exposure was taken 105 seconds after TRACE. In panels 2-4 they are within 20 seconds of each other, and in the final panel XRT followed TRACE by 2 minutes. In the centre 3 panels the brightest emission (80% contours) was found to match well with the TRACE ribbon brightenings, while the 60% contours outlined the extent of the moss regions. It was therefore straightforward to correct for the pointing difference between TRACE and XRT by moving the XRT images by hand. An offset of $2''$ in the x and $29''$ in the y directions was found in all exposures.

XRT emission in the first panel was saturated but defined the outer extent of the flaring region. As the impulsive phase progressed the loops became brighter but their overall size and shape changed little. The two bright TRACE 171 \AA footpoints in the north, and the single ribbon area in the south, also became increasingly well bounded by the brightest XRT emission (magenta contour), with the 80% intensity contour completely surrounding the flare ribbon in the fourth image. The observation that at least part of the hot SXR emission is contained within the same location of the TRACE bright points is compelling, and supports our view that TRACE is indeed showing us flare footpoints. Secondly, it demonstrates that the footpoint plasma present reaches temperatures of up to 8 MK, but without imaging in others filters we cannot determine this temperature with any more accuracy.

3.2 Hinode EIS data

A sequence of 12 EIS rasters using the HH_AR+FLR_RAS_H01 study were found running during the flare impulsive phase, with more following in the decay phase after the data break. The study is a sparse, fast-raster mode, meaning that the spectrometer slit scans across a small region quickly in non-contiguous steps, making multiple rasters during the evolution of the event. These rasters scanned East to West over a region of $240''$ by $240''$ by moving the $1''$ slit in $10''$ steps. A slit exposure time of 5s was used at each step, giving a total raster time of 150s. While the mode provides rapid sampling of the impulsive phase, it is at the expense of spatial information. We reinforce here that the spectrometer spatial resolution is not affected by the sparse raster mode —

the 1'' slit point spread function is still around 3'' (see Section 2.4.1) — but the effect of the sparse scanning is that the image will have no information between slit positions. The study also provided a wide temperature range from $\log T_{\max}$ 4.7 – 7.2 (K) and was covered by emission lines in 17 available wavelength windows; ideal for the study of dynamic behaviour in the impulsive phase. Among these lines were 3 density sensitive diagnostic pairs, in Fe XII, Fe XIII, and Fe XIV. The ratio of intensities in each pair is sensitive to the electron density, and we discuss how the densities are derived in the following section.

3.2.1 Data Preparation and Uncertainties

Focused spectra are recorded digitally on the EIS detector before being sent back to Earth (see Section 2.4.1), and the raw intensity data must be prepared before any analysis is made. The downloaded Level-0 EIS FITS files have minimal calibration applied and contain the intensity counts for each wavelength window, raster timing, and any instrument and pointing information. The raw data is first calibrated and cleaned by the SolarSoft routine `EIS_PREP`. This performs a dark current and pedestal subtraction, removal of cosmic ray hits, and flags saturated and hot pixels. Finally a radiometric calibration converts the CCD DN output into the specific intensity units $\text{ergs cm}^{-2} \text{s}^{-1} \text{sr}^{-1} \text{\AA}^{-1}$ and produces the Level-1 FITS output.

Once the data is calibrated we make Gaussian fits to the line intensity profiles using the `EIS_AUTO_FIT` routine which uses a least squares minimisation (Young 2013b). The 3 Gaussian parameters, plus 2 for a linear background, are then obtained for each pixel in the raster. Fits were made for each available spectral line in the raster; including both lines of the density diagnostic pairs for Fe XII, Fe XIII and Fe XIV. Further details of the fitting, accounting for blends, are found in Section 3.2.3, and all of the lines discussed are shown in Table 3.1.

The uncertainties in the measured EIS intensities are found through a combination of instrumental and fitting errors. The online EIS Wiki contains a large resource of documentation on the EIS analysis software and we summarise here for reference what

is found in [Young \(2013a\)](#). The first step involves converting the observed data number (DN) to a photon number which is done at the `EIS_PREP` stage. The Level-0 data from the detector is saved as DN which is the analogue-to-digital conversion of the detector output voltage in one pixel, this is then converted to photon number from knowledge of the CCD characteristics. The noise is given by \sqrt{P} where P is the photon number in one pixel. The dark current uncertainty σ_{dc} is also taken into account and added in quadrature. The photon error is then

$$\sigma_P = \sqrt{P + \sigma_{dc}^2}. \quad (3.1)$$

The measured intensity is found using the telescope effective area, exposure time, slit size, and many more factors so that the intensity can be written as $I = t(\lambda)P$, where $t(\lambda)$ contains all of the instrument parameters. If we pass the photon error through this, then the 1- σ error on I becomes

$$\frac{\sigma_I}{I} = \frac{\sigma_P}{P}. \quad (3.2)$$

The calculation of σ_I is handled by `EIS_PREP` which returns a structure containing the specific intensity in each wavelength bin for the line profile in addition to the uncertainty. The `EIS_AUTO_FIT` routine then fits these profiles taking into consideration the measurement errors. The output then contains the best fit line peak, width, centroid, and background parameters, along with their associated 1- σ uncertainties. The integrated intensity is given by the relation $I = \sqrt{2\pi}WI_s$ where W and I_s are the Gaussian line width and peak specific intensity respectively. Finally, we find the 1- σ error by combining the errors on W and I_s — note since these parameters are assumed to be correlated there is a factor of 1/2 in the error estimate.

3.2.2 Wavelength Calibration

The plasma velocities found in this chapter are all derived by comparing the measured centroid position of a line to its rest wavelength through the expression

$$\frac{v}{c} = \frac{\lambda - \lambda_0}{\lambda_0}, \quad (3.3)$$

where λ and λ_0 are the measured and rest wavelengths, and c is the speed of light. Accurately determining the line Doppler shift depends on a good definition of the rest wavelength, as we wish to measure the movement of flaring plasmas relative to their quiet stationary state. Uncertainties exist in the theoretical rest wavelengths of lines, and gradual motions on longer time scales than the flare dynamics mean that the quoted λ_0 value is not always valid. A small quiet area near the region can be used as a guide (Milligan 2008) by which to calibrate each line's rest wavelength. However, this can be difficult in complicated active regions, where continuous plasma flows are commonly found at the footpoints of coronal loops and in the loops themselves. In selecting a region we avoid contributions from the flaring regions and overhead loops by checking the area in bright transition region lines and hotter coronal lines. For each raster, the average line centroid position of a $100''$ by $10''$ quiescent region between $[-500'', -240'']$ and $[-400'', -230'']$ was used to calibrate the velocity shifts. The area is free of active region mass, and the coronal loops seen do not contribute much to the average spectral profile, which was checked in each raster for anomalous shifts or large intensity variations.

EIS suffers from a 98 minute variation in the position of line centroids during raster sequences. This corresponds to the orbital period of the spacecraft and is due to thermal effects changing the position of the spectrometer grating relative to the CCD. The effect was corrected for using an empirical model developed by Kamio et al. (2010) which is implemented in the standard EIS SolarSoft routines.

Two further corrections must be made to account for deviations in the light path that cause different emission lines to occur at different spatial Y-positions on the detector CCD. First the grating tilt, the angle of the grating dispersion axis relative to the CCD, was measured in Young et al. (2009) and is corrected using the `EIS_CCD_OFFSET` routine. Secondly, a spatial offset exists between the short and long wavelength CCD's (see Section 2.4.1), which means the same solar feature will not appear at the same

Y-coordinate on each CCD. In addition to this offset, during these rasters the EIS spectrograph was also slightly out of focus (Warren et al. 2008), and as a result there is also a small offset of around 2 pixels in the X-position. We have corrected these last two offsets in both directions by cross-correlating the raw intensity data between two emission lines observed on each CCD. The two lines were chosen at similar temperatures from either CCD to ensure that the images had a similar morphology to correlate on. We have used Fe XII 195.120Å and Fe XIV 274.200Å, as both are strong lines showing coronal features at $\log T = 6.1 - 6.3$ K.

For the correlation, images in these two wavelengths were created from the total Level-1 calibrated specific intensity in each wavelength window, as we wish to correlate prior to fitting. An upper and lower intensity threshold was set at a percentage of the maximum brightness in each image. This ensured that the same stable coronal features were visible in both rasters, and that any flare brightening were excluded which may interfere with the correlation. The maps were then passed to the SolarSoft 2D cross-correlation method CROSS_CORR to find the offset between the two rasters. The data in all of the remaining wavelengths in the long wavelength band were then shifted according to the Fe XII/Fe XIV offset.

This method has the added effect of being able to remove any spacecraft pointing drift over time. Since our analysis examines relatively small features - only a couple of pixels across - in a number of wavelengths and over time, it is paramount to ensure the same feature is identified in subsequent rasters. Using the same technique, but this time correlating subsequent Fe XII images with the first image in the series, drifts of up to $\sim 5''$ were found between raster images during the flare. The raster positions were then updated relative to the first raster accordingly. Based on this process, and some manual adjustment, we estimate that the EIS rasters are co-aligned within $1.5''$ in x and $1.5''$ in y .

3.2.3 Line Analysis

The FWHM spectral resolution of EIS is 47 mÅ at 185 Å (Culhane et al. 2007), sufficient to resolve narrow EUV emission lines in great detail. However, lines from different species and ionisation states can often be blended with the profile of even the brightest lines. Careful line identification and analysis is therefore required to accurately determine the intensity and profile of the line in question; especially when using these parameters in a density or velocity analysis. Using the CHIANTI v6.0 atomic database (Dere et al. 1997, 2009), and information given in Young et al. (2007a) and Brown et al. (2008), we have identified the lines within each selected profile. The most significant blended contributions in each profile were then removed. The selection and de-blending process for lines in the velocity and density analysis is described below with details of the lines found in Table 3.1.

He II — The helium resonance lines (these lines are discussed in Section 4.2.1) are notoriously difficult to interpret and have anomalously large intensities compared to other transition region lines; this is clear in the third panels of Figures 3.15 to 3.18. Photon scattering and other radiative transfer effects, due to the high opacity at these temperatures, have been suggested as contributions to the intensity (Smith 2003; Pietarila & Judge 2004; Judge & Pietarila 2004). The He II 256.320 line in this study is blended with contributions from Si X 256.37 Å, Fe XII 256.41 Å, and Fe XIII 256.42 Å. We do not have all of the necessary lines available to fully de-blend He II as per the discussion in Del Zanna et al. (2011), but justify its use here - albeit with caution - from inspection of the line profiles. The most prominent contribution is in an extended red wing, likely the strong Si X contribution, which has been removed by using a double Gaussian fit. Since the line will be used only for calculation of velocity shifts, the profile is more important than the absolute intensity in this case, so the aforementioned opacity effects can be ignored for now.

Si VII — Si VII 275.350 Å is un-blended but has a weak signal across part of the

Table 3.1: Emission lines found in the EIS raster wavelength windows. Lines marked with * are excited from a metastable level.

| Line | Wavelength (\AA) | $\log T_{\max}(K)$ | Notes/Blends |
|----------|-----------------------------|--------------------|--------------------------|
| He II | 256.320 | 4.7 | Si x, Fe XII and Fe XIII |
| Si VII | 275.350 | 5.8 | Poor signal |
| Fe VIII | 185.210 | 5.8 | Ni XVI |
| Fe X | 184.540 | 6.0 | ... |
| Fe XI | 188.230 | 6.0 | ... |
| Fe XII* | 186.854 + 186.887 | 6.1 | n_e pair |
| Fe XII | 195.120 | 6.1 | n_e pair |
| Fe XIII* | 203.797 + 203.828 | 6.2 | n_e pair |
| Fe XIII | 202.040 | 6.2 | n_e pair |
| Fe XIV* | 264.780 | 6.3 | n_e pair |
| Fe XIV | 274.200 | 6.3 | n_e pair |
| Fe XV | 284.160 | 6.3 | ... |
| Fe XVI | 262.980 | 6.4 | ... |
| Ca XVII | 192.820 | 6.7 | O V and Fe XI |
| Fe XXIII | 263.760 | 7.1 | Peak only |
| Fe XXIV | 192.023 | 7.2 | Fe XI and Fe VIII |
| Fe XXIV | 255.100 | 7.2 | S X and Fe XVII |

footpoint regions, making determination of velocity shifts difficult. However, shifts measured in Si were similar to that of the stronger He II line which will be used as our low temperature reference here.

Fe IX - XIV — We have omitted Fe XI 188.230 due to its close proximity to Fe XI 188.299 which adds uncertainty in obtaining Doppler shifts. Fe X is similar in temperature with a cleaner profile and is used instead. Fe XII 186.88 \AA is a blend of two Fe XII lines at 186.854 \AA and 186.887 \AA . For our density diagnostics we have used the sum of both lines referred to as 186.88 \AA . A small S XI blend at 186.84 \AA is reported but from the available wavelength windows this potential blend could not be directly quantified, although the blend is predicted to be only 5% of λ 188.88. The ratio of

intensity of 188.88 Å to 195.12 Å is around 3 to 1 at high densities, therefore the small blend of Si XI should not have a significant effect on the density diagnostic. Fe XIII 203.82 Å has a significant blend in its red-wing, identified as Fe XII 203.72 Å, although this is easily removed by fitting the line with a second Gaussian profile to pick out the smaller Fe XII component from the main Fe XIII line. The Fe XIII 203.82 Å line itself is composed of two Fe XIII lines at 203.828 Å and 203.797 Å, and again the total of both is used in the density diagnostics. The final diagnostic line Fe XIV 274.20 Å has a documented blend with Si VII 274.18 Å. The ratio of Si VII 274.18/275.35 is seen to be no more than 0.25 (Young et al. 2007a), so by fitting the available Si VII 275.35 Å line, the blend of Si VII 274.18 Å with Fe XIV 274.20 Å can be safely removed.

Ca XVII and Fe XXIII - XXIV — Not all of the hotter flare lines present were suitable for analysis. The relatively small nature of the flare meant that good line profiles were often completely masked by lower temperature blends, or that the signal was too weak to be reliable. Doppler measurements of Ca XVII 192.820 Å were not used as strong blends of Fe XI and O V in the wings obscured the centroid position (we will return to this part of the spectrum in Section 5.2). Fe XXIV 192.023 Å was strong during the impulsive phase in bright loop regions although Fe XIV and Fe XI blends make double component fitting for velocity analysis difficult. Fe XVII 254.87 Å is present in the Fe XXIV 255.100 Å window but can be resolved sufficiently using a double Gaussian fit. The reported weak S X presence does not appear to contribute significantly in footpoint regions, hence there was no requirement for a third Gaussian fit. Finally, Fe XXIII is relatively un-blended but only strong enough to observe in a few rasters near the flare peak. Now that the data has been adequately prepared, and the emission lines of interest fitted and de-blended, we can move onto the flare diagnostics.

3.3 Hinode EIS plasma diagnostics

The emission lines in Table 3.1 were fitted for all rasters using the SolarSoft EIS_AUTO_FIT procedure, returning a 5 parameter fit for each line comprising of the maximum height, Gaussian width, and centroid position, plus the gradient and intercept of the linear background. To convert from specific intensity (per Å) to the integrated intensity of a line we use $I = \sqrt{2\pi}I_0\sigma$, where I_0 is the maximum height, and σ is the Gaussian width. Throughout this thesis, when referring to the *intensity* of a line, the integrated intensity is assumed unless otherwise specified.

In the TRACE 171Å images (Figure 3.3) two footpoint regions were seen evolving during the impulsive phase on either side of a central filament. The same features are present across a wide temperature range in many of the EIS lines; starting from He II at $\log T = 4.7$ K, and up to the hot Ca XVII line at $\log T = 6.7$ K. Our first question to ask about these regions was simple; if this emission is originating from the lower solar atmosphere, what is the density of the material present, and does it correspond with our understanding of flare energy deposition?

Within the raster wavelength windows, three density diagnostic pairs were available for Fe XII, Fe XIII, and Fe XIV, capable of estimating the plasma electron density at temperatures between 1-2 MK. Out of the numerous rasters taken during the flare, five rasters were chosen that best display the evolution of the flare, based on the selection process given in Section 3.1.3. The fitted rasters for each of the diagnostic pairs are shown in Figures 3.6, 3.7 and 3.8, with each row corresponding in time to the TRACE 171 Å images in Figure 3.3. It should be noted that because of the sparse raster run, all of the EIS rasters are stretched by 10 pixels in the X direction using the CONGRID method in IDL. This duplicates a pixel across 10 pixels to maintain the correct aspect ratio when making comparisons with other images, but does not impose any extra spatial information by interpolation or smoothing.

In the top row of the figures, the morphology of the region in these iron lines is similar to that seen in TRACE; starting with localised enhancements leading to extended ribbon structures, with the northern areas leading the southern by a few

minutes. The situation is supported by a similar picture in the lower temperature lines He II and Si VII (not shown), which appear more sensitive to early impulsive phase activity.

Note that in the fourth raster shown there is a drop in intensity towards the left-hand edge. This occurs because *Hinode* was beginning to pass into eclipse. However, this occurs far enough after the time at which the slit was over the footpoint regions not to affect our results. The third and fourth rasters shown cover the two peaks seen in the RHESSI 12-25 keV light curve at 16:02:40 UT and 16:09:52 UT (Figure 3.1), with both peaks occurring while the slit was in a position near the flaring region. Without any subsequent rasters until 16:38:12 UT this is the best picture we have of the flare energy deposition phase.

3.3.1 Intensity, Density and Velocities across the region

The derived intensities, velocity shifts, and densities for each wavelength are shown in Figures 3.6, 3.7 and 3.8. In each of these figures, the intensity for both of the spectral lines used in the density diagnostic is shown. The top row shows the transition excited from the metastable level and the row underneath shows the other transition, excited from the ground state. To recap what was discussed in more detail in Section 2.2, the density sensitivity of diagnostics in this configuration arises from the very low radiative decay rate of the metastable lower level. Electrons excited into this level do not de-excite quickly like those in an allowed transition, therefore as collisional excitation increases, through the rising electron density, the relative level population increases. The transition excited from this state is then preferentially enhanced, making the ratio of the two transitions density sensitive.

In Figures 3.6, 3.7 and 3.8, and particularly evident in the third and fourth rasters, the transition involving the metastable level increases dramatically at similar locations to the TRACE 171Å emission compared the transition to the ground state (referred to here as the allowed transition), as should be expected when high densities are present.

The intensity of the allowed transition will also rise, proportional to the square of the density, but not as quickly as the metastable transition. Here, the images in the second row show that the ground state lines do brighten less than the metastable transition. If the allowed transitions are not being enhanced by more than the n_e^2 proportionality it indicates a change in the electron density at the formation temperature of these lines, but without a substantial change in the temperature (i.e. the fraction of emission from a particular Fe ion is not increasing). We consider this more closely in Section 3.4.

These diagnostics work by measuring the ratio of intensity between the two transitions, and comparing it to the theoretical ratio as a function of density. The theoretical ratios are calculated using the atomic physics database CHIANTI v6.0 (Dere et al. 2009) and are shown in Figure 3.9. The diagnostics are most sensitive where the curves are steep and become insensitive at high densities. These calculations assume that the plasma is in thermal and ionisation equilibrium and is optically thin. The consequences of relaxing these assumptions is discussed in Chapters 4 and 5. At this stage we have assumed that as the plasma temperature and density are high, temperature changes will reach equilibrium quickly, the ionisation stage will reflect the true plasma temperature, and that the plasma is optically thin.

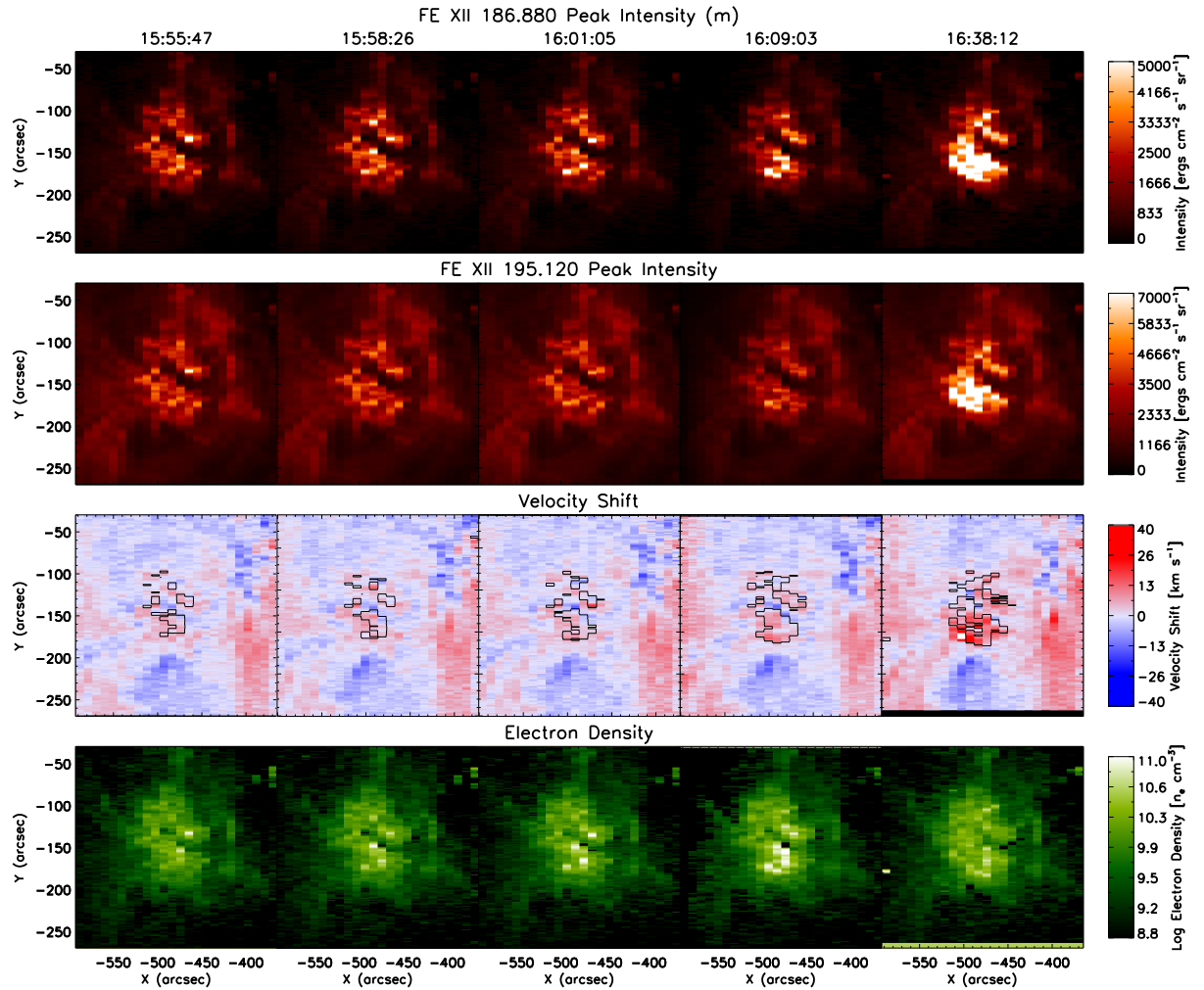


Figure 3.6: Fitted intensities, velocity shifts, and electron densities for Fe XII. The top and second row show the intensities of the two lines of the diagnostic pair, with the upper row emission produced by excitation from the metastable (density sensitive) level. Velocity maps were produced using the allowed 195.120 Å transition and overlaid with density contours at $\log n_e = 10.2$. The times in each column are matched to the TRACE images in Figure 3.3.

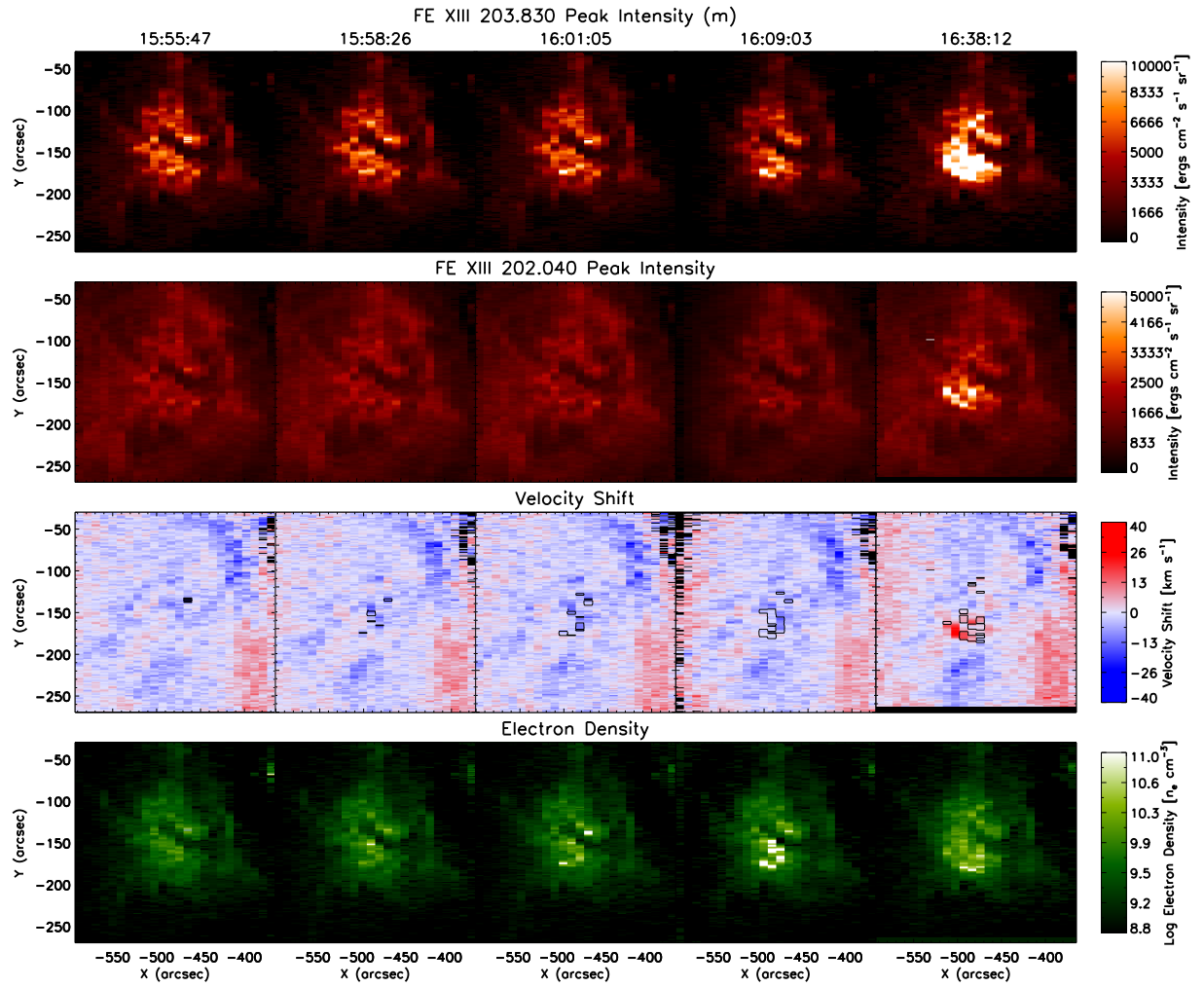


Figure 3.7: As in Fig. 3.6 but for Fe XIII. Velocity maps were produced using the 202.04 Å line and overlaid with density contours at $\log n_e = 10.2$.

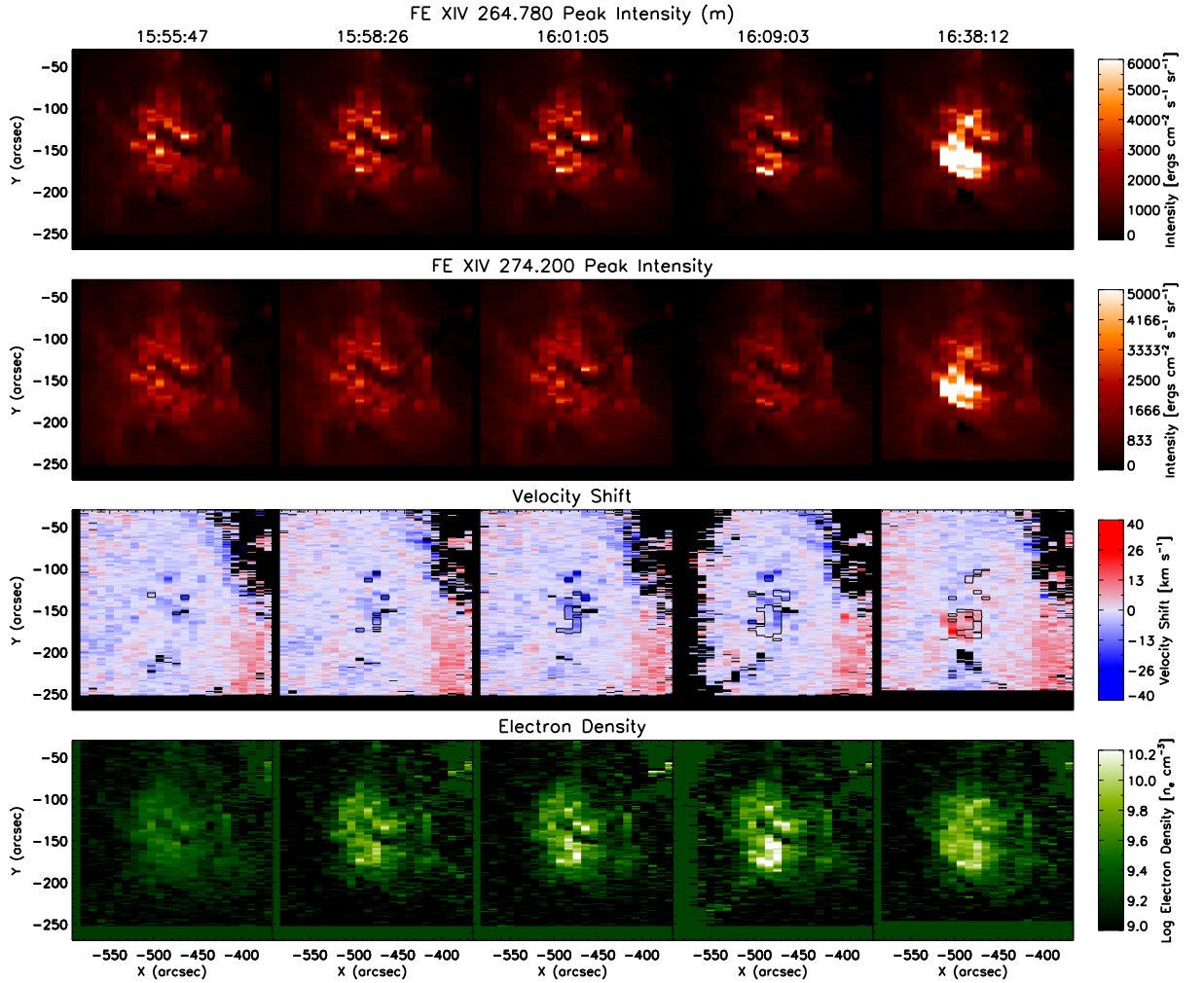


Figure 3.8: As in Fig. 3.6 but for Fe XIV. Velocity maps were produced using the 264.78 Å line and overlaid with density contours at $\log n_e = 9.9$

Densities — The electron density calculated for each raster is found on the bottom row. This is estimated for each pixel by interpolating the measured flux ratio onto the theoretical density curve, shown in Figure 3.9. The uncertainties in the density estimate using this method, and in the atomic physics, are discussed in detail in the next section. Density enhancements are clearly present, and have a similar structure, in all of the diagnostic ratios we have calculated. Small enhancements are seen forming at the beginning of the impulsive phase in the Fe XII raster starting at 15:55:47 UT. The enhancements situated north of the dark filament structure in centre form first, slightly

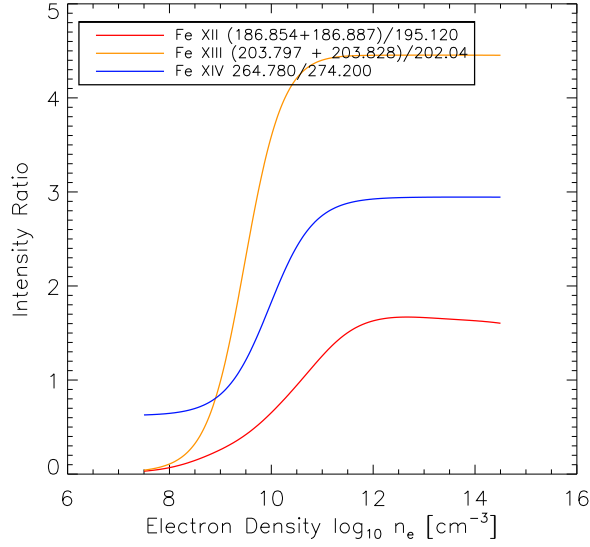


Figure 3.9: Diagnostic curves for the 3 diagnostics used showing the ratio of theoretical intensities versus density for each line pair.

preceding those in the south. They both persist to become part of two high density areas on either side of the filament, matching the pattern of the EUV ribbons seen in TRACE at 16:10:12 UT. In the final post-flare raster, both lines in the diagnostic pair show strong intensity enhancements, as well as a density increase. Bright post-flare loops, also seen at 16:38 UT in TRACE, are very clear in the density maps, as denser evaporated material will have gathered in the loops. Perhaps clearest in Fe XIV is a faint bright arc linking the northern and southern areas, which was also seen in the XRT images. The southern ribbon region is still enhanced compared to the the post-flare loops reaching towards the north, but at this time it is difficult to distinguish the loop emission from any residual cooling that may be happening in the footpoints.

Velocities — The line-of-sight velocity shifts relative to the ‘rest’ wavelength are found in the third row of Figures 3.6, 3.7 and 3.8. Over-plotted are black contours of the density enhancements, at 80% of their maximum value, highlighting the overlap with velocity shifts. Low velocities, on the order of 20-25 km s^{-1} are seen within these contours. Small blue-shifted areas in Fe XIII and Fe XIV are found, while Fe XII shows

signs of small red-shifted areas in the third raster. Though we do not show all of the raster images, blue-shifts (up-flows) are seen predominantly in lines from ionisation stages above Fe XIII and red-shifts (down-flows) are seen from lower ionisation lines (see Figures 3.15 - 3.18). A similar picture was found by Milligan & Dennis (2009), where temperatures of $\sim \log T = 6.2$ represented a turn over in flow direction. In the decay phase, strong down-flows and density enhancements occur in all lines as material cools and falls. We have also noted the blue-shifted region to the north-west, corresponding to the fan of loops seen in the TRACE images, and we believe this may be the same phenomenon as the large scale flows from the edge of active regions reported by Harra et al. (2008).

3.3.2 Footpoint Selection

The character of points of strong intensity or density enhancement appears to vary widely across the region bounded by the flare ribbons. The clearest velocity shifts or density enhancements appear to be contained in a number of compact areas, and also form earlier in the impulsive phase. From this behaviour we can mark them as candidates for the location of flare energy deposition — the footpoints. To better understand the temporal evolution of these footpoints, we have selected three points for a closer analysis, these are displayed with their corresponding number on Figure 3.10. Each position was chosen on the basis of it having large density enhancements or interesting flow patterns. Position 0 marks the earliest footpoint brightening seen, found in the region at the end of the northern ribbon. The highest electron density observed during the event was found at Position 1, and Position 2 marks the earliest enhancement found in the southern ribbon.

3.3.3 High Velocity Flows

The footpoint areas were also visible in lines much hotter and colder than the density diagnostic pairs. The high temperature lines were found to display high speed up-flows

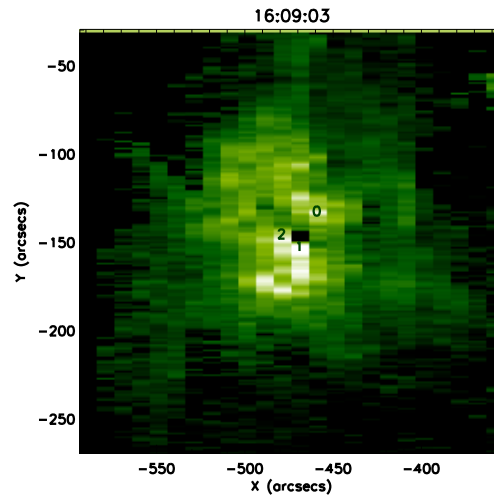


Figure 3.10: Footpoint pixels chosen for further analysis, displayed on the Fe XII electron density image at the 12-25 keV peak.

at the location of the footpoints and in the nearby area. Figure 3.11 displays velocity maps from the third raster at 16:01:05 UT for Fe XVI 262Å and Fe XXIV 255Å. This time was chosen for the example as the flows in most lines reach their maximum velocity here. It is also the raster coincident with the first peak in the 12-25 keV light curve — we look at the full evolution next in Section 3.4. In Figure 3.11, the morphology in Fe XVI appears to be very similar to the cooler lines, while emission in Fe XXIV is mostly found to the East of the ribbon region, as like the SXR loops in Figure 3.5. However, the Fe XXIV line is still present at Position 0 (see Figure 3.10).

The symmetrical Gaussian line profile of a plasma at rest mostly arises from the Maxwellian distribution of random particle speeds — dominating the much weaker instrumental effects, pressure, and opacity broadening. If the entire plasma is moving relative to us, then the centroid position shifts accordingly, but the profile remains symmetrical. In the absence of blends, the profile is effectively a velocity distribution, and any asymmetry can be viewed as plasma that is not co-moving with the bulk distribution. When interpreting these motions, it is common practice to assume that the observed line profile is a superposition of more than one emitting component,

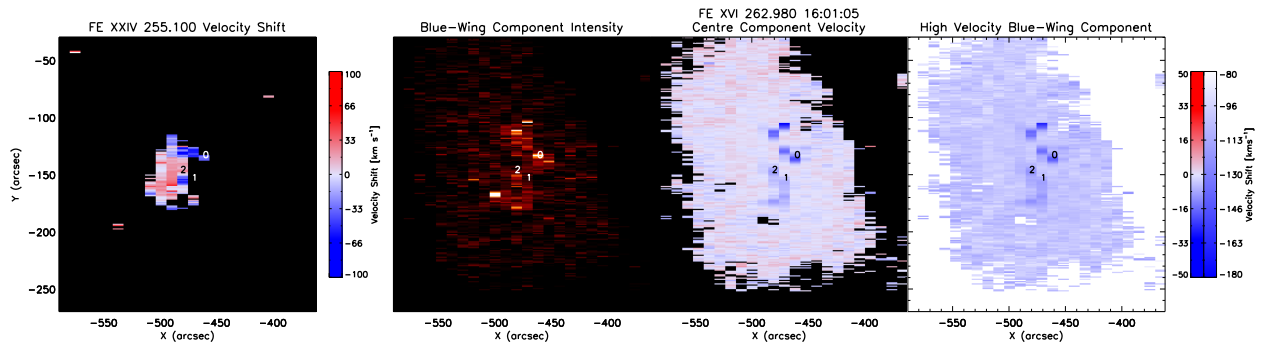


Figure 3.11: Velocity analysis for Fe xxiv (left hand image) and Fe xvi (right hand images). Velocity shifts derived from a single Gaussian fit are shown for Fe xxiv in the left hand image, while images from a double Gaussian fit for Fe xvi are shown on the right. From left to right: the intensity of the second Gaussian component, the velocity shift in the centre component, and the velocity shift of the second component found in the blue-wing. Note the corresponding velocity ranges are shown on the right for each image. The positions marked are the same as those shown in Figure 3.10 and Section 3.4

frequently one with a relatively small line shift, and a second with a much larger shift. This has been performed to good effect in the chromosphere (Peter 2000), where it was apparent that a double component Gaussian fit was required in the chromospheric network. More recently McIntosh et al. (2012) showed that a single component is insufficient at the base of coronal features. In flare studies (Milligan & Dennis 2009; Del Zanna et al. 2011), second components with up-flow velocities of $> 200 \text{ km s}^{-1}$ are routinely observed.

An asymmetric enhancement in the blue-wing of the Fe xvi line profile was observed in rasters approaching the flare peak. Fe xvi, formed at $\log T_{\text{max}} = 6.4$, is a good diagnostic of dynamic motions as it is clearly observed with a large flux and no blends. In our rasters it was therefore the only reliable line in which a double Gaussian fit could be reliably performed. We used the fitting routine `EIS_AUTO_FIT`, with a two-Gaussian template to produce the images found in Figure 3.11, along with a single component fit for Fe xxiv — the close proximity of Fe xvii 254.885 makes determining line shifts

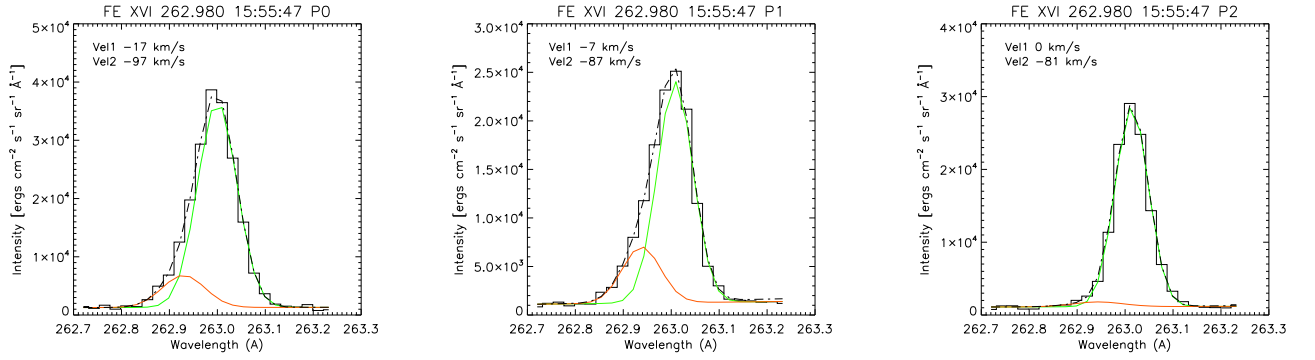


Figure 3.12: Double Gaussian component fits for Fe XVI at footpoint positions 0, 1, and 2. The individual fit components are shown in orange and green with the total fit shown in the black dashed line.

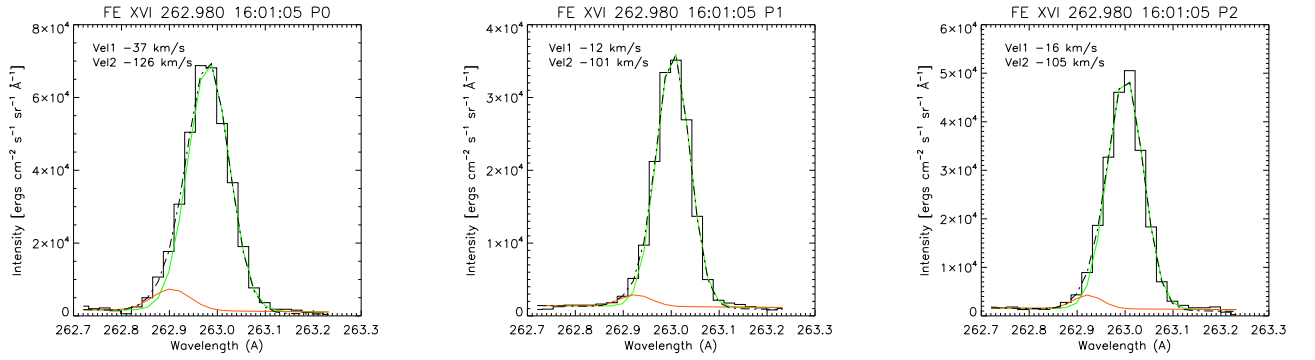


Figure 3.13: As in Figure 3.12 at 16:01:05 UT.

from double component fits difficult. In Figure 3.11 we find that the central Gaussian component of Fe XVI is blue-shifted in the flare ribbon regions by up to 40 km/s. At the same locations the second Gaussian component was found to be strongest in intensity with blue-shifts of 110 to 130 km s⁻¹. Example fitted spectra are found in Figures 3.12 and 3.13 corresponding to the footpoint positions marked in Figure 3.10. The earlier time shows significant blue-wing components with up-flows of up to 100 km s⁻¹. At the later time a high velocity component of nearly 130 km s⁻¹ is present in Position 0 although it is relatively weak compared to the earlier time. Significant blue-shifts of 40-60 km s⁻¹ were also measured in Fe XXIV 255.100 Å and asymmetries in the blue wing were observed, suggesting that the velocities from a single fit are a lower limit

for the evaporating plasma at this temperature. In the other Fe XXIV line at 192.028Å strong blends from cooler lines (Fe XI) obscured any line shifts in the footpoints where the hot emission is weak.

Red-Blue Asymmetry — Double-Gaussian fitting by nature can be susceptible to creating acceptable but unphysical fits to data. For instance, the fitting method does not guarantee that the best fit is unique, as a pair of Gaussian profiles can be placed at many different centroids with widths and intensities that will minimise the chi-squared. In addition, the decision that there should be two separate components of plasma is somewhat arbitrary, and placing restrictions on their relative size and position is adding information that may not represent the true state of the plasma. However, for spectra where the shifted components are very distinct, placing constraints on each component's centroid position based on a judgement by eye will often return sensible fits. The observed Fe XVI 262Å spectra used to produce the fits found in Figures 3.12 and 3.13 did not always have clear shifted components, and the shifted component had to be constrained to an area in the blue-wing between 262.860Å and 263.160Å. An unconstrained fit would for some footpoint pixels result in a large slightly blue-shifted component with a very small centre component or very broad second components with little blue-shift. While adding constraints helps remove these artefacts we have in the following described a method to set the constraints with a more physical basis.

For the three positions of interest, marked on Figure 3.10, the line profiles of Fe XVI were examined more carefully after developing an alternative method. The signal was first binned with the 2 pixels above and below in the y -direction to ensure a high signal-to-noise ratio. Next, we used the Red-Blue Asymmetry method described in De Pontieu et al. (2009) to find the position of maximum asymmetry within the line profile. This method was originally used for the detection of transient up-flows associated with spicules in the quiet sun, and has also been successful in finding high speed features in the chromospheric network. In our analysis, we start by taking a single Gaussian fit to the observed line which is plotted on a velocity axis centred with 0 km s^{-1} at the line centre. Each wavelength now corresponds to a velocity given by

Equation 3.3. For a velocity interval, δV , the difference between the fit and observed profile can be compared to that on the opposite side of the fitted centroid, and the difference used as a measure of the line asymmetry at δV . By measuring the asymmetry across the profile for a small δV , we build up a profile of the Red-Blue line asymmetry in velocity space.

Here, in an attempt to improve our fitting, we have used this to find the position of maximum asymmetry in the line, and then the second Gaussian component is constrained to within a limited range of this velocity (wavelength). The aim of this is to provide the second component with some physical basis to its location without an *a priori* assumption. Only the Gaussian widths were further constrained by using a lower limit equal to the instrumental width. Fitted profiles at the positions marked on Figure 3.10 for a selection of rasters are found in Figure 3.14. As we have used a $\delta V = 10 \text{ km s}^{-1}$ we apply an uncertainty of $\pm 10 \text{ km s}^{-1}$ on the measured line shifts. This δV was chosen as it was small enough to give a smooth asymmetry distribution while being greater than the minimum Doppler shift that can be measured by EIS. A larger δV will decrease the precision that the second component can be placed at but very small values will create a noisy asymmetry distribution which is difficult to obtain a maximum value from.

In the first row of Figures 3.14 (a) to 3.14 (c), at Position 0, a blue wing asymmetry is clearly seen compared to the single central component in green. The fitted second high speed component in orange is surprisingly strong in the earliest raster, and while reducing in intensity at 16:01 UT moves from up-flows of 100 km s^{-1} to 140 km s^{-1} . The centre component is also blue-shifted at 16:01 UT to around 40 km s^{-1} . In Figures 3.14 (d)-(f) a large 40 km s^{-1} flow is found in Position 1, but only in the early raster, and again in Position 2, a faster but weaker flow of 115 km s^{-1} is found at 16:01 UT but no later. The central component in Position 2 at 16:01 UT is also blue-shifted, similar to Position 0. At these temperatures the event appears to have a tendency toward a high speed up-flowing component forming very early in the impulsive phase, which is later followed by a slower movement of the bulk plasma. Interestingly, this does not fit a situation where high speed up-flows found at flare footpoints coin-

cide with stationary background emission such as in [Del Zanna et al. \(2011\)](#), where the high speed evaporated emission is superimposed on a stationary footpoint. Our result tends to suggest that the majority of the plasma at this temperature is also, albeit for a short time, rising. Further analysis would be required to find if this is true at other temperatures.

To remark on the R-B fitting technique, we find that in general it returns similar fits and velocity estimates to the simple constrained method used to generate the fits in [Figures 3.12 and 3.13](#), although there are some differences. For Position 0 the measured velocities agree to within 5 km s^{-1} at 15:55:47 UT, however at 16:01:05 UT the R-B technique fits a high velocity component that is 17 km s^{-1} faster. For Position 1 the high velocity component is found to be 45 km s^{-1} *slower* at 15:15:47 UT. These differences highlight the influence that setting constraints can have on the resulting velocity measurements. With no constraint the fits may be unreliable, yet setting limits by eye can introduce observational biases. The R-B technique addresses this concern by placing a constraint based on properties of the asymmetric line. In circumstances where there is considerable deviation between techniques we are thus inclined to trust the R-B method over fitting using constraints set by eye.

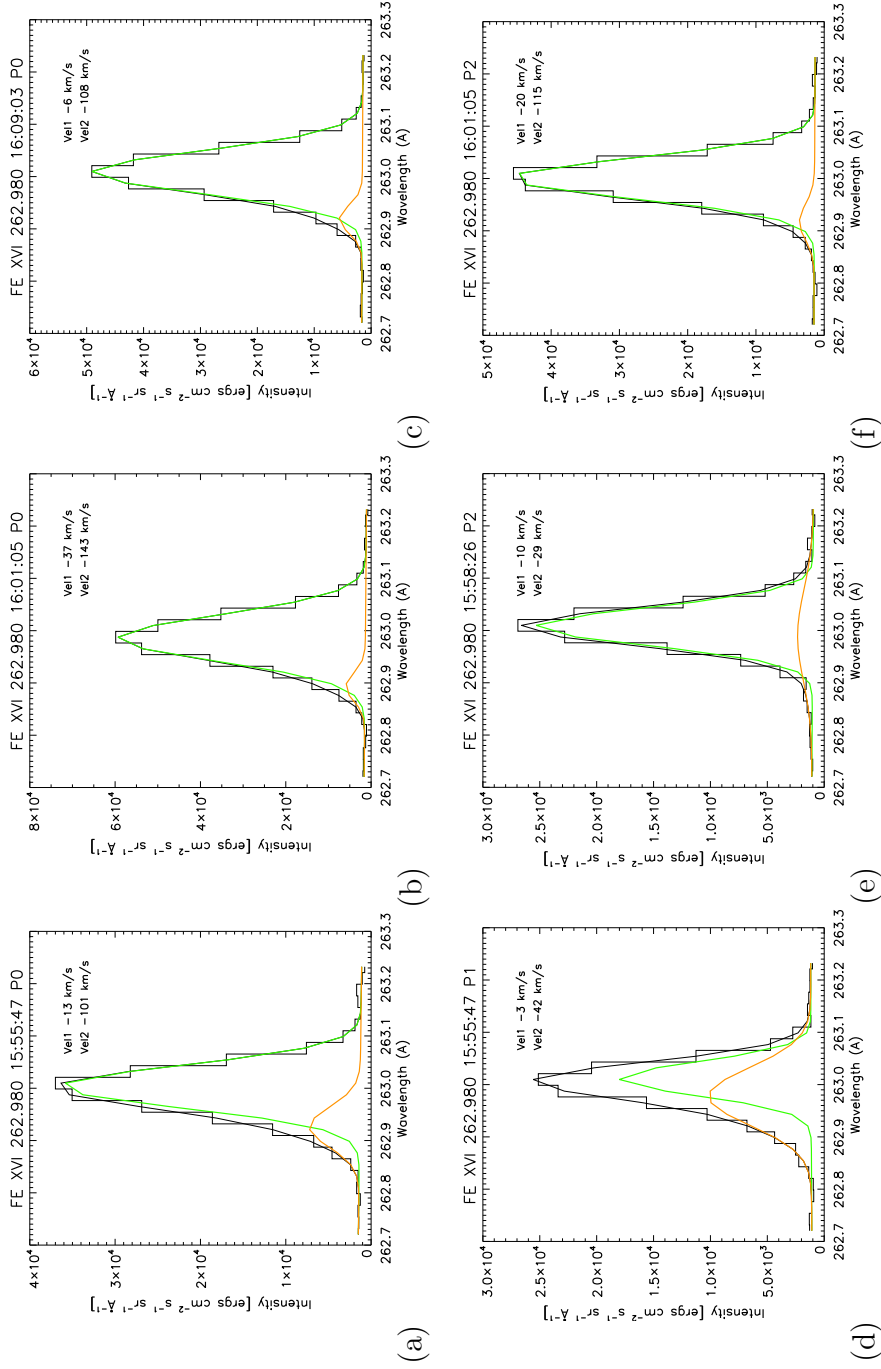


Figure 3.14: Fe XVI double component fits using the R-B asymmetry constraint for the positions shown in Figure 3.10.

The two Gaussian components of the fit are marked in green and orange, and the total fit by the solid black line. The EIS data is shown by the stepped black line. The velocities of both components are shown on the plots where *Vel1* is green component and *Vel2* the orange. In the top row the evolution of Position 0 is shown, where the enhanced blue wing component is strong in the first panel. In the other two positions, shown on the bottom row, the enhancement is only prevalent early on in Position 1 and only just noticeable at Position 2.

3.4 Time Evolution of Selected Footpoints

The 150s cadence of the raster set, while compromised to provide wider spatial coverage, is sufficient to observe changes in plasma flows and densities during the flare impulsive phase. The time evolution of plasma parameters from the positions in Figure 3.10 are shown in Figures 3.15 to 3.18. In each position the fit parameters of the pixel were averaged with the pixels above and below in the y direction, partly to improve the signal to noise ratio, and to account for any residual correlation errors. Pixels were not binned in the x direction, as doing so would sample flux from a $20''$ wide area due to the slit spacing.

Position 0 — The evolution of Position 0 is shown in Figure 3.15, where at 16:01 UT oppositely-directed flows are immediately apparent, indicating that this is a location of strong evaporation. The Fe XVI, Fe XIV and Fe XIII lines are all blue-shifted almost simultaneously, while slight red-shifts on the order of 10 km s^{-1} appear in the cooler Fe XII, Fe X, and He II lines. The up-flow velocity increases with line temperature above Fe XII, reaching almost 40 km s^{-1} in the centre component of Fe XVI. As seen in Section 3.3.3, high speed up-flows of nearly 140 km s^{-1} are also found in the Fe XVI blue-wing component at this time, however, as they were only significant in a few rasters they are not plotted here. Fe XXIV is also blue-shifted by at least 35 km s^{-1} at 16:01 UT. Clear footpoint emission in the hottest lines was not observed in every raster so we do not have the data to compare the evolution here.

Given the spectral resolution of EIS, velocities can be measured from centroid shifts to within $\pm 5 \text{ km s}^{-1}$ (Culhane et al. 2007). However, the accuracy of our chosen rest wavelength is difficult to quantify, and may introduce a systematic uncertainty in the results. The quiet area chosen in Section 3.2.2 was selected where the average line centroid shift compared to the theoretical rest wavelength was close to zero. The deviation in all pixels was mostly within 5 km s^{-1} . While we can discuss relative velocity shifts with confidence, we estimate that the absolute velocities could be off by a maximum of 10 km s^{-1} .

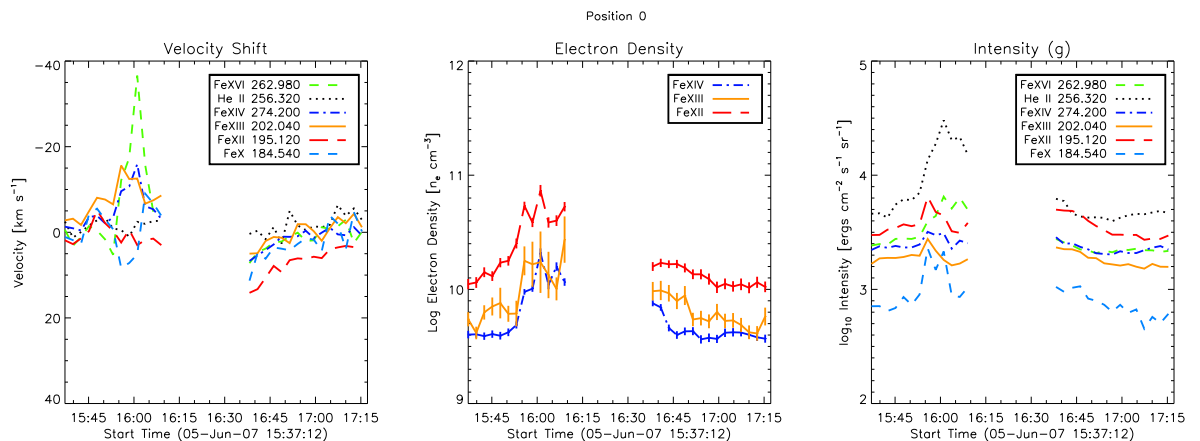


Figure 3.15: Time evolution of plasma parameters for Position 0 in Fig. 3.10.

The panels show, from left to right, the evolution of the line-of-sight velocity shift in five iron transitions plus helium, the electron density, and the intensity including the components of the density diagnostic excited from the ground state. The velocities shown for Fe XVI are derived from the centre component of the double fits in Section 3.3.3.

As the velocity shifts peak at 16:01 UT, the electron number density also peaks at $\log n_e = 10.9$ in the Fe XII diagnostic and at $\log n_e = 10.3$ (n_e in cm^{-3}) in Fe XIV. The Fe XIII diagnostic used saturates about $\log n_e = 11.3$ but due to problems in the atomic physics may be inaccurate above $\log n_e = 10.3$ (Young et al. 2009). Although it appears to follow the behaviour of the other diagnostics reasonably well, it fluctuates more at high densities. While the velocities sharply rose at 16:01 UT (also the time of the first 12-25 keV peak), the densities rise more gradually during the impulsive phase. We have where possible interpolated the upper and lower limits of the measured intensity ratios onto the density curve, returning the possible range of electron densities, however, these do not include errors in the atomic physics calculations which may account for more systematic variations.

The intensities of the spectral lines excited from the ground state are enhanced significantly between 15:55 UT and 16:01 UT. The mid-temperature lines, between Fe X and Fe XIV, peak at 15:55 UT with Fe XVI rising a few minutes later. The very steep

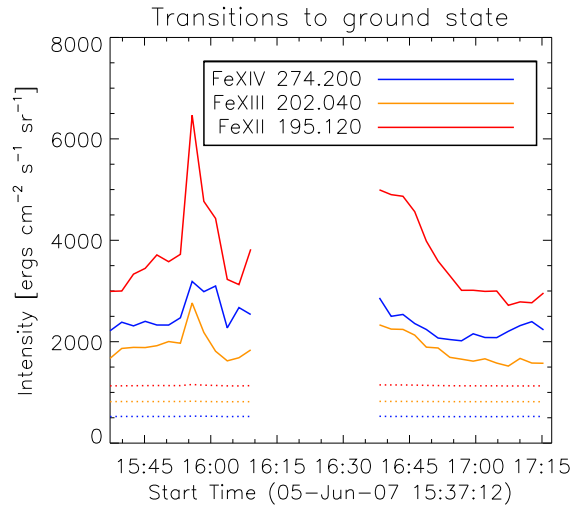


Figure 3.16: Intensity variation of transitions to the ground state in the diagnostic pairs (solid lines) and the same intensity divided by the square of the measured density (dotted lines).

rise in the cool He II line can often be associated with the time of energy deposition and HXR emission of the flare. This event is no different, and the earlier 12-25 keV peak is matched by the He II rise.

As mentioned earlier in Section 3.3.1, the intensity of the allowed transitions in the diagnostic pairs is proportional to n_e^2 . If a cool plasma of constant density were to be heated, any allowed transition with a formation temperature T_{max} would brighten as more plasma is heated to T_{max} . Our diagnostics show that the *density* is increasing. If the plasma were to be at constant temperature, the intensity would rise with n_e^2 . Any additional increase may be interpreted as a temperature rise in the local plasma. In Figure 3.16 the intensity for the transition excited from the ground state for diagnostic pairs is plotted, and the same intensities are shown divided by the measured n_e^2 to remove the density proportionality — an arbitrary constant is added to display them together. The resulting time profiles are remarkably flat with only very small variations, thus the intensity change can almost be entirely attributed to the change in density with very little temperature change.

Positions 1 & 2 — The other two footpoints are similar in character but with some key differences. The electron density at Position 1 (Figure 3.17) located on the southern side of the filament reaches the highest seen during the flare, rising to $\log n_e = 10.3$ in Fe XIII and Fe XIV, and to $\log n_e = 11$ in Fe XII. However, the hot lines while blue-shifted do not display the same well defined shifts as at Position 0. He II and Fe XII are only slightly red-shifted at 16:01 UT. There is some evidence of a higher speed up-flow present in Fe XVI of 42 km s^{-1} (Figure 3.14) at 15:55 UT but the centre component is not significantly shifted at 3 km s^{-1} . Fe XXIV also has no strong signal here.

Finally, Position 2 (Figure 3.18) is where a density enhancement in the southern ribbon first arises, eventually forming the ‘U’ shaped density enhancement south of the filament. Measured densities do not appear to rise until after 15:55 UT where all three diagnostics suddenly jump in density, with Fe XIV showing $\log n_e = 10.2$, with $\log n_e = 10.8$ in Fe XII. The rapid rise in density can possibly be explained by the scanning slit passing over the edge of the flare kernel, which may be smaller than the $10''$ raster spacing. Again there are significant up-flows in lines hotter than Fe XIII but only to speeds of around half that of Position 0. Simultaneous red-shifts are present at this position in Fe X and He II on the order of $5\text{-}10 \text{ km s}^{-1}$. Although weaker than at Position 0, here we see Fe XVI blue-wing flows of 115 km s^{-1} .

We can summarise this somewhat exhaustive list of observations with three key points: (1) electron densities are increasing across all of the EUV footpoint regions during the flare impulsive phase, (2) we deduce that the apparent density rises in the footpoints, although while the footpoints *are* being heating, the temperature does not appear to be contributing to the diagnostic line intensities, and (3) high speed evaporative up and down flows are seen in at Positions 0 & 2, while Position 1 exhibits very little plasma motion, but has the same enhanced electron density.

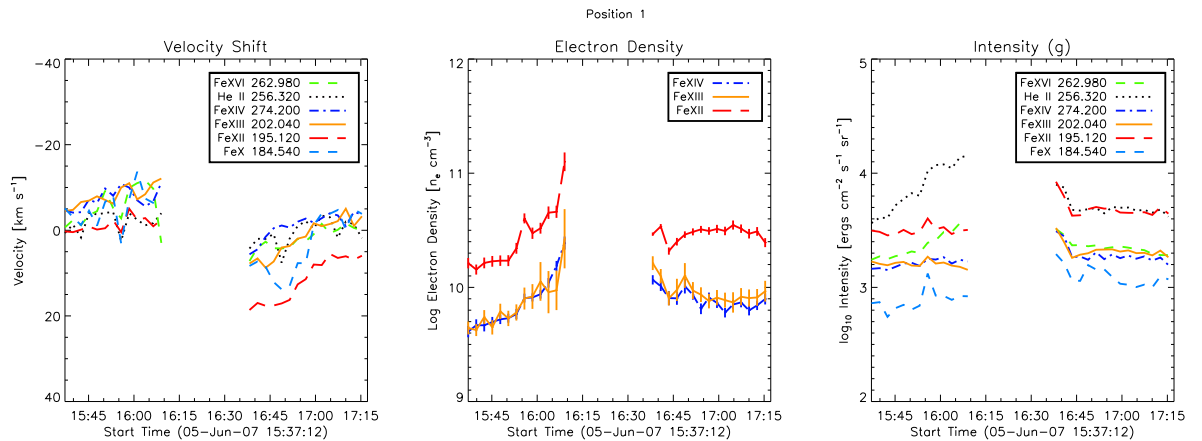


Figure 3.17: As in Fig. 3.15 but showing parameters for Position 1

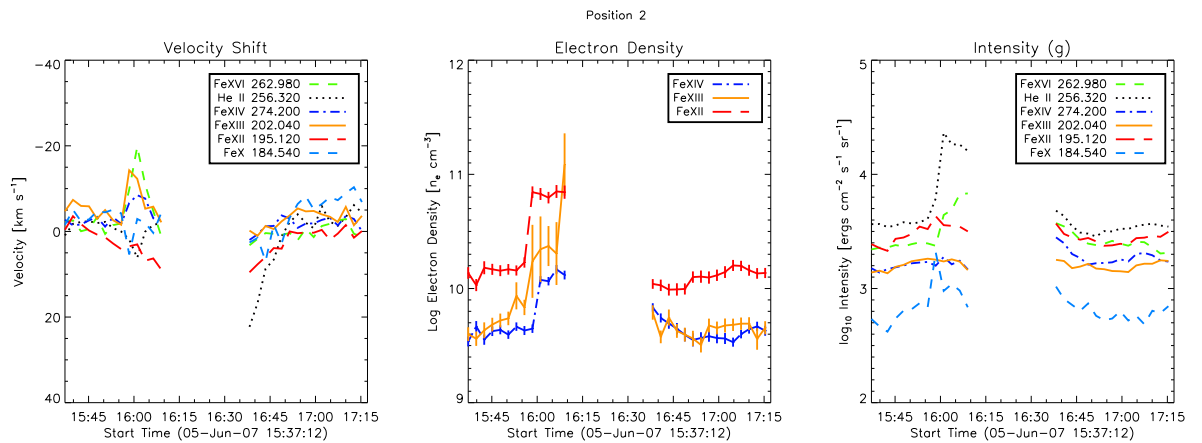


Figure 3.18: As in Fig. 3.15 but showing parameters for Position 2

3.5 RHESSI data analysis

RHESSI X-Ray observations are the final piece of this multi-wavelength puzzle. In the thick-target model of flare energy deposition, accelerated electrons lose energy and heat the chromosphere through Coulomb collisions. The presence of these electrons is detected observationally by a HXR non-thermal power-law component of the photon spectrum. If we assume the footpoint heating is driven by these electrons, then the energy flux deposited in the chromosphere can be estimated from the HXR spectra (Section 1.3.1). RHESSI is also capable of imaging the location of HXR emission using

techniques discussed in Section 2.4.5, which will determine if the energy deposition is occurring at the same location as our EUV footpoints.

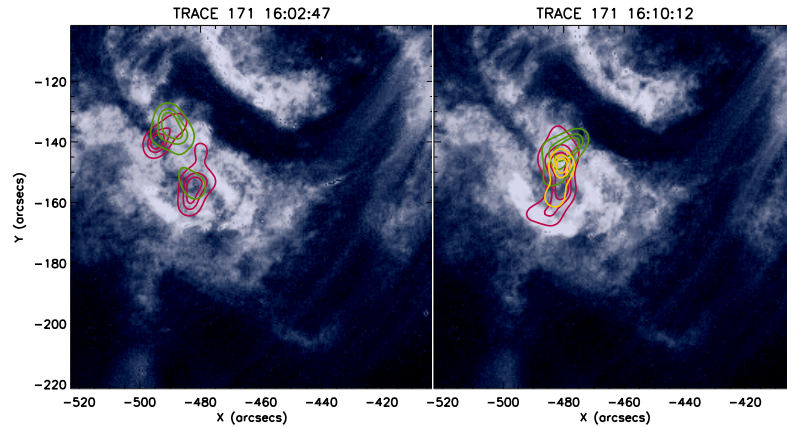


Figure 3.19: Impulsive phase TRACE 171 images with RHESSI 60%, 80% and 90% intensity contours overplotted in 6-12, 12-18 and 18-25 keV energies (magenta, green and yellow respectively).

The RHESSI data preparation and spectral fitting described here was performed by I. Hannah in [Graham et al. \(2011\)](#). The times for spectral analysis in RHESSI were chosen to match the two peaks in the 12-25 keV emission whilst avoiding periods when the A1 attenuating shutters were in place. These shutters are at times placed in front of the germanium detectors to prevent what is known as pulse-pileup. This is an artefact found at high photon fluxes, caused when a second photon arrives in the detector before the energy of the first has been processed. The result is that both are read as a single photon with their combined energy. The data was background subtracted using a level taken from during an eclipse period, where the X-ray flux is at its lowest. The RHESSI images were produced using counts from detectors 3, 4, 5, 6, and 8 using the CLEAN algorithm. Detector 1 had the best energy resolution and lowest background during this pre-anneal time and was selected to perform the spectral analysis (an anneal is a heating procedure carried out every few years to help remove crystal defects in the RHESSI germanium detectors, which reduce their efficiency. Doing this ensures the

detector response is uniform (Hannah et al. 2010)). The OSPEX package was used to fit a thermal (Maxwellian) plus thick-target non-thermal model (Section 1.3.1) to the spectral data. The CLEAN algorithm and OSPEX package were discussed in Section 2.4.5.

Imaging — The difference in pointing between TRACE and RHESSI is unknown, making aligning the HXR image onto the EUV emission difficult, but it is possible to align the images via other instruments. We have used continuum images from the Michelson Doppler Imager (MDI) on board SOHO and also white light (WL) images from TRACE to align the RHESSI imaging. The pointing for SOHO/MDI is well known as it is centred on the solar disc. RHESSI can also very accurately find the limb with its aspect sensors which allows it to be co-aligned with MDI. The MDI continuum and TRACE WL images also display the same features, and these can be cross-correlated to find the residual pointing difference between TRACE and the solar disc centre, which we assume equates to the pointing difference between RHESSI and TRACE. Since the TRACE 171Å images should be aligned with the TRACE WL images, both the TRACE 171Å and RHESSI HXR images can be aligned.

MDI continuum is only available a few times a day, in this case at 12:29 UT, while the closest TRACE WL image to the flare peak was at 15:31 UT. The MDI image was rotated using the SolarSoft DROT_MAP software to account for the solar rotation between these times. Their offset was found using the CROSS_CORR routine with some manual adjustment, and as SOHO is positioned at the L1 Lagrange point, a further correction for the Earth parallax shift of the TRACE orbit was required. Spacecraft drift between TRACE 171 Å images was corrected for by tracking the movement of stable bright points north of the filament using the same procedure as the EIS rasters (Section 3.2.2). After these corrections, we estimate the pointing of TRACE with respect to RHESSI to be within 1.5'' in each direction.

The results for two RHESSI images at times corresponding to the 12-25 keV peaks are shown in Figure 3.19. The RHESSI contours for three energy bands, 6-12, 12-18, and 18-25 keV, lie on top of bright TRACE 171 Å regions which we associate with chro-

ospheric emission. The HXR emission is localised in the southern ribbon area, yet surprisingly there is no evidence for a HXR footpoint at Position 0 (Figure 3.15) north of the small filament. Position 0 showed the most convincing chromospheric evaporation signatures of the positions studied, along with strong density enhancements, yet we see that the HXR sources are found in the southern ribbon, where evaporation signatures are weaker. An offset of $\sim 20''$ between the TRACE and RHESSI images would be necessary to align RHESSI sources with Position 0. Given our careful co-alignment process, we believe that such an error in relative pointing is unlikely. Furthermore, the shape of the HXR footpoints seen match well with the TRACE emission. This implies the energy input from non-thermal electrons must be relatively weak here compared to the southern region, if indeed that is what is driving the evaporation. It should be noted that we use the term ‘hard’ X-ray here loosely. The two impulsive bursts of 12-25 keV emission under the slow rising GOES SXR curve are characteristic of emission from non-thermal electrons, but compared to the electron spectra found in larger flares (where footpoints are seen at much higher energies) the distinction between non-thermal and thermal components is not obvious as will be seen in the spectra below.

Spectra — When the incoming photon flux is high RHESSI is capable of reconstructing the photon spectra from individual footpoint areas. The count rate in this event however was relatively low, so the spatially integrated photon flux was used to create the spectra found in Figure 3.20. The spectra corresponding to both images in Figure 3.19, both peaks of the 12-25 keV light curve, are shown in the top and bottom panels of Figure 3.20. For each time step the photon spectra was fitted with two models; a thick-target model single power-law plus a single thermal component, and with a pair of thermal components. The thick-target fit returns the best fit parameters describing the bremsstrahlung photon spectra for non-thermal electrons interacting via Coulomb collisions with the background chromospheric plasma (Brown 1971; Holman 2003). The fit uses an accelerated electron distribution of the form $f(E) \propto E^{-\delta}$, where δ is the electron spectral index. The total electron number flux, N_e , of the incoming beam is thus given by $N_e = \int_{E_C}^{E_{high}} f(E)dE$, where E_C is the electron low energy cut-off.

The high energy cut-off, E_{high} , while used to constrain the problem, does not have a significant effect on the fit and is not shown in the following discussion. Each thermal fit gives the photon spectra emitted by electrons in a thermal Maxwellian distribution, described by the total emission measure, EM , and the core temperature, T . The fitted parameters for the spectra shown are found in Table 3.2, and further details on the production of bremsstrahlung X-ray spectra, their fitting, and fit parameters are found in Section 1.3.1.

The background level for this event (plotted in grey) is elevated due to degraded detector performance at this time. The outcome is that the non-thermal component, shown in blue on the left hand plots of Figure 3.20, is not particularly clear at high energies (above 20 keV). However, the thermal + non-thermal fit here is considerably closer than the single thermal fit (red line) above ~ 12 keV, which breaks away considerably from the data. The spectral index varies slightly between 9.3 and 9.7 for the earlier and later times, suggesting that while the second 12-25 keV peak was larger in flux, the spectra was ‘harder’ earlier in the flare, leading to more footpoint heating and evaporation. The photon energy above which the spectrum can be referred to as non-thermal is parameterised in the fit by the cut-off energy E_C . Labelling this transition with a hard cut off is somewhat un-physical, as the spectrum represents a continuous distribution of energies, however, it does represent the most probable photon energy that originates from the accelerated electrons. In these fits $E_C \sim 16$ keV for both times during the event.

In the right hand of Figure 3.20 plots we show the double thermal component fits. The reasoning behind this came from the referee for [Graham et al. \(2011\)](#), who suggested that given the relatively soft X-ray spectra observed, a pair of thermal components may be better fit the observations — this would imply the flare heating was not directly the result of accelerated electrons. A pair of thermal components (red and orange lines) does appear to provide an acceptable fit to the data as seen in the plots, but again the high background level makes it difficult to determine at higher energies. The higher temperature thermal component (orange line) drops away from the data at high energies slightly more than in the non-thermal model (blue line). However, visu-

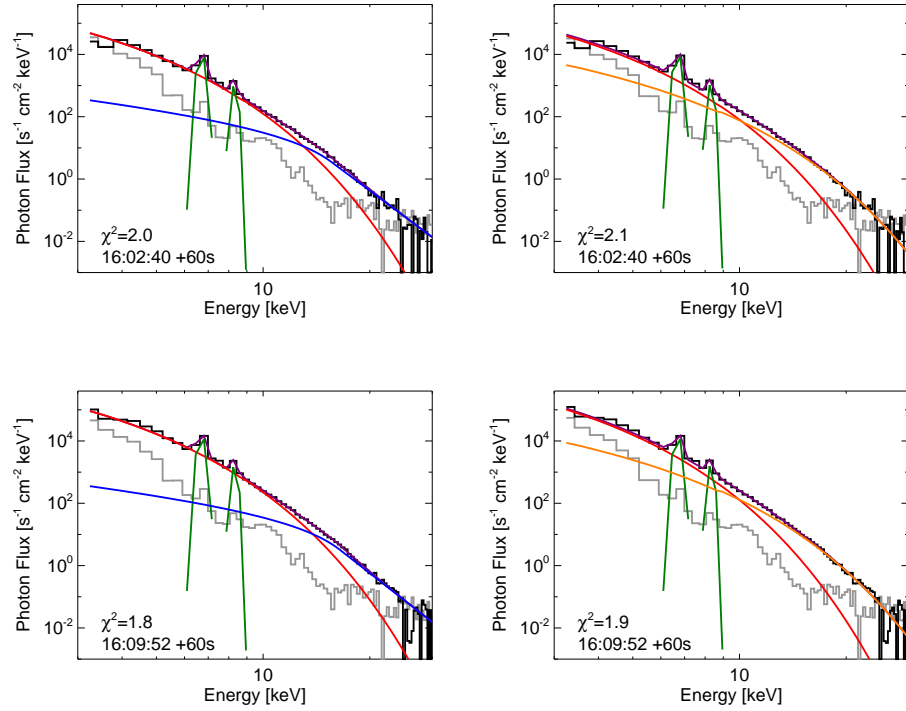


Figure 3.20: RHESSI photon spectra times corresponding to the first (top) and second (bottom) 12-25 keV peak. The data for both peaks is fitted with two models: in the left hand panels, a single thermal component (red) plus thick target model of accelerated electrons (blue); and in the right hand panels, a pair of thermal components (orange and red).

ally, and even from the χ^2 values, all between $\chi^2 = 1.9 - 2.1$, there is little evidence to favour one model over another. Nevertheless, the implications of both are discussed in the next section.

Looking back at the morphology of the RHESSI contours in Figure 3.19, the earlier frame appears more consistent with hot footpoint emission. Two regions of similar size to the patchy bright regions in TRACE lie in the 6-18 keV energy range. From both spectral fits, we find that at energies up to 12 keV the emission is dominated by a hot thermal component at around 16 MK; the central concentration of SXR emission in Figure 3.5 confirms this picture for plasma with a temperature of at least 8 MK. Interestingly, the imaging at this time showed no sources between 18-25 keV. In the

later frame, the emission is less localised, possibly outlining the shape of a loop at 6-12 keV, yet the concentration at 18-25 keV hints at a footpoint contribution from below, and is at the location of the largest density enhancement (Position 1).

Table 3.2: Model parameters for the RHESSI photon spectrum at 16:02 UT and 16:09 UT. Parameters for both thermal plus thick-target and double thermal fits are shown. EM and T are the emission measure and core temperature of each thermal component, δ is the electron spectral index, E_C the electron low energy cut-off, and N_e the electron number flux.

| Fit | Time | EM_1 (10^{48}cm^{-3}) | EM_2 (10^{46}cm^{-3}) | T_1 MK | T_2 MK | δ | E_C (keV) | N_e ($10^{35} \text{electrons s}^{-1}$) |
|---------------|----------|--|--|----------------|----------------|---------------|----------------|--|
| Th \times 2 | 16:02:40 | 0.6 ± 0.1 | 4.3 ± 0.9 | 15.7 ± 1.0 | 27.0 ± 0.8 | ... | ... | ... |
| Th + TT | 16:02:40 | 6.8 ± 0.2 | ... | 16.4 ± 1.1 | ... | 9.3 ± 0.4 | 15.6 ± 0.6 | 2.7 ± 1.0 |
| Th \times 2 | 16:09:52 | 1.7 ± 0.5 | 8.5 ± 2.3 | 14.3 ± 0.8 | 25.9 ± 0.9 | ... | ... | ... |
| Th + TT | 16:09:52 | 1.3 ± 0.3 | ... | 16.2 ± 0.6 | ... | 9.7 ± 0.3 | 16.5 ± 0.5 | 2.6 ± 0.7 |

3.6 Processes taking place at the flare footpoints

The observational parameters that describe the flare energy input flux in the footpoints have now been estimated, along with diagnostics of the plasma heating and dynamic response to the energy flux. We are now in a position to investigate how our new observation, that electron densities at the footpoints during the impulsive phase are enhanced, ties in with our current understanding of flares. The observations can be summarised as follows. During the impulsive phase, energy is deposited into a number of small regions in the chromosphere/transition region, visible as ribbons and footpoints in UV and EUV, and also in SXR images, implying that the plasma is at low heights but heated to temperatures of a few MK. *Hinode*/EIS iron density diagnostics formed at around 1.5 MK show the electron density increases here during the early impulsive phase, typically up to a few times 10^{10}cm^{-3} , but since the ground state transition only increases slightly beyond its n_e^2 dependence, we infer that any variation in temperature of the plasma emitting these lines is small. A number of the footpoints show line-of-sight velocity shifts during the impulsive phase — on the order of 20-140 km s^{-1} — at the time of the n_e enhancements, and with a tendency for lines cooler than Fe XIII to be red-shifted and those hotter to be blue-shifted. These are followed in the gradual phase by substantial red-shifts in most lines, associated with the draining of hot material. Unexpectedly, the footpoint showing the strongest impulsive-phase line shifts (Position 0 in Figure 3.10 and regions north of the filament) does not have any detectable RHESSI source. This last point, and the high observed densities, are two of the questions that we will try to answer.

What process is leading to the increasing n_e values? The most straightforward explanation is to assume that the observed iron emission is emitted primarily by plasma at the temperature of maximum ionisation fraction, T_{max} , of the relevant ion, and that during the flare impulsive phase deeper layers of the atmosphere are heated to this temperature. Correspondingly, the dominant emission will originate from regions of increasing density, but always at around T_{max} . The small increase in intensity of the ground state transition beyond the density proportionality (see Figure 3.4) does suggest

that there is a small contribution to the line intensity in addition to dominant effect of heating denser layers. We interpret this as heating of plasma in different layers within the same optically thin column. A second case for a density enhancement would be to assume a scenario whereby already hot plasma at a depth in the transition region is compressed resulting in a higher density, such as in the case of a downward moving conduction front driving evaporation (Fisher 1989). However, in this case the location of the front is still moving to regions of higher density and these two effects may be difficult to separate diagnostically.

Modelling of gentle evaporation, and of the gentle early phase of a flare which later displays more explosive evaporation caused by an electron beam (Fisher et al. 1985; Allred et al. 2005), shows that the position of the transition region (i.e. the location of rapid increase in atmospheric temperature) moves downwards slightly in the atmosphere and the density just below the transition region increases, which is roughly consistent with what we see here. Although the majority of the velocity shifts observed in this small event are fairly low compared to similar events (Milligan & Dennis 2009; Watanabe et al. 2010), the presence of high speed flows in Fe XVI suggests that there is some dynamic plasma motion here consistent with more explosive evaporation (the difference between gentle and explosive evaporation is detailed in Section 1.3.2). In the model found in Fisher et al. (1985), a transition between gentle and explosive evaporation is found at non-thermal input fluxes of around $F_p \sim 10^{10}$ ergs cm⁻² s⁻¹. We calculate this flux via the RHESSI spectra in the next section and attempt to explain the evaporation characteristics. However, it should be noted that the existing models often use input electron spectra that are much harder and typically have a higher cut-off energy than we infer from HXR measurements, so that the majority of collisional energy input occurs deeper in the atmosphere. Direct comparisons of our results with these models may not always be reliable.

The diagnostics show that n_e increases typically to a few $\times 10^{10}$ cm⁻³ while the high-density sources remain compact (i.e. not loop-like). This places the emission location relatively low in the atmosphere. In a non-flaring (but still active) atmosphere, for example the VAL-E model for bright network (Vernazza et al. 1981) appropriate for

the active region locations where the flare occurs, a density of $n_e \sim n_h = 4 \times 10^{10} \text{ cm}^{-3}$ occurs at a column depth of $5.8 \times 10^{18} \text{ cm}^{-2}$, where the hydrogen ionisation fraction is approximately equal to unity. In some instances, for example the Fe XII diagnostic at Position 1, n_e approaches 10^{11} cm^{-3} , which corresponds to regions in the VAL-E atmosphere where the plasma is only partially ionised. In such cases, it is possible that an electron beam, containing sufficiently high energy electrons, could lead to an increase in the observed electron number density due to collisional ionisation, followed by heating. To do this, the electron beam must be able to penetrate to regions where ionisation fraction is less than one — in the VAL-E model the ionisation fraction drops off at depths below around 2000 km in the chromosphere. We clearly see heating at chromospheric heights in this event, and in a thick target regime, as we show below, we find that driving ionisation at these depths is not a demanding condition. In the next few sections we use the RHESSI fit parameters in a quantitative manner to verify if these observations can be explained by electron beam heating or otherwise.

3.6.1 Electron Stopping Depth

The depth at which a non-thermal beam of electrons is stopped in the chromosphere can be estimated from the collisional thick target model. Starting from the equation found in [Emslie \(1978\)](#), the stopping depth, N_{stop} , of an electron of energy E and speed v can be found using the following expression

$$\frac{dE}{dN} = \frac{-2\pi e^4}{E} [x\Lambda + (1-x)\Lambda'] n_H v, \quad (3.4)$$

where Λ is the Coulomb logarithm, Λ' is the associated Coulomb logarithm, and e the electron charge. In this case the target plasma is hydrogen of total number density n_H and ionisation fraction x . The Coulomb logarithms, electron velocity, and ionisation fraction are functions of the column depth N and electron energy, hence it is not straightforward to integrate to find the stopping depth. This expression was integrated computationally by L. Fletcher in [Graham et al. \(2011\)](#) to find the stopping column depth as a function of the initial electron energy, and is shown in [Figure 3.21](#) using

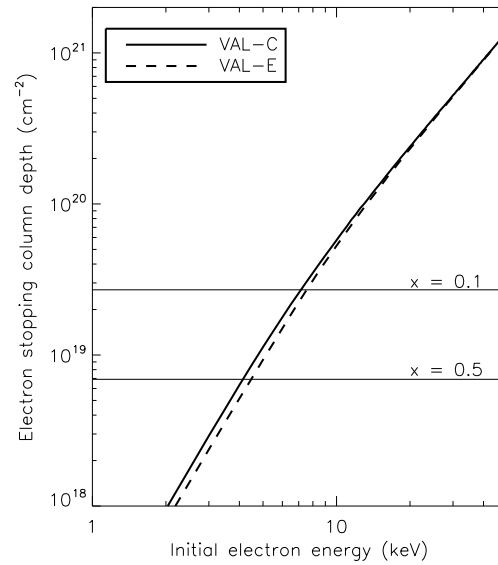


Figure 3.21: Stopping column depth as a function of the injected electron energy for the VAL-C and VAL-E model atmospheres. The depth at which the VAL-E atmosphere is 10% and 50% ionised is shown by the horizontal lines.

parameters from the VAL-C and VAL-E models. As expected electrons with a higher input energy travel further into the chromosphere before being stopped by collisions. Horizontal lines on Figure 3.21 indicate the approximate locations at which the VAL-E atmosphere is 50% and 10% ionised. With the value of E_C , found from the RHESSI fitting, of 15.6 keV the beam energy is mostly deposited around $5 - 10 \times 10^{19} \text{cm}^{-2}$. Electrons of this energy will easily penetrate to depths where the atmosphere is partially ionised (almost neutral) and have the potential to increase the hydrogen ionisation fraction. The increased free electron count may contribute to the electron densities found via the diagnostics, but without further calculation it is unclear by how much, and how long the plasma can remain out of equilibrium at high density (see Section 2.1).

3.6.2 Electron Beam Power

The total power deposited by a beam of accelerated electrons can be calculated from parameters of the X-ray photon spectra fit. In the thick-target interpretation this energy is assumed to be delivered into the chromosphere and is the source of the flaring processes that we see. In Section 3.5, the RHESSI photon spectrum was fitted with a collisional thick-target model for accelerated electrons. The accelerated electron distribution could be described as $f(E) \propto E^{-\delta}$, where δ is the spectral index and the total number flux of electrons is given by $N_e = \int f(E)dE$ electrons s^{-1} . The best fit parameters for the observed spectra were shown in Table 3.2. It can be shown that the total power in the beam is given by

$$P = \int f(E)EdE = 1.6 \times 10^{-9} N_e E_C \frac{\delta - 1}{\delta - 2}, \quad (3.5)$$

where E_C is the electron cut-off energy and the power is in units of erg s^{-1} (see Holman et al. (2011)). Using the fitted parameters shown in Table 3.2 the equation returns a power in the non-thermal electrons at 16:02:40 UT of $(7.7 \pm 2.9) \times 10^{27}$ ergs s^{-1} and at 16:09:52 UT $(7.8 \pm 2.2) \times 10^{27}$ ergs s^{-1} . Both times return very similar power values and which suggests that the energy deposition rate was similar at both times.

The power per unit area, F_P , is a useful measure which can be obtained by estimating the HXR source size. Measuring footpoint sizes from RHESSI imaging can be notoriously uncertain, due to the way in which images are reconstructed, however, the CLEAN algorithm is capable of resolving sources down to $2''$ where the count rate is good. In our event the brightest EUV footpoints do appear to be compact, and are comparable in width to the 12-18 keV sources found in both panels of Figure 3.19, therefore we estimate the size of these sources to be approximately $5''$ wide. The higher energy source (18-25 keV) is slightly more compact, so we suggest that the majority of the beam power is delivered to an area with an upper limit of $5'' \times 5''$, giving a footpoint area of 1.3×10^{17} cm^2 . If we use the power from the 16:02 UT spectra, since it corresponds better with the peak velocity flows, we find that the power per unit area

is $F_P = 5.9 \pm 2.2 \times 10^{10}$ ergs cm⁻² s⁻¹ for electrons above the cut-off energy 15.6 keV. The uncertainty in this value is found by propagating the errors from the fit parameters in Table 3.2. Although the fitted uncertainties in E_C and δ are small, as the power in electrons above the cut-off energy E_C depends on $E_C^{2-\delta}$ (since $N_e \propto E^{1-\delta}$), and the spectral index is very steep; a small increase in the low-energy cut-off value can change the power derived by a significant factor.

So through the parameters found by spectral fitting we have arrived at a beam power leading to energy fluxes of $F_P \sim 10^{10}$ ergs cm⁻² s⁻¹, comparable to those above which explosive evaporation occurs in modelling (Fisher et al. 1985). However, at the same time there is sufficient uncertainty in our results, should the source size be larger or E_C higher, that they may also be consistent with a case of gentle evaporation. We can also consider this uncertainty with respect to the footpoint at Position 0. As we mentioned in the previous section, the footpoint here displays no clear HXR source, yet harbours high speed evaporation flows at high temperatures. The dynamic range of RHESSI is only around a factor of 10, meaning that in a single image, features with a brightness of less than 10% of the strongest feature will not be observed. If the uncertainties in F_P were to allow for a factor of 10 increase, then if we reduced the F_P value at Position 0 corresponding roughly to RHESSI's dynamic range, it would bring the footpoint within the modelling requirement for explosive evaporation, although this would be stretching the observational limits rather far. By changing the footpoint size alone, a width of $\sim 1.6''$ would be sufficient to raise F_P by a factor of 10, although such small source sizes may not be unreasonable (see Battaglia & Kontar (2011) and Battaglia et al. (2012)). Nevertheless, we first we must consider if the flow speeds are indeed characteristic of explosive evaporation.

3.6.3 Flow Speeds

One of the requirements for explosive evaporation is that the flow speeds are faster than the local plasma sound speed, as will occur if the heating time scale is shorter than the hydrodynamic expansion time scale. We can compare the spectroscopically-

determined line-of-sight flow speeds observed in Figures 3.15 to 3.18 to the relevant sound speed C_s via the expression

$$C_s = 9.79 \times 10^5 \left(\frac{\gamma Z T_e}{\mu} \right)^{\frac{1}{2}}, \quad (3.6)$$

where for ionised hydrogen the atomic number is $Z = 1$, the adiabatic index $\gamma = \frac{5}{3}$, and $\mu = m_i/m_p = 1$. Taking the temperature of formation of the Fe XIII line as $T_e = 1.58$ MK, the sound speed of the plasma is $c_s = 147$ km s⁻¹, and for Fe XVI $c_s = 185$ km s⁻¹. Our observational upper limit of 140 km s⁻¹ for Fe XVI is lower than, though reasonably consistent, with these speeds. What is perhaps best demonstrated by these findings is that in a flare of relatively small energy such as this, there is no clear cut case for either evaporation scenario with the input flux being on the border of driving both cases. What we have learned though is that the locations of enhanced density are also sites of evaporation, and the densities are high at the transition between downward and upward flows — this point will be returned to in Chapter 4.

3.6.4 Electron Beam Heating

To produce the observed iron line emission requires heating the chromospheric plasma from its ambient state to around 1.5×10^6 K. If we start from the VAL-E model atmosphere, which we assume to be a reasonable pre-flare atmosphere, the temperature at a density of a few $\times 10^{10}$ cm⁻³ is around 20,000 K. From Equation (36) in Emslie (1978) we can estimate the heating rate per target particle for a collisional thick target beam. At a column depth N the heating rate due to a beam electrons above E_c in a fully ionised hydrogen plasma is given by

$$Q = \pi \Lambda e^4 (\delta - 2) B \left(\frac{\delta}{2}, \frac{1}{3} \right) \frac{F_P}{E_C^2} \left[\frac{6\pi \Lambda e^4 N}{E_C^2} \right]^{-\delta/2} \text{ ergs s}^{-1}, \quad (3.7)$$

where B is the Beta function. By inserting the fitted values for δ and E_C , and using $N = 5.8 \times 10^{18}$ cm⁻² (where $n_e \sim 4 \times 10^{10}$ cm⁻³ in the VAL-E atmosphere) we find that our derived input flux yields a heating rate per particle of $Q \sim 7.8 \times 10^{-6}$ erg s⁻¹.

At this density, and by using a value from the radiative loss function of [Martens et al. \(2000\)](#) at around $\log T = 6.2$, $f(T) \sim 10^{-21}$ ergs s⁻¹ cm³, we can estimate the radiative energy loss rate per particle, which is given by $n_e f(T) = 4 \times 10^{-10}$ erg s⁻¹. The conductive energy loss rate per particle can also be estimated by $\sim 10^{-6} T^{7/2} / n_e h^2$ ([Spitzer 1962](#)). If we use a temperature $T \sim 2 \times 10^6$ K, and an approximate scale height for the transition region, $h \sim 10^7$ cm, then the loss rate is approximately 2×10^{-9} ergs s⁻¹. The incoming heating flux is therefore well in excess of both of these loss rates, and clearly the plasma will heat quickly.

3.6.5 Thermal Heating

If we consider the double thermal fits in [Figure 3.20](#), where the spectrum is modelled by a high and low temperature component, the fit parameters ([Table 3.2](#)) suggest that we see around 5% of the plasma at a temperature of 26 MK. The emission measure in the hot component at 16:01 UT is around 5×10^{46} cm⁻³, and using the same footpoint size estimate, we find the column emission measure is $\sim 4 \times 10^{29}$ cm⁻⁵. Knowing that the column emission measure is $n_e^2 h$, and assuming a constant density of 5×10^{10} cm⁻³, we find that the thickness of the emitting region should be around 1500 km — on the order of the thickness of the chromosphere. It is slightly unrealistic to assume that the entire chromosphere is heated to this temperature, but our chosen density gives a very conservative estimate of the entire thickness. Increasing it to 10^{11} cm⁻³ returns a thickness of around 380 km, comparable with the idea of a thin heated slab in the upper transition region, cooling by conduction into the lower atmosphere (see the discussion in [Chapter 4](#)). Again this may be viable where the electron cut-off energy is low, since electrons will be stopped higher in the transition region where it is easier to heat to the high temperatures observed.

If we continue along this line of reasoning, the conductive flux from a plasma at a temperature T can be expressed as

$$F_c = \kappa T^{5/2} \frac{dT}{dh} \text{ ergs cm}^{-2} \text{ s}^{-1}, \quad (3.8)$$

where $\kappa = 10^{-6} \text{ ergs K}^{-7/2} \text{ cm}^{-1} \text{ s}^{-1}$ (Spitzer 1962). If the temperature gradient dT/dh is assumed to be the difference between the implied 26 MK second thermal component and 20,000 K pre-flare atmosphere, taken over the estimated 1500 km chromospheric emitting region, the conductive flux is found to be $F_C \sim 6 \times 10^{11} \text{ ergs cm}^{-2} \text{ s}^{-1}$. This is sufficient to drive explosive evaporation, according to modelling, by an order of magnitude. The estimate is very much an upper limit, as we have assumed that classical conductivity applies (see Section 4.6), that energy losses from flows and radiation are negligible, and that the density is constant throughout the region, although it does demonstrate that there could be a significant energy flux present from conduction alone. These numbers give us some explanation to the absence of HXR sources at the strong evaporation sites, however, the transition region still requires heating to high temperatures via some energy release. The conclusion drawn from morphology of the X-ray sources discussed in Section 3.5 was that of compact footpoint sources, with little evidence for a hot loop connecting the strong evaporation site (Position 0) to the RHESSI sources. If the RHESSI sources were that of a hot loop top, the fainter loops seen in XRT could in theory conduct heat to the northern region. Recalculating the flux using a loop length of $20''$ gives $F_C \sim 6 \times 10^{10} \text{ ergs cm}^{-2} \text{ s}^{-1}$, which is still comparable to the non-thermal beam case. Yet without clearer observations we still cannot be certain of either case, and a combination of both conductive and non-thermal heating is likely, nonetheless it is worth exploring all avenues that these observations allow for.

3.7 Conclusions

The initial objective of this analysis was to obtain an estimate for the footpoint electron density during the impulsive phase using data from *Hinode*/EIS. After finding an event which had excellent coverage in a number of instruments, it quickly led on to exploring the physics that could be extracted from so many co-aligned multi-wavelength observations. In this chapter we have shown that *Hinode*/EIS imaging spectroscopy is capable of capturing the evolution of compact flare footpoints during the impulsive

phase, and that along with many supporting observations, diagnostics can be made of the plasma which are reasonable in the scheme of recent modelling of flare energy deposition and can question which models are most suitable for small flares.

We found through a detailed application of *Hinode*/EIS spectral diagnostics evidence for an increase in flare footpoint plasma density emitting at temperatures $\sim 1.5 - 2$ MK, and at depths which are consistent with a downward motion of the transition region during gentle evaporation. RHESSI X-ray spectroscopy, interpreted using the collisional thick-target model, placed limits on the energy flux of an electron beam producing the observed flare chromospheric heating. Combined with an estimate of the RHESSI non-thermal source size, the derived beam power per unit area was in excess of that which should lead to explosive evaporation, though a very soft spectrum and uncertainties in the low energy cut-off make the result somewhat speculative. We therefore considered an alternative double thermal model, which fits the data equally well, and may feasibly explain the observed evaporation site with no HXR source by implying heating through a conduction flux. However, the imaging at two periods in the impulsive phase suggests the HXR emission is dominated by footpoint sources and not loop structures heated to flare temperatures.

Diagnostics of this nature are clearly extremely important in determining the response of the lower atmosphere during flare heating to various energy input methods. The results within this chapter may be fairly inconclusive, but have explored and refined diagnostic techniques which can be focused on observations with better spectral coverage, as will be seen in the following chapters.

Chapter 4

Impulsive Phase Flare Footpoint Emission Measure Distributions

In this chapter, we have furthered the investigation of footpoint heating by employing a new technique to recover the first emission measure distributions (EMD) of impulsive phase footpoint plasma using *Hinode*/EIS data, allowing us to view the emission measure as a function of temperature with excellent spatial resolution. The bulk of the work in this chapter was published in [Graham et al. \(2013\)](#) for 6 flares occurring during a period between May and December 2007. What is presented here describes the same analysis but provides more insight in interpreting the results and testing the inherent assumptions.

During the impulsive phase of a solar flare, the temperature distribution of the heated footpoint plasma provides a critical constraint on the distribution of energy injected from the flaring mechanism. When heating a stratified pre-flare atmosphere, the depth in the atmosphere of energy input, methods of energy transfer within the plasma, and magnitude of the input energy flux will all have an effect on the footpoint temperature distribution. Our motivation was thus, if the recovered EMDs were sufficiently robust, i.e. more sensitive to changes in the plasma than the uncertainties in the method, we could make comparisons with EMDs calculated from modelling to infer what physics is involved in the observed heating.

Prior to our analysis, this observable had never before been measured using an instrument with as high spatial and spectral resolution as EIS; although several studies had been made with EUV data from instruments onboard the *Skylab* space station (see [Tousey \(1977\)](#) for an overview), the results were somewhat compromised by the instrumental limitations at the time. We find that our EMDs derived from EIS give a clearer picture of the heated flaring atmosphere, however, though they supersede the earlier work we find our results from EIS are comparable to some of the EMDs extracted from the *Skylab* data. We compare our EIS EMDs with these prior results in more detail in [Section 4.5.1](#) and [4.6](#), finding the slope of the EMD to be an important diagnostic tool.

In our analysis of EIS footprint data, the EMD is obtained from intensity measurements across a wide range of temperatures in conjunction with knowledge of the emission line contribution functions. In our analysis we have used a regularized inversion method developed by I. Hannah ([Hannah & Kontar 2012](#)) — adapted from the inversion of RHESSI HXR spectra — which inverts the key equation

$$I = \int G(T, n_e) \xi(T) dT \quad (4.1)$$

to find the differential emission measure, $\xi(T)$, in the form

$$\xi(T) = n_e^2 \frac{dh}{dT} \text{ cm}^{-5} \text{ K}^{-1}. \quad (4.2)$$

We use observed EIS line intensities, I , and the contribution functions, $G(T, n_e)$, from CHIANTI v7.0 ([Dere et al. 1997](#); [Landi et al. 2012](#)) in order to perform the inversion and find $\xi(T)$ which gives us the EMD(T). The distinction between DEM and EMD is clarified in [Section 4.1](#) and full details of the inversion method are found in [Section 4.4](#).

Even though interpreting EMDs can be notoriously ambiguous ([Brown et al. 1991](#); [Judge et al. 1997](#); [McIntosh et al. 2000](#)), the resulting temperature distribution is extremely useful. For example, in our analysis it was immediately clear that the plasma

is not isothermal, and that a distribution exists which must result from some temperature gradient. We have taken steps to ensure that physics extracted from our EMDs can be trusted: 1) by using line intensities that are spatially resolved and de-blended; 2) by using an inversion method that returns EMD uncertainties and makes no *a priori* assumptions about the plasma; 3) by testing the method on various solar features; and finally 4) by understanding the assumptions inherent in the atomic physics. From our analysis and comparing to theoretical models we have concluded that the resulting EMDs are compatible with an atmosphere heated by non-thermal electrons in a relatively thin, hot layer, which then transfers energy via conduction into cooler layers emitting the observed EUV radiation. We find that the technique allows one to learn about the energy transfer within the plasma column, and of the thickness of heated regions — a parameter which is not always readily available from line of sight optically thin EUV observations.

4.1 Secrets of the EMD

As mentioned the EMD can provide an observational description of the plasma properties of the lower atmosphere footpoints of solar flares and is a critical constraint on the distribution of the flare excess energy in this region, and hence the profile of flare energy deposition and its possible modes of transport. In the previous chapter we saw that the temperature coverage of EIS makes it extremely well suited to studying heated footpoint plasma and that we find evidence for temperatures on the order of 8 MK present in the lower atmosphere. To determine the EMDs we take advantage of the EIS temperature range to find the temperature distribution of emitting plasma from 250,000 K to over 10 MK.

4.1.1 DEM to EMD

Before going any further this is a good place to make the distinction between the *differential emission measure* (DEM) and *emission measure distribution* (EMD). It

is a simple point, but is often overlooked and important when making comparisons between the results of different authors. The DEM, as defined above, arises from the mathematics shown in Section 2.3 and is a function of the emitting material weighted by the inverse temperature gradient. The inversion method used will return $\xi(T)$ and has the units $\text{cm}^{-5} \text{K}^{-1}$ for a plasma column of unit area.

The quantity $\xi(T)$ is physically not very illuminating on its own. We can therefore integrate $\xi(T)$ over the width of each temperature bin to give the total emission measure within a small temperature range ΔT as a function of temperature. This also helps when comparing to results where the EMD(T) was found for individual line intensities in isolation and not through an inversion (Widing 1982). Del Zanna et al. (2002) defined the emission measure within a temperature range ΔT centred at temperature T_i as

$$EM(T_i) = \int_{T_i - \Delta T/2}^{T_i + \Delta T/2} \xi(T) dT. \quad (4.3)$$

Our inversion technique used in this chapter recovers $\xi(T)$ on a finite temperature grid. We can therefore find $EM(T_i)$ for each temperature bin to give us the emission measure distribution with temperature — EMD(T). To perform the conversion to EMD(T) we multiply the DEM by a factor $f(T)$ given by

$$f = N_{bin} 10^{\log T} \ln(10^{d \log T}) \quad (4.4)$$

where N_{bin} is the number of temperature bins, $\log T$ is the array of temperatures in \log_{10} space, and $d \log T$ is the spacing between.

4.1.2 EMD Gradients

Part of the reason why EMDs remain such an attractive observable is the fact that analytical forms can be predicted from theory. The functional shape of an EMD, found to be sensitive to the plasma density, pressure, and balance of heating and

cooling, is therefore a great meeting point for observation and modelling. The work by [Widing \(1982\)](#) showed that their observed EMD could be described by a simple model atmosphere where conductive and radiative energy losses were balanced. Since Widing's EMD gradient is close to what we eventually find in EIS, it is useful here to demonstrate how the EMD gradient can be found; for this simple model we therefore derive an analytical expression for the EMD(T) relation following the discussion in [Widing \(1982\)](#) and assisted by the results of [Rosner et al. \(1978\)](#).

The author's argument begins by choosing to study a chromosphere which is heated by conduction from a hot corona (where the majority of the flare energy deposition is assumed to occur) and which is not in the process of evaporating. If we recall from [Section 1.3](#), if the flare footpoint receives more input flux than can be radiated away then the plasma will be heated and expand resulting in evaporative flows back into the corona. The authors do not observe much high temperature loop emission so limit their model to a case where radiative cooling by the chromosphere is balanced by the conductive flux from the hot region above — in [Section 4.6](#) further clarification on how this relates to our events is shown.

The seminal paper by [Rosner et al. \(1978\)](#), containing the often cited *RTV* relations, takes the case of a one dimensional loop model, explaining the soft X-ray emission in the quiescent corona through the balance of energy inputs and losses in a closed system. It assumes that there is no cross-field conduction out of the loop boundaries and the mass flux into the loop is negligible. [Widing \(1982\)](#) begins from this by taking the expression for energy balance and simplifying it for only the balance between conductive flux and radiative losses in the chromosphere. In doing this it is assumed that there is no additional external heating source; meaning the flare energy deposition does not directly influence this layer, supplying only a conductive flux at the boundary. The only energy loss mechanism in the deeper plasma is via radiation.

We can start with the expression for energy balance,

$$\nabla \cdot F_c = E_R \tag{4.5}$$

where $\nabla \cdot F_c$ is the conductive flux across the region and E_R is the radiative loss rate. The conductive flux in the direction of the magnetic field is

$$F_c = \kappa T^{\frac{5}{2}} \frac{dT}{ds} \text{ ergs cm}^{-2} \text{ s}^{-1} \quad (4.6)$$

where $\kappa = 10^{-6} \text{ ergs K}^{-7/2} \text{ cm}^{-1} \text{ s}^{-1}$ for Spitzer conductivity (Spitzer 1962). The radiative loss rate is expressed as

$$E_R = n_e^2 \Lambda(T) = \left(\frac{p^2}{4k^2 T^2} \right) \Lambda(T) \text{ ergs cm}^{-3} \text{ s}^{-1} \quad (4.7)$$

where the usual expression $p = 2nkT$ for pressure is used and Λ is the radiative loss function. Inserting these expressions into Eq. 4.5 and taking the flux divergence across the length of the loop only, or in our case depth in the atmosphere, leads to

$$\nabla \cdot F_c = \frac{dF}{dT} \frac{dT}{ds} = \frac{dF}{dT} \left(\frac{F_c}{\kappa T^{\frac{5}{2}}} \right) = \left(\frac{p^2}{4k^2 T^2} \right) \Lambda(T). \quad (4.8)$$

Assuming that the pressure is constant throughout the atmosphere, Rosner et al. then integrate this expression to find the conductive flux as a function of temperature. Here, we have

$$\int_{T_b}^T \frac{dF}{dT} \left(\frac{F_c}{\kappa T^{\frac{5}{2}}} \right) dT = \int_{T_b}^T \left(\frac{p^2}{4k^2 T^2} \right) \Lambda(T) dT \quad (4.9)$$

leading to

$$[F_c^2(T) - F_c^2(T_b)] = \frac{\kappa p^2}{2k^2} \int_{T_b}^T T^{\frac{1}{2}} \Lambda(T) dT. \quad (4.10)$$

Finding accurate forms for the radiative loss function has been the subject of much investigation and many authors have proposed analytical forms for $\Lambda(T)$ using combined atomic physics calculations and measured elemental abundances. Rosner et al. (1978) shows that the complicated piece-wise function can be fitted over a temperature range by a single function where the approximation is within the calculation uncertainties. As a result the integral in the right hand side of Equation 4.10 can be approximated by $10^{-18.81} T$ for temperatures above $10^{5.1}$ K. If conductive losses across

the base of the chromosphere are assumed in this case to be negligible, so $F_c(T_b) = 0$, then Equation 4.10 becomes

$$F_c^2(T) = \frac{\kappa p^2}{2k^2} 10^{-18.81} T. \quad (4.11)$$

If we take our original definition for the conductive flux (Equation 4.6) then rearranging and multiplying by n_e^2 gives the following useful form,

$$n_e^2 \frac{ds}{dT} = 10^{9.4} \frac{(2\kappa)^{\frac{1}{2}}}{4k} p, \quad (4.12)$$

where the left hand side of the equation now resembles the differential emission measure. Since the aim is to find EMD(T) one more step is needed. Earlier in Section 4.1.1 we found that the EMD can be obtained by integrating the DEM across a chosen temperature bin ΔT . The path length spanning this temperature range may be defined as

$$\Delta s = \frac{ds}{dT} \Delta T, \quad (4.13)$$

and knowing that the emission measure in this region is $\int n_e^2 ds = n_e^2 \Delta s$, the above relation allows us to write

$$EMD(T) = n_e^2 \frac{ds}{dT} \Delta T = 6.432 \times 10^{21} p \Delta T. \quad (4.14)$$

In [Widing \(1982\)](#) the emission measure was obtained at a range of temperatures from individual line intensities where each line was emitted over a temperature range specified by its contribution function. Here the authors reasonably assume that $\Delta T = 0.7T$ for each line — an approximation routinely employed in EM analysis to avoid directly evaluating $G(T)$. Conversely, the inversion method used in the following returns a continuous fit from the data but has a finite temperature resolution specified by the inversion parameters, and for the EMDs derived in the following a binning of $\Delta T = 1.14T$ is used.

To conclude, Equation 4.14 is a very neat result, demonstrating that for a constant pressure atmosphere heated by conduction and cooling by radiation, the EMD is lin-

early proportional to T . Observations with $EMD(T) \sim T$ may then be consistent with a lower flare atmosphere radiating following a conduction input, while the direct flare heating remains in a confined region. We should also note though that if p is not constant then the proportionality with T will change. We will return to the implications of this model again in later sections.

The balance of energy inputs and losses for solar atmospheres is therefore a key starting point for modelling, and many other examples can be found in literature which return different EMD gradients — not only for flares, but the quiet sun, transition region, and coronal heating. For example, a more general case than we discussed here was presented in [Jordan \(1980\)](#) for the transition region including an energy deposition term. The energy deposition was shown to be sensitive to not only the EMD gradient, but to the absolute EM, base pressure and coronal temperature.

4.1.3 Early Skylab Observations

There have been several previous EMD studies of the rise and decay phases of solar flares using the *Skylab* Naval Research Laboratory (NRL) slitless spectroheliograph S082A ([Tousey et al. 1977](#)) and the NRL slit spectrograph S082B ([Bartoe et al. 1977](#)). The slitless spectrograph was a curious instrument, where unlike many recent slit imaging spectrometers (EIS, SUMER, CDS) spectra were obtained by dispersing the full focused image of the solar disc onto photographic film. An image of the whole 170-630Å spectral range could be recorded simultaneously with each image in a strong emission line offset by a small distance on the film. Bright features, such as flares, could be easily identified as the sources were much brighter than the background disc. However, as the focused images in neighbouring emission lines did overlap, it could lead to confusion between larger sources and emission lines, hence the term “overlappogram”.

The slit spectrograph was more akin in operation to EIS where a narrow 2'' x 60'' slit is positioned on the solar disc and its image dispersed onto two photographic film detectors, one at 970-1970Å and another at 1940-3940Å. Unlike EIS, due to the design there was no image resolved along the length of the slit and the spatial resolution

was limited to $2'' \times 60''$, complementary imaging from either the spectroheliograph or ground based telescopes was required to estimate the contribution of various features along slit position.

[Dere & Cook \(1979\)](#) used both spectroheliograph and spectrograph data to find EMDs during the evolution of a compact flare on August 9th 1973 (SOL1973-09-05T18:32). The EMD was recovered from the spectra at intervals starting from roughly the peak of the impulsive phase at 1553 UT. Between temperatures of 10^6 K and 10^7 K the EMD(T) slope flattened from $T^{3.5 \pm 0.5}$ at 1553 UT to $T^{3.0 \pm 0.4}$ at 1557 UT during the decay phase. Below these temperatures the EMD reached a minimum at $10^{5.7}$ K which falls to $10^{5.3}$ K at 1557 UT. The authors then argue that as the slit position may include both loop and footpoint emission, the steep high temperature part of the EMD is the result of iso-thermal loop top material above $10^{5.5}$ K, while cooler material is confined to the footpoints. We should note that the authors used a slightly different definition of the EMD to those in [Widing \(1982\)](#) and [Graham et al. \(2013\)](#), defining instead the logarithmic DEM, $\xi_l(T)$, where

$$\xi_l(T) = \frac{dT}{d \ln T} \xi(T) = T \xi(T). \quad (4.15)$$

The result should therefore differ only by the constant factor introduced between the choices of $\ln(T)$ and $\log_{10}(T)$ ranges and the gradients will remain consistent.

The flare EMD shown by [Widing \(1982\)](#) is taken from a spectroheliograph of the December 22nd 1973 event (SOL1973-12-22T00:24). The 19 second exposure sampled the peak and beginning of the decay phase and showed a bright footpoint kernel in cooler lines. The EMD had a shallow slope of $T^{0.8}$ from $10^{5.4}$ K up to $10^{6.2}$ K. Also, since the emission was weak in lines above 10^6 K it suggests that the footpoint EMD contains little contamination from evaporated material in hot loops making it perhaps the best footpoint EMD from these early observations.

The follow up work by [Widing & Hiei \(1984\)](#) presented EMDs from two compact flare sources just after the impulsive peak of the January 21st 1974 event (SOL1974-01-21T23:24) that also coincided with a HXR burst. This time the EMDs for both

sources show wildly different gradients, one of which had a shallow slope of $T^{0.6}$ up to a maximum temperature of 10^6 K, similar to [Widing \(1982\)](#), and the other showing a steep slope of T^3 up to $10^{6.9}$ K. The later hot source does not have any appreciable cool emission below Fe XIII and appears in later decay phase spectroheliograms. The cooler source brightened early and was coincident with the fast rise in SXR. The authors conclude that this may have been the energy deposition site while the hot source is part of the gradual phase SXR emission.

Widing also emphasises that these slopes are different from the $T^{3/2}$ slopes which are often assumed to be characteristic of flares models — for example the 1-D modelling for the cooling of evaporative coronal loops by [Antiochos & Sturrock \(1978\)](#). Other observations have been obtained during decay phases of flares ([Widing & Spicer 1980](#)), and have also tended to attract more theoretical attention ([Machado & Emslie 1979](#)).

Thus we find that there are many flare EMD gradients, both theoretical and observed, in literature, ranging from $T^{0.6}$ to $T^{3.5}$. It is clear that difficulties in identifying sources in the *Skylab* instruments and the timing of the observations during the event must account for at least part of the variety of the results. The objective of this chapter is now very apparent. Given the capabilities of EIS, can we isolate the EMD for individual footpoints and find a consistent measurement of the EMD(T) for a number of flares? The short answer is yes, the spatial resolution is certainly an advantage, but uncertainties are always present in the data and analysis, and as shown by some further calculations we also find ourselves closer to the limits of the standard atomic physics assumptions.

4.2 EIS Data Preparation

In searching for flares for this study we ran across the usual problems associated with multi-instrument studies. Our ideal search initially included flares with EIS raster coverage during the impulsive phase containing emission lines across a wide range of formation temperatures. XRT and RHESSI observations were also required to cover the high temperature response and to locate the energy deposition site. Given the uncertain

nature of inverting the DEM, a set of multiple observations was also a high priority to ensure that the technique was reliable across a range of flare sizes. Recent EIS rasters, although being run regularly and often catching the impulsive phase footpoints (Young et al. 2013), had too few emission lines to fill the temperature range and safely invert the data. This is in part due to the choice of raster studies being run, but also since March 2008 the Hinode spacecraft has been limited in telemetry and the wavelength windows used now are far more restrictive. We therefore focused our search to earlier observations prior to 2008.

A series of EIS rasters using the active region CAM_ARTB_RHESSI.b.2 study (from here on referred to as the *Cambridge* rasters, after the group that designed them (Chifor 2008)) were found running periodically between May and December 2007. Many small B to C class flares were observed but no suitable higher energy M class flares were found as this was a very quiet period for solar activity. This study fulfilled our requirements for a wide temperature range with around 30 lines present in each raster and a relatively short cadence of under 4 minutes. The rasters use the 2'' slit with a 10 second exposure time to scan a 40'' x 140'' area in 3 min 52 s. This gives an effective spatial resolution (Culhane et al. 2007) ample to distinguish footpoints from coronal structures in these small events. Five density sensitive line pairs also make these rasters extremely versatile.

Hinode/XRT imaging was available in some of the events, although image timing, filter selection, and exposure times were not always consistent between the events. Some testing was done in a few EMDs using a high temperature XRT constraint, but it was not found to improve the EMD significantly as the responses plateau at very high temperatures. Again the impulsive phase was seen by RHESSI for some of the events but not all, so the decision was made to relax the requirement for HXR spectra at this time and focus on having the best EIS data. Based on our experience in the previous chapter, and work by others (Milligan & Dennis 2009), we can infer the footpoint locations without HXR imaging through EUV observations and density diagnostics — further details on determining the energy deposition site is described shortly in Section 4.3.

In this chapter (and as presented in [Graham et al. \(2013\)](#)) the results are focused on 6 flares for which we were able to isolate the footpoints and determine their impulsive phase EMDs. There were more flares available in the rasters for which the same analysis was made, but which suffered from poor signal to noise leading to spurious EMDs.

4.2.1 Line Selection

Over 30 emission lines were present in the Cambridge raster set. Whilst it is tempting to throw all of these into the DEM inversion, in a quest to iron out the intensity uncertainties, the inversion may not respond favourably. [Craig & Brown \(1976\)](#) and [Brown et al. \(1991\)](#) highlighted the need for careful line selection for DEM analysis to ensure solutions of the inversion are meaningful. The degree to which the problem is ill-conditioned (see Section 4.4) depends not only on the uncertainties in I but also the width of the contribution functions, $G(T)$, in temperature space, where in the extreme case, as the $G(T)$ functions tend to delta functions the problem becomes increasingly well conditioned. The number and temperature spacing of lines also influences the temperature resolution of the inversion, with many lines of narrow and evenly spaced $G(T)$ being desirable. Secondly, as we saw in Section 2.3 and will be later investigated in Section 6.1, the contribution function is bivariate in both temperature and density, therefore the density dependence must be minimised if we hope to recover knowledge of the temperature distribution.

Resonance Lines — [Craig & Brown \(1976\)](#) and [Brown et al. \(1991\)](#) also remark on the use of *resonance lines* for temperature analysis. Resonance lines are emission lines arising from transitions between the first few excited levels ($n = 2, n = 3$, etc.) to the ground state of an ion. The ground state is in most conditions far more populated than any excited levels and resonance transitions decay almost immediately with no intermediate transitions — the spontaneous transition rate A_{ji} is very large. The coronal approximation is therefore valid and the contribution function is proportional to the collision rate coefficient for excitations which varies with temperature, the ionisation

abundance — also a steep function of only temperature — and a number of constants. Electron density does not influence any of these parameters strongly. Of course, in the full calculation for the relative level population of the ground state, transitions to other levels are included which may have a density dependence of their own, however the reduction in population of the ground state is minimal and the coronal approximation will still hold.

Another attribute of these lines is their very high transition probabilities (also known as the oscillator strength, see Section 5.5.4) meaning that they easily absorb and re-emit photons of equal energy to the transition energy. The re-emitted radiation is known as resonance radiation and was discovered by Robert Wood whilst studying Sodium vapour (Wood 1905). For use in DEM(T) analysis this quality can make them much brighter, reducing measurement uncertainties. The resonant behaviour varies from ion to ion and at the time of writing Graham et al. (2013) we did not have access to enough information to base the line choice entirely on such lines though a selection of resonance lines are tabulated in Pottasch (1964). Also, the limited selection of lines available did not afford us the luxury of picking only resonance lines. However, without fully understanding the emission and re-emission characteristics, difficulties may arise in estimating the optical depth of resonance lines in the transition region. We discuss this further in Chapter 5 but mention here that the high oscillator strength makes them very susceptible to absorption and scattering (Andretta & Jones 1997). We feel it was important to note these effects for future analysis and EIS study design since it has not been explicitly mentioned in many recent DEM analyses.

Density Sensitivity — In spite of this we can still check the temperature and density sensitivity of the available lines before selecting them. Of the lines present in these rasters we have narrowed the selection down to 15 which cover the temperature range $\log T = 5.0 - 8.0$. Heavily blended lines or those with high optical depths (e.g. Helium II) have also been ignored. Details of the lines are found in Table 4.1. Figure 4.1 shows the $G(T)$ functions calculated for an electron density of 10^{11} cm^{-3} , coronal abundances (Feldman et al. 1992) and CHIANTI's own ionisation equilibrium file

(Landi et al. 2012). The reasoning behind these choices is left to Section 4.4.1.

The peak temperature contributions are spread evenly across the range up to $\log T = 7.0$ where the high temperature lines start to tail off. In most lines $\sim 90\%$ of the function is contained within $\log \Delta T \sim 0.5$, bearing in mind that the plot is logarithmic so the contributions functions in Figure 4.1 appear far more sharply defined on a standard scale. Some lines are not ideal but are the only choice to cover certain temperatures. The high ionisation energy of He-like O VII leads to enhanced recombination at high temperatures back into O VI (Mariska 1992). The O VI contribution function therefore has an elongated high temperature tail, yet most of contribution here should be sufficiently small compared to the peak. The resonance Fe XV 248Å line is also very broad but is well observed in EIS.

The density sensitivity of a line's contribution function is shown by plotting them at the line's peaks formation temperature against density. It is clear from Figure 4.2 that $G(T_{max}, n)$ for most lines varies by less than 25% for transition region densities of $\log n_e = 10.0 - 14.0$. In the iron $G(n)$ functions, left hand figure, Fe XIII and Fe XIV rise at densities below $\log n_e = 10.0$. These are not the density sensitive transition of the diagnostic pair used in Chapter 3 but some dependence on density will arise as some of the level population migrates to the metastable levels. However, footpoint densities observed in these lines are on the order of at least 10^{10} cm^{-3} so this should not concern us. The reasoning is the same for O V, although its $G(n)$ flattens above 10^{12} cm^{-3} . In Graham et al. (2013) these lines were part of the EMD, but subsequent research on diagnostics at the formation temperature of O V ($\log T = 5.4$) in Chapter 5 suggests that the footpoint density may be higher than the $\log n_e = 11$ set here. It may be sensible in future to set the DEM contributions at a constant $\log n_e = 12$ to minimise uncertainty here, or indeed adjust the line selection.

Intensities — As mentioned earlier, data uncertainties inherently lead to non-unique EMD solutions being returned by inversion methods. To minimise this we require careful measurement of the integrated line intensity, therefore for lines blended with multiple temperature components, contributions must be carefully removed from the

Table 4.1: Emission lines selected for EMD analysis with rest wavelengths and peak formation temperatures.

| Ion | λ (\AA) | $\log_{10}T$ (K) |
|----------|----------------------------|------------------|
| O v | 248.460 | 5.4 |
| O vi | 184.118 | 5.5 |
| Fe viii | 185.213 | 5.7 |
| Mg vi | 268.991 | 5.7 |
| Si vii | 275.361 | 5.8 |
| Fe x | 184.537 | 6.1 |
| Fe xi | 188.216 | 6.2 |
| Fe xii | 195.119 | 6.2 |
| Fe xiii | 202.044 | 6.3 |
| Fe xiv | 274.204 | 6.3 |
| Fe xv | 284.163 | 6.4 |
| Fe xvi | 262.976 | 6.4 |
| Ca xvii | 192.853 | 6.8 |
| Fe xxiii | 263.766 | 7.2 |
| Fe xxiv | 192.028 | 7.2 |

line in question — see Section 4.2.3. Lines harbouring large undocumented blends, or those which are blended with multiple lines of similar intensity and centroid position are ignored.

If for example a pair of lines at similar temperatures are present within one profile, the sum may be used in conjunction with the total of both contribution functions, but this situation is not common within the EIS spectrum. An extension of this analysis is useful for spectrometers with low spectral resolution such as the EUV Variability Experiment (EVE) (Woods et al. 2012) on board the Solar Dynamics Observatory (SDO) (Pesnell et al. 2012), and in Chamberlin et al. (2012) multiple lines at similar

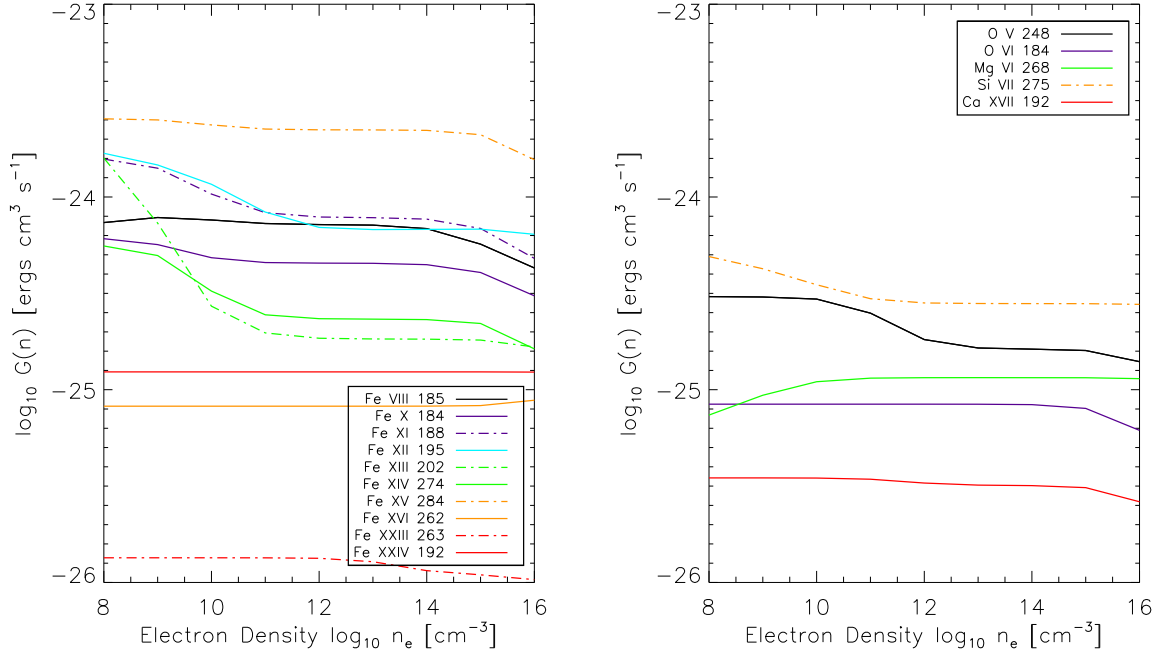


Figure 4.2: Peak contribution functions for EMD lines as a function of density.

Temperature is held constant at the contribution function peak T_{max} and coronal abundances with CHIANTI's own ionisation equilibrium file are used for the calculation.

the impulsive brightenings seen in EIS are on the order of 1-2'' and the same is true in the events used here. The strongest footpoint emission is mostly contained within one slit position 2'' wide in the x direction and 2-3'' in the y . We have averaged the centre pixel with those above and below to match the slit width and improve the signal to noise ratio. To equally bin in the x -direction would sample 6'', gathering too much of the surrounding area. Our binning accounts for the spatial extent of the footpoint and again covers some of the uncertainty in correlating between the long and short wavelength CCDs.

The choice of centre footpoint point pixel was made using the brightest pixel in the cool Fe VIII raster. In the previous chapter we found low temperature lines brighten quickly and are a good indicator of the low atmosphere response to flare energy deposition (Fisher et al. 1985). While He II is thought to radiate extremely well during

impulsive heating (Allred et al. 2005), it has a number of higher temperature blends so Fe VIII chosen as an alternative bright transition region line. More recent work has also begun to shed light on the early temporal evolution of impulsive phase footpoints, especially since the advent of high cadence instruments on board SDO (Chamberlin et al. 2012; Qiu et al. 2013).

At the time we decided not to subtract a pre-flare background from the footpoint emission. The reasoning was that it allowed us to make consistent comparisons with the EMDs from historical observations, which did not make a subtraction either, and with the theoretical work discussed in Section 4.6; which treats emission from the entire emitting column, not only the flare excess. Yet it does remain a point of interest, as the shifted evaporating components of the lines may show a different distribution to any stationary one. A brief discussion on this is given later.

4.2.3 Line Blending

Even after careful selection, a number of transitions contained unavoidable blends that needed removal. In blended lines the true intensity can be often recovered very successfully using various fitting techniques and other observed lines within the raster set. The CHIANTI v7.0 atomic database Dere et al. (1997); Landi et al. (2012) was used to identify lines contributing to the measured line profiles. Synthetic spectra are created for a variety of DEMs. CHIANTI does this by calculating I for all lines within a wavelength range using the $G(T)$ functions, a prescribed DEM, abundances and density. Here we use the same density and abundances as before, but check the predicted intensities using both the CHIANTI flare Dere & Cook (1979) and active region DEMs Vernazza & Reeves (1978). While this method is not perfect, it does assume we have some knowledge of the plasma to begin with, it will highlight the more significant blends. We now discuss the significant blends in our line selection.

O v — The 248.460Å line has a small blend of Al VIII at 248.459Å which is predicted to be less than 10% during flare conditions. It is too small to accurately remove by

fitting but we estimate it should not be significant during flares. A blend in the blue wing is also seen in the footpoints and is removed using a second Gaussian component — Section 5.2 has more details on these blends.

Fe VIII — Two predicted blends of Ni XXIV 185.166 and Ni XVI 185.230 are present in the low temperature Fe VIII 185.213 line. A triple Gaussian fit finds these effectively and revealed very small contributions of Ni XVI 185.230 in the footpoints, around 8% of the Fe VIII intensity, and a negligible amount anywhere else. In some footpoints the red wing Ni XVI 185.230 was stronger than the almost negligible intensity predicted by CHIANTI flare DEM — as much as 17% in one footpoint. Interestingly, in some events a very large contribution was found in regions 2-3'' away from the footpoint. This is puzzling as the line has a formation temperature of $10^{7.2}$ K. It is possible that the line is misidentified in CHIANTI, or perhaps is a highly red-shifted component of the Fe VIII line. Either way it far enough away from the footpoints to not be a concern for our EMD.

Fe XXIV — Care must be taken to extract Fe XXIV 192.028 as even though it normally dominates in flare loop conditions, the nearby transition region lines of Fe VIII 192.004 and Fe XI 192.021 are bright in the active region. This work concentrates on an earlier phase in the flare where the Fe XXIV emission may be much fainter, therefore these blends must be removed. While they are too close in wavelength to accurately fit [Del Zanna et al. \(2011\)](#) described a method to remove them using intensity ratios to other lines. The target Fe XI 192.021 line forms a known intensity ratio with an other observed Fe XI line at 201.734Å. The measured $\lambda 201$ intensity can then be used to estimate the $\lambda 192$ intensity in the footpoint. We find the ratio of 192.021/201.734 intensities in background moss/active regions to be 0.43 compared to the CHIANTI value of 0.6. This difference is possibly due to some Fe XII emission within the 201Å line that decreases the flux ratio. We have therefore used the predicted ratio of 0.6 to remove the 201Å blend, as in this case we are less likely to over estimate the Fe XXIV intensity.

The Fe VIII 192.004 intensity is predicted by CHIANTI to be around 10% of the Fe XI line and is almost negligible. The referee for the published paper on this work suggested the lower temperature lines such as Fe VIII may be preferentially enhanced during the impulsive phase and contribute more to the blend than Fe XI. While a sound suggestion we see no evidence for this as enhanced emission is found in lines extending to all temperatures. In most of the events the rasters are also sampled some way into the impulsive phase and high temperatures plasma will have had time to form. Accounting for these contributions removes the majority of the active-region emission from the Fe XXIV raster (seen in Figure 4.4). If we look at the corrected average mean background level, in areas away from the footpoint, the level is now lower than the uncertainty for the bright footpoint. We are therefore confident the remaining intensity is from Fe XXIV alone.

Ca XVII — The Ca XVII 192.853 line is found in a complex grouping of six O V and two Fe XI lines. The extraction of this challenging but is well documented (Ko et al. 2009; O’Dwyer et al. 2010; Del Zanna et al. 2011). We have adopted the approach in Ko et al. (2009) but as one of the O V lines forms a density diagnostic we have explained it in far more detail in Section 5.2.

4.3 Flare Observations and Footpoint Selection

The Cambridge rasters were run during a period of mild solar activity towards the end of the last solar cycle. For durations of 1-3 hours the study was run while centred on a flaring active region. The rasters were repeated in continuous sequence and caught six small flares with compact footpoints fitting our requirements. The flares range from B1.8 to C1.1 in GOES energies and are identified in Table 4.2 with the GOES 1-8Å light curves plotted in Figure 4.3.

The light curves for these events are highly impulsive. In most events the rise phase is completed within 4-5 minutes with the slowest peaking in just under 10 minutes. While a steep SXR curve can be a good indication of strong footpoint emission, it

does mean that the 3 min 52 sec raster cadence is only capable of taking one or two snapshots of the impulsive footpoints, and unlike the previous chapter not much can be learned about the temporal evolution from the EUV rasters.

Ideally RHESSI HXR imaging and spectroscopy would be used to verify that the EUV enhancement corresponds to the HXR energy deposition site. However, RHESSI HXR data were not consistently available in all events. As a substitute, the time derivative of the GOES SXR emission can be used as a proxy for the HXR emission. Following the work by [Neupert \(1968\)](#) (see the discussion in [Section 1.3](#)) we now find that in a high proportion of flares the rate of change of the SXR emission follows the HXR light curve. Assuming this, we have systematically used the GOES derivative to find the time of maximum energy deposition; a dashed line on the light curves in [Figure 4.3](#) marks the peaks and was used as a guide to select the EIS raster corresponding to the impulsive phase peak. In most events this was academic as the entire impulsive phase was contained within the raster limits shown by the dotted lines. For Event (d) we found the SXR derivative was close to the SXR peak and the raster represents both peaks. In Event (c) while the derivative peaked early during the SXR rise, the peak was very close to the end of the early raster, as little EUV enhancement was found in footpoint for this raster we have chosen the later one.

We must also note that each x position within the raster represents a 10 second time interval and the flare evolves as the slit position scans West to East. For the footpoints discussed below, the time at which the slit crosses the footpoint is marked by a diamond on the light curve. In Event (a) the observed footpoint position is slightly ahead of the SXR derivative peak, Events (d) and (e) occur roughly near the SXR peak, and by chance the footpoint position in Event (b) fell precisely at the derivative peak!

The selected rasters are shown in [Figure 4.4](#) for the Fe VIII and Fe XXIV lines, illustrating the flare appearance at 500,000 K and 16 MK. In all events bright emission has risen dramatically in both lines and is found at the same location. Fe VIII tends to appear more compact and Fe XXIV, while rooted in the same spot, extends further across the region. Event (b) exhibits the classic flare appearance, compact emission at cool temperatures, while a larger loop structure reaches to the South-East in Fe XXIV.

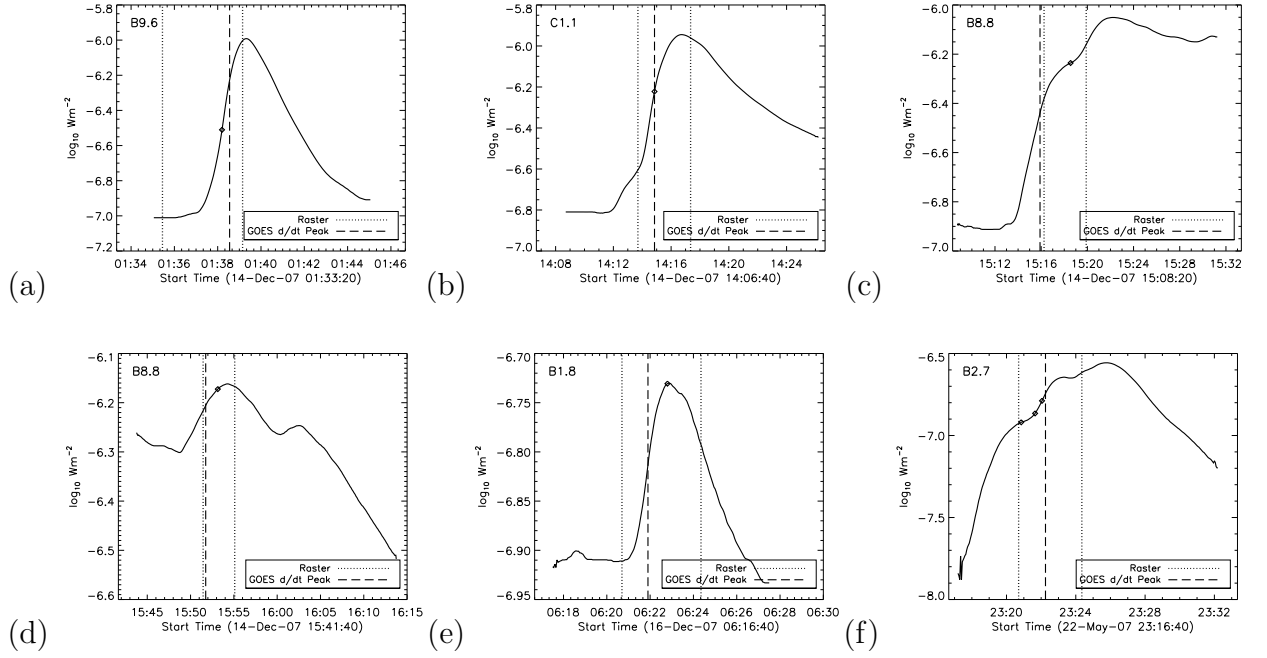


Figure 4.3: GOES 1-8Å light curves of each event. A pair of dotted vertical lines represent the start and end times of the EIS raster and a single dashed line marks the GOES derivative maximum for the event. The time at which the spectrometer slit scans each footpoint is marked with a diamond on the light curve.

Event (a) is sampled slightly earlier in its impulsive phase and both of its footpoints are bright, and compact, in both lines. At a later stage Fe XXIV becomes more significant as evaporating hot material begins to fill loop structures. Other events such as (f) have more elongated ribbon structures, yet in all events at least a small component of Fe XXIV emission is found covering the same location as Fe VIII. From the earlier work by [Milligan & Dennis \(2009\)](#) and [Graham et al. \(2011\)](#) we have learned that compact brightenings in the EUV can be associated with RHESSI HXR observations revealing the flare energy deposition site. Also, as found in the previous chapter and in [Milligan \(2011\)](#) enhanced densities have been seen to occur at the location of impulsive-phase footpoints. In the diagnostics performed in Chapter 5 we will show that this is still the case for these events. Given this morphology throughout the EIS temperature range

we are confident in identifying the flare footpoints, as marked with white arrows in Figure 4.4.

A number of the flares in question have been studied in detail before (but not for the purpose of finding EMDs) and the findings may help us later. High velocity evaporation flows were found in Event (b) by Milligan & Dennis (2009) using EIS, and were found to be co-spatial with EUV enhancements and HXR footpoints imaged by RHESSI. Milligan (2011) examined the flare further on the subject of non-thermal line broadening. Event (f) in Del Zanna et al. (2011) exhibited chromospheric evaporation signatures along with footpoint electron density enhancements. The evaporating component of the emission was also suggested to have an iso-thermal emission measure at ~ 10 MK.

4.4 DEM Technique

As we discussed in Section 2.3 the inversion of Equation 4.1 is an ill-posed problem given the uncertainties in the line flux and contribution functions. A single solution for $\xi(T)$ should exist based on the conditions in the footpoint plasma. However, not only do uncertainties in the measurements of I lead to a range of non-unique solutions, the uncertainties in $\xi(T)$ are amplified by any attempts to directly invert the equation. Over the years many different methods to find $\xi(T)$ have been developed each with their own advantages and disadvantages (Fludra & Sylwester 1986; Monsignori Fossi & Landini 1991).

Forward fitting approaches exist in various forms but most start from a model or functional form for the DEM. For example Weber et al. (2004) used a series of spline functions, with Aschwanden & Boerner (2011) forcing a number of iso-thermal Gaussian profiles. The minimisation is straightforward to perform but the results can only verify how well a single model represents the data. H. Hudson & P. Chamberlin are developing a technique of fitting the entire SDO/EVE spectrum and minimising a DEM based on the synthetic CHIANTI spectrum. While extremely slow computationally it will remove the need for any model, although it is still at the whim of uncertainties in

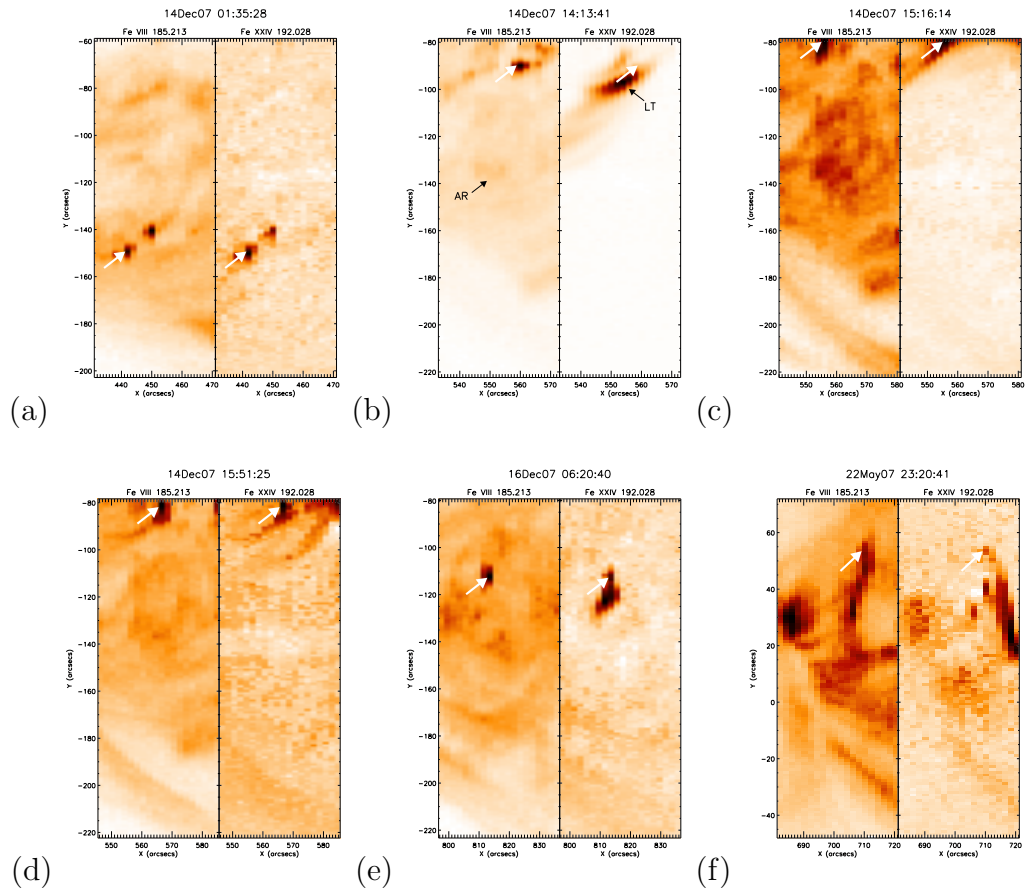


Figure 4.4: EIS rasters for each event in Fe VIII at 500,000K and Fe XXIV at 16 MK showing the morphology at low and high temperatures. A white arrow marks the footpoint positions chosen for EMD analysis in each raster. Black arrows in panel (b) also highlight the regions used in determining a loop top and active region EMD (see Section 4.6).

the atomic data. Markov chain Monte Carlo (MCMC) approaches also do not require any *a priori* model (Kashyap & Drake (1998) from the PINTofALE software library) but are again very slow and occasionally prone to finding un-physical temperature components if not used with care (Hannah & Kontar 2012).

The technique we have used to invert Equation 4.1 was developed by Hannah & Kontar (2012) based on the inversion of RHESSI photon spectra in recovering the electron energy distribution (this is explained fully in Kontar et al. (2004)). The Hannah & Kontar

(2012) inversion (HK) used here has the advantage of requiring no *a priori* knowledge of the expected DEM form, and errors in both the temperature and emission measure domain can be found. While not a major concern for a small number of events, the technique is computationally fast.

Hannah & Kontar (2012) compared the new technique to other more established MCMC methods using both simulated and observed data. The results are indeed favourable for the regularized method which is capable of robustly returning the DEM in a wide variety of cases. Recently more authors have begun to make use of the high speed inversion (Battaglia & Kontar (2012), Fletcher et al. (2013), Hannah & Kontar (2013)), finding it especially suited to producing large sets of time-dependent DEMs with data from SDO's Atmospheric Imaging Assembly (Lemen et al. 2012). Here, we supply the reader with enough background to understand the meaning of the inputs and generation of errors in the method, based on what is shown in Kontar et al. (2004) & Hannah & Kontar (2012), but refer them to the references for a more complete explanation and derivation of the solutions used.

For a discrete number of observable line fluxes, I_i , the original problem to invert Equation 4.1 must be written as a system of linear equations. The integral equation can be rewritten in the form

$$I_i = \sum_{j=1}^N \mathbf{K}_{i,j} \xi(T_j) \quad (4.16)$$

where $\mathbf{K}_{i,j}$ is a matrix of the i contribution functions over a discrete temperature range of j intervals, and $\xi(T_j)$ is the DEM defined over the same range and assumed to be constant within each temperature interval. We therefore aim to solve the system of linear equations given in matrix form by

$$I_i = \mathbf{K}_{i,j} \xi(T_j). \quad (4.17)$$

Essentially the problem becomes a minimisation of

$$\left\| \frac{\mathbf{K}\xi(T) - I}{\delta I} \right\|^2 = \min \quad (4.18)$$

to find the best fit $\xi(T)$ where $\|\mathbf{x}\|^2$ is the Euclidean norm defined by $\sum_{j=1}^N x_j^2$. When uncertainties are present in both I and K , solutions to this quickly amplify the uncertainties and introduce non-physical oscillatory components. In order to avoid these unrealistic solutions, [Tikhonov \(1963\)](#) showed that such integral inversions can be performed using constraints requiring that the inverted solution, $\xi(T)$, must be subject to some conservation law or have a continuous form for example. The addition of constraints to help better condition the problem is known as Tikhonov regularization. Using Lagrangian multipliers the problem can be rewritten as

$$\|\mathbf{K}\xi(T) - I\|^2 + \lambda \|\mathbf{L}(\xi(T) - \xi_0(T))\|^2 = \min . \quad (4.19)$$

where λ is regularization parameter, \mathbf{L} is the constraint matrix, and $\xi_0(T)$ an initial guess solution. The constraints can take many forms depending on the problem at hand. Where $\mathbf{L} = \mathbf{1}$, i.e the identity matrix, the regularization is said to be of zero-order. In our case a zero-order constraint means the integral of the inverted DEM in temperature must be less than the total emission measure in all observed lines. Simply, the total number of electrons predicted can not be greater than the total number observed. In all the DEM inversions used here we make the restriction that the DEM solution must be differentiable, ensuring it is a smooth and not discontinuous function, which is reasonable if the temperature distribution can be described by a differential equation as in [Section 4.1.2](#). To achieve this *first-order* regularization \mathbf{L} becomes a differentiation operator ([Kontar et al. 2004](#)). We should note, however, that this may be a strong assumption in certain cases. The DEM of a loop in conductive equilibrium theoretically has a discontinuous, high temperature cut-off. Steep high temperature loop components were also thought to be observed in the EMDs of [Widing & Hiei \(1984\)](#) that merge with the shallow footpoint component. However, our improved spatial resolution will ensure such blending of EMDs is minimal.

Attempts to solve [Equation 4.19](#) are computationally intensive. General Singular Value Decomposition (GSVD) [Hansen \(1992\)](#) can be used to find a solution giving $\xi_\lambda(T)$ which depends on the regularization parameter λ . Not only is this approach

faster computationally, it can also help suppress unwanted oscillatory solutions.

The choice of regularization parameter is not uncovered through the solution however, and is left to either foresight of the problem or trial and error. A value for λ , which gives the full solution $\xi_\lambda(T)$, can be found based on the expected residuals of the data. By forming the minimisation

$$\frac{1}{N} \left\| \frac{\mathbf{K}\xi_\lambda(T) - I}{\delta I} \right\|^2 = \alpha, \quad (4.20)$$

known as Morozov's discrepancy principle (Morozov 1963), and by iterating the method one finds the value for λ , therefore $\xi_\lambda(T)$, that meets the requirement α . The value α is the regularization *tweak* parameter which controls the expected degree to which the residuals between the observed intensities and intensities predicted by $\xi_\lambda(T)$ are distributed — in essence it sets the χ^2 required of the fit. Lower values of α place more emphasis on the data and regularization will be strongly bounded by the observations. On the other hand, higher values leave the regularization with more freedom, which can help for poorly sampled data, but the solution may start to resemble the constraints as opposed to the actual plasma distribution. In our DEMs the effects of this *over-regularization* are clearly seen in DEM errors and we find that $\alpha = 2 - 3$ returns a solution that has no oscillatory components yet is not over-regularised (see Figure reffig:alpha). A final constraint we make is to ensure that the DEM solution is positive for all temperatures by choosing the regularization parameter that minimises Equation 4.20 while maintaining $\xi_\lambda(T) > 0$

An initial guess solution $\xi_0(T)$ can be obtained by taking the emission measure given for an isothermal plasma in each contribution function. The isothermal solutions represent the maximum emission possible at each temperature given by $I_i/G(T_j)$; also known as EM-Loci curves, they are used here as a physically realistic place to start the minimisation.

Turning to the errors in the DEM solution, the HK method returns both an uncertainty $\delta\xi(T)$, and temperature resolution δT at each point in the DEM solution. We will not delve into much detail as their origin is not essential to understanding the

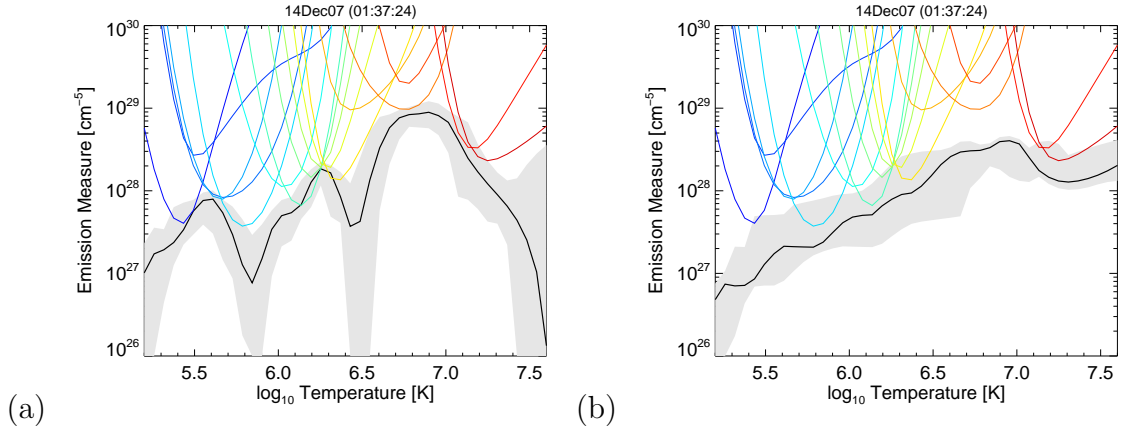


Figure 4.5: Example EMDs using a regularization tweak parameter of $\alpha = 1.0$ (left) and $\alpha = 5.0$ (right).

solutions (it is well covered in [Hannah & Kontar \(2012\)](#)), but note that they tell us about both the limitations of our data, and when the solution is over-regularised.

Figure 4.5 shows two test EMDs derived from data for the HK technique. The EM-Loci curves are displayed in coloured lines bounding the EMD shown in black. The grey shaded error represents the extent of the errors in both EM and temperature space, a solution can therefore be found anywhere in this region. The EMD in the left hand figure, for $\alpha = 1.0$, is strongly constrained by the minimum EM-Loci curves and the data in places, yet displays the oscillatory behaviour of an under regularized solution, i.e the two sharp dips with large errors in the middle of the temperature range. In the right hand figure a large α of 5.0 is used and the effects of an over-regularised solution are apparent. The temperature uncertainties are ballooned and therefore any temperature resolution is lost. In our fitting we aim to choose α to ensure that our solution sits somewhere between these two extremes.

4.4.1 DEM Inputs and Uncertainties

Now that we have decided on a suitable set of lines and $G(T)$ functions, obtained the footpoint line intensities and uncertainties, we are in a position to perform the inversion

to find $\xi(T)$. One final point is that the $G(T)$ functions are not completely accurate and have an inherent uncertainty themselves arising from errors in the calculation of cross sections, transition rates etc. In a private communication with P. Young, a founding member of the CHIANTI team, a systematic error 20% was agreed to account for the total calibration uncertainty between lines. The error is added to the existing flux errors for the inversion.

The contribution functions were seen in Section 4.2.1 where coronal abundances, the CHIANTI ionisation equilibrium file, and a constant density of 10^{11}cm^{-3} were used in their calculation. The value of electron density was chosen based on the footpoint observations (see e.g. [Watanabe et al. 2010](#); [Graham et al. 2011](#); [Milligan 2011](#)). While the atmosphere is unlikely to be homogeneous in density, the contribution functions are not strongly affected by density variations as the density-sensitive lines have been removed from the analysis. The choice of density is therefore not critical.

Elemental abundances relative to hydrogen however may bias the shape of an EMD. Low first ionisation potential (FIP) elements are found to be enhanced in coronal material compared to the photosphere while high FIP elements are unchanged. In the standard flare model, material in the footpoints is brought to coronal temperatures and rises into loops through evaporation. The chromospheric, possibly part photospheric material, then mixes with plasma in the corona. The abundances will therefore depend on the relative amount of footpoint to coronal material within the loop. In the footpoint it is likely a similar picture, as downward moving plasma can move material from its favoured quiescent height. In terms of flare spectra, the choice of abundances is not straightforward ([Athay 1994](#); [Feldman et al. 2004](#)). Only O v and O vi in our analysis are high FIP and should be relatively insensitive to the abundances. For elements like iron that are low FIP, the abundances can change by a factor of 4 between the photosphere and corona. We have picked coronal abundances to start with but we will investigate the effects of varying the abundances fully later in Section 4.5.4.

The ionisation equilibrium files set the abundances of each ion relative to its parent element. They differ slightly based on how they are determined and the experimental data used, therefore the choice is similarly uncertain. We test this later but use the

default CHIANTI set for now.

4.5 Flare EMDs

The EMD derived from EIS data for the six events are presented in Figure 4.6. The inverted $\xi(T)$ solutions have been converted to emission measure units of cm^{-5} by integrating over the temperature spacing $\Delta T = 1.14$ as shown in Section 4.1.1 — the errors are converted likewise. The best fit solutions for the EMD are shown in black lines and are bounded by the inversion errors in a grey shaded area. The area represents the extent of both errors in $\text{EMD}(T)$ and in $\log T$ space, therefore the solution may lie anywhere within these bounds. The regularized solutions for all events remain within the bounds of the coloured EM-Loci curves confirming that they fall below the expected maximum total emission.

For each EMD the regularization tweak parameter α was adjusted by hand through integer values to achieve the best solution. To recall, this sets the expected χ^2 value for the inversion to target with a lower α placing more weight on the data. To gain the most physical information from the inversion we try to set this as low as possible without creating spurious inversions. The solutions were relatively insensitive to α between the limits of over and under-regularisation so no further iterative method was required.

The data in Events (a) and (d) seemed to invert very well and the EM was mostly within $\pm 10^{0.15} \text{ cm}^{-5}$. Event (f) proved tricky to balance being over regularized and returning a stable solution. The highest χ^2 that gave a smooth solution quickly gave rise to very broad temperature errors. We put this down to perhaps line blending given the complicated ribbon morphology in this event. If this is true it is interesting to find the inversion has some inherent capability in identifying bad data. At temperatures above 10^7 K the solutions all appear to fall off in EM expectedly and have no anomalous high temperature components, although the temperature resolution above 10^7 K is poor due to the broad $G(T)$ response in Fe XXIII and Fe XXIV so the exact cut off is uncertain. This lack of constraint makes it impossible to make physical conclusions beyond these

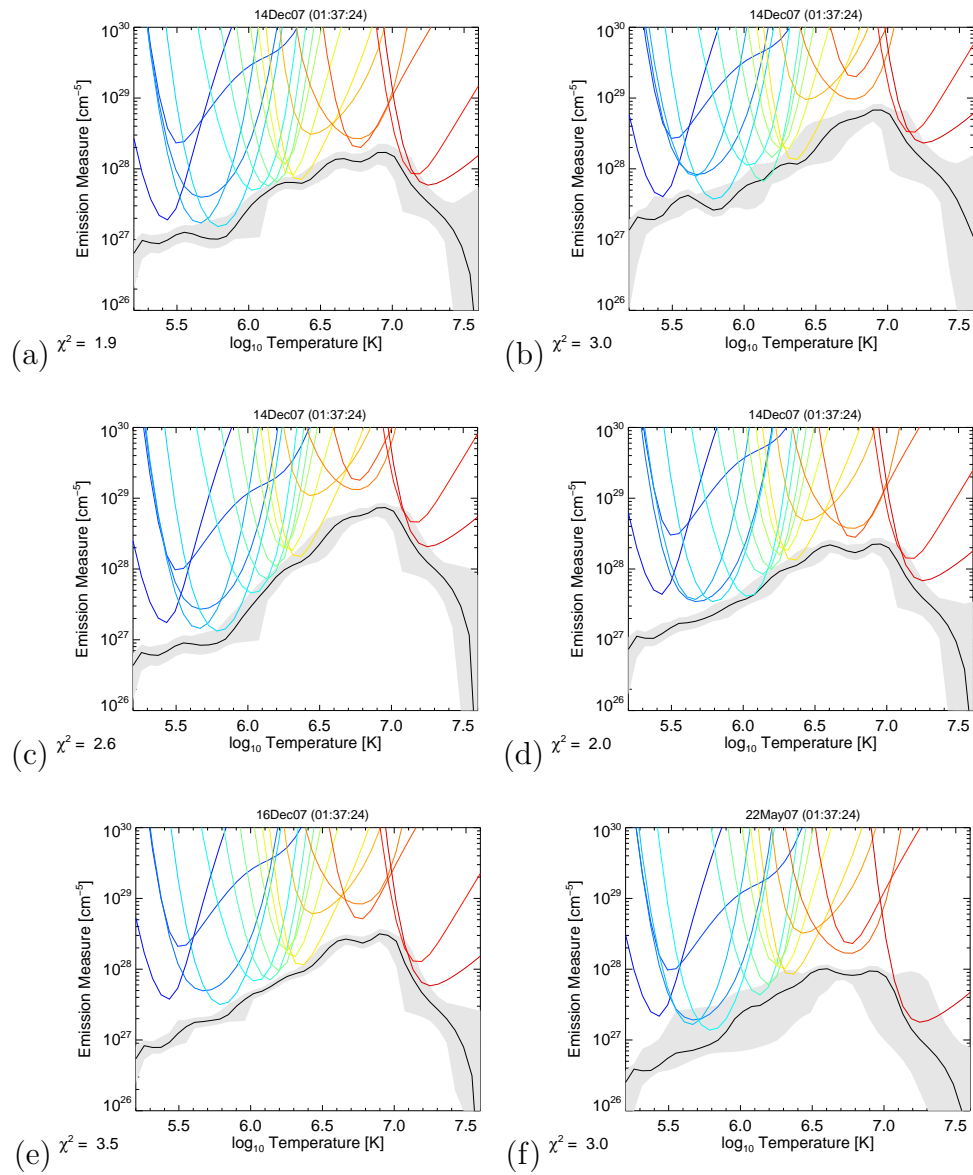


Figure 4.6: EMDs shown in black for each event in emission measure units cm^{-5} and the uncertainty limits of the solution by a shaded grey area. The coloured curves show measured line intensity divided by the contribution function indicating the maximum possible emission, i.e. the EM loci curves.

temperatures. Unsaturated, soft X-Ray observations from *Hinode*/XRT could have helped but were unavailable for all flares.

4.5.1 Measured Footpoint EMD Profiles

While performing the EMD inversion the first striking point was the similarity of the EMD profiles and consistency of what appeared to be an almost constant gradient. Naturally, this led to a literature check on EMD gradients and formed the direction of this chapter. In the footpoint EMDs above they share a similar profile; increasing with an almost constant gradient of $EM(T) \sim T$ to a peak around $\log T = 6.9$ and falling off quickly at higher temperatures. However, a closer look shows that there are deviations from a constant slope and variations between the events. The bumpy appearance of the EMD in Events (a), (b), and (f) is most likely a result of uncertainties in either the intensities or atomic data, as the undulations are of a comparable size to the width of the shaded error region. Event (e) is perhaps the best example of a constant gradient as the EMD is very well constrained.

Looking at the profiles, we can roughly estimate the gradient up to the peak by taking a line between two end points at $\log T = 5.5 - 6.9$. We start from $\log T = 5.5$ on the basis it is far enough in to avoid the badly constrained edges. An estimate of the spread of possible gradients is made by taking the maximum and minimum of the EM error boundary at the low temperature end, and finding the slope to the opposite bounds at the high temperature end. For Event (b) we measure a slope of $EM(T) \sim T^{0.95 \pm 0.27}$, very close to the $\log EM \propto T$ expected for a conduction-balanced atmosphere. For all of the events the gradients do not vary significantly and a gradient of 1 is certainly possible within the error ranges shown in Table 4.2.

A discontinuity at high temperatures like that observed in [Widing & Hiei \(1984\)](#) is not seen in any event. However, there is evidence to suggest a marginal break at $\log T = 5.7$ in the Events (a), (b), and (c), where the EMD flattens at very low temperatures. Taking the gradient in Event (b) from $\log T = 5.7 - 6.9$ returns a steeper gradient of 1.04 ± 0.45 ; as this event is the earliest sampled it may hint that the conduction/radiation balanced part of the atmosphere extends to lower temperatures as the heating continues, though we reinforce that the evidence could be marginal given the uncertainties in the inversion. On the other hand the break in Event (c) is certainly

significant compared to the size of the shaded error region.

Peak emission measures occur at $\log T = 6.9$ and vary between 10^{28} and 10^{29} cm^{-5} and do not appear to be strongly correlated to the GOES class, perhaps expected for a small selection of low energy events not sampled at consistent times (these values are tabulated alongside the gradients in Table 4.2). The emission measure in all events falls off quickly above $\log T = 6.9$ suggesting that this may be a limit to the maximum footpoint temperature observed, although we do not have any higher temperature data to confirm this. However, if we look at the radiative loss curve (as seen in Figure 1.4), we see that radiative losses from plasma above $\log T = 6.9$ also fall off rapidly by a factor of around 8 to a minimum at $\log T = 7.2$. It may be expected then that as the flare energy input increases (moving from GOES C class to M or X) the peak temperature of the EMD remains unchanged, as higher temperatures will contribute less to the distribution. Free-free emission above $\log T = 7.0$ may still of course be observed by XRT or RHESSI.

If the total flux from non-thermal electrons was to rise then the overall emission measure would be expected to rise across the temperature range. More importantly, the shape of the EMD in temperature may depend on the spectral index and low energy cut-off of the HXR spectra. In a collisional thick-target model higher or lower energy electrons will penetrate to different depths, heating different layers of the atmosphere. For example a relatively soft spectrum, as seen in Chapter 3, could deposit energy higher in the atmosphere where it is easier to heat. If the EMD is sensitive to these parameters then a study using a wide range of flare energies and HXR coverage could be used to confirm such a model. Creating synthetic EMDs using a range of beam parameters from a model such as [Allred et al. \(2005\)](#) would be an ideal starting point to investigate this.

4.5.2 EMDs for Different Solar Plasmas

Consistent flare EMDs are desirable but on the other hand the inversion method is subtle, and in principle could influence the results. We can verify that the similarity

Table 4.2: Event EMD parameters sorted by GOES Class. The gradient is calculated between temperatures of $\log T = 5.5 - 6.9$.

| Flare ID | GOES Class | Event | Peak Temp $\log_{10} T$ (K) | Peak EM $\times 10^{28} \text{cm}^{-5}$ | Gradient |
|------------------------|------------|-------|--------------------------------|--|-----------------|
| SOL2007-12-16T06:22:40 | B1.8 | (e) | 6.9 | 4.0 | 1.00 ± 0.21 |
| SOL2007-05-22T23:25:50 | B2.7 | (f) | 6.9 | 1.0 | 0.87 ± 0.23 |
| SOL2007-12-14T15:22:00 | B8.8 | (c) | 6.9 | 8.0 | 1.38 ± 0.28 |
| SOL2007-12-14T15:54:15 | B8.8 | (d) | 6.9 | 2.0 | 0.84 ± 0.28 |
| SOL2007-12-14T01:39:20 | B9.6 | (a) | 6.9 | 2.0 | 0.82 ± 0.37 |
| SOL2007-12-14T14:16:30 | C1.1 | (b) | 6.9 | 6.0 | 0.95 ± 0.27 |

of the EMDs determined for different events is not an artefact of the regularization by testing it with the line fluxes from active region (AR) and flare loop top (LT) plasma. Event (b) displayed a classic high temperature loop and the brightest pixel in Fe XXIV was picked for the EMD. A non-flaring region bright in Fe XII was selected in the active region background to represent the AR EMD; these locations are marked for reference by black arrows on the second panel of Figure 4.4.

The footpoint EMD is plotted in Figure 4.7 inside a green error boundary and EMDs for the AR and LT regions are found in orange and blue regions respectively. EMDs extracted from the AR and LT are indeed different from that of the footpoint, confirming that the regularization method is responsive to the different plasma distributions. Noticeable features are the matching EMD gradients of the AR and LT between $\log T = 5.8 - 6.3$, beyond which the AR plateaus and quickly falls off above $\log T = 6.8$ while the LT keeps rising, at a gradient close the footpoint, up to a peak of $\log T = 7.1$. We note that both rise with a slope steeper than $EM(T) \sim T^{\frac{3}{2}}$, a commonly observed gradient for the transition region and low corona (Jordan 1980); this is plotted for reference in a dashed line.

The referee for Graham et al. (2013) had some invaluable insight which helped

further understand the relationship between these EMDs if we consider the AR EMD to be a pre-flare situation. Emission in the footpoint between temperatures of $\log T = 5.2 - 6.2$ was seen to be greater than in the AR by up to an order of magnitude. As we suspect from a conventional understanding of flares, this enhancement is likely to be chromospheric plasma in the process of being heated to flare temperatures. The point at $\log T = 6.2 - 6.3$ where all 3 EMDs meet is intriguing. While the matching absolute EM may be coincidental, the break in similarity between AR and LT EMDs gradients here may indicate that only plasma above $\log T = 6.2$ will make it into the loop as there is no enhancement at temperatures below this. The flow measurements in [Milligan & Dennis \(2009\)](#) agrees with the picture, as plasma above $\log T = 6.2$ is blue-shifted (upflowing) and plasma below this temperature is red-shifted. Analysis of the plasma velocities will be important in future studies, but we found it reassuring to see that such arguments can be made from the results and that the behaviour of the EMDs varies in reasonable ways through the event.

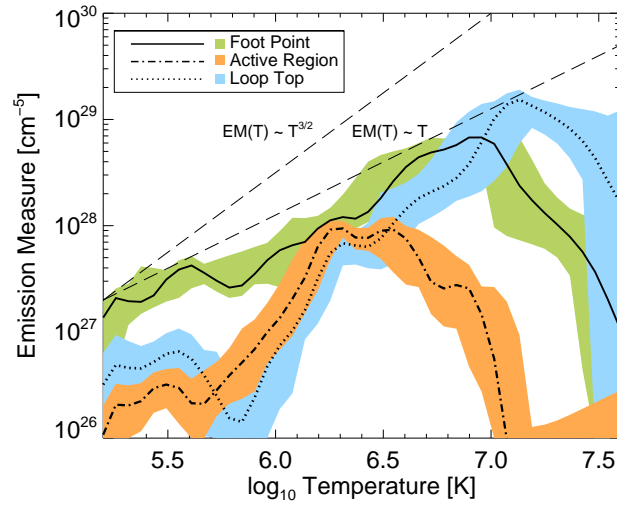


Figure 4.7: A comparison of footpoint, loop, and active region EMDs in Event (b). The purpose of this is to check the regularization response to different temperature distributions. Gradients of $EM(T) \sim T$ and $EM(T) \sim T^{\frac{3}{2}}$ are added in dashed lines.

4.5.3 Examination of the Assumptions Used

When interpreting spectra during flares we must be aware of the built-in assumption in the atomic physics. The $G(T)$ functions in CHIANTI are calculated for an optically thin plasma in a thermal Maxwellian distribution and in ionisation equilibrium. Is this assumption sensible in an impulsively heated footpoint? Here we have made some arguments to check, although a full analysis of the assumptions in one flare will be carried out later in Chapter 5.

Thermal Equilibrium — We know from RHESSI HXR observations that the electron spectra in the footpoints have an inherently non-Maxwellian component, due to bremsstrahlung emission from high energy electrons. While these are responsible for heating the footpoint plasma, their energy content may be small compared to the total energy of the distribution; see [Krucker et al. \(2011\)](#). Heating in the footpoint is intense, easily taking plasma from 10,000 K to over 10^6 K in a matter of minutes. If we discount the non-thermal component for now, can the core of the Maxwellian plasma remain in thermal equilibrium if it is heated so quickly? The electron-electron collision time-scale gives us a handle on the rate at which temperature changes can be equilibrated. For an electron density of 10^{11} cm⁻³ and temperatures of $10^{5.5}$ K and $10^{6.9}$ K the collision times are 3×10^{-5} and 1×10^{-3} seconds (see Section 5.5.3). This is much faster than the duration of the impulsive phase, which in Event (b) is ~ 4 minutes, so the plasma should thermalise quickly.

Ionisation Equilibrium — In low density plasmas the temperature may evolve faster than the ionisation state of the plasma can catch up. For example O v may not completely ionise into O vi before the temperature has reached the T_{max} for O vi. The ionisation stage therefore does not match the temperature and lags behind. We discuss this again in more detail in Section 5.5.2 but note here the calculations of non-equilibrium ionisation (NEI) states by [Bradshaw \(2009\)](#), who finds that at densities of 10^{10} cm⁻³ the ion peak formation temperatures can shift by up to $\log T = 0.3$ K, but

by $n_e = 10^{12} \text{ cm}^{-3}$ the difference is negligible. For our footpoint densities at around 10^{11} cm^{-3} ionisation equilibrium could be a safe assumption. Section 5.5.2 investigates the effect this has on electron density diagnostics, however, it is not clear at this stage how to implement NEI states into an EMD analysis. If all of the ion peak formation temperatures move by a similar amount the EMD slope might be preserved but shifted in temperature. Of course, this is merely an observation and requires further work in future.

Optical Depth — The data here extend to much lower temperatures than in the previous chapter and presumably higher densities if we extend the heating to deeper layers (see Chapter 5 for evidence of this). Line fluxes could be influenced as this means the atmosphere may not be completely optically thin throughout the whole region in which the EMD is produced. From the work in Bloomfield et al. (2002) and Milligan (2011) we found a means to estimate the optical depth for a given emission line. In Chapter 5 we improve on the brief calculation in Graham et al. (2013), which ignored the full integral over depth, and found the optical depth for lines emitting through a VAL-E atmospheric profile.

Here we show the results for lines used in the EMD analysis in Table 4.3 but refer the reader to Section 5.5.4 for more details. For the standard VAL-E atmosphere it appears that many of the lines have relatively large optical depths of over $\log \tau = 1$, however, we must remember that the VAL-E atmosphere is not representative of flares and even when moving into its transition region temperatures are below 1 MK. The model can be made more representative for our footpoints if we arbitrarily set the temperature of the entire atmosphere to $\log T = 6.8$, comparable with the maximum EM from the EMD. We do not suggest that the entire atmosphere is heated to this temperature, but it serves to calculate a lower limit for τ . The values in the table now drop below $\log \tau = 0$ which is reasonable. As shown later an optical depth of 1 corresponds roughly to a reduction in intensity of 30% which is comparable to our $I + G(T)$ errors. In most of the lines $\log \tau$ is much less than 1.0 so the optically thin assumption may stand.

Two lines do come to our attention though. Fe VIII and Fe XV still have optical depths of $\tau = 1$ at the higher temperature, indicating they may be problematic at lower temperatures. Fe XV 248Å is a known resonance line with a high transition probability and Fe VIII 185Å is excited from a line above the ground state and has high relative population; both of these factors will increase the optical depth of a line. The EMD analysis can be rerun after removing these lines and can be seen in Figure 4.8. The overall profile is not significantly altered by this change although the χ^2 to achieve a positive stable solution is now increased in some events due to the reduced constraint. The break in profile slope at around $\log T = 5.8$ for Events (a) and (c) is perhaps clearer now but further constraint at these temperatures would be needed to test this further.

Through these tests we arrived at the conclusion that the plasma state may indeed be close to the required assumptions and that the EMD is not strongly influenced; though we have only arrived at the conclusion through some simple analysis. To fully understand the effects of non-equilibrium and radiative transfer in a flare atmosphere is a serious undertaking which requires further modelling and tailored observations. This is beyond the scope of the chapter but should not be ignored in future studies.

Table 4.3: Optical depths at line centre calculated at $n_e = 10^{11} \text{ cm}^{-3}$ using the VAL-E atmospheric parameters. Also shown are the optical depths for a modified VAL-E model, where the temperature is held constant ($\log T = 6.8$) and is assumed to be fully ionised ($n_e = n_h$).

| Ion | λ (\AA) | $\log \tau_0$ | $\log \tau_{mod}$ |
|----------|----------------------------|---------------|-------------------|
| O v | 248.460 | -4.75 | -7.19 |
| O vi | 184.118 | -4.04 | -6.49 |
| Fe viii | 185.213 | 2.35 | -0.02 |
| Mg vi | 268.991 | 1.08 | -1.28 |
| Si vii | 275.361 | 1.37 | -0.99 |
| Fe x | 184.537 | 1.77 | -0.60 |
| Fe xi | 188.216 | 1.78 | -0.58 |
| Fe xii | 195.119 | 1.92 | -0.43 |
| Fe xiii | 202.044 | 0.28 | -2.08 |
| Fe xiv | 274.204 | 1.44 | -0.91 |
| Fe xv | 284.163 | 2.35 | -0.02 |
| Fe xvi | 262.976 | -5.13 | -7.58 |
| Ca xvii | 192.853 | 0.45 | -1.92 |
| Fe xxiii | 263.766 | -0.33 | -2.70 |
| Fe xxiv | 192.028 | 1.10 | -1.28 |

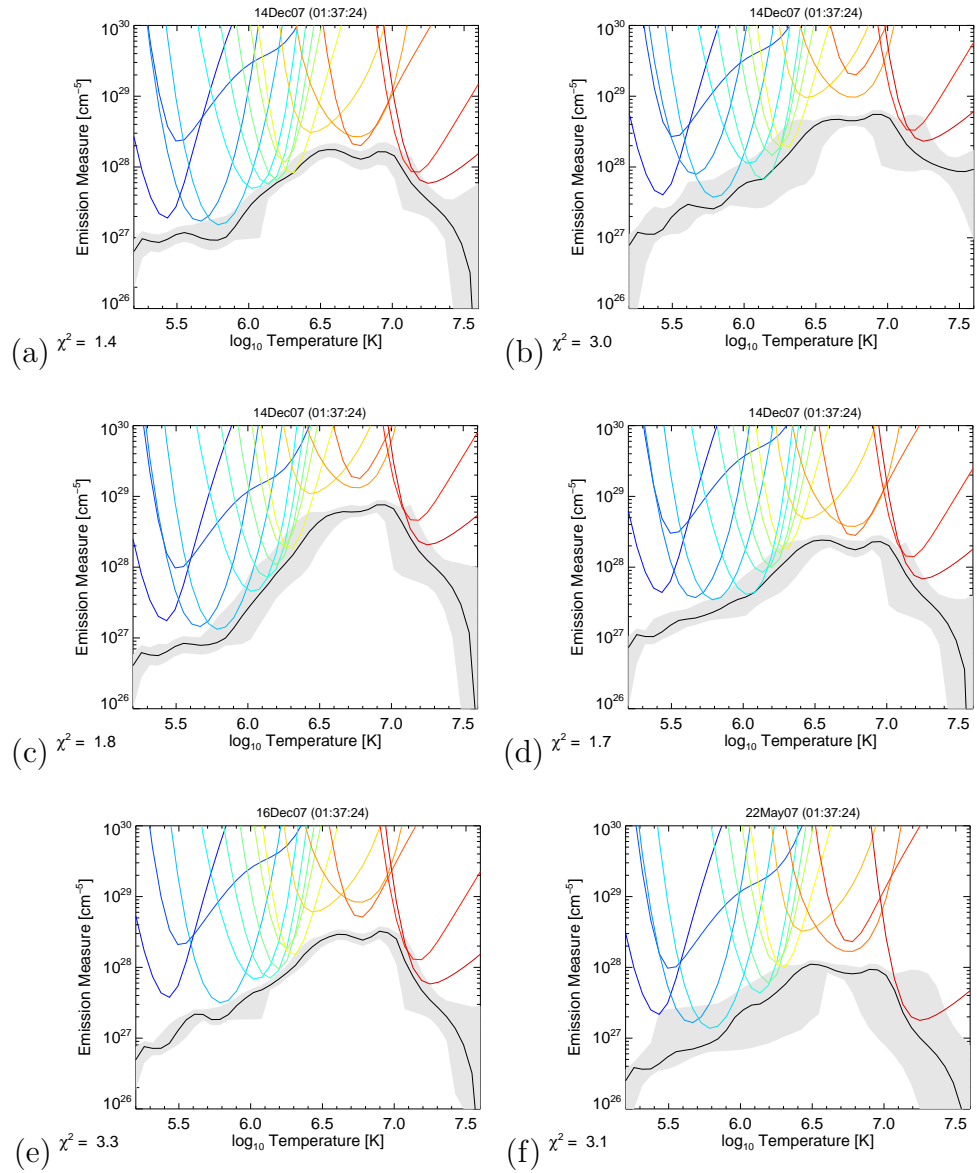


Figure 4.8: EMDs shown the same data but removing the Fe VIII and Fe XV lines to check for optical depth effects.

4.5.4 Varying the Abundance and Ionisation Equilibrium

The difficulty in choosing the appropriate values of elemental abundances in the footpoint plasma was discussed in Section 4.4.1. It was also not clear which set of ionisation equilibrium files should be used. The analysis was repeated for Event (b) using various ionisation files with photospheric (Grevesse & Sauval 1998) and coronal abundances (Feldman et al. 1992). The CHIANTI ionisation equilibrium file (Landi et al. 2012) was compared to two commonly used sets from Mazzotta et al. (1998) and Bryans et al. (2009).

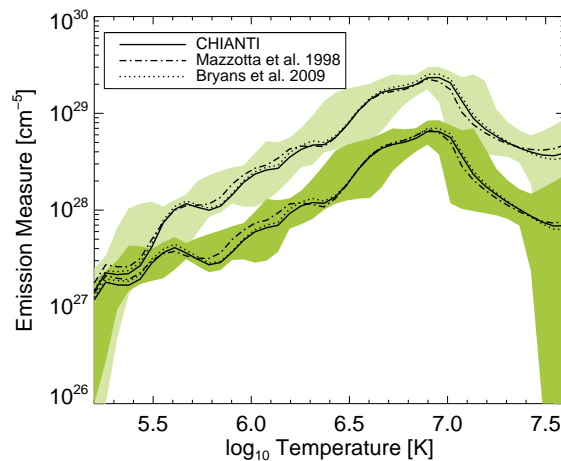


Figure 4.9: Footpoint EMD of Event (b) using photospheric and coronal abundances and a variety of ionisation equilibrium theories. EMDs are shown by the black lines within a shaded error boundary. Curves within the lighter shaded area are from photospheric abundances and the darker from coronal abundances. For each abundance file three ionisation equilibrium theories are tested and plotted in different line styles.

In Figure 4.9 the EMDs within the light shaded area are determined using photospheric abundances and the dark shaded areas from coronal. We see that the effect of using coronal abundances is to decrease the EMD by a constant factor of 4-5, although at low temperatures there is less deviation. It was expected that high FIP elements

such as oxygen would remain unchanged, and as oxygen lines here are only present at low temperatures it is to be expected that the EMD only changes above $\sim \log T = 5.6$. As a result the majority of the EMD gradient remains unaffected. In a side note, the differences in EM between abundance sets are greater in places than the EM uncertainty. Now that we have gained confidence in the inversions sensitivity to changes in the plasma, in principle some forward fitting approach to minimise the residuals could reveal information about the abundances. A procedure was sketched up and briefly tested; a note of this is found in the future work chapter.

Finally we also notice that changing the ionisation equilibrium parameters (solid, dashed, and dotted lines) has very little effect on the EMD. The small variations between these files must have little effect compared to the data and $G(T)$ uncertainties as differences in the inverted EMD all lie within the error boundaries plotted.

4.5.5 Electron Densities and Emitting Region Thickness

From the emission measure the depth of the emitting region, Δs , can be estimated for a specified temperature. Each point in the EMD symbolises the EM within a temperature range specified by the binning $\Delta T = 1.14T$, where the height of the region is given by $\Delta s = EM(T)/n_e^2$. By choosing a density at the appropriate temperature we can find Δs .

As we saw in Chapter 3 line diagnostics can reveal the electron density within the emitting footpoints. During the flare impulsive phase the density rose in the footpoint to around 10^{11} cm^{-3} at temperatures of $\log T = 6.2$. A number of density diagnostics were also available in the Cambridge rasters allowing densities to be estimated in the same manner for each footpoint — the line ratios are shown in Table 5.2.

Chapter 5 focuses on the O v ratio for the same events, so we refrain from discussing it here in detail but use the results from the diagnostic in the following discussion. The Fe XII, Fe XIII, and Fe XIV diagnostics are familiar though Fe XII uses a different line ratio than before. We use only the Fe XII and Fe XIV diagnostics here, as Fe XIII almost matches the densities in Fe XIV and covers the same temperature range. Mg VII and

Table 4.4: Density sensitive line pairs available in the Cambridge rasters.

| Ion | Wavelength (Å) | $\log T_{\max}(K)$ | $\log n_e$ range |
|---------|---------------------------|--------------------|------------------|
| O v | 192.904 / 248.460 | 5.4 | 10.5 - 13.5 |
| Mg VII | 280.742 / 278.404 | 5.8 | 8.5 - 11.0 |
| Si x | 258.374 / 261.057 | 6.2 | 8.0 - 10.0 |
| Fe XII | 196.640 / 195.120 | 6.2 | 9.0 - 11.5 |
| Fe XIII | 203.797+203.828 / 202.044 | 6.2 | 8.5 - 10.5 |
| Fe XIV | 264.789 / 274.200 | 6.3 | 9.0 - 11.0 |

Si x unfortunately proved to be unreliable in returning densities consistent with the iron ratios, and in places showed no enhancement compared to the background. Given that Mg VII fills a gap in the temperature range, further work on fitting the lines in this ratio could yield interesting results.

The estimated footpoint densities are displayed in Table 4.5 along side the average uncertainty given by the difference of their maximum and minimum values (Chapter 3 explains how the uncertainties were found). The Fe XII and Fe XIV diagnostics return densities expected by our prior work; around 10^{11} cm^{-3} in Fe XII and 10^{10} cm^{-3} in Fe XIV. The Oxygen diagnostic returns extremely high densities and understanding the implications of this is deserving of a chapter itself. In some events the diagnostics returned a density higher than the diagnostic is sensitive to (i.e saturated); the maximum and minimum densities are therefore equal which is indicated where there is no error present. Fe XII was also not available for Event (f).

We do not discuss the densities further here, but use them to calculate Δs , the thickness of the emitting region, for the corresponding temperatures as shown in Table 4.6. The uncertainty in the thickness is given by calculating Δs for the maximum and minimum estimated densities. It is clear that the combination of high density and low emission measure at $\log T = 5.4$ leads to extremely small emitting depths with Δs equalling much less than a km, though the n_e^2 dependence on density does

Table 4.5: Footpoint electron density n_e . Where the density error is shown as — it indicates the diagnostic was saturated and the density represents a minimum value. For Event (f) there was no Fe XII diagnostic available.

| Flare ID | O v | Fe XII | Fe XIV |
|----------------------------|----------------------|----------------------|------------------|
| SOL2007-12-14T01:39:20 (a) | $14.50 \pm \text{—}$ | 11.12 ± 0.20 | 9.77 ± 0.09 |
| SOL2007-12-14T14:16:30 (b) | 12.30 ± 0.30 | $12.50 \pm \text{—}$ | 10.17 ± 0.04 |
| SOL2007-12-14T15:22:00 (c) | 13.94 ± 2.58 | 11.08 ± 0.14 | 10.04 ± 0.04 |
| SOL2007-12-14T15:54:15 (d) | 11.86 ± 1.24 | 10.95 ± 0.20 | 9.77 ± 0.05 |
| SOL2007-12-16T06:22:40 (e) | $14.50 \pm \text{—}$ | 11.02 ± 0.19 | 9.78 ± 0.07 |
| SOL2007-05-22T23:25:50 (f) | 11.23 ± 0.50 | — | 9.89 ± 0.08 |

Table 4.6: Emitting region thickness Δs in km.

| Flare ID | $\log T = 5.4$ | $\log T = 6.2$ | $\log T = 6.3$ |
|----------------------------|---------------------------------|---------------------|----------------|
| SOL2007-12-14T01:39:20 (a) | $1 \times 10^{-7} \pm \text{—}$ | 3.28 ± 3.11 | 1848 ± 813 |
| SOL2007-12-14T14:16:30 (b) | 0.005 ± 0.008 | $0.01 \pm \text{—}$ | 533 ± 99 |
| SOL2007-12-14T15:22:00 (c) | $1 \times 10^{-6} \pm 0.01$ | 5.14 ± 3.54 | 939 ± 157 |
| SOL2007-12-14T15:54:15 (d) | 0.02 ± 0.1 | 9.22 ± 9.66 | 2958 ± 688 |
| SOL2007-12-16T06:22:40 (e) | $1 \times 10^{-7} \pm \text{—}$ | 6.14 ± 5.56 | 2312 ± 814 |
| SOL2007-05-22T23:25:50 (f) | 0.15 ± 0.45 | — | 812 ± 311 |

mean that uncertainties in the inversion and diagnostics can lead to a wide range in emitting thickness. However, even with a conservative density of $\log n_e = 12.0$ the emission measure still needs to equal at least 10^{29} cm^{-5} to give a thickness of 1 km. In [Graham et al. \(2013\)](#) a calculation was made using column depths measured by [Milligan \(2011\)](#) to derive the emission measure independently of the inversion. Using the measured densities from each available diagnostic (excluding O v) and the line

intensities, Δs could be found and the EM estimated. The emission measures in the footpoints were found to be $10^{28} - 10^{29} \text{ cm}^{-5}$ at temperatures between $\log T = 5.8 - 6.3$, confirming what we find here to an order of magnitude.

The unusually small emitting thickness does raise questions about the true temperature of the plasma at the measured densities. By relaxing the assumption of non-equilibrium ionisation this may be possible and we discuss its impact on the density diagnostics in Section 5.5.2. If the formation temperature of ions used is higher, due to non-equilibrium effects, the emission measure according to the EMD is larger, therefore the estimated thickness becomes significantly greater.

At $\log T = 6.2$ Fe XII returns a plasma thickness on the order of a few kilometres given the densities of around 10^{11} cm^{-3} , though using densities determined at temperatures just 400,000 K higher, (from Fe XIV) which are an order of magnitude lower, increases Δs to the order of 1000 km. The existence of two regions of plasma with two very different densities in close proximity is indeed puzzling, and in context of the structure of the region it may fit with the picture of plasma beginning to evaporate as Fe XIV temperatures are reached; we discuss this further shortly. To summarise, it is perhaps at this point best not to draw any solid conclusions from these calculations and instead take it as evidence for an extremely steep temperature gradient, akin to the quiescent transition region but at higher temperatures, in the flaring atmosphere.

4.6 Discussion

Balance of the energy inputs and losses during a solar flare produces EMDs of different slopes and a well-determined EMD may provide a good diagnostic of this energy balance within the flare plasma. As we saw from Section 4.1.2, the modelling by Rosner et al. (1978) and Widing (1982) found that the layer of an atmosphere where conduction input and radiation losses balance returns an EMD slope proportional to T . As with interpreting the spectra, simplifying assumptions can be made to reduce the complexity of the energy balance equation - for example, in the aforementioned case the plasma is assumed to be contained within a closed 1-D loop where evaporation flows are ignored,

i.e the conduction input is sufficiently balanced by radiation.

A very early treatment by [Shmeleva & Syrovatskii \(1973\)](#) examined also the region of direct flare energy deposition. The atmosphere was thus divided into two layers. The energy arriving either from the flare rapidly heats the atmosphere it encounters. As it reaches its peak temperature, the parameters used by [Shmeleva & Syrovatskii \(1973\)](#) give $T_{peak} \sim 10^7$ K, the radiative loss curve drops off and radiation becomes less and less efficient at removing the energy. The model assumes that at this stage radiative losses can be ignored, and the plasma is cooled by conduction to the dense layers below. In this lower, cooler layer, radiative losses are very efficient and can balance the conductive input from above — as in the [Widing \(1982\)](#) study.

The model above was calculated for both a long duration heating with constant pressure, and a fast heating where the density can not adjust and remains constant. The authors find in the constant pressure case the thickness of a region between $T = 10^{4.0} - 10^{5.7}$ is only ~ 6 km at a density of 10^{13} cm^{-3} , agreeing with what we find in [Section 4.5.5](#). The authors argue constant pressure is therefore an acceptable assumption in the high temperature transition region, where the pressure scale height is ~ 500 km at $\log T = 4.0$.

For the [Graham et al. \(2013\)](#) paper, Figure 5 in [Shmeleva & Syrovatskii \(1973\)](#) was interpreted by L. Fletcher, finding the EM gradient to be around $T^{1.2}$ in the constant pressure case and $T^{2.2}$ for a constant density. Constant pressure was also assumed in [Widing \(1982\)](#) and its gradient is slightly shallower by 0.2 which could be a result of the difference in radiative loss functions used.

Overall we find the two models both show comparable EMD gradients with a common reason; that flare emission below around 10 MK is the result of conductive heating and *not* direct heating via the flare mechanism. Similar behaviour was inferred through SDO/AIA imaging by [Brosius \(2012\)](#) for a C6.6 class flare. Hot coronal Fe XIX emission appeared early in the impulsive phase, later followed by a rise of transition region lines (O V, Si XII and He I). As the Fe XIX emission occurred in the same location as the transition region emission it was interpreted as evidence for transition region plasma being heated by thermal conduction from directly heated coronal plasma.

In our analysis the average footpoint EMD appears to be robust and with the same slope close to 1 in a number of flares. Do we have enough grounding to arrive at the same conclusion, implying that the footpoint emission is determined by the balance between conductive heating and radiative cooling, as in these models? The inversion method's ability to return robust EMDs from data is certainly encouraging, and the fact different gradients can be obtained away from the footpoints. Justifying the atomic physics assumptions is always difficult in flaring situations, yet at a first order test they appear mostly sound and any uncertainties they introduce may be insignificant when combined with other lines and errors. In the end the match between observation and model could come down to the selection of data and models themselves.

If the model and observations are accurate, it suggests that the injected flare energy is localised to a layer at the very top of the flaring atmosphere at a temperature $\log T \sim 6.9$ and direct flare heating below this is negligible. Though when we say 'top' the true depth could still be deep into the transition region where it has been raised to this temperature; our density diagnostics certainly seem to suggest this — see the next chapter.

Looking more closely at the model, the assumption of constant pressure appears to be valid as shown. The observation of a bright compact footpoint tends to imply that the emission is confined and conduction losses across the direction of the magnetic field will be small compared to the flare input. A 1-D case is therefore reasonable. In these models the form of the conductivity used is the classical Spitzer conductivity (Spitzer 1962) which assumes that the electron mean free path is much smaller than the temperature scale length. Where this is not the case the conductive flux reaches a limit and calculation of the flux begins to depend on the plasma density and temperature profile of the entire atmosphere rather than just the local conditions. We do find the temperature gradient is extremely steep over the transition region which does question the assumption of classical conductivity. Battaglia et al. (2009) and Fletcher et al. (2013) have used the non-classical approach to calculate conduction rates in solar flare plasmas by adding a correction term to the flux that depends on the temperature and density. One further step would be to insert this into the balance equation from

Section 4.1.2 and re-evaluate the EMD slope, if possible analytically. In a final note, from studying Figure 6 in Battaglia et al. (2009) we note that the classical case will still apply at transition region temperatures and densities, and these effects may be limited only to the initial hot boundary. The effect in the EMD may only be localised to high temperatures.

In both the Widing and Shmeleva & Syrovatskii (1973) models the heating is assumed to be gentle enough to allow the conductive flux to be balanced by radiation, therefore the plasma is not in a situation where it needs to expand to compensate for the energy input, i.e via evaporation. Nevertheless, Milligan & Dennis (2009) did observe clear explosive evaporative up flows in Event (b) which must be considered in a complete model. For example, Underwood et al. (1978) showed that the effect of evaporation tends to flatten the slope of the EMD.

The location of the moving plasma could be important here and perhaps a third layer of the atmosphere should be considered. The layer above where the energy deposition occurs will not be empty, and the models neglect to consider the effect of conductive fluxes and heating into this plasma. Shmeleva & Syrovatskii (1973) point out that radiative losses are negligible in the 10 MK heated region, and assume it cools entirely by conduction to the plasma below, but as Fisher et al. (1985) find, this means the plasma will not remain stationary and will expand back into the corona. A combination of models could be feasible; the lower layer is isolated from the flare heating and radiates the incoming conduction flux efficiently, the directly heated layer redistributes the flare energy by conduction and through evaporation, while part of the heated plasma evaporates and fills the flare loops.

Milligan & Dennis (2009) and others observe that the upflows are only present above temperatures of $\log T \sim 6.2$ so again only part of the EMD may be affected. If the heated layer is indeed 10 MK, and everything below is in a stable balance as the EMD observations suggest, then seeing upflows from *lower* temperatures is unintuitive. We can either suggest that the evaporated material begins its journey early in the impulsive phase as the heating is progressing, or that the emission measure of the upflowing material is small in comparison to the bulk EMD. This brings us to the

point of understanding the data better. The emission line is integrated along the line of sight and may contain more than one component of plasma. A future study could make double component fits to the stationary and flowing component of the lines and compare the EMDs for both.

4.7 Conclusions

We set out with the aim of obtaining the first emission measure distributions of solar flare footpoint plasma using *Hinode*/EIS. Prior observations had revealed a form of the EMD that could be compared to models of the energy balance in the transition region, yet were limited by the instrumental capabilities and could not distinguish loop from footpoint plasma. We successfully extracted the first EMDs from EIS during the impulsive phase of 6 solar flares by application of a regularised inversion method. The inversion method was found to be reliable and yielded EMDs that were free from *a priori* model assumptions. The EMDs could then be characterised between temperatures of $\log T = 5.5 - 6.9$ by an EM with a slope of $EM(T) \propto T$. The EMDs all peaked at $\log T = 6.9$ with an EM of $10^{28} - 10^{29} \text{ cm}^{-5}$ which implied a substantial amount of the footpoint material was heated to very high temperatures.

The recovered EM slope was in relatively close agreement with two models that both deposit flare energy at the top of a flare chromosphere/transition region heated to around 10 MK. The heated region then loses energy to the plasma below by conduction and this plasma then radiates efficiently, lighting up the atmosphere in EUV radiation. It is clear that further work is needed to fully understand the effects of relaxing the assumptions within the models. Evaporative flows for example are observed but not included in the model, as is the effect of non-local, or saturated conduction flux. Other areas to explore are alternative descriptions for the flare energy input, the radiative loss functions, and the assumptions within the atomic physics.

Finally, using density diagnostics in conjunction with the EMD shows that the temperature gradient of the atmosphere may be extremely steep at low temperatures. How this changes as the temperature increases could help explain the structuring of the

atmosphere, although more work is required in understanding the density diagnostics and new observations should include at least one diagnostic at higher temperatures.

Obtaining reliable measurements of footpoint EMDs is not only of theoretical interest as they can be used to better estimate synthetic line intensities. In flares this is important for identifying blends in other events, or in instruments where the spectral resolution is lower (e.g the SDO/EVE spectrometer). A broad response of the plasma in temperature space is also desirable for calibrating instrumental responses for future instruments like IRIS. We discuss these instruments further and the potential of EMDs using EVE in the future work chapter.

Chapter 5

Measurements of High Densities in Flare Footpoints

We have found evidence for very high densities at transition region temperatures in flare footpoints using a *Hinode*/EIS density diagnostic not previously used for flare studies. Footpoint plasmas at densities above 10^{13} cm^{-3} are found emitting with an apparent temperature of $2.5 \times 10^5 \text{ K}$; this is the density at the very bottom of the chromosphere, yet seemingly heated to the temperature of the transition region. Such high densities are seldom seen in recent flare observations and the result may either be a new piece in the puzzle of flare footpoint heating or may be unearthing a previously unknown nuance of the diagnostic. We consider how, and if, heating can reach such dense layers, and secondly how the diagnostic may yield false densities when the assumption of optically thin plasma in ionisation equilibrium is relaxed. In either case a diagnostic at this temperature is found to be of great value and should be recommended for further EIS studies.

High densities, where we refer to ‘high’ as greater than those commonly measured with EIS in flare loops and footpoints, e.g. $> 10^{11} \text{ cm}^{-3}$, were documented in the late 70’s and early 80’s by those involved in the *Skylab* NRL normal incidence slit spectrograph S082B (Bartoe et al. 1977) and the Ultraviolet Spectrometer and Polarimeter (UVSP) instrument on board the Solar Maximum Mission (SMM) (Woodgate et al.

1980). Both of these instruments shared similar wavelength ranges and diagnostics at transition region temperatures. [Doschek et al. \(1977\)](#) and [Feldman et al. \(1977\)](#) used *Skylab* slit data to derive densities from O IV ratios at 10^5 K. The lines observed had clear velocity-shifted components; the density of the stationary component was between 10^{11} and 10^{12} cm^{-3} while densities over 10^{13} cm^{-3} were seen in the downward moving (~ 50 km/s) component. The two components were also shown to be from two distinct volumes within the flare. Another analysis by [Cheng et al. \(1982\)](#) used the density sensitive ratio between the O IV 1401Å and Si IV 1402.7Å lines at the same temperature, finding a pre-flare density of 2.5×10^{11} cm^{-3} rising to 3×10^{12} cm^{-3} during the flare impulsive phase. The high density was localised to a footpoint kernel with a strong magnetic field gradient. A HXR burst matched the time of density, leading the authors to the conclusion of accelerated electrons being the source of UV emission, although originating within a low lying transition region loop. Neither of these papers directly questioned the origin of the high density plasma at transition region temperatures other than hinting at pressure related changes from mass motions. The low spatial resolution in these instruments also made the distinction between loop and footpoint sources difficult.

Now that a similar diagnostic has been found in EIS we can verify these results but use the higher resolution of EIS to our advantage. Plus, we have the additional benefit of RHESSI HXR coverage and density diagnostics made previously at higher temperatures. The diagnostic was available within the Cambridge rasters used for the EMD analysis in Chapter 4 for all of the flares studied. In this chapter we have used the O V $\lambda 192.904$ Å/ $\lambda 248.460$ Å ratio which is sensitive to densities between 10^{11} and 10^{14} cm^{-3} at a temperature of 2.5×10^5 K. Fitting the 192Å line is challenging and deserves careful attention but gives intensities which return very large ratios to 248Å even when applying generous fitting errors.

As we will show, heating via a collisional thick target model may not provide sufficient energy to heat plasma at these densities to the observed temperature, even though the same reasoning was used successfully in Chapter 3 at lower densities. Alternative reasons for the 192Å intensity enhancement are considered including relaxing

the assumption of ionisation equilibrium and accounting for opacity effects. However, it remains difficult to completely reconcile the high densities by altering the diagnostic assumptions or by accounting for fitting errors. We are therefore cautiously confident in stating that there is hot plasma with a density at the very least of 10^{13} cm^{-3} within the footpoints.

5.1 Oxygen Diagnostics

The diagnostics available in the Oxygen lines were first noticed while fitting the Ca XVII 192.853Å line in the previous Chapter. Ca XVII is one of the only strong lines found in the EIS spectral range at $\log_{10} T = 6.8$; for EMD work this puts it in a very useful position between Fe XVI and the hottest Fe XXIV lines. Blended with the Ca XVII profile is the strong O V 192.904Å transition, which is density sensitive at much lower temperatures than the iron lines used in Chapter 2 and could be of great use for flare diagnostics. Details of the spectrum as viewed by EIS in this wavelength range can be found in [Landi & Young \(2009\)](#).

Early atomic physics calculations were made by [Widing et al. \(1982\)](#); [Keenan et al. \(1991\)](#) for transitions within the $n = 2$ and $n = 3$ levels of O V, including the 192Å, 210Å, 220Å, and 248Å lines all available in the EIS wavelength range. Intensity ratios were also calculated by them as a function of density, demonstrating the sensitivity of many combinations of these lines. We are primarily concerned with the 192.904Å to 248.460Å ratio that is sensitive to densities above 10^{13} cm^{-3} , where the 192.904Å transition is strongly density-dependent. Both of these lines are included in the Cambridge raster sets used in the previous chapter and the diagnostic ratio is formed in a similar manner to the four level diagnostics used in Chapter 3 and introduced in Section 2.2. In Figure 5.1 the energy levels involving the diagnostic transitions are shown (extended from the diagram found in [Munro et al. \(1971\)](#)). The $2s2p \ ^3P_2$ level here is metastable which results in an elevated population and an enhancement in the 192Å transition at high densities. By the same process the 760Å and 630Å transitions also form a density sensitive pair although are not observed by EIS.

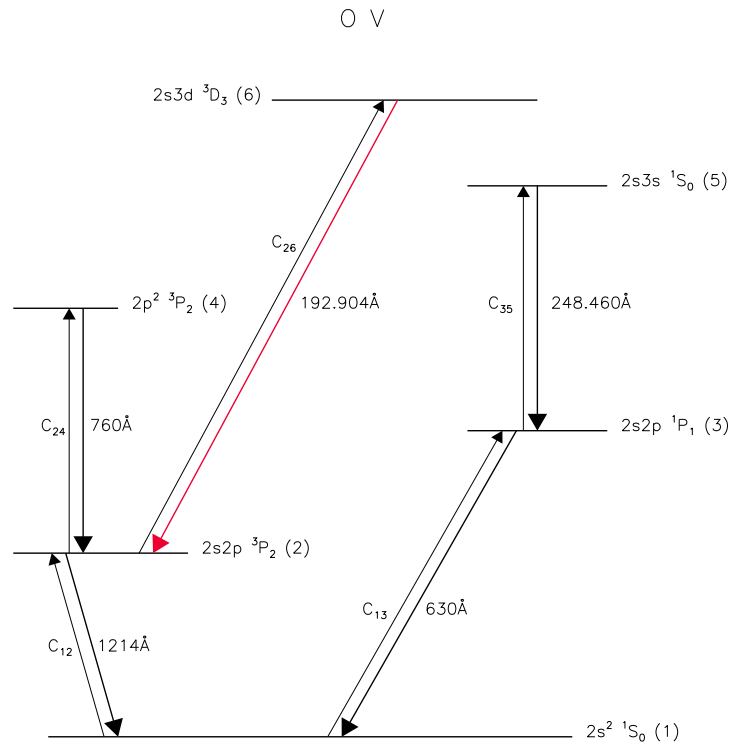


Figure 5.1: A term diagram showing the energy levels involved in the 192.904/248.460Å diagnostic. In this configuration the $2s2p\ ^3P_2$ (2) level is metastable. The 192Å transition is excited from the metastable level and becomes enhanced at high densities (shown in red).

In the early work, *Skylab* Spectroheliograph data were used to demonstrate these diagnostics for two impulsive flares, showing density enhancements on the order of 10^{12} cm^{-3} for the single unresolved flare source. The later updated calculations of Keenan et al. (1991) find more consistent measured densities between the ratios, but it is also interesting to note that they found deviations between the different ratios were smaller for a temperature of $T_e = 2.5 \times 10^5\text{ K}$ rather than at $T_e = 2.0 \times 10^5\text{ K}$. As $T_e = 2.5 \times 10^5\text{ K}$ is the maximum fractional abundance for O v in ionisation equilibrium the authors take this as evidence for the plasma being close to ionisation equilibrium — more on this in Section 5.5.2.

Among EIS studies the O v density diagnostic has been largely overlooked. It does

not appear to have been used to derive densities, at least for flare studies; possibly due to the difficulty in reliably obtaining the intensities and the fact that the lines are formed at temperatures commonly found in the lower atmosphere, where opacity effects may begin influence the line strengths. Yet it is worth exploring this diagnostic because as mentioned before we may be able to argue that the plasma is optically thin, and at the expected higher densities, in ionisation equilibrium. If not, then it may tell us how far from equilibrium we really are. Nevertheless, the lines in isolation have been used in DEM or temperature based studies and much literature exists on the analysis of the 192Å spectral region. For example, early EIS observations from [Young et al. \(2007b\)](#) discovered bright transition region emission in O v emitted by a non-flaring related active region brightening. In this event the O v was distinct from the very weak Ca xvii emission and could be fitted easily, but in our flare analysis strong Ca xvii emission must be expected, making the fitting more challenging.

5.2 Fitting

The O v and Ca xvii lines at 192Å are found among a complex grouping of multiple Oxygen and Iron transition region lines. A total of 6 O v lines are present along with 2 strong Fe xi transitions — the lines involved are shown in [Table 5.1](#). Analysis of this wavelength window is therefore complicated but may reward the patient (or stubborn) solar physicist with a wealth of temperature and density diagnostics. As mentioned in the extremely useful paper by [Young et al. \(2007a\)](#) this is a part of spectrum where the EIS detector is very sensitive, therefore, to our advantage the signal strength is high and the background low. To fit every line in the profile would require multiple independent Gaussian fits each with 3 parameters plus two for the background, and given the difficulties seen in unambiguously pinning down a pair of Gaussian components within a profile for velocity analysis, 9 presents significantly more degrees of freedom. In fact with $N_{param} = 30$ the parameter number is approaching the number of spectral bins.

Instead we base our fitting on the technique demonstrated by [Ko et al. \(2009\)](#) with some improvements, whereby using what we know from other lines, and making

Table 5.1: Strong lines found within the 192Å grouping. The relative line strengths for the Oxygen lines relative to 192.904Å are calculated from CHIANTI v7.1. for densities of $\log n_e = 11$ and $\log n_e = 14$.

| Ion | Wavelength (Å) | I/I_{192} $\log n_e = 11$ | I/I_{192} $\log n_e = 14$ |
|---------|----------------|-----------------------------|-----------------------------|
| O v | 192.750 | 0.19 | 0.21 |
| O v | 192.797 | 0.39 | 0.45 |
| O v | 192.801 | 0.14 | 0.16 |
| O v | 192.904 | 1.0 | 1.0 |
| O v | 192.911 | 0.13 | 0.15 |
| O v | 192.915 | 0.01 | 0.01 |
| Fe XI | 192.627 | - | - |
| Fe XI | 192.814 | - | - |
| Ca XVII | 192.853 | - | - |

some assumptions, the number of free fit parameters can be drastically reduced. For reference, a plot of the predicted spectrum calculated from CHIANTI v7.1 (Dere et al. 1997; Landi et al. 2013) for coronal abundances and the CHIANTI default ionisation equilibrium is found in Figure 5.2, where we have used the DEM derived in Chapter 4 for Event (b). The following describes the fitting procedure.

To start with, the Fe XI 192.814Å contribution can be estimated from the clean and well observed Fe XI 188.216Å line. From CHIANTI the 192/188Å intensity ratio is 0.20, and by also using the 188Å line width and relative centroid position (to account for any velocity shifts) we can specify the 192Å line parameters. Fe XI 192.627Å is distinct enough to include in our fit without additional constraints, and the only requirement is to limit the width to within $\pm 20\%$ of the measured 188Å line width. The O v 192.904Å line is the target fit and its parameters are left mostly free. We can however reduce the variation of the 192.904Å line width to $\pm 10\%$ of the measured O v 248.460Å width to keep the width within realistic bounds — i.e. the line widths of lines formed at similar

temperatures should not deviate much in equilibrium. The centroid position is also limited to velocity shifts of -15 to 40 kms^{-1} as the line is more likely to be red-shifted. The remaining O v lines are specified by their predicted intensities relative to 192.904\AA and its fitted width and relative centroid position.

Some of the weaker O v lines do display some density sensitivity themselves although the variation is small compared that of 192.904\AA . As seen in Table 5.1 the relative intensity of the 192.797\AA line changes by only 6% between 10^{11} and 10^{14} cm^{-3} . As we are fitting the lines to find the density, we do not have an accurate density to predict the weaker O v line intensities prior to fitting. However, if the differences in intensity between $\log n_e = 11 - 14$ are added in quadrature we find the total error in all lines is at most 7% of the 192.904\AA line intensity, smaller than the eventual fitting errors. We do not believe that this will have a significant effect on the fitted 192.904\AA intensity, therefore we have used the relative intensities for a fixed density of 10^{11} cm^{-3} , as was used in Chapter 4. It should also be noted here that since the writing of [Graham et al. \(2013\)](#) CHIANTI has been updated to v7.1, yet the relative strengths of the Oxygen lines have changed marginally, on the order 2-3%. Such small changes should have a negligible effect on the earlier derived EMD's when convolved with the other lines.

Finally, the Ca xvii parameters are left mostly free but with some bounds on the minimum and maximum line widths. We impose this because the measured line width can not be less than the instrumental line width for EIS (54 m\AA as specified by [Brown et al. \(2008\)](#)), thus avoiding the fit acquiring very narrow lines, which may minimise the residuals but are unphysical. We have now reduced the fit down to 11 free parameters, 3 Gaussians plus a linear background. These are passed to the IDL minimisation routine MPFITFUN to return the best-fit spectra for each line.

The $1-\sigma$ parameter errors given by MPFITFUN (as shown in Section 3.2.1) are very small for the multi-Gaussian fit, on the order of 1%; while providing an estimate on how the data uncertainties translate into fit parameter errors, they are a poor representation of the uncertainty in balancing the intensity of each line within a complicated fit such as this. [Ko et al. \(2009\)](#) performed a Monte Carlo simulation (their Figures 2 & 3) to

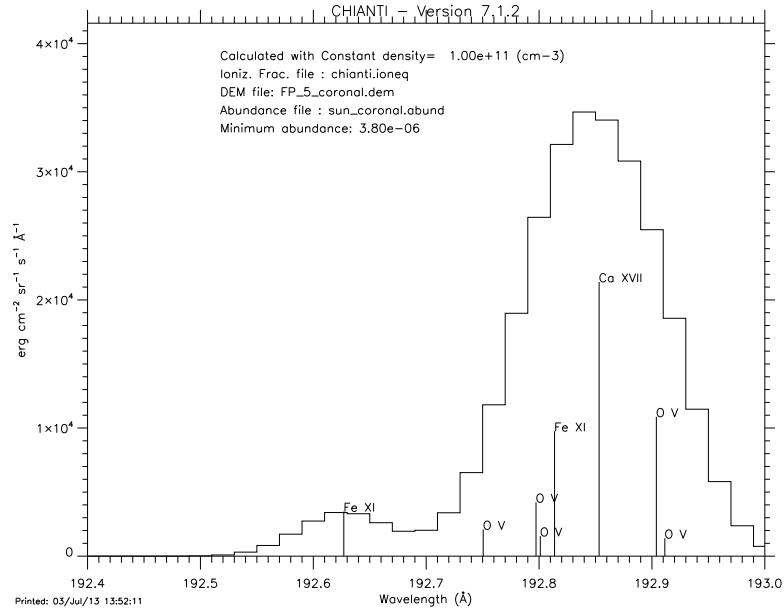


Figure 5.2: Spectrum of the 192Å region from CHIANTI v7.1.

study the uncertainties in retrieving the O v and Ca xvii intensities by varying the input line strengths, finding that the errors in each of the line intensities are correlated with each other. We have not repeated the simulation but note three things from the authors analysis: where the Ca xvii/Fe xi ratio increases above 1.0 the Ca xvii intensity uncertainty is found to fall below 20%; again as the O v/Fe xi ratio approaches 1.0 the O v error drops below 10%, and finally that the fit is deemed physical if the O v or Ca xvii line intensities are greater than 10% of the blend with Fe xi. The spectra in all of our footpoints meet these criteria and for the O v diagnostic used in this Chapter we assign a maximum error of 10% on the line intensity in addition to the fit parameter error, although in many cases the lines are very strong and this will be an overestimate.

For the 192/248Å diagnostic, fitting of the 248.460Å line is much simpler. A small contribution from Al viii at 248.459Å is documented but due to its location is impossible to remove directly; a partner Al line is also not available in our rasters. However, from CHIANTI the contribution is shown to be no more than 10% of the total intensity even in the most extreme flaring scenarios and the blend is therefore considered as part

of the uncertainty. A more significant blend in the blue wing around 248.600\AA can be seen in some footpoints but is removed using a second Gaussian component — this blend is possibly a combination of the theoretical Fe x 248.540\AA line along with Ar XIII at 248.690\AA . Unfortunately the effective area of the instrument at this wavelength is low — the signal strength is around 10 times weaker than the 192\AA line — and fitting errors are therefore larger, up to 10%, and comparable to the 192\AA line.

5.3 Fitting Results

The technique above was used to extract the Ca XVII intensities for each footpoint in Chapter 4. Before fitting the line profiles the raw spectra in each pixel was averaged with the two pixels above and below to improve the signal to noise ratio — again not including those east and west due to the $2''$ slit width. The spectra at the time were not discussed in detail but there is much to learn about the events from them. In Figure 5.3 we show the fitted spectra for 3 footpoints in events from Chapter 4, finding that there is much diversity amongst the events. To start we note the fitting method indeed is capable of returning physically reasonable spectra; parameters stay within the prescribed width and centroid position limits and the total fit profile — smooth black line — remains close to the data. The fit only deviates noticeably in the red wing of Figure 5.3 (3), possibly due to the very strong Ca XVII emission being slightly blue-shifted beyond the parameter limits.

The relative O v to Ca XVII intensity varies widely between events. In Figures 5.3 (1) and (2) the O v emission is much brighter than would be expected for a spectrum predicted by the CHIANTI flare DEM, where the hot Ca XVII is expected to dominate, or even compared to using our own EMD (see Figure 5.2). This enhancement of O v is what prompted the analysis in this Chapter, to find out whether it is caused by excess heating, density changes, or the local plasma abundances. In the opposite case, Ca XVII emission is far brighter in the event shown in Figure 5.3 (3). The flare (Event (b)) is of similar GOES class and returned an EMD of a similar profile, but more loop-like structures are visible in the high temperature lines which may explain some of the

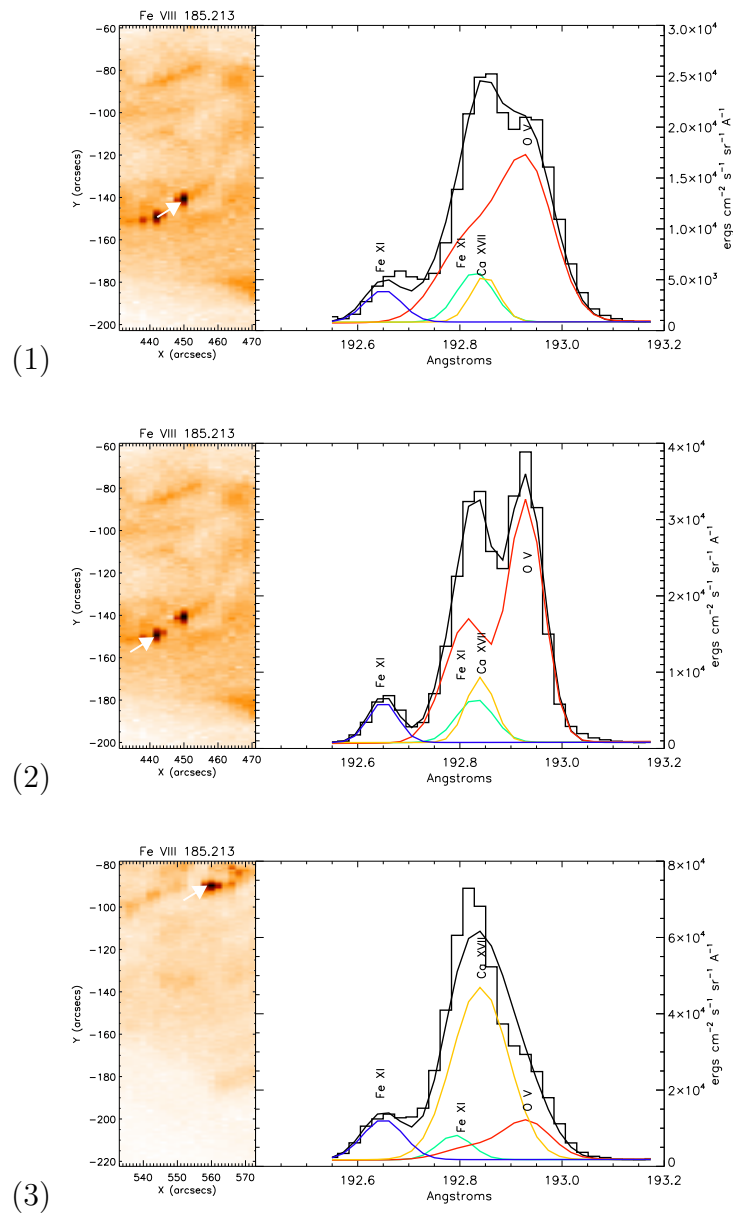


Figure 5.3: Fitted spectra for 3 footpoint locations taken from Events (a) and (b) in Chapter 4. The top two panels show two footpoints from within the same raster for Event (a). The red line for O v is a sum of all 6 Oxygen lines. In panels (1) and (2) the O v line is very clear and almost resolvable itself. In panel (3) Ca xvii makes a much stronger contribution, but the O v emission is still present.

excess hot material seen in the spectrum.

We can also consider the temporal evolution. Due to the slit scanning in the EIS

raster images, the spectra for both footpoints in Figures 5.3 (1) and (2) are sampled at slightly different times, with (1) at 01:37:24 UT and (2) at 01:38:11 UT — placing (1) just after the initial rise of the GOES SXR light curve (see Figure 4.3). From our imaging at multiple wavelengths both footpoints appear morphologically similar, both exhibiting enhancements throughout the temperature range. Therefore, it is fair to say that the footpoint in Figure 5.3 (1) is, at least weakly, a representation of the footpoint in Figure 5.3 (2) at an earlier stage of the flare evolution. The temporal evolution of these events was not considered in Graham et al. (2013) due to the low raster cadence, but this sidetrack may give us some extra insight.

If we look at the EMD for the earlier footpoint, Figure 5.4, we find that it contains less plasma at temperatures above $\log T = 6.5$ with a small peak at $\log T = 7.0$, the second peak being at a similar temperature to those in Chapter 4. According to the picture discussed in Shmeleva & Syrovatskii (1973) and Graham et al. (2013) this fits with an early direct heating of the upper transition region to around 10 MK. Plasma below this layer is then heated purely by conduction and remains in balance by radiating. Furthermore, between these two times the O v 192Å emission intensifies, suggesting again that the electron density is increasing around the ion formation temperature, but this time at a much lower temperature than in the Fe XII - XIV diagnostics studied previously, of 2.5×10^5 K. This is a curious result, as we did not expect to see the density being enhanced so far at these temperatures, thus the next section will clarify exactly how dense the footpoints become and what implications it has on our understanding of the event.

5.4 Footpoint Densities

Electron densities are now derived by comparing the measured line strengths to the theoretical ratio in the same manner as Section 3.3.1. The theoretical ratio versus density curve can be seen in black on Figure 5.5, and unlike many other EUV diagnostics extends to electron densities over 10^{13} cm^{-3} . Maps of the density for a selection of events are found in Figure 5.6. Immediately apparent are the bright enhanced re-

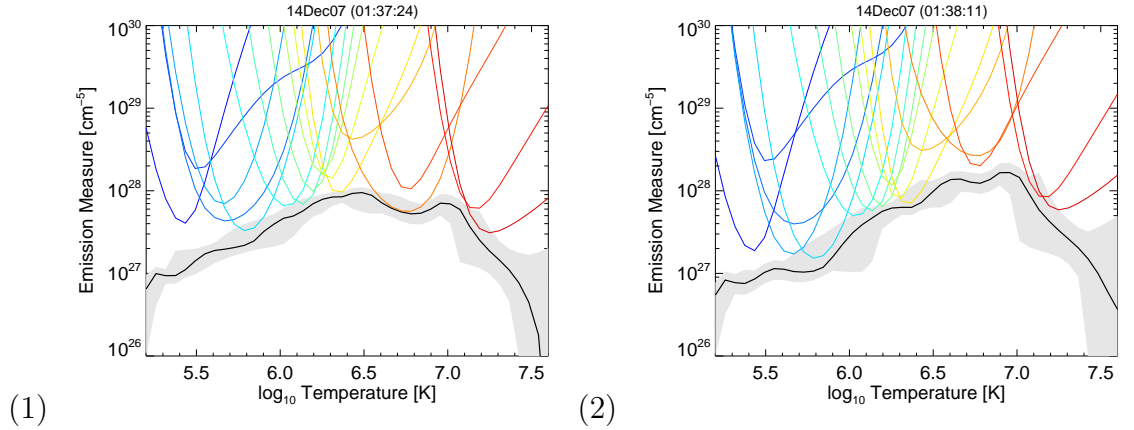


Figure 5.4: EMDs for both footpoints in Event (a).

Table 5.2: Density sensitive line pairs available in the Cambridge rasters and approximate range of sensitivity.

| Ion | Wavelength (\AA) | $\log T_{\max}(K)$ | $\log n_e$ range |
|---------|-----------------------------|--------------------|------------------|
| O v | 192.904 / 248.460 | 5.4 | 10.5 - 13.5 |
| Mg VII | 280.742 / 278.404 | 5.8 | 8.5 - 11.0 |
| Si x | 258.374 / 261.057 | 6.2 | 8.0 - 10.0 |
| Fe XII | 196.640 / 195.120 | 6.2 | 9.0 - 11.5 |
| Fe XIII | 203.797+203.828 / 202.044 | 6.2 | 8.5 - 10.5 |
| Fe XIV | 264.789 / 274.200 | 6.3 | 9.0 - 11.0 |

gions of density around the footpoint regions, matching the low temperature emission highlighted in Figure 4.4. Similar behaviour found in Chapter 3 and Graham et al. (2011) was attributed to heating of progressively deeper atmospheric layers. Only in the centre two images of Figure 5.6 does this picture vary, as the area of high density is more extended than in the cool emission; possibly from cross contamination of the hot Ca XVII, or that the source is indeed larger at $\log T = 5.4$.

Background active region emission in O v 248 \AA is very weak and reflected in the

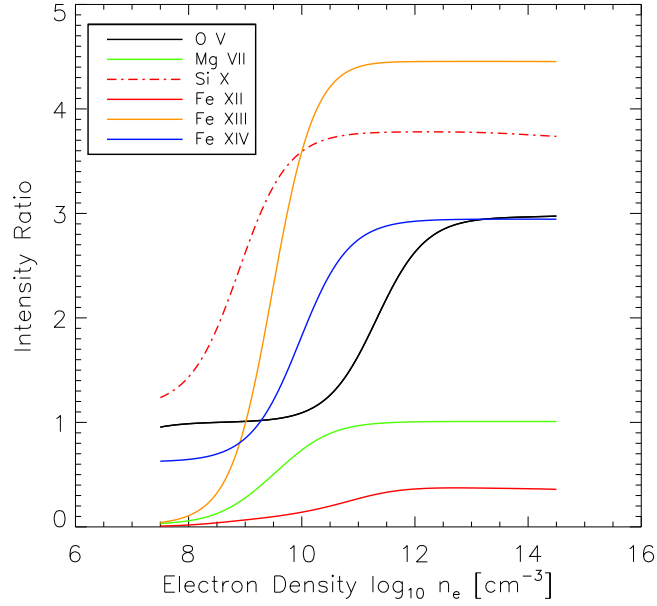


Figure 5.5: Diagnostic curves for ratios found in Table 5.2.

diagnostic by dark areas where no density is calculated for ratios close to zero. The O v 192Å intensity is also comparable to the intensity of its various blends in these locations making the fit less reliable. One might expect a low-temperature diagnostic to be useful in such non-flaring, but as the ratio does not rise until beyond 10^{10} cm^{-3} , and the VAL-E model density is below this value at $\log T = 5.4$, we are restricted to using it in regions where the density at $\log T = 5.4$ is high.

Densities extracted from each footpoint in Figure 5.6 are given in Table 5.3 including both footpoints from Event (a). Densities derived from the diagnostic in both footpoints for Event (a) are easily greater than 10^{13} cm^{-3} , with the measured ratio in the later sampled footpoint (b) nearly double the maximum of the diagnostic ratio, implying densities of over 10^{14} cm^{-3} . Such an extreme result was not expected here, certainly not for small flares like these, so we must be cautious. An error margin on these measurements is found by combining both intensity uncertainties in quadrature to give an estimate on the measured ratio, thus providing an upper and lower limit to the derived density. For the lower density footpoints, Events (b) & (f), the density can

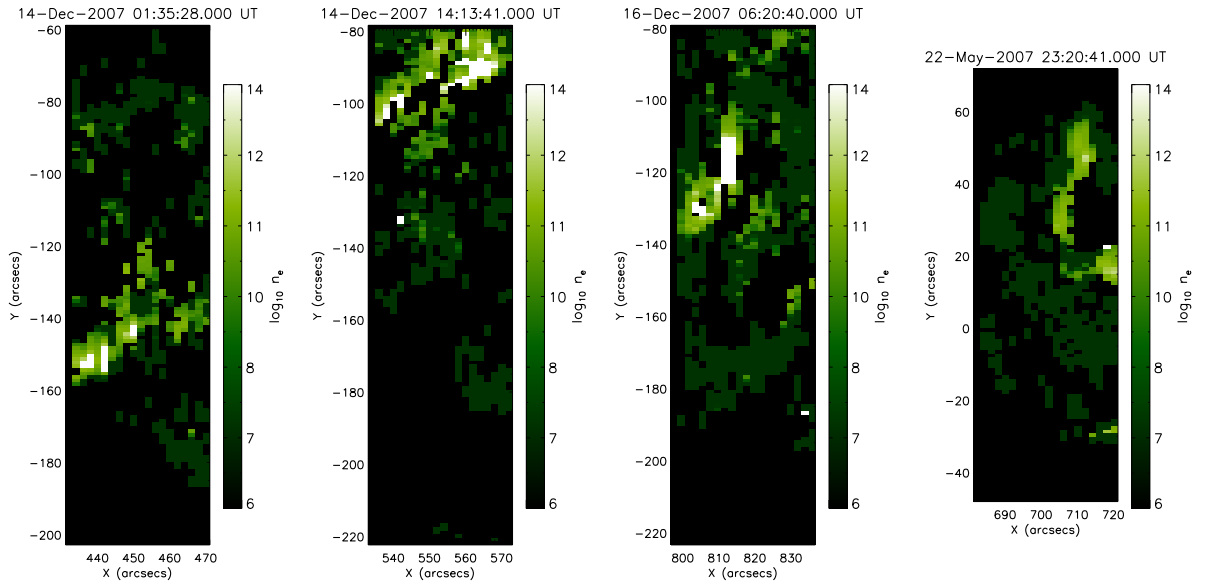


Figure 5.6: O v electron density maps for four events in cm^{-3} . Image colour tables are scaled to 95% of the maximum density in each map.

be found to within half an order of magnitude. At higher densities, the uncertainties are inherently larger as the ratio becomes flat close to the maximum density, but for footpoint (b) we find even the *lower* limit is still $\log n_e = 14.5 \text{ cm}^{-3}$.

At the footpoint location in Event (b) densities are lower, with $\log n_e = 12.30 \text{ cm}^{-3}$, yet the diagnostic in the area a few arc seconds to the north east is saturated, suggesting densities of at least $\log n_e = 14.5 \text{ cm}^{-3}$ (seen as a white area in second image of Figure 5.6). Given the binning used, and weak signal in the 248\AA line, it is difficult to make exact claims about the source size but regions of high density for this diagnostic ($> 10^{10} \text{ cm}^{-3}$) do appear to be larger than the source size in the intensity maps for low temperature lines.

Results for the 22nd May 2007 event show lower densities present in the flare ribbon, in the northern section reaching just over 10^{11} cm^{-3} . Over the region the signal strength in O v 248\AA is comparable to the other events, and O v 192\AA is just as prominent as before. We therefore rule out any instrumental effects as a cause of the reduced density, and suggest the fact that this was a lower energy flare (B2.7) accounts for the reduced enhancement at these temperatures.

Table 5.3: Footpoint electron densities using the O v diagnostic (calculated at $\log T = 5.4$). Shown are the intensity ratio for the two lines, derived electron density, and upper and lower density limits found via the uncertainty in the I_{192}/I_{248} ratio. For Event (b) densities of $\log n_e = 4.50$ are found 2-3'' to the north-west of the marked footpoint — note where $\log n_e$ reaches 14.50 the diagnostic is saturated.

| Footpoint | I_{192}/I_{248} | $\log_{10} n_e$ (cm^{-3}) | $+\delta n_e$ | $-\delta n_e$ |
|--------------------------------|-------------------|--------------------------------------|---------------|---------------|
| Event (a) 14-Dec-07 $_{FP(1)}$ | 3.59 ± 0.64 | 13.68 | 14.50 | 13.53 |
| Event (a) 14-Dec-07 $_{FP(2)}$ | 6.45 ± 1.12 | 14.50 | 14.50 | 14.50 |
| Event (b) 14-Dec-07 | 2.68 ± 0.39 | 12.30 | 12.45 | 12.15 |
| Event (e) 16-Dec-07 | 4.58 ± 0.72 | 14.50 | 14.50 | 14.50 |
| Event (f) 22-May-07 | 1.89 ± 0.27 | 11.23 | 11.48 | 10.97 |

5.5 Interpretation

Following the argument in Chapter 3, we believe that flare energy deposited in the chromosphere will heat progressively deeper layers during the impulsive phase. As the plasma reaches the peak formation temperature of the chosen diagnostic ion, the diagnostic will show the local plasma density — assuming of course that the plasma is in ionisation and thermal equilibrium. Here, this leaves us with the problem of explaining how the flare heating mechanism can heat plasma at densities characteristic of the deep chromosphere to around 250,000 K. An electron density of 10^{14} cm^{-3} puts the emission near the bottom of the chromosphere in the VAL-E model where the quiescent temperature is around 10,000 K (see Figure 5.7). Perhaps more relevant is the Allred et al. (2005) flare model, where the input beam energy drives a pressure increase, pushing a wave of material upwards, increasing the density in the lower flare atmosphere. For a beam flux of $10^{10} \text{ ergs cm}^{-2} \text{ s}^{-1}$ a maximum density of 10^{13} cm^{-3} is found at 1000 km, while the $F = 10^{11} \text{ ergs cm}^{-2} \text{ s}^{-1}$ model is needed to see a density

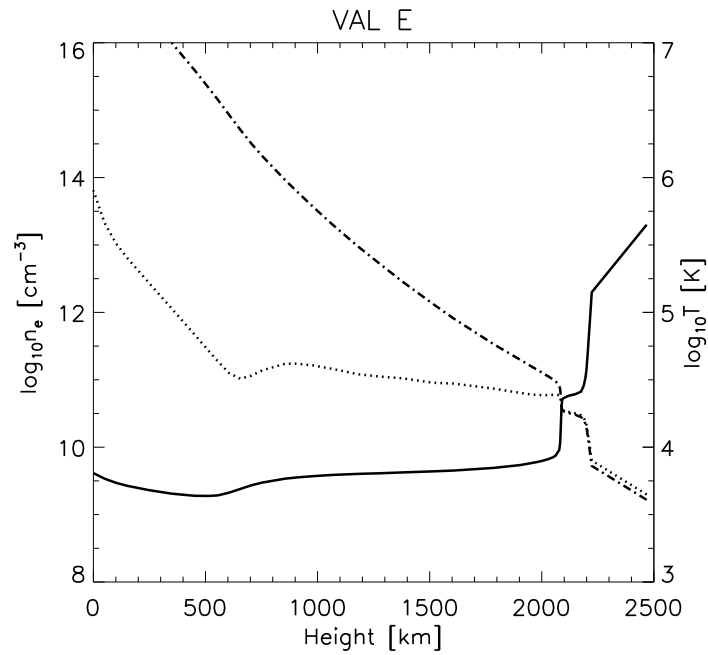


Figure 5.7: Hydrogen density (dash/dotted line), free electron density (dotted line), and temperature (solid line) as a function of height in the VAL-E model.

enhancement of 10^{14} cm^{-3} at the same height. For reference we have reproduced the F10 figure from [Allred et al. \(2005\)](#) in [Figure 5.8](#), this shows the density enhancement forming at around 0.8 Mm and the steep transition region moving towards lower depths.

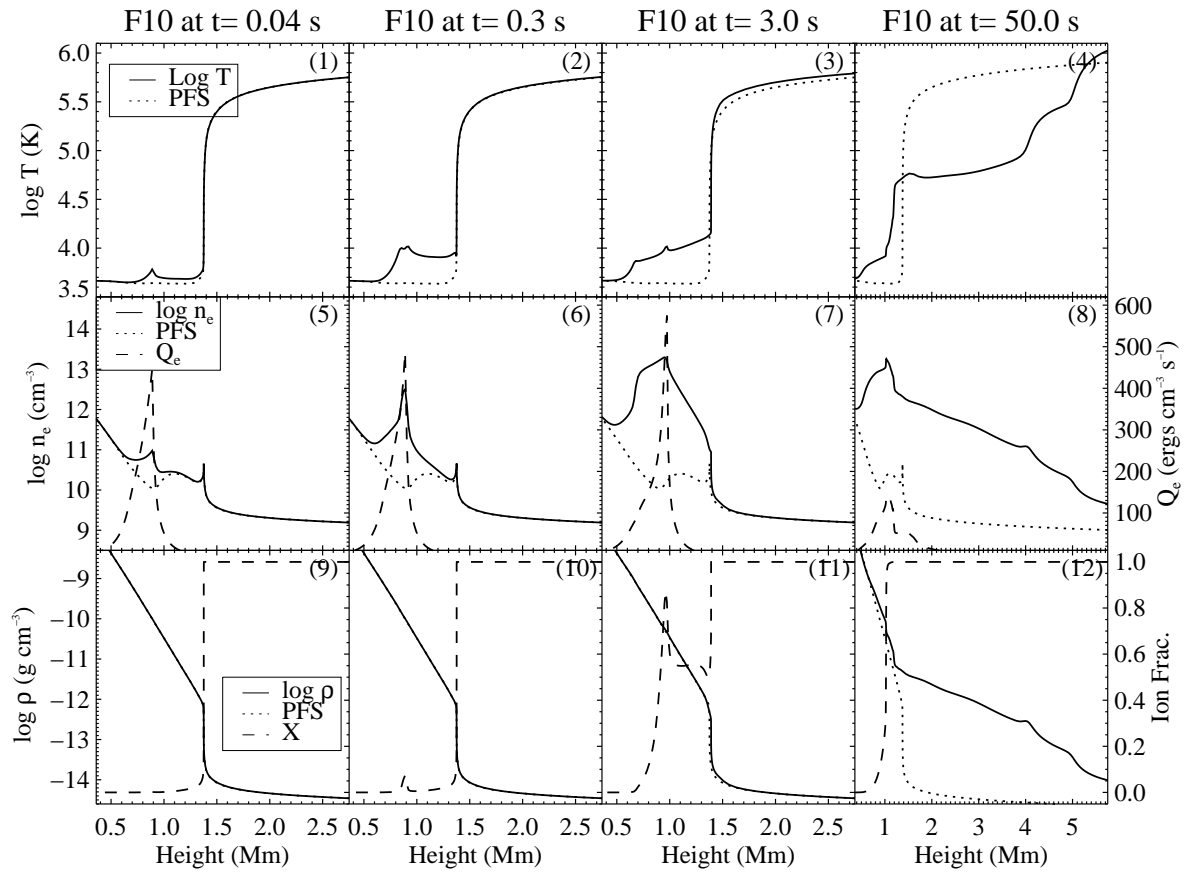


Figure 5.8: Example flare model reproduced with permission from [Allred et al. \(2005\)](#). Shown are the model parameters for a beam input flux of $10^{10} \text{ ergs s}^{-1} \text{ cm}^{-2}$. Note the high density region forming at around 0.8 Mm.

5.5.1 A Collisional Thick Target Approach

Should the observed densities be the result of directly raising chromospheric plasma to transition region temperatures, as suggested by the diagnostic, we can show that this is extremely difficult in the regime of a collisional thick target model. In a similar vein to Section 3.6.4 the plasma heating rate can be found. As the atmosphere at these densities is likely to be partially ionised we have this time used the heating rate in the form shown by Hawley & Fisher (1994) (based on that found in Emslie (1981)) for a constant ionisation level with depth. An electron beam losing energy via collisions will impart an energy per particle at a position with column depth N in the ambient plasma given by

$$Q(N) = \frac{\pi e^4 \gamma (\delta - 2)}{\mu_o} B \left(\frac{\delta}{2}, \frac{2}{(4 + \beta)} \right) \frac{F_P}{E_C^2} \left[\frac{N}{N_c} \right]^{-\delta/2} \text{ ergs s}^{-1}, \quad (5.1)$$

where N_c is the stopping depth reached by an electron with the spectral cut off energy E_c for $N_c = \mu_o E_c^2 / 2(2 + \beta/2) \gamma \pi e^4$. β contains the Coulomb logarithm, Λ , and effective Coulomb logarithms, Λ' and Λ'' where $\beta = [2x\Lambda + (1 - x)\Lambda''] / [\Lambda' + x(\Lambda - \Lambda')]$. The electron beam pitch angle, μ_o , has been taken to equal one in this case, implying all of the electrons are directed in a collimated beam towards the footpoint with no angular distribution, and we use the Coulomb logarithm definitions found in Hawley & Fisher (1994) which are quoted from Ricchiazzi (1982) (also see Spitzer (1962)). These are defined as:

1. $\Lambda = 65.1 - \ln(E) - 0.5 \ln(n_h)$
2. $\Lambda' = 25.1 + \ln(E)$
3. $\Lambda'' = 12.3 + 0.5 \ln(E)$.

To calculate these quantities we use the electron cut off energy E_c for the typical electron energy E and the hydrogen density n_h taken from the VAL-E model as a function of depth. We find that these are relatively insensitive and are roughly $\Lambda = 22$, $\Lambda' = 7.5$, $\Lambda'' = 3.5$ for most conditions.

Again the VAL-E model (for reference the density and temperature parameters of this are plotted against height on Figure 5.7) can be used to determine the column depth of material the beam must traverse to reach an electron density of 10^{14} cm^{-3} ; which in the VAL-E model represents the very bottom of the atmosphere. The column depth, in units cm^{-2} , can be found by multiplying the height by the density encountered. As the density is a function of height it is straightforward to integrate to find the total column depth traversed by a beam to reach a given density. Equation 5.1 depends on the ionisation state and is assumed to be constant throughout the atmosphere. It could be argued that a more thorough analysis should use the form of Equation 5.1 for a varying ionisation level with height, yet for our purposes of demonstration here the effect this would have on the heating rate is minimal and we use a constant case for simplicity.

As we did not have consistent RHESSI HXR spectra for all events we are limited to the beam parameters derived for Event (b) by Milligan & Dennis (2009). Since the flare is of a similar GOES class to the rest of the events the beam parameters should be reasonably representative of a medium sized flare, and certainly in comparing them to those found for the June 5th 2007 flare in Section 3.5 they differ very little. A beam flux, cut off energy, and spectral index of $F_p = 5 \times 10^{10} \text{ ergs cm}^{-2} \text{ s}^{-1}$, $E_c = 13 \pm 2 \text{ keV}$, and $\delta = 7.6 \pm 0.7$ are given.

The heating rate as a function of electron density reached by the heating, or depth in the model atmosphere, is shown in Figure 5.9. As found in Section 3.6.4 we find a heating rate per particle at an electron density of 10^{11} cm^{-3} of $Q \sim 10^{-6} \text{ ergs s}^{-1}$, greater than any radiative or conductive losses at this height. However, if we move to densities greater than this the heating rate drops rapidly. If we take the $x = 0$ case — as the atmosphere is mostly un-ionised beyond these depths — for a density of 10^{13} cm^{-3} the estimated heating rate is only $4 \times 10^{-11} \text{ ergs s}^{-1}$ per particle, or approximately 25 eV. The electron beam energy is mostly lost through collisions with other electrons, followed by the ionisation of neutral hydrogen, therefore it is the ambient electrons that gain 25 eV per electron. While an electron with 25 eV is sufficient to ionise hydrogen collisionally, it is much smaller than the energy required to excite the observed O v 192Å

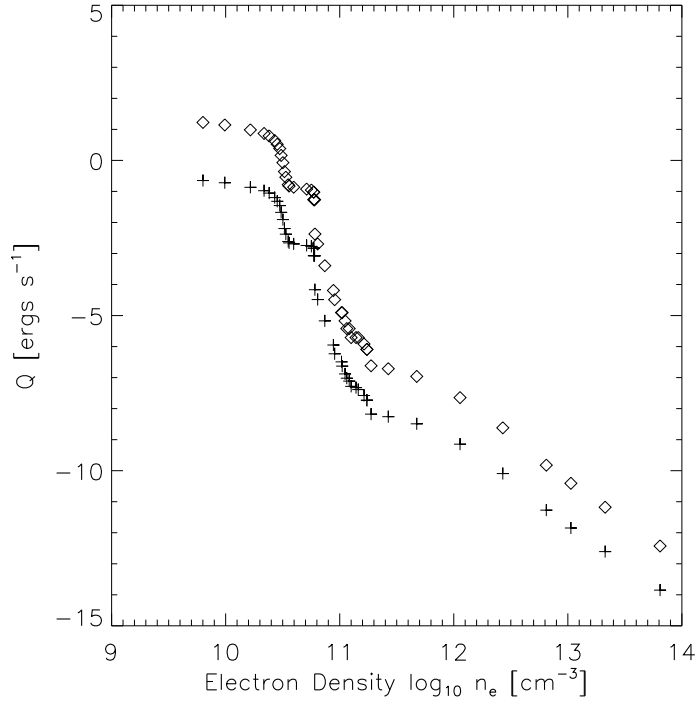


Figure 5.9: Particle beam heating rate for the VAL-E atmosphere. Q is calculated for a column depth of material traversed to reach the given density and with ionisation fractions of $x = 0$ and $x = 1.0$ marked by diamonds and crosses respectively.

transition (64.5 eV). However, we know there will always be some fraction of the local Maxwellian plasma distribution capable of exciting this transition. If the 25 eV per electron results in a thermal distribution where $T \sim E/k$, this roughly corresponds to a peak temperature of 290,000 K, where approximately 17% of electrons in the Maxwellian tail will have an energy above 64.5 eV (Fletcher et al. 2013).

The radiative loss rate per particle, calculated for $n_e = 10^{13} \text{ cm}^{-3}$ in the same manner as Section 3.6.4, is $F_R \sim 10^{-8} \text{ ergs s}^{-1}$ or $F_R \sim 6 \text{ keV}$. Compared to the beam energy the radiative losses are several orders of magnitude larger at this depth. If this is true any energy gained by the plasma will quickly be lost via radiation while not raising the ambient temperature. Clearly heating of this nature can not explain our observations alone and we need either to suggest an alternative model, such as

including plasma dynamics which may be able to create high density regions across evaporation fronts, or reconsider how we arrive at such high densities.

In the case of the more extreme footpoints of Event (b) and (e), should the implied densities not be physical, what other scenarios could cause such a large disparity between the line strengths? Allowing for unknown blends in the 248Å line does not necessarily help us as this would only decrease the O v contribution and increase the ratio. To bring down the ratio in Event (a) FP(b) to give $n_e \sim 10^{14} \text{ cm}^{-3}$ requires reducing the 192Å intensity by around 50%, and even from a cursory examination of Figure 5.3 it is clear that problems in the fitting can not be entirely responsible.

5.5.2 Testing for Ionisation Equilibrium

One possible explanation for the high intensities of the 192Å line could be that the assumption of ionisation equilibrium is invalid. In optically thin conditions the rate of ionisation is balanced by an equal recombination rate, both of these are assumed to be slower than the electron collision rate. This allows ionisation and recombination processes to be treated independently from the thermal collisional excitation and radiative decay that gives rise to our observed spectral lines. Should the plasma temperature be changed more quickly than the ionisation state can equilibrate, the plasma will remain in an ionisation state which is not representative of its true temperature. An example can be seen in Figure 5 of Bradshaw (2009), where during rapid plasma heating the peak formation temperature of a given ion may move significantly from its equilibrium position to a higher temperature. If it is the case in our events, this will alter our diagnostics. In Section 4.5.3 we argued that at high densities this effect should be minimal based on the Bradshaw (2009) calculations. However, should the assumption not be valid, we have quantitatively considered the influence of moving the peak ionisation temperature on the derived densities.

The CHIANTI routine `EMISS_CALC` finds the line emissivities emitted by an ion for a given temperature and density. By specifying temperatures away from the equilibrium T_{max} the dependence of temperature on the I_{192}/I_{248} ratio can be investigated. Plotted

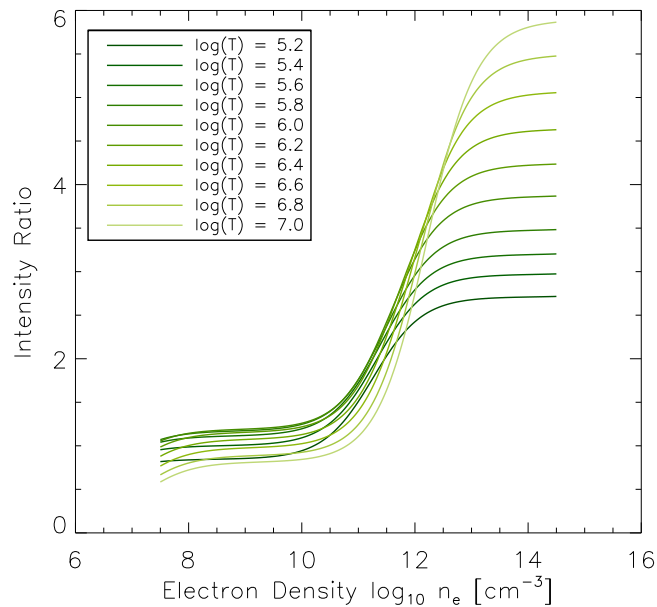


Figure 5.10: I_{192}/I_{248} ratios as calculated by CHIANTI v7.1 for a wide range of plasma temperatures.

Table 5.4: Footpoint electron densities using the O v diagnostic calculated for a plasma temperature of $\log_{10} T = 6.8$. Again the intensity ratio for the two lines, derived electron density, and upper and lower density limits found via the ratio uncertainties are shown.

| Footpoint | I_{192}/I_{248} | $\log_{10} n_e$ (cm^{-3}) | $+\delta n_e$ | $-\delta n_e$ |
|--------------------------------|-------------------|--------------------------------------|---------------|---------------|
| Event (a) 14-Dec-07 $_{FP(a)}$ | 3.59 ± 0.64 | 12.25 | 12.98 | 11.98 |
| Event (a) 14-Dec-07 $_{FP(b)}$ | 6.45 ± 1.12 | 14.10 | 14.50 | 13.73 |
| Event (b) 14-Dec-07 | 2.68 ± 0.39 | 11.85 | 12.10 | 11.64 |
| Event (e) 16-Dec-07 | 4.58 ± 0.72 | 12.69 | 13.63 | 12.35 |
| Event (f) 22-May-07 | 1.89 ± 0.27 | 11.51 | 11.66 | 11.35 |

in Figure 5.10 are the diagnostic curves at intervals between $\log T = 5.2 - 7.0$ where for densities above 10^{12} cm^{-3} the deviation from the equilibrium case is clear.

Through the EMDs derived in Chapter 4 (Figure 5.4) we found that for most events a significant portion of the footpoint plasma is emitting near $\log T = 6.8$. If for the sake of argument we assume our dense plasma is emitting at this temperature we can recalculate a new set of footpoint densities using the new ratio for $\log T = 6.8$. The results are found in Table 5.4. As expected some of the more extreme ratios (Event (a)) now correspond to lower densities while those originally around 10^{12} cm^{-3} are relatively unchanged. Although the density in Event (a) FP_b still remains very high ($> 10^{14} \text{ cm}^{-3}$) it is at least now within the bounds of the diagnostic curve.

So what does this tell us? Firstly, should the atomic physics behind these diagnostics be trustworthy, densities of at least 10^{14} cm^{-3} can be present in heated footpoint plasma even up to a temperature of $\log T = 6.8$. If the plasma is indeed out of ionisation equilibrium the temperature of peak formation needs to be known before the true density can be found; although for ratios as high as ~ 6 the density must be at least 10^{14} cm^{-3} since we cannot push the curve in Figure 5.10 higher without assuming unrealistically high footpoint temperatures.

In principle these curves could be used to pin down the formation temperature of O v if the density was known independently of these diagnostics. However, other methods to obtain the density, for example by combining the EM with a volume estimate, require knowledge of the temperature to choose the correct $EM(T)$ — unless the plasma is assumed to be isothermal. One could of course invoke the use of a model but it would sidestep from the original motivation of the thesis, whereby we wish to discover as much as possible about the plasma via diagnostics before interpreting using models.

5.5.3 Electron-Ion Equilibration Time

Is it possible for the plasma to reach an out-of-equilibrium state in a different manner? Due to the much greater mass of the ion or neutral atom (predominantly hydrogen in the solar atmosphere) the energy exchange from the electron beam to thermal ions is far less efficient than for electron-electron collisions. If we recall that our diagnostics

reveal only the *electron* density of the plasma, electron beam heating could in principle provide enough energy to quickly bring only the electrons at a depth corresponding to $\log n_e = 13$ up to 250,000 K, and thus showing up in the diagnostic, while the temperature of the ions and neutrals lags behind. If so, the beam energy required to initially heat the only electrons at these depths is less than for the entire plasma, which may help to explain the high densities observed.

The difference in collision time scales between the electrons and ions can help illustrate this. The early work by [Spitzer \(1940\)](#) and [Spitzer \(1962\)](#) (summarised in [Somov \(2006\)](#)) calculated collision times including thermal particle motions for electron-electron, ion-ion, and electron-ion interactions. For electron-electron collisions we have

$$\tau_{ee} = \frac{m_e^2 (3k_b T_e / m_e)^{\frac{3}{2}}}{\pi e_e^4 n_e (8\Lambda_{ee})} \frac{1}{0.714} \text{ s} \quad (5.2)$$

where m_e , n_e , and e_e are the electron mass, density, and charge in *cgs* units. T_e is the electron temperature in K and Λ_{ee} is the Coulomb logarithm for electron-electron collisions. The same expression holds for ion-ion collisions if the electron specific parameters are replaced with those for the relevant ion. For a fully ionised hydrogen plasma in equilibrium the ion-ion collision time scale is around a factor of 40 longer than for electrons. More relevantly, the time for the electron and ion temperatures to reach equilibrium can also be given by

$$\tau_{ei} = \frac{m_e m_i [(3k_b (T_e / m_e + T_i / m_i))^{\frac{3}{2}}]}{e_e^2 e_i^2 n_e \sqrt{6\pi} (8\Lambda_{ii})} \text{ s} \quad (5.3)$$

which is again longer than for the equivalent ion-ion time. For our case of a plasma with an electron temperature of 2.5×10^5 K, ion temperature 10^4 K, and density $\log n_e = 13$ the equilibrium time is $\tau_{ei} = 4 \times 10^{-4}$ s. With an impulsive phase duration on the order of 100 – 200 s an equilibrium time of less than a second is unlikely to produce a significant effect on data from a 7 s exposure time. Increasing the electron

temperature to 8 MK as in the previous section increases τ_{ei} to ~ 0.1 s, and only by reducing the electron density (as was discussed in Section 4.5.3) to $\log n_e = 11$ does τ_{ei} become greater than 5 seconds. We can conclude that such a scenario would be unlikely to occur at these densities as the ions will also heat quickly.

5.5.4 Testing for Optical Depth Effects

Since the footpoint plasma appears to be in ionisation equilibrium, or at least exhibits high densities even in an out-of-equilibrium situation, there is one more avenue to explore that may influence the diagnostic ratio. At high densities and low temperatures in the chromosphere the mean free path of a photon is shorter than in the corona and radiation from a transition may be scattered, absorbed and re-emitted. Should the optical depth in either O v line be high the resulting intensity ratio and inferred densities will change. The optical depth of a given transition at line centre can be checked via the expression found in the detailed resource by [Mitchell & Zemansky \(1961\)](#) and later re-expressed by others ([Bloomfield et al. 2002](#)) in the form

$$\tau_0 = 1.16 \times 10^{-14} \lambda f_{ij} \sqrt{\frac{M}{T}} n_i h \quad (5.4)$$

where λ is the line wavelength in angstroms, f_{ij} the oscillator strength of the transition, h the region thickness, and M is the mass of the ion. T is the electron temperature and is assumed to be equal to the ion temperature.

The oscillator strength represents the probability of an ion to absorb or emit a photon compared to a single electron in a theoretical harmonic oscillator. A high f_{ij} is more likely to produce an optically thick line in high density conditions because of the ion's ability to absorb nearby photons. For our diagnostic $f_{192} = 0.538$ and $f_{248} = 0.0172$. The number density of ions in the lower level of the transition, n_i , can be evaluated if expanded into the quantities

$$n_i = \frac{n_i}{n_{ion}} \frac{n_{ion}}{n_{el}} \frac{n_{el}}{n_H} \frac{n_H}{N_e} N_e. \quad (5.5)$$

Many of these ratios are familiar and have been used before and we refer the reader

to Section 2.1 for further details. The term n_i/n_{ion} is the relative population of ions in the lower level to all other levels in the ion. Fortunately this is available from CHIANTI and can be obtained as a function of electron density. At $\log n_e = 13$ we have relative populations of 0.38 and 2.9×10^{-5} for the lower levels of the 192Å and 248Å transitions respectively. Here the metastable lower level for 192Å makes itself apparent by giving rise to the high population density in contrast to the allowed 248Å transition from an excited lower level. n_{ion}/n_{el} is the relative ion to element number density given by the CHIANTI ion equilibrium file, and is 0.61 at the equilibrium T_{max} , and n_{el}/n_H is the elemental abundance for Oxygen which is $10^{-3.11}$ for coronal abundances.

We wish to find τ_0 for a chosen depth in the atmosphere. As the temperature and density are functions of the depth, we must evaluate Equation 5.4 as an integral from emitting depth z to the surface. If the elemental abundances and ion to element abundances are assumed constant throughout the atmosphere then we have

$$\tau_0(z) = 1.16 \times 10^{-14} \lambda f_{ij} M^{\frac{1}{2}} \left(\frac{n_{ion}}{n_{el}} \right) \left(\frac{n_{el}}{n_H} \right) \int_z^{z=0} T^{-\frac{1}{2}} n_H \left(\frac{n_i}{n_{ion}} \right) dh \quad (5.6)$$

where n_H and T are functions of height, and the relative level population n_i/n_{ion} is a function of electron density, and therefore height. By dividing the atmosphere into discrete slices of $\Delta h = 1$ km we can use the VAL-E model to evaluate the integral over a specified depth z . To do this the model parameters were first interpolated onto a 1 km height grid with $d\tau_0$ found for each slice of the atmosphere. The optical depth for a line emitted at say 2000 km is then the total of $d\tau_0$ from 2000 km to 0 km.

Figure 5.11 shows the optical depth (black line) as a function of depth in the VAL-E model for the 192Å line, where a depth of 2500 km represents the bottom of atmosphere. Alarming, the optical depth for this line rises rapidly with increasing depth in the atmosphere. The VAL-E density at each depth is plotted in the dotted line for reference, and if we find where $\log n_e = 13$, the optical depth is over $\log \tau_0 = 7$. In fact, even at $\log n_e = 10.5$ the optical depth is still ~ 1 . The 248Å transition by comparison (red dashed line) is a good example of an optically thin line, only markedly increasing in optical depth in the last 250 km of the atmosphere, and if the same alterations to the

model are used the optical depth is negligible.

The interplay of the parameters in Equation 5.6 is complex due to the dependencies on electron density, level population, and ionisation fraction. Obviously the high oscillator strength of the 192Å transition and significant level population are partly responsible for the high optical depth, but the chosen active region VAL-E model is not an ideal model for a flare footpoint. For example, the maximum temperature is just under 1 MK yet we have observed significant emission at nearly 10 MK.

VAL-E is however a useful model of the density profile in the lower atmosphere. To better represent a flare atmosphere we have imposed a constant temperature of $\log T = 6.8$ throughout the model and recalculated the optical depth, shown by the orange curve on Figure 5.11. The optical depth now drops to $\tau_0 = 1$ at just below $\log n_e = 11$ but is still high at lower depths. If we further suggest that the flaring atmosphere should be fully ionised, either through collisions from the beam electrons or through heating, the optical depth drops again (green line), this time to more manageable levels with $\tau_0 < 10$ for depths above 2000 km. While this is not a comprehensive approach to modelling the flaring atmosphere, it does serve to demonstrate a lower limit to the optical depth for 192Å. Whereby if the density is below around $\log n_e = 12$ then $\tau_0 < 10$.

What effect will high opacity have on line fluxes and the density diagnostic? Consider that the probability of a photon reaching an observer without scattering out of the line of sight is proportional to the optical depth. Known in many treatments as the escape factor, P_{ij} , it couples with the transition probability to reduce the observed intensity in the form $I_{ij} \propto A_{ij}P_{ij}$, so as $\tau \rightarrow \infty$, as for optically thick lines, $P \rightarrow 0$ and the intensity is attenuated. Should one side of the diagnostic pair be optically thick, the diagnostic can be expected to change accordingly to the reduced intensity.

There have been several discussion of the passage of photons through a field of absorbing ions in literature, beginning as early as Holstein (1947), with the escape factor defined in Irons (1979), then more carefully discussed including the distinction of escape in the direction of the observer in Kastner & Kastner (1990). These contain lengthy derivations, each depending on the profile of the emitting spectral line, which shall not be repeated here but we can show the form of one used in Mathioudakis et al. (1999)

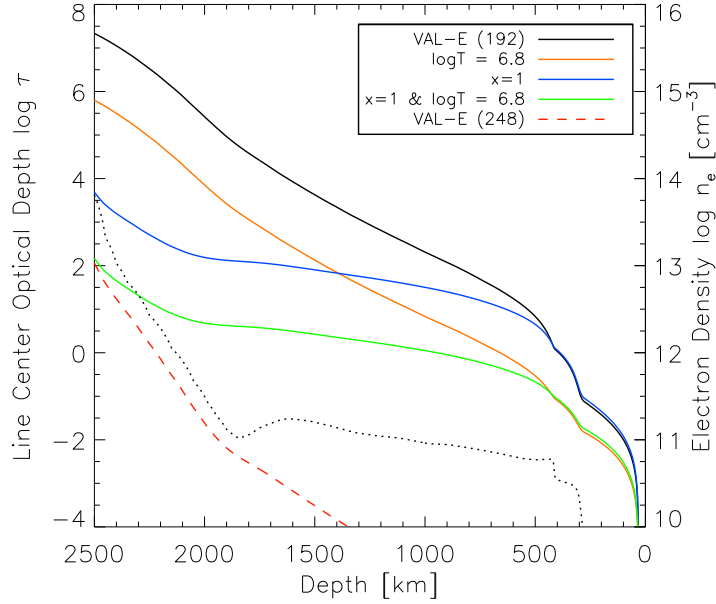


Figure 5.11: Optical depth for the 192Å transition calculated as a function of depth in the VAL-E model (solid line). Electron density at the corresponding height is plotted for reference in the dotted line. Optical depth in the VAL-E model for the 248Å transition is shown by the dashed red line.

and [Bloomfield et al. \(2002\)](#) giving the escape factor for a homogeneous distribution of emitters and absorbers as

$$P(\tau_0) = \frac{1}{\tau_0 \sqrt{\pi}} \int_{-\infty}^{\infty} [1 - \exp(-\tau_0 e^{-x^2})] dx, \quad (5.7)$$

where $x = (\nu - \nu_0/\sigma)$ describes the Doppler line profile for a half width σ . The integral is not simple to solve but thankfully the results for a range of τ_0 are tabulated in [Kastner & Kastner \(1990\)](#). Using $\tau_0 = 0.1, 1, 10, 100$ we have $P_{192} = 0.96, 0.72, 0.19, 0.025$; so even by an apparent optical depth of 1 the intensity is already being reduced by 28% (although this is nearly comparable with measured intensity uncertainties of 10%) and at $\tau = 0.1$ the reduction is lower still.

We find that for the 192Å line $\tau_0 \sim 10$ at a density of $\log n_e = 12$. According to

these calculations the apparent line intensity will be reduced by $\sim 81\%$, the number of emitted photons by the density sensitive transition should then be 81% higher in the source. Since $P_{248} \sim 1$ the 192/248Å ratio is increased by this amount which does not help explain away the high densities! Also, the fact that the model predicts such a high optical depth at moderate densities is questionable. One possible explanation may lie in the depth of atmosphere integrated in the model to reach these high densities. The calculation used to create Figure 5.11 assumes a plane-parallel atmosphere where emission from low depths must shine through the entire atmosphere above. This is a strong assumption given the fine structure observed in the chromosphere and transition region. It is possible that material at low heights may be seen emitting from the base of magnetic structures with little coronal material along the line-of-sight. It may also be incorrect to assume that the high densities are not to be found higher up in the atmosphere. If the $\log n_e > 13$ plasma was found at 2000 km (see Figure 5.7) then the optical depth should drop significantly. A similar calculation should be performed with a flaring model atmosphere in future.

We note also that the 192Å line is well observed, and that the line widths are not suggestive of any excess opacity broadening (Milligan 2011), nor of a self-reversal which is observed in some optically thick lines under certain circumstances. The optical depth of a transition line varies across its profile as a function of wavelength. If the line centre is strongly attenuated then a self-reversal is expected in the profile where the centre is absorbed more than in the wings.

As we saw earlier in this chapter, different transitions are affected by opacity to varying degrees depending on their respective energy levels and oscillator strength. Optical depth effects are perhaps best demonstrated in observations from the chromosphere and photosphere. Using the SOHO Solar Ultraviolet Measurements of Emitted Radiation (SUMER) instrument (Wilhelm et al. 1995) Warren et al. (1998) found that the Ly α to Ly ϵ lines are self-reversed, while Lyman transitions from lower energy levels are flat topped. Later SUMER observations by Tian et al. (2009) found no self-reversal in the profiles of the Lyman lines in sunspots and in sunspot plumes. The plage regions did however display reversals — as routinely seen in the quiet-sun. The magnetic field

configuration of these regions plays a strong role in determining the depth of absorbing hydrogen in the line-of-sight and therefore the profile of spectral lines. A more extended transition region with a lower optical depth was used to explain the lack of a reversal in sunspot measurements. A similar picture may be true in our footpoints where the field is assumed to be aligned vertically and less tightly confined than in the plage regions.

The escape factor in our earlier interpretation only considers the probability of seeing an uninterrupted photon from the source and not what effect the absorbed photons have on neighbouring ions. In [Jordan \(1967\)](#) a situation was devised to help explain the unexpectedly large intensity ratio of two C I lines at 1657.4Å and 1993.6Å in solar limb observations. Using the same equation for τ_0 as above Jordan goes on to find 1657Å is optically thick, whilst 1993Å is optically thin. Both of these lines originate from a shared upper level which may decay to a number of lower levels. However, because 1657Å has a high opacity there is a probability of re-absorption of the photon, repopulating the upper level. It was suggested that the optically thin line will be enhanced by the increased upper population as it will be freely emitted by the increased population while the optically thick transition will continue to be re-absorbed.

It is thought-provoking material but the transitions in our diagnostic share no common energy level so a direct comparison with [Jordan \(1967\)](#) is not possible. Plus, it would not appear to help explain the apparent enhancement of the optically *thick* 192Å transition in our diagnostic. What it does demonstrate is the complexity of individual ions and that processes may exist in the O v ion which lead to the enhancement of the 192Å through photon absorption; the metastable lower level may play a part in this as it already holds a high population density. Further investigation into the behaviour of O v at high opacities will require level-by-level calculations of excitation and de-excitation rates. Extracting this information from CHIANTI is in principle possible but the time is not available to pursue such a large project here and will be left until a later date.

What we have learned is that opacity will play some role in the Oxygen diagnostic,

perhaps most significantly between densities above $\log n_e = 12.5$, where the attenuation becomes comparable to the uncertainties in intensity. We have shown the measurement of optical depth is very sensitive to the assumed atmospheric parameters and shows the VAL-E model is not entirely suitable for this purpose. A new model or a different technique will be required before we can definitively say if opacity is affecting the diagnostic. Adopting a method involving the ratio of lines such as in later sections of [Jordan \(1967\)](#), [Bloomfield et al. \(2002\)](#), and [He & Zhang \(2013\)](#) may avoid the need to prescribe model parameters by having some atmospheric parameters cancel, and could be performed given suitable observations.

5.6 Discussion

We are left in this chapter with a somewhat inconclusive result. The diagnostic after careful fitting returns apparent densities of over 10^{14} cm^{-3} at the O v formation temperature, yet under a thick-target approximation it is difficult to heat plasma to the appropriate temperature at this density. The collisional heating rate is below $10^{-10} \text{ ergs s}^{-1}$ per particle at densities above $\log n_e = 12$ which is lower than any radiative or conductive loss rates by several orders of magnitude.

We ruled out the possibility of non-equilibrium situation between ion and electron temperatures by finding that the time scale for equilibrium is far shorter than the flare impulsive phase. Increasing the plasma temperature from the equilibrium $2.5 \times 10^5 \text{ K}$ altered the theoretical density diagnostic ratio, and densities prescribed by the observed ratios could be reduced. The newly calculated ratios brought the densities down in the highest density flares by less than 2 orders of magnitude, leaving 2 footpoints still with high densities of $\log n_e = 12.7$ and 14.1 . Accounting for opacity effects showed that the optical depth could indeed be a problem for the 192\AA transition for densities above $\log n_e = 12$. However, we do not entirely trust this result using the model prescribed, as it predicts that the line will be almost completely attenuated. In either case optical depth effects serve to reduce the intensity of the 192\AA line which does not help to reduce the observed density. This interpretation of the effect of optical depth on these

line strengths may however not be accurate, and a more in depth study of the ion transitions will be required in future.

The results leave us with a number of situations giving rise to such high densities, each with their own implications:

1) If ionisation equilibrium is a sound assumption, then by following the interpretation in Chapter 3, plasma at very low pre-flare temperatures ($\sim 10,000$ K) deep in the atmosphere is raised to around $250,000$ K. A simple collisional thick-target model cannot deposit enough energy into the atmosphere at these depths to do this. Either a model which can directly heat plasma further into the atmosphere must be considered, or it implies the plasma is heated indirectly — i.e via conduction.

2) The emitting plasma did not necessarily originate from depths where the density is high and could be a moving pressure front created from the evaporation dynamics such as in Fisher et al. (1985) and Allred et al. (2005). This appears to possible in the Allred models as a low temperature, high density, bump appears in the flare atmosphere, although this is found at $\log n_e = 13$ in the F10 model, or quickly mixed with plasma at much hotter temperatures in the F11 model.

3) If ionisation equilibrium is not a valid assumption, and the peak formation temperature of O v has moved to ~ 8 MK, then we have plasma at slightly lower densities for most events ($10^{12-14} \text{ cm}^{-3}$) but which is extremely hot. This raises questions about the observation of a hot slab cooling via conduction, as found in Chapter 4, where the EUV emission originates from plasma which is heated via conduction from the hot plasma above. If the density of the slab itself is very high, are the densities in the conducting region yet higher? If there is no evaporation front, as assumed in the conduction model, then it still places the directly heated flare plasma very low in the atmosphere.

4) Some combination of all these factors is also likely. Unfortunately for us the more processes adjusting the apparent densities or temperatures, the more difficult it becomes to distinguish one from the other. To add to this we observe the whole event through a single line of sight, multiple components of plasma may be superimposed within one diagnostic.

5) Finally, the diagnostic itself may be influenced by an optical depth effect in the 192Å transition which *increases* its intensity as seen in [Jordan \(1967\)](#), although this is merely speculation at this stage and requires further analysis.

5.7 Conclusion

If the observation of heated footpoint plasma at low chromospheric heights (high densities) is true then it places new challenges on the models to explain this observation for small flares and attempting to find the location of this material within the atmosphere is extremely important. We have made the necessary observations using EIS in this chapter and discussed the validity of the result. It remains to further concentrate efforts on modelling these densities and understanding the effects of opacity on the diagnostic.

Lastly, it shows that there is much to learn from this type of analysis, and limiting flare diagnostics to mostly ‘coronal’ temperatures is an unnecessary restriction which hopefully new EIS rasters or new instruments will improve upon. The Interface Region Imaging Spectrograph (IRIS), a NASA Small Explorer (SMEX) mission successfully launched on June 27th 2013, is the latest spectroscopic solar observatory which will observe the transition region at unprecedented spectral, spatial, and temporal resolution, including the O IV and Si IV diagnostic lines at 1401Å. These lines are in exactly the temperature range we require and form density diagnostics which are well understood. The opportunities for flare science that can be attempted with this instrument are extremely exciting and observations have already begun. Data is expected to become available in the coming months and the logistics for flare campaigns are yet to be announced.

Chapter 6

Determining Density and Temperature Profiles Through $\xi(T)$ and $\zeta(n)$

Throughout the analysis in this thesis we have found ourselves repeatedly turning to a model of the density and temperature in the flaring atmosphere to help us explain our observations, namely the VAL-E ([Vernazza et al. 1981](#)) or [Allred et al. \(2005\)](#) models (Figures 5.7 and 5.8). While these models are intricately detailed, they may not necessarily represent the conditions present in every flare. What we propose here is a method to *fine tune* a simple model of the density and temperature dependence with height based on the previously obtained differential emission measures (DEMs) and density sensitive line intensities.

The idea for the work in this chapter came through a reading of [Brown et al. \(1991\)](#), where the authors presented a generalised form of the differential emission measure, not only as a function of temperature but also as a function of the plasma density. By making some simple assumptions about the emitting plasma, it was shown that both DEMs in temperature and density could be related via the density-temperature gradient $|dn/dT|$ of the plasma. The technique appeared to be the key to relating our density diagnostic and DEM(T) results, while shedding more light on the structure of

the footpoint region. If the relation of the plasma density with temperature, $n(T)$, could be extracted, then perhaps models of the underlying height profiles of density and temperature could be implied from observation.

We showed in Chapter 4, that for a careful selection of emission lines the DEM(T) could be found for footpoints. It is suggested in Brown et al. (1991) that through the use of intensities derived from emission lines strongly sensitive to density, such as the forbidden or inter-combination lines used in Chapter 3, that the relation $n(T)$ may be determined. The authors tested whether the observable line intensities were sensitive to the choice of $n(T)$ by using a parameterised empirical model, finding that some model parameters could indeed be recovered. Our aim here was to further test this using measured DEMs in temperature from EIS, combined with the density sensitive line intensities available in the Cambridge rasters. In our method we forward fit parameterised atmospheric models, using a genetic algorithm, to gather information about the temperature and density profiles as a function of height in the atmosphere. Through the isolated use of DEMs in temperature or density, diagnostics of these functions are never truly possible without *a priori* assumptions, due to the bivariate nature of the contribution functions. In this analysis, however, we hope to pin down the temperature and density simultaneously to gain information about the vertical structure of the plasma. We begin by describing the problem and a forward fitting method to recover $n(T)$.

6.1 A Differential Emission Measure in Density - Defining the Problem

Section 2.3 detailed the generalised form of the DEM(T) problem in temperature by defining the integral of emission within a volume as an integral over surfaces of temperature. The atomic physics within the contribution function, $G(n_e, T)$ is dependent on density, and we know from earlier work that an $n(T)$ relation clearly exists within the footpoint plasma, but the choice of lines could be restricted to those with minimal

density sensitivity in order to recover $\xi(T)$ independently of density. We discussed the choice of such lines in Section 4.2.1

In a similar manner the DEM can be defined in density, $\zeta(n)$, and recovered using only density-sensitive line intensities. These lines are assumed to be emitted at a known temperature, corresponding to the ion's temperature of peak formation, T_o , therefore their contribution functions can be fixed in temperature and become a function of only density $G(n, T_o)$. [Almleaky et al. \(1989\)](#) described how the DEM problem can be cast in terms of density, and through the use of pairs of density-sensitive line strengths, be used to obtain information about the density inhomogeneity of the plasma via an inversion method. In principle, if enough intensities are specified across the density range, the degree of inhomogeneity can be determined through an inversion in the same way as before to determine $\zeta(n)$. However, this method is not commonly used in isolation, as the functions of $G(n)$ are not as sharply defined as in the temperature case, and combined with few observed diagnostic lines in most studies the inversion becomes inherently more unstable. The approach used in this chapter avoids tackling this inversion head on by taking advantage of the density information available in these lines, and combining it with what we have already learned from the DEM in temperature. The problem will now be defined.

As shown in [Brown et al. \(1991\)](#) and Equation 2.20 the intensity integral in the case of a fixed density is given by

$$I_{\alpha}^T = \int_T G(T)\xi(T)dT, \quad (6.1)$$

where I_{α}^T denotes the set of α temperature-sensitive lines, $G(T)$ is chosen for a single density, while the DEM in temperature is defined by

$$\xi(T) = \sum_{i=1}^N \left(\int_{S_T} n^2(\mathbf{r})|\nabla T|^{-1}dS \right)_i. \quad (6.2)$$

Likewise, the same problem can be posed as a function of plasma density by integrating the volume over surfaces of constant density. The integral then becomes

$$I_{\alpha}^D = \int_n G(n, T_o) \zeta(n) dn, \quad (6.3)$$

where I_{α}^D now applies to a set of strongly density-sensitive lines for a known formation temperature T_o . The DEM in density is defined by

$$\zeta(n) = \sum_{i=1}^N \left(\int_{S_n} n^2(\mathbf{r}) |\nabla n|^{-1} dS \right)_i, \quad (6.4)$$

which now describes the amount of emission from a plasma of density n . We can relate both DEMs by making some simple assumptions. First, the sums over disjoint surfaces may be ignored, and the surfaces within the integrals can be assumed to be constant as our observed footpoint size is comparable to the EIS spatial resolution — i.e. the shape of each surface of constant density within a single pixel is unresolvable. We can further assume that the density and temperature gradients within the footpoint atmosphere are aligned along the gravitational axis and that the loop magnetic field is locally vertical, meaning surfaces of density and temperature will coincide at the same height and not intersect each other. This leaves us with the expression

$$\xi(T) = \zeta(n) \frac{|\nabla n|}{|\nabla T|} = \zeta(n) \left| \frac{dn}{dT} \right|, \quad (6.5)$$

that can be then inserted into Equation 6.3 to give

$$I_{\alpha}^D = \int_n G^D(n(T), T) \xi(T) dT. \quad (6.6)$$

What we have here is extremely useful because it links the observables $\xi(T)$ and I_{α}^D via the density temperature structure, $n(T)$, of the atmosphere. To find I_{α}^D , the contribution function must now be evaluated at a density specified by $n(T_o)$ for the line's formation temperature. If $\xi(T)$ is obtained from data, along with a number of density sensitive line intensities, then $n(T)$ is the only unknown and can in theory be found.

6.2 Finding $n(T)$

The problem of determining $n(T)$ from observations of $\xi(T)$ and I_α^D using Equation 6.6 is another example of an integral inversion, and has a similar form to the temperature DEM inversion from earlier. Finding a suitable solution for $n(T)$ thus depends on the inversion technique and on the uncertainties in the data supplied by I_α^D and $\xi(T)$. It was decided that inverting Equation 6.6 using the regularised inversion method for finding $\xi(T)$ would be impractical for a number of reasons. First, the data to obtain $\xi(T)$ has already been inverted once, and the solution will have accumulated additional uncertainties. By inverting again, we can not be guaranteed of the uniqueness of the solution for $n(T)$. Secondly, as $n(T)$ resides within the contribution function, the inversion will return a $G(T)$ function which fits the line intensity, but the density that leads to that function will still have to be obtained; for example, from a lookup table of $G(T)$ functions created from CHIANTI. With this in mind, a forward fitting approach was chosen as the most suitable.

We propose an outline for the method here, while details of the computational method are shown in the next section. As we wish to find out the height profiles of the plasma, we start from model functions of $n(z)$ and $T(z)$, where z is the height above the photosphere. The function $n(T)$ can then be obtained either analytically, if possible, or by plotting $n(z)$ and $T(z)$ against each other if the height axes are identical. For each emission line, the function $G(n(T), T)$ within the integral is then evaluated for a model density from $n(T)$ corresponding to the line's temperature of formation T_o . The DEM in temperature $\xi(T)$ is already known from the prior observations, so it is straightforward to multiply by the calculated contribution function to find the model line intensity. By using an iterative method, in our case a genetic algorithm, the model parameters can then be varied to minimise the difference between the model and observed line intensities and thus find the best fitting model to the data. The basic idea is relatively simple, yet understanding the effects uncertainties in the data have on the fitting, and testing of the robustness of the method, will be the crux of this technique.

6.3 Forward Fitting with PIKAIA - A Genetic Algorithm

A breakdown of the code we have used to find $n(z)$ and $T(z)$ is as follows:

1. Create parameterised models for $n(z)$ and $T(z)$
2. Recover $\xi(T)$ from inversion of footpoint data
3. Find a number of density sensitive line intensities I^D
4. Create a function $n(T)$ from a set of model parameters
5. Calculate $G(n(T_o), T)$ for each line using the model density at the formation temperature T_o
6. Evaluate Equation 6.6 to find model intensities I^{model}
7. Find the residuals $I^D - I^{model}$
8. Minimise the residuals by adjusting model parameters in Step 4.

In the following sections, each step in the code is discussed in turn including the input observations that can be used. For now we jump to Step 8. and explain how a *Genetic Algorithm* (GA) can help us fit our model and how to go about it. While introducing the inversion method for $\xi(T)$ in Section 4.4, we briefly discussed the merits and problems in using forward fitting techniques versus direct inversion, and argued that the *a priori* assumptions used in forward fitting were restrictive to return a non-biased $\xi(T)$. In the situation in this chapter such an inversion was not appropriate, and we opted for a forward fitting approach, but one which allows for some ‘intelligence’ in the parameter search. In most numerical methods, such as Markov chain Monte Carlo, a set of starting trial solutions randomly ‘walk’ through the parameter space, evaluating the residuals between the data and model observables at each step, for example using the χ^2 estimate. The GA is another means of iteratively finding the solution, but differs

from others by making the initial set of trial solutions persistent, in the sense that they make their next step based on the success of the last.

A genetic algorithm approaches the problem of finding the *fittest* solution based on the theory of natural selection (Darwin 1859) by treating the trial solutions as a *population*, each with their own individual genetic code — this step from adaptation within a biological environment to computation was investigated by Holland (1962). By selectively *breeding* the fittest trial solutions the best fit solution can be determined. In the PIKAIA algorithm that we use, each member of the population is represented by a string of integers corresponding to its position in the parameter space. The breeding takes place by taking two random population members, splitting their integer string into two parts at a random point, and swapping one part with the other member. In general, the algorithm follows a series of steps as follows:

1. Create a random population of trial solutions across the parameter space.
2. Evaluate the fitness of the trial solutions, for example, via the χ^2 statistic.
3. Rank the population by fitness, then create a new population by breeding those above a threshold.
4. Evaluate the fitness of the new population.
5. Replace the old population with the newly created one and test the fitness of each member again.
6. If the fitness has not yet reached a prescribed target, then return to Step 3.

By following this, the algorithm breeds only the best solutions in a population, ensuring that the new population is randomised, but keeps only the best solutions. Each iteration of the GA between Step 3 to Step 6 is known as a generation. The number of generations that the GA runs for can be controlled by setting a target fitness, which one of the population must reach, or by setting a maximum number of generations. A large number of generations will take longer computationally, but may

avoid the algorithm ending prematurely if it encounters an extreme fitness which is not a sensible solution. In first the few attempts the user can use this to check how the fitness is evolving. The advantage of using a GA lies in its robustness to find solutions over parameter space which may have many *local* maxima in addition to the *global* maximum. By evolving the population, it has the robust ability to avoid begin trapped in a local maxima on its way to finding the best global solution.

The fitting in this chapter uses the PIKAIA code written by P. Charbonneau and B. Knapp (Charbonneau 1995) at the High Altitude Observatory in Boulder, CO. and we use a version adapted for IDL by S. McIntosh. The routine has been used successfully by many authors and documentation and further citations can be found in Charbonneau (2013).

6.3.1 Trial Models for $n(h)$ and $n(T)$

Many well established models for the solar atmosphere currently exist, modelling the quiet sun and active regions (VAL-C, VAL-E, Vernazza et al. (1981)), and the atmospheric response to various forms of flare heating (Allred et al. 2005; Klimchuk et al. 2008; Cargill et al. 2012). It would at first seem reasonable to choose of one these as an input to our forward fitting regime. However, whilst these models are now capable of reproducing the observed EUV emission to a high standard, they do not often have an analytical form for the density and temperature profile in height. On these grounds they are too complex to begin testing our method with. If we hope to learn the nuances of our technique, and test if the data really can recover sensible model parameters, we need to start with a simple scenario.

We chose two functions scaled from a height $z = 0 - 10$ Mm that contain the basic characteristics of the solar atmosphere. First, we use an exponentially decreasing form for the density profile, expressed as

$$n(z) = n_o \exp\left(\frac{-z}{H}\right). \quad (6.7)$$

Here, H is an equivalent density scale height which adjusts how quickly the den-

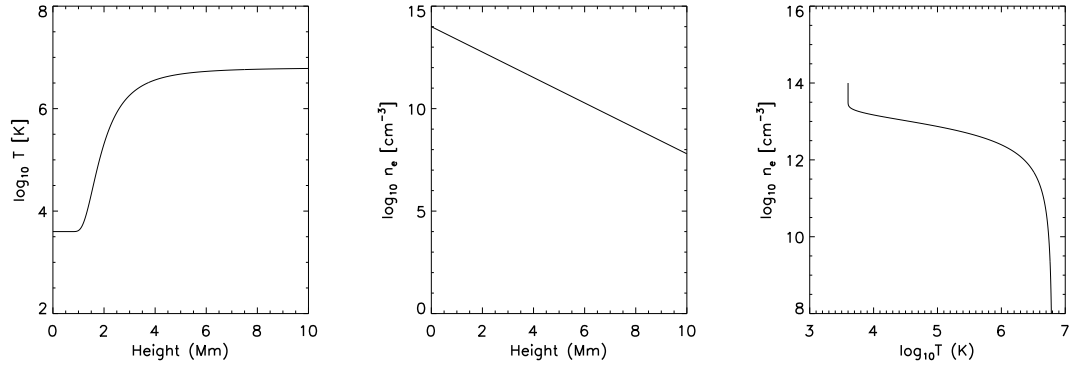


Figure 6.1: Example of $T(z)$, $n(z)$, and $n(T)$ for the test model using model parameters $n_o = 10^{14}$, $H = 0.7$, $\alpha = 5.0$, $\delta = 3.0$, $T_{max} = 6.8$.

sity falls off with height, and n_o is the density at the base of the atmosphere. The temperature function is slightly more complicated and is given by

$$\log_{10} T(z) = T_{base} + (T_{max} - T_{base}) \exp\left(\frac{-\alpha}{z^\delta}\right), \quad (6.8)$$

where T_{base} is lowest temperature, T_{max} is the peak coronal temperature, and α and δ are dimensionless parameters which adjust the height and steepness of the transition region respectively. As shown on the left of Figure 6.1 we have attempted to recreate the temperature profile of the transition region using this expression, including the dramatic temperature rise above the chromosphere. The base temperature, T_{base} , is fixed at the temperature of the photosphere (~ 5700 K) and T_{max} will vary the maximum temperature of the corona, though we may find we can fix this parameter from observations. Parameters α and δ are dimensionless and have no real physical meaning, but we should reinforce that our first intention here is to find out how far the GA needs to push these parameters to find any change in the model intensities.

On the far right hand plot of Figure 6.1 we see the $n(T)$ relation for the two height profiles, obtained by plotting the two vectors of T and n against each other. In Step 5 of our code, the value of density at the line formation temperature T_o is extrapolated to evaluate $G(n(T), T_o)$. We must though restrict ourselves to monotonically increasing or decreasing height functions. The reason for this is that if we have a temperature profile

that rises at low heights, before dropping and then rising again into the corona, the function will have a single temperature defined at two heights. Two density values will therefore map to a single temperature, meaning that $n(T)$ cannot be a singly defined function. An impulsively heated footpoint may develop a similar high temperature ‘bump’ in the transition region very early on in the flare development (see Figure 5.8) which we will not be able to resolve with our technique in its current form. For example, in the Allred et al. (2005) ‘F10’ model, there is a time ~ 70 s into the beam heating when hydrogen and He II have been almost completely ionised at the beam input height. The radiative losses here become insufficient to balance the beam energy input and the atmosphere heats rapidly. Periods like this are thought to be short lived, and the temperature profile returns to a smoothly varying character which can be probed by our method, although much different to the pre-flare case. The $\xi(T)$ that we have chosen to use from Chapter 4 was found to be compatible with an epoch of energy balance, and so restricting our test models to monotonic functions will not necessarily prevent us from learning about the height structure.

Adding a parameterised Gaussian component to the temperature (or density) function with height would allow us to characterise a temperature bump in the test models. However, using line-of-sight, optically-thin emission lines with individual $n(T)$ measurements makes it impossible to directly determine the width of a bump as different densities measured with the same temperature will simply be averaged by a density diagnostic. Likewise, breaking the models into several separate functions will still incur the same problems, as the emission is optically thin. If the technique was to be run with a sufficiently high cadence during the impulsive phase, the appearance of an unusually high temperature at a high densities may correspond to such a temperature bump. Although we could not be certain of the model shape we could at least note time when a smooth model is not applicable. Although an ideal goal, discovering fine structure in the temperature and density functions from this method will be limited by the current diagnostics. Currently we only have a relatively small selection of diagnostics across one order of magnitude in temperature. What we hope to learn is the height of a steep transition region during a flare and if it changes significantly from a

pre-flare model atmosphere. An uncertainty in the height of the transition region can be added to account for any deviations from a smooth model.

6.3.2 Test Event $\xi(T)$ and Line Intensities

To test the forward fitting technique, we have started with data used in the previous two chapters. The EIS data at this time were rich with diagnostic lines and spanned a broad temperature range. Since we require many lines for a DEM(T) inversion, plus those for a density analysis, we are currently unlikely to find a better data set without designing a new study for this purpose. We have chosen the 14th Dec 2007 C1.1 event at 14:13 UT to begin with. The footpoint here was bright and well defined in all lines, while the $\xi(T)$ inversion was reliable and the density diagnostics showed a range of measured densities between $10^{10} - 10^{13} \text{ cm}^{-3}$ (see Section 4.5.5 and Chapter 5).

The integration of Equation 6.6 must be performed over a temperature range common with the contribution function and $\xi(T)$. This requires interpolating both the existing $\xi(T)$, and contribution functions, onto a common temperature grid between $\log_{10} T = 4.0 - 9.0$. Since the temperature grid spacing is linear and the functions are smooth, the exact form of interpolation used is not crucial, and we use the standard IDL INTERPOL routine with a least-squares quadratic fit between data points.

6.3.3 Density-Sensitive Emission Lines

A set of density sensitive line intensities I^D , which cover temperatures from $\log_{10} = 5.4$ to 6.3, can be obtained from the diagnostic pairs used in Chapters 4 and 5. While $\xi(T)$ spans up to 10 MK, there are no density sensitive lines in the raster at this temperature. However, what we have includes an order of magnitude in T at perhaps a depth where the atmosphere is rapidly varying in density and temperature. The high temperature lines observed, while not density sensitive, may be used later to help constrain the high temperature limit of the models. The diagnostic lines, I^D , used in the analysis are shown in Table 6.1. Well-specified uncertainties in the line intensities are also important for determining how responsive the model solutions are to changes

Table 6.1: Density sensitive lines used for forward fitting.

| Ion | Wavelength (\AA) | $\log_{10} T_{\max}$ (K) |
|---------|-----------------------------|--------------------------|
| O v | 192.904 | 5.4 |
| Mg VII | 280.742 | 5.8 |
| Si x | 258.374 | 6.2 |
| Fe XII | 196.640 | 6.2 |
| Fe XIII | 203.797+203.828 | 6.2 |
| Fe XIV | 264.789 | 6.3 |

in I^D . These are found in the same manner as in Section 3.2.1, and for the O v line, as discussed in Section 5.2.

6.3.4 Contribution Functions

Once the model $n(T)$ has been generated, the contribution functions must be found for each corresponding emission line. The purpose of this step is to find the model density $n(T_o)$, specified by the peak formation temperature T_o of each given diagnostic line, before calculating the contribution functions at these densities.

First, we need to find where T_o occurs on the model temperature function $T(z)$. The array index is found by locating the minimum of $|T - T_o|$ — this is accurate to within ± 1 of the height grid spacing. As $T(z)$ and $n(z)$ use the same height grid, $n(T_o)$ can then be read from the same index on the $n(z)$ function, where the density uncertainty is again given by the adjacent grid spacing. Where the density is slowly varying in temperature, the uncertainty in density will be insignificant, but as $n(T)$ steepens, particularly around the ends of the transition region, the error will increase. A high-resolution grid spacing keeps the error to a minimum, and will be used until any issues with computation time arise.

In most cases the method described here is stable but problems occurred if T_o was

greater than the maximum trial model temperature. However, we get around this by demanding that the model parameter T_{max} must always be greater than the hottest diagnostic line temperature, which is true by definition as the line must have been emitted from plasma of at least this temperature.

CHIANTI v7.0 is used to generate the contribution function for the coronal abundances and CHIANTI ionisation equilibrium file used in Chapter 4. The peak value of $G(n, T_o)$ is plotted against density for each line on Figure 6.2, where their sensitivity to density can be seen. As was mentioned in Section 4.2.1, these functions are not as strongly peaked as their $G(T)$ counterpart, and change by less than an order of magnitude over the chosen range. However, given that the observed intensity errors are on the order of only a few percent, adjustments to the test model should still alter the model intensities by enough to be distinguished from the observational errors.

To calculate $G(n, T_o)$, the value $n(T_o)$ was originally passed straight to CHIANTI to calculate the contribution function, but this proved to be extremely slow computationally as the GA must make thousands of iterations. Instead, for each line a lookup table of $G(n, T)$ was generated for densities between $\log n_{GT} = 7.5 - 15.5$ at intervals of $\log n = 0.01$.

As in case for finding the temperature array index, the position the model density takes on the $G(n, T)$ grid is found by taking the minimum of $|n_{GT} - n(T_o)|$. The selected $G(T)$ function is then interpolated with its nearest neighbours to account for the error in positioning n on the lookup table grid. We have ensured the grid spacing of the lookup tables is small, and is comparable to the precision in finding $n(T_o)$, ensuring small variations in the trial model will be reflected in the calculated model intensities. Finally, if the trial model density exceeds the limits of lookup table the model is discarded, as models including such high or low densities are unlikely to represent a flare atmosphere.

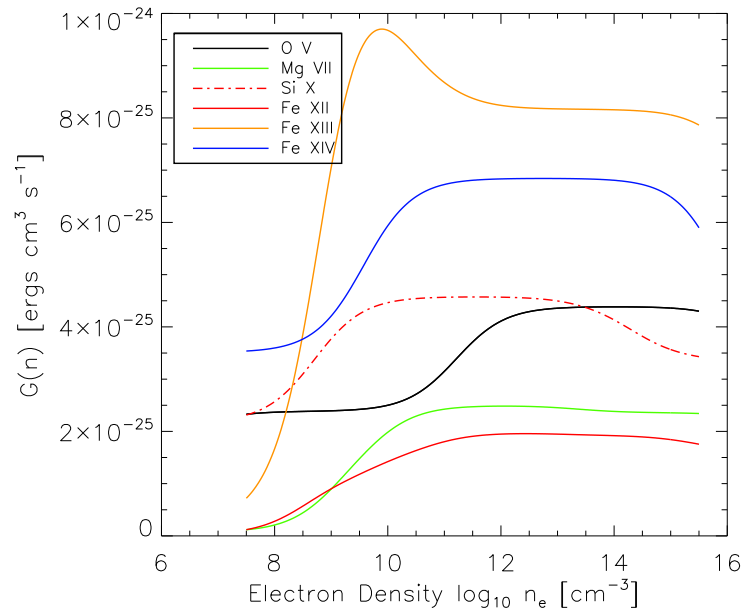


Figure 6.2: Plots of $G(n, T_{max})$ for the various diagnostic lines. The y-axis corresponds to the value of the contribution function at the peak formation temperature T_o .

6.3.5 The Integral

We now have everything we need to find the model intensities, and must integrate Equation 6.6 numerically to find them. Equation 6.6 can be written in the matrix form

$$I_i^{model} = \mathbf{K}_{i,j} \xi(T_j), \quad (6.9)$$

where $\mathbf{K}_{i,j}$ is a matrix of the contribution functions for i lines over the temperature bins j . Matrix multiplication performed by IDL then gives the model intensity I_i^{model} for each line. We find this method gives a good approximation to the numerical integration tools in IDL, but is faster and gives more consistent results. Residuals for the regularised inversion method used in Chapter 4 were also calculated in the same manner.

6.3.6 Fitness and Residuals

The GA will home in on the best model parameters by evolving the starting population based on a target fitness test. Here we use a simple chi-squared test between the model and observed intensities given by

$$\chi^2 = \sum_{i=1}^N \frac{(I^D - I^{model})^2}{I^D}, \quad (6.10)$$

where the sum is over the N diagnostic lines. The GA maximises the population fitness test, so the reciprocal $f = 1/\chi^2$ is used for the fitness. One point we shall consider in the results is where the difference between model and observed intensities approaches the observational uncertainty. If the algorithm can reach trial models with a χ^2 lower than the average observational uncertainty of the lines themselves, then we will find the limit of the model sensitivity. In future a full study should be carried out to determine the parameters that are most affected. However, in our testing the model intensities do not yet get close enough for this to be the case.

6.4 First Results

In its current state, the full forward-fitting method using the GA will now run in a stable manner, returning reasonable model intensities and fitting parameters. We show an example the best-fit model from one instance in Figure 6.3. The model here was returned using a population of 200, running for 50 generations (a run time of ~ 2 minutes). These are rough starting values, but the optimum number of generations can be found by watching the χ^2 evolve during the GA, as it will normally reach a plateau relatively quickly, although this also depends on the population number.

In Figure 6.3, the temperature model reaches a maximum at $\log T = 6.1$, slightly lower than highest diagnostic temperature, while the transition region is positioned at around 1000 km (the base temperature is set $\log T = 3.7$). As most of the density diagnostics are confined to the $\log T = 6.2$ region, we find a sharp drop in density at high temperatures in the $n(T)$ model (far right hand plot), while the single observation

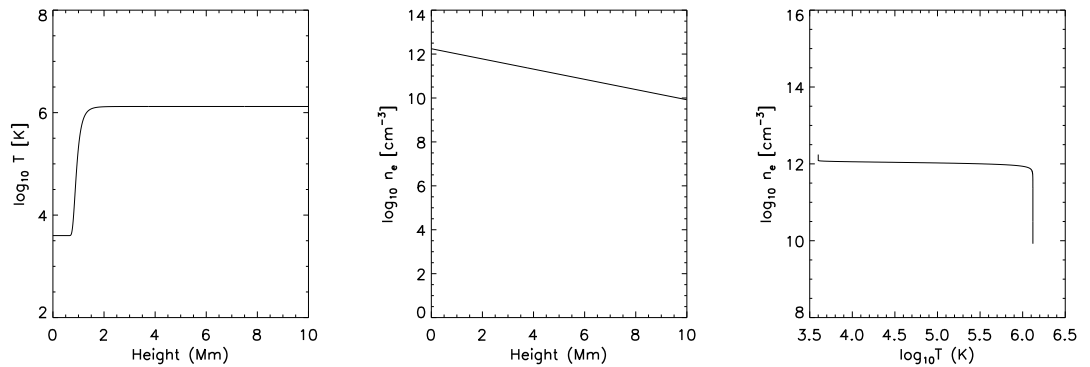


Figure 6.3: Atmospheric model as forward fitted by the GA for $T(z)$, $n(z)$, and $n(T)$. The best fit model parameters were $n_o = 1.7 \times 10^{12}$, $H = 1.87$, $\alpha = 0.38$, $\delta = 7.45$, $T_{max} = 6.12$.

at $\log T = 5.4$ appears to define the flat part at $\sim \log n = 12$. While the technique in the early stages of development, it is encouraging to see that it responds to the observations to give results that are not nonsensical. In the second panel of Figure 6.3, the density profile decreases from just over 10^{12} to 10^{10} cm^{-3} . These values are similar to the densities derived from ratio method used in previous chapters for O V and Fe XIV. If the $G(n)$ functions were completely insensitive to density, then the GA would struggle to settle on any reasonable value here. We have demonstrated this further for multiple GA runs in the next section.

The final residuals between the model and observations are seen in Figure 6.4 — Si XII was not used in this instance as the residuals were consistently large; we also found this diagnostic was unreliable in Chapter 4. We find the lower temperature lines are within $\sim \log I^D = 0.1$ while Fe XII could not get closer than $\sim \log I^D = 0.3$. All of these residuals are considerably larger than the uncertainties in the measured intensities ($< 10\%$).

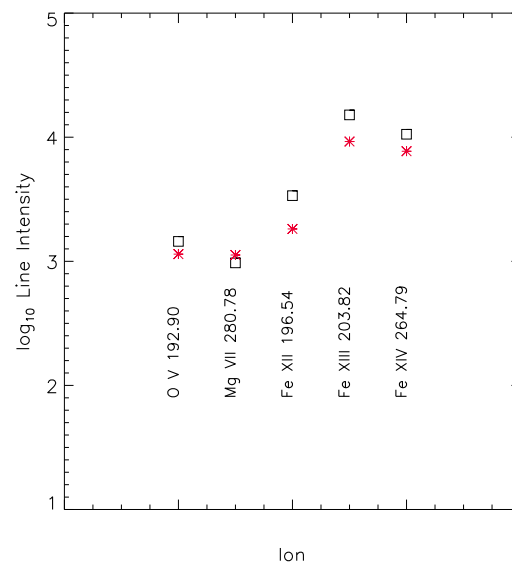


Figure 6.4: Final residuals for the forward fitting model. Squares represent the measured intensity and red crosses mark the model solution.

6.5 Multiple GA Realisations

One fitted model is not sufficient to say that we completely trust the technique yet. For the same input observations and GA parameters, the fitting was run for 1000 realisations to determine the spread of results. The variation for every parameter can be seen in Figure 6.5, where each dot represents one complete GA run. To ensure that the algorithm did not return unstable models, the parameters were restricted within the bounds of the dotted horizontal lines in each panel, however, the boundaries were wide enough to allow the GA some freedom to explore the parameter space.

The distribution in the two parameters for the density model, H and n_o , appears to be roughly centred on two values around $H = 1 - 2$ and $\log n_o \sim 12$, although n_o has a considerable spread to higher densities. H represents the scale height, and n_o the maximum density of the atmosphere. We find here n_o is partly limited by the lack of observations below $\log T = 5.4$, as the $O \vee G(n)$ function becomes insensitive to density above $\sim 10^{13} \text{ cm}^{-3}$. We can see this in the GA results, as it is less likely to find a solution with a maximum density above this.

The two parameters defining the position and steepness of the transition region, α and δ respectively, are less well defined. The position, α , spreads over many orders of magnitude and encounters the lower boundary at $\log \alpha = -3$, while δ is almost randomly distributed. T_{max} on the other hand is extremely well centred at $\log T_{max} = 6.1$, this was expected as the diagnostics currently limit the maximum temperature, but in future a more realistic value determined from high temperature lines should be used (as the temperature of $\log T_{max} = 6.1$ is in fact lower than the formation temperature for Fe XIV, it also suggests there might be a systematic error somewhere in the algorithm). The lack of convergence for α and δ suggests that the temperature model itself may be poorly constructed. A model where the parameters can vary so much with little change in the outcome is clearly not useful in a case like this.

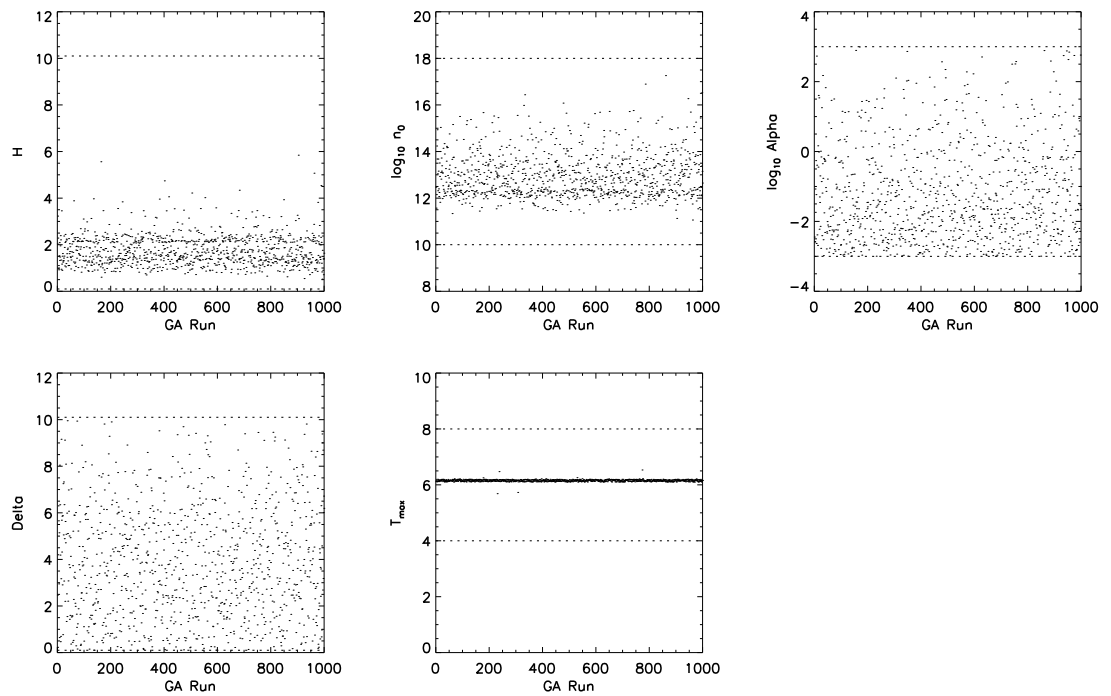


Figure 6.5: Fitted model parameters for 1000 realisations of the GA method. The parameters range from being recovered extremely well, e.g. T_{max} , to seemingly random in the case of δ . The horizontal lines represent the arbitrarily set parameter limits.

6.6 Conclusions and Future Plans

While it is too early to extract any meaningful conclusions from the model results, we can at least see that the diagnostic line $G(n)$ functions can be sensitive enough to the model density to produce a model with maximum and minimum densities close to those found using the ratio method (second panel of Figure 6.3). However, the model used for temperature (Equation 6.8) does not appear to be sensitive enough to parameter changes to allow the GA to determine a best fit parameter. It appears that a number of further steps are required to improve and better understand the forward fitting technique:

1. A systematic analysis of the input parameters. By manually varying the model parameters, and viewing the output functions and model intensities, we can de-

termine what parameter values and model functions are suitable.

2. An analysis of the effect of errors in the measured intensities. Given a Gaussian distribution of intensity measurements, what range of model parameters does this correspond to?
3. Testing of the density sensitive contribution functions $G(n)$. By manually varying the model density, what changes in the measured intensities can be seen.
4. Test incorporating densities measured directly from ratio diagnostics to define $n(T)$ directly from observation. The forward fitting method will then minimise the difference of measured $n(T)$ values to the model function.

Now that the computational components are in place, it will come down to the above points to determine if this is viable method of building a model atmosphere from observation. Only then can we begin to use more complex analytical models, such as those found in [Rosner et al. \(1978\)](#). It is also possible that we will be restricted by the observations, as $n(T)$ is currently only defined for 5 points in the atmosphere, 3 of which are very closely spaced in temperature. As we have mentioned throughout this thesis, the optical depth of the plasma as we move to lower heights may also be restrictive. It is clear that there is much work still to be done here. We have however introduced the problem of attempting to recover the height structure of the footpoint atmosphere via observation, something which has not been tackled using recent instrumentation, however, it remains the ultimate goal for those wishing to directly compare flare heating models with spectroscopic observations.

Chapter 7

Conclusions and Future Work

The footpoints of solar flares can be regarded as an extreme case of plasma heating in a gravitationally stratified atmosphere. The energy that is released from the corona is focused into an area, which in comparison to the coronal loop structure, is extremely small. During the heating phase, the footpoint atmosphere rises in temperature by a factor of nearly 1000 in a matter of minutes, and changes from being in hydrostatic balance to moving with speeds of hundreds of km s^{-1} . Naturally, these areas are of much interest to those wishing to understand the mechanism for the onset of a flare, the nature of the resulting emission, or to test theories of high energy physics otherwise unobtainable in the laboratory. Through the work in this thesis, we have begun to better understand how the atmosphere is structured in height while subject to these energy fluxes. Our observations of temperature and density are the fundamental building blocks of any flare model, and we have explored ways to use them to better understand and question current models.

In the work shown in Chapter 3 we began with what was a simple diagnostic of electron density in the flare footpoints during the impulsive phase. 3 footpoint areas were identified using TRACE and RHESSI imaging, and from the RHESSI HXR spectra shown to contain a component of 12-25 keV non-thermal electrons. From *Hinode*/EIS spectral diagnostics, we found that the electron density rose during the heating period from around 10^{10} to 10^{11} cm^{-3} at temperatures of $\sim \log T = 6.2$,

and that evaporative plasma up-flows were found in two of the footpoints of up to 140 km s^{-1} . The density increase at these locations was interpreted as the heating of progressively deeper layers of the chromosphere, or a movement of the transition region to lower heights in the solar atmosphere. The RHESSI HXR photon spectra could be equally well fitted with a thermal component plus a non-thermal power-law, or by a pair of thermal components. The fitted non-thermal spectral component was interpreted with a thick-target beam model to give the energy input flux from the flare. At $\sim 10^{10} \text{ ergs s}^{-1} \text{ cm}^{-2}$ this was close to a theoretical cut-off between gentle and explosive evaporation, although uncertainties in the measurements of both the flux, and evaporative velocities, meant that we could not be certain of either case. In addition, from the double thermal fit, it was also found that there is sufficient energy in the hot component to drive the same evaporative flows but via a conduction flux — ignoring any radiative losses or a saturated conduction flux. Both conduction from a hot slab at the top of the flare chromosphere, and from an extended hot loop, were considered and found to both provide enough flux to drive the observed evaporation.

Throughout this thesis we have often compared our observations to the VAL-E model. We do this as it is representative of the pre-flare atmosphere in which the flare energy is deposited, but also as the model output data can be easily interpreted. However, we know that the temperature and density profiles of the atmosphere evolve during the impulsive heating phase, and that the VAL-E model will quickly cease to be valid. Models incorporating an electron beam input, such as the Allred model (Allred et al. 2005), are more suitable and can be run for a variety of flare input parameters. The published results from Allred et al. (2005) use much harder spectral parameters than we observed for the event in Chapter 3, and in future studies we plan to run the models for beam parameters derived from our own fitted RHESSI HXR spectra. From the output temperature and density profiles we can generate synthetic EMDs, although, as we briefly discussed in Chapter 6, non-monotonically increasing model atmospheres will present problems in determining the height profiles, although we can justify the use of the technique in cases where the atmosphere is balanced by radiative losses.

Chapter 4 continued the theme of EIS spectral diagnostics, whereby a regularized inversion method was used to obtain the EMD of footpoint plasma during the impulsive phase. We found that the footpoints of 6 different flares shared a remarkably similar EMD profile, with a constant gradient of T^1 between temperatures of $\log T = 5.5 - 6.9$, and peaking at $\sim \log T = 6.9$. This peak temperature suggests that a significant portion of the footpoint plasma is emitting at around 8 MK. Through a discussion of the modelling by Shmeleva & Syrovatskii (1973) and Widing (1982), we found that the EMD gradient was consistent with an atmosphere dominated by conductive heating and cooled via radiative losses. The energy deposition is therefore implied to be confined to a hot slab (8-10 MK) above the main emitting region, and does not directly heat the plasma that we see emitting in EUV. The emitting thickness of plasma at temperatures below $\log T = 6.2$ was also found to be less than 5 km, indicating that a steep temperature gradient exists. We have found in this analysis that the choice of abundances is influential in the obtained profile of the EMD, and that at lower temperatures, some lines can be affected by the plasma optical depth. We have suggested ways to avoid these issues through careful line choice which should be considered when designing future observing plans.

In Chapter 5 evidence for extremely high footpoint densities, on the order of $10^{13} - 10^{14} \text{ cm}^{-3}$, was found using a line ratio diagnostic for the O v 192.904 / 248.460Å lines that had previously been unused for flare studies. The density sensitive 192Å line was shown to be significantly enhanced compared to the 248Å line by nearly a factor of 6, far more than expected. In the VAL-E model an electron density of 10^{14} cm^{-3} corresponds to a pre-flare plasma temperature of 10,000 K. By again interpreting the enhanced densities as the heating of progressively deeper layers of the atmosphere, observing this density in O v implies that deep chromospheric plasma has been heated to the line's formation temperature of $T_{max} = 250,000 \text{ K}$. For the SOL2007-12-14T14:16:30 flare, RHESSI observations made by Milligan & Dennis (2009) allowed us to calculate the heating rate as predicted from a collisional thick-target model. Using parameters from the VAL-E model, we found that the heating rate per particle at a density of 10^{13} cm^{-3} was $\sim 25 \text{ eV}$, compared to a much larger radiative loss rate per particle of

~ 6 keV. Any beam energy deposited here will therefore be lost to radiation and not heat the local plasma.

This presents a problem for either our diagnostics or the thick-target model itself. To reconcile this, we first suggested that the VAL-E atmospheric model may not be representative of the flare atmosphere, and that the high densities may partly be the result of a pressure rise due to evaporative flows, as seen in the Allred flare model. This reduces the column depth at which the beam must heat plasma of this density. We also suggested that by relaxing the assumption of ionisation equilibrium, the plasma emitting the O v lines may be at a higher temperature than the line equilibrium formation temperature. By increasing the plasma temperature to $\log T = 6.8$, the density diagnostic yields lower footpoint densities of between $10^{12} - 10^{13} \text{ cm}^{-3}$, although they are still too high to be heated effectively. Lastly, we calculated the optical depth of each diagnostic line, finding that the 192Å line had a much higher optical depth than 248Å. At these high densities we have calculated that the 192Å line should be strongly attenuated, which seems unreasonable as we see the line in emission and not absorption. We can possibly attribute this to the choice of the VAL-E model, and we show that the optical depth is more reasonable ($\tau \sim 10$) in a case where we assume that the model atmosphere has a constant temperature of $\log T = 6.8$. However, from a standard interpretation of the line being attenuated by a high optical depth, this effect will not reduce the observed 192Å intensity, and therefore the implied densities will remain high. We discussed a process shown by [Jordan \(1967\)](#) that could preferentially enhance some line strengths within an ion due to the transfer of level populations from resonant absorption. This will require further investigation before we can apply it to the O v diagnostic but it is essential that we fully understand the opacity effects before trusting diagnostics at these temperatures. Future flare observing campaigns would be also wise to include the O IV 1401Å diagnostic lines available from IRIS. These are formed at a similar temperature to O v and the capabilities of IRIS would be ideal for studying footpoints.

Future Modelling and Analysis — It is clear from the work in Chapters 3 and 5

that understanding the nature of the flare energy deposition from the EUV diagnostics hinges on the assumed model atmosphere density and temperature relations $T(z)$ and $n(z)$. In measuring the density at prescribed temperatures we can define points on the atmospheric $n(T)$ relation, however, to know the depth z of the emission requires a model for $T(z)$ and $n(z)$. In Chapter 6 we proposed a method, based on the theoretical foundations by [Brown et al. \(1991\)](#), to forward fit model atmospheres to observationally determine the density and temperature structure of the atmosphere with height. To do this the $\xi(T)$ obtained from Chapter 4 was multiplied by the set of contribution functions corresponding to each density-sensitive line in the Cambridge rasters, resulting in a set of model line intensities. The residuals between these and the observed line intensities were then minimised by a Genetic Algorithm to determine the best fit parameterised model atmosphere for $T(z)$ and $n(z)$. While the method is shown to be stable and can return sensible models, it appears to be too insensitive to the inputs to converge on a single set of model parameters. We have suggested routes in which to test the method and improve the input models, involving manually varying the model parameters to test the range of possible models, to determining the sensitivity of the $G(n, T)$ functions to changes in the model $n(T)$ functions. Again observations of more density diagnostic lines would help to better specify the $n(T)$ function. What we have shown here is that such a forward fitting method may be possible, and once this testing is complete we will be able to test more sophisticated atmospheric models.

There are a few natural conclusions from this work that will need to be addressed in future. Firstly, as we mention above, we can only fully understand these diagnostic results if we have a suitable flare model atmosphere to compare them with, although we have proposed a method in which to obtain a model semi-empirically. Secondly, since the flare heating appears to extend to layers of the atmosphere which are not optically thin, the assumption of optically thin plasma in these footpoint regions may not be valid, and efforts should be made in interpreting the emission from these regions. Spectroscopic observations at these temperatures will soon be available from IRIS, and combined with expertise in chromospheric modelling and observation, for example from the groups at the University of Oslo and the High Altitude Observatory

(HAO) in Boulder, much progress could be made in this area. As the flare heating clearly extends to these depths, diagnostics here should not be ignored. Lastly, it is possible that the modelling work in Chapter 6 will be limited by the number of data points we can prescribe on the $n(T)$ function. A solution could be to design an EIS study including many more density-sensitive lines. Unfortunately EIS is limited in bandwidth and the line selection is compromised. However, as we have seen in numerous studies now, the footpoints of medium sized flares are on the order of 2-3'' across in the EIS rasters. If the flaring region were to be identified quickly, a small raster window could be used that compromises on spatial information, but gives better spectral and temporal coverage. Supporting SDO/AIA imaging can always be used to give context information in the EUV.

SDO/EVE Flare Observations — During the course of the research in this thesis extensive efforts were made to investigate the possibilities of using the Extreme Ultraviolet Variability Experiment (EVE) on board SDO ([Woods et al. 2012](#)) for flare studies. EVE is a full solar disc integrated spectrometer covering a wavelength range of 50-1050Å with a 10 second cadence. The design means that no spatial resolution is available, however, it makes uninterrupted measurements of the spectrum 24 hours a day. This has the advantage of being able to capture every flaring event on the Sun with the same spectral coverage each time, and has since observed all of the largest X-class flares in the current solar cycle. We started to use the instrument not long after the first data release alongside H. Hudson, who looked at Doppler shifts within the line profiles ([Hudson et al. 2011](#)).

While working at HAO in collaboration with Dr. Scott McIntosh we began to adapt the EMD inversion method from Chapter 4 to EVE data. The reasoning behind this was to estimate the flaring flux of select coronal emission lines in the IRIS spectral window for different flare sizes, which is important for the instrument's exposure calibration. By subtracting the pre-flare background level, we made significant progress in using the technique to obtain the EMD for many flares. The high cadence EVE data allowed us to view the EMD throughout the flare evolution, although we were cautious

in interpreting these as we could not guarantee that the emission was entirely from the footpoints. Whilst we have only made a preliminary analysis, we found that for around 10 events, the earliest EMD in the impulsive phase often had a peak temperature of around $\log T = 7.1$, which then cooled quickly to around $\log T = 6.8$ at the impulsive phase peak. A more gradual cooling then followed in the decay phase. A more in-depth investigation is planned for later this year, which will further test the EVE spectra for blending effects, make use of the new Level-3 EVE data which has since been released, and fine tune the EMD inversion method. If this result is still robust, then it may be further evidence for a footpoint atmosphere radiating to balance the conductive flux from a hot layer above. An ideal test study would include observations from both EIS and AIA to better estimate the effect of blends in the EVE lines, and better estimate the contribution of footpoint emission in the EVE spectrum.

Elemental Abundance Determination — After determining flare EMDs using the EVE data we moved on to designing a method which could in principle be used to determine the elemental abundances from an EMD observation. As we discussed in Chapter 4, the choice of abundances is often made from a limited selection of prior observations, yet we found that they do contribute significantly to the profile of the EMD. We began to develop a method of forward fitting a set of abundances by minimising the residuals of the EMD inversion, which would remove the need to specify them in advance. By starting with a simple quiet-sun set of line intensities from EVE, a trial set of abundances were used to find the line contribution functions, before inverting to find a trial EMD. The residuals between the observed intensities and those derived from the EMD were then returned. A Genetic Algorithm was used in the same manner as Chapter 6 to minimise these residuals by varying the input abundances. If the technique is sensitive enough to the input abundances, then the GA should return the most suitable set of abundances for the plasma. This does assume that any other systematic errors that influence the derived line intensities are smaller than those due to the abundances, although we have seen in Chapter 4 that the choice of abundances *can* change the EMD by factor much larger than the EMD uncertainty. Also by us-

ing EVE data sampled over longer time-scales the intensity errors can be minimised. Currently, the method successfully runs but does not yet converge quickly on a set of abundances, although we believe this may be helped by adjusting the regularization tweak parameter. In future we plan to test the robustness of the technique in a similar manner to Chapter 6, and further tune the line choice to include as many different elements as possible. This technique would not just be suitable for flare analysis, but for many solar features, such as determining the difference between abundances in an open field coronal hole, and the closed field quiet sun.

Closing Remarks — Currently we are living in an era with an unsurpassed variety of solar specific ground and space-based instrumentation. As demonstrated in this thesis, and by many other authors, *Hinode*/EIS is extremely capable of revealing the nature of plasma heating and dynamics in a flare footpoint. In addition, *Hinode*/XRT and *Hinode*/SOT are available for supporting soft X-ray and optical observations, while SDO/AIA and SDO/EVE take uninterrupted imaging and spectral data in the EUV. RHESSI, currently in its 11th year of operation, continues to operate and provides essential high energy X-ray observations.

On the horizon is the combined JAXA/NASA/ESA Solar-C mission which is the successor to the *Hinode* mission. The objective of Solar-C is to obtain solar spectra with continuous coverage from white light through to X-rays. This an ambitious project, but having a single set of instruments observe the response of the solar atmosphere from photosphere to corona will be a great step forward in understanding any energetic process on the Sun. The Daniel K. Inouye Advanced Technology Solar Telescope (DKIST) is another exciting new project with prospects for flare research. Focusing on obtaining ground-based observations in white light, it will provide much needed high resolution optical spectra that are essential for understanding the long standing puzzle of white light emission in flares. Finally, the imminent release of IRIS UV data is extremely exciting, as we have yet to see what the first flare observations will reveal. The work here highlights the importance of multi-instrument observation campaigns, as no one instrument alone can show the vast range of plasma energetics, temperatures,

and dynamics found in a solar flare. Co-operation between all of these instruments is clearly the only way forward in fully understanding such energetic events, so we look forward to seeing what these new observations will hold.

Bibliography

- Allred, J. C., Hawley, S. L., Abbett, W. P., & Carlsson, M. 2005, *Astrophysical Journal*, 630, 573
- Almleaky, Y. M., Brown, J. C., & Sweet, P. A. 1989, *Astronomy and Astrophysics*, 224, 328
- Andretta, V. & Jones, H. P. 1997, *Astrophysical Journal*, 489, 375
- Antiochos, S. K. & Sturrock, P. A. 1978, *Astrophysical Journal*, 220, 1137
- Aschwanden, M. J. & Boerner, P. 2011, *Astrophysical Journal*, 732, 81
- Athay, R. G. 1994, *Astrophysical Journal*, 423, 516
- Avrett, E. H. 2003, in *Astronomical Society of the Pacific Conference Series*, Vol. 286, *Current Theoretical Models and Future High Resolution Solar Observations: Preparing for ATST*, ed. A. A. Pevtsov & H. Uitenbroek, 419
- Bartoe, J.-D. F., Brueckner, G. E., Purcell, J. D., & Tousey, R. 1977, *Applied Optics*, 16, 879
- Battaglia, M., Fletcher, L., & Benz, A. O. 2009, *Astronomy and Astrophysics*, 498, 891
- Battaglia, M. & Kontar, E. P. 2011, *Astrophysical Journal*, 735, 42
- Battaglia, M. & Kontar, E. P. 2012, *Astrophysical Journal*, 760, 142

- Battaglia, M., Kontar, E. P., Fletcher, L., & MacKinnon, A. L. 2012, *Astrophysical Journal*, 752, 4
- Bloomfield, D. S., Mathioudakis, M., Christian, D. J., Keenan, F. P., & Linsky, J. L. 2002, *Astronomy and Astrophysics*, 390, 219
- Bradshaw, S. J. 2009, *Astronomy and Astrophysics*, 502, 409
- Brooks, D. H. & Warren, H. P. 2009, *Astrophysical Journal, Letters*, 703, L10
- Brosius, J. W. 2012, *Astrophysical Journal*, 754, 54
- Brown, C. M., Feldman, U., Seely, J. F., Korendyke, C. M., & Hara, H. 2008, *Astrophysical Journal, Supplement*, 176, 511
- Brown, J. C. 1971, *Solar Physics*, 18, 489
- Brown, J. C., Dwivedi, B. N., Sweet, P. A., & Almlucky, Y. M. 1991, *Astronomy and Astrophysics*, 249, 277
- Bryans, P., Landi, E., & Savin, D. W. 2009, *Astrophysical Journal*, 691, 1540
- Cargill, P. J., Bradshaw, S. J., & Klimchuk, J. A. 2012, *Astrophysical Journal*, 752, 161
- Carmichael, H. 1964, *NASA Special Publication*, 50, 451
- Carrington, R. C. 1859, *Monthly Notices of the Royal Astronomical Society*, 20, 13
- Chamberlin, P. C., Milligan, R. O., & Woods, T. N. 2012, *Solar Physics*, 279, 23
- Chandrasekhar, S. 1961, *Hydrodynamic and hydromagnetic stability*
- Charbonneau, P. 1995, *Astrophysical Journal, Supplement*, 101, 309
- Charbonneau, P. 2013, <http://www.hao.ucar.edu/modeling/pikaia/pikaia.php>
- Cheng, C.-C., Bruner, E. C., Tandberg-Hanssen, E., et al. 1982, *Astrophysical Journal*, 253, 353

- Chifor, C. 2008, PhD thesis, Univ. of Cambridge, UK.
- Craig, I. J. D. & Brown, J. C. 1976, *Astronomy and Astrophysics*, 49, 239
- Culhane, J. L., Harra, L. K., James, A. M., et al. 2007, *Solar Physics*, 243, 19
- Darwin, C. 1859, *On the Origin of the Species by Means of Natural Selection: Or, The Preservation of Favoured Races in the Struggle for Life* (John Murray)
- De Pontieu, B., McIntosh, S. W., Hansteen, V. H., & Schrijver, C. J. 2009, *Astrophysical Journal, Letters*, 701, L1
- Del Zanna, G., Landini, M., & Mason, H. E. 2002, *Astronomy and Astrophysics*, 385, 968
- Del Zanna, G., Mitra-Kraev, U., Bradshaw, S. J., Mason, H. E., & Asai, A. 2011, *Astronomy and Astrophysics*, 526, A1
- Dennis, B. R. & Zarro, D. M. 1993, *Solar Physics*, 146, 177
- Dere, K. P. & Cook, J. W. 1979, *Astrophysical Journal*, 229, 772
- Dere, K. P., Landi, E., Mason, H. E., Monsignori Fossi, B. C., & Young, P. R. 1997, *Astronomy and Astrophysics, Supplement*, 125, 149
- Dere, K. P., Landi, E., Young, P. R., et al. 2009, *Astronomy and Astrophysics*, 498, 915
- Domingo, V., Fleck, B., & Poland, A. I. 1995, *Solar Physics*
- Doschek, G. A., Feldman, U., Kreplin, R. W., & Cohen, L. 1980, *Astrophysical Journal*, 239, 725
- Doschek, G. A., Feldman, U., & Rosenberg, F. D. 1977, *Astrophysical Journal*, 215, 329
- Emslie, A. G. 1978, *Astrophysical Journal*, 224, 241

- Emslie, A. G. 1981, *Astrophysical Journal*, 245, 711
- Feldman, U., Dammasch, I., Landi, E., & Doschek, G. A. 2004, *Astrophysical Journal*, 609, 439
- Feldman, U., Dorschek, G. A., & Rosenberg, F. D. 1977, *Astrophysical Journal*, 215, 652
- Feldman, U., Mandelbaum, P., Seely, J. F., Doschek, G. A., & Gursky, H. 1992, *Astrophysical Journal, Supplement*, 81, 387
- Fisher, G. H. 1989, *Astrophysical Journal*, 346, 1019
- Fisher, G. H., Canfield, R. C., & McClymont, A. N. 1985, *Astrophysical Journal*, 289, 425
- Fletcher, L. & de Pontieu, B. 1999, *Astrophysical Journal, Letters*, 520, L135
- Fletcher, L., Dennis, B. R., Hudson, H. S., et al. 2011, *Space Science Reviews*, 159, 19
- Fletcher, L., Hannah, I. G., Hudson, H. S., & Innes, D. E. 2013, *Astrophysical Journal*, 771, 104
- Fludra, A. & Sylwester, J. 1986, *Solar Physics*, 105, 323
- Freeland, S. L. & Handy, B. N. 2012, *SolarSoft: Programming and data analysis environment for solar physics*, astrophysics Source Code Library
- Gabriel, A. H. 1976, *Royal Society of London Philosophical Transactions Series A*, 281, 339
- Golub, L., Deluca, E., Austin, G., et al. 2007, *Solar Physics*, 243, 63
- Graham, D. R., Fletcher, L., & Hannah, I. G. 2011, *Astronomy and Astrophysics*, 532, A27
- Graham, D. R., Hannah, I. G., Fletcher, L., & Milligan, R. O. 2013, *Astrophysical Journal*, 767, 83

- Grevesse, N. & Sauval, A. J. 1998, *Space Science Reviews*, 85, 161
- Handy, B. N., Acton, L. W., Kankelborg, C. C., et al. 1999, *Solar Physics*, 187, 229
- Hannah, I. G., Hudson, H. S., Battaglia, M., et al. 2011, *Space Science Reviews*, 159, 263
- Hannah, I. G., Hudson, H. S., Hurford, G. J., & Lin, R. P. 2010, *Astrophysical Journal*, 724, 487
- Hannah, I. G. & Kontar, E. P. 2012, *Astronomy and Astrophysics*, 539, A146
- Hannah, I. G. & Kontar, E. P. 2013, *Astronomy and Astrophysics*, 553, A10
- Hansen, P. C. 1992, *Inverse Problems*, 8, 849
- Harra, L. K., Sakao, T., Mandrini, C. H., et al. 2008, *Astrophysical Journal, Letters*, 676, L147
- Harrison, R. A., Sawyer, E. C., Carter, M. K., et al. 1995, *Solar Physics*, 162, 233
- Hawley, S. L. & Fisher, G. H. 1994, *Astrophysical Journal*, 426, 387
- He, J. & Zhang, Q. 2013, *Advances in Space Research*, 51, 2002
- Hirayama, T. 1974, *Solar Physics*, 34, 323
- Högbom, J. A. 1974, *Astronomy and Astrophysics, Supplement*, 15, 417
- Holland, J. H. 1962, *J. ACM*, 9, 297
- Holman, G. D. 2003, *Astrophysical Journal*, 586, 606
- Holman, G. D., Aschwanden, M. J., Aurass, H., et al. 2011, *Space Science Reviews*, 159, 107
- Holstein, T. 1947, *Physical Review*, 72, 1212
- Hudson, H. S., Woods, T. N., Chamberlin, P. C., et al. 2011, *Solar Physics*, 273, 69

- Hurford, G. J., Schmahl, E. J., Schwartz, R. A., et al. 2002, *Solar Physics*, 210, 61
- Irons, F. E. 1979, *Journal of Quantitative Spectroscopy and Radiative Transfer*, 22, 1
- Jordan, C. 1967, *Solar Physics*, 2, 441
- Jordan, C. 1980, *Astronomy and Astrophysics*, 86, 355
- Judge, P. G., Hubeny, V., & Brown, J. C. 1997, *Astrophysical Journal*, 475, 275
- Judge, P. G. & Pietarila, A. 2004, *Astrophysical Journal*, 606, 1258
- Kamio, S., Hara, H., Watanabe, T., Fredvik, T., & Hansteen, V. H. 2010, *Solar Physics*, 266, 209
- Kashyap, V. & Drake, J. J. 1998, *Astrophysical Journal*, 503, 450
- Kastner, S. O. & Kastner, R. E. 1990, *Journal of Quantitative Spectroscopy and Radiative Transfer*, 44, 275
- Keenan, F. P., Dufton, P. L., Harra, L. K., et al. 1991, *Astrophysical Journal*, 382, 349
- Klimchuk, J. A., Patsourakos, S., & Cargill, P. J. 2008, *Astrophysical Journal*, 682, 1351
- Ko, Y.-K., Doschek, G. A., Warren, H. P., & Young, P. R. 2009, *Astrophysical Journal*, 697, 1956
- Kontar, E. P., Piana, M., Massone, A. M., Emslie, A. G., & Brown, J. C. 2004, *Solar Physics*, 225, 293
- Kopp, R. A. & Pneuman, G. W. 1976, *Solar Physics*, 50, 85
- Kosugi, T., Matsuzaki, K., Sakao, T., et al. 2007, *Solar Physics*, 243, 3
- Krucker, S., Hudson, H. S., Jeffrey, N. L. S., et al. 2011, *Astrophysical Journal*, 739, 96
- Kumar, P. & Manoharan, P. K. 2013, *Astronomy and Astrophysics*, 553, A109

- Landi, E., Del Zanna, G., Young, P. R., Dere, K. P., & Mason, H. E. 2012, *Astrophysical Journal*, 744, 99
- Landi, E. & Young, P. R. 2009, *Astrophysical Journal*, 706, 1
- Landi, E., Young, P. R., Dere, K. P., Del Zanna, G., & Mason, H. E. 2013, *Astrophysical Journal*, 763, 86
- Lemen, J. R., Title, A. M., Akin, D. J., et al. 2012, *Solar Physics*, 275, 17
- Lin, R. P., Dennis, B. R., Hurford, G. J., et al. 2002, *Solar Physics*, 210, 3
- Machado, M. E. & Emslie, A. G. 1979, *Astrophysical Journal*, 232, 903
- Mariska, J. T. 1992, *The solar transition region*
- Martens, P. C. H., Kankelborg, C. C., & Berger, T. E. 2000, *Astrophysical Journal*, 537, 471
- Mathioudakis, M., McKenny, J., Keenan, F. P., Williams, D. R., & Phillips, K. J. H. 1999, *Astronomy and Astrophysics*, 351, L23
- Mazzotta, P., Mazzitelli, G., Colafrancesco, S., & Vittorio, N. 1998, *Astronomy and Astrophysics, Supplement*, 133, 403
- McIntosh, S. W., Charbonneau, P., & Brown, J. C. 2000, *Astrophysical Journal*, 529, 1115
- McIntosh, S. W., Tian, H., Sechler, M., & De Pontieu, B. 2012, *Astrophysical Journal*, 749, 60
- Milligan, R. O. 2008, *Astrophysical Journal, Letters*, 680, L157
- Milligan, R. O. 2011, *Astrophysical Journal*, 740, 70
- Milligan, R. O. & Dennis, B. R. 2009, *Astrophysical Journal*, 699, 968
- Mitchell, A. C. G. & Zemansky, M. W. 1961, *Resonance Radiation and Excited Atoms*

- Monsignor Fossi, B. C. & Landini, M. 1991, *Advances in Space Research*, 11, 281
- Morozov, V. 1963, *Dokladi Akademii SSSR*, 175, 1225
- Mrozek, T. & Tomczak, M. 2004, *Astronomy and Astrophysics*, 415, 377
- Munro, R. H., Dupree, A. K., & Withbroe, G. L. 1971, *Solar Physics*, 19, 347
- Neupert, W. M. 1968, *Astrophysical Journal, Letters*, 153, L59+
- O'Dwyer, B., Del Zanna, G., Mason, H. E., Weber, M. A., & Tripathi, D. 2010, *Astronomy and Astrophysics*, 521, A21
- Pesnell, W. D., Thompson, B. J., & Chamberlin, P. C. 2012, *Solar Physics*, 275, 3
- Peter, H. 2000, *Astronomy and Astrophysics*, 360, 761
- Peter, H. 2001, *Astronomy and Astrophysics*, 374, 1108
- Pietarila, A. & Judge, P. G. 2004, *Astrophysical Journal*, 606, 1239
- Pottasch, S. R. 1964, *Space Science Reviews*, 3, 816
- Qiu, J., Sturrock, Z., Longcope, D. W., Klimchuk, J. A., & Liu, W.-J. 2013, *Astrophysical Journal*, 774, 14
- Raftery, C. L., Bloomfield, D. S., Gallagher, P. T., et al. 2013, *Solar Physics*, 286, 111
- Ricchiazzi, P. J. 1982, PhD thesis, California Univ., San Diego.
- Rosner, R., Tucker, W. H., & Vaiana, G. S. 1978, *Astrophysical Journal*, 220, 643
- Russell, A. J. B. & Fletcher, L. 2013, *Astrophysical Journal*, 765, 81
- Schwartz, R. A., Csillaghy, A., Tolbert, A. K., et al. 2002, *Solar Physics*, 210, 165
- Sherrill, T. J. 1991, *Sky and Telescope*, 81, 134
- Shmeleva, O. P. & Syrovatskii, S. I. 1973, *Solar Physics*, 33, 341

- Smith, G. R. 2003, *Monthly Notices of the Royal Astronomical Society*, 341, 143
- Somov, B. V. 2006, *Plasma Astrophysics, Part I: Fundamentals and Practice*
- Spitzer, L. 1962, *Physics of Fully Ionized Gases*
- Spitzer, Jr., L. 1940, *Monthly Notices of the Royal Astronomical Society*, 100, 396
- Stix, M. 2004, *The sun : an introduction*
- Sturrock, P. A. 1966, *Nature*, 211, 695
- Tian, H., Curdt, W., Marsch, E., & Schühle, U. 2009, *Astronomy and Astrophysics*, 504, 239
- Tikhonov, A. N. 1963, *Soviet Math. Dokl.*, 4, 1035
- Tousey, R. 1977, *Applied Optics*, 16, 825
- Tousey, R., Bartoe, J.-D. F., Brueckner, G. E., & Purcell, J. D. 1977, *Applied Optics*, 16, 870
- Tsuneta, S. 1997, *Astrophysical Journal*, 483, 507
- Tsuneta, S., Ichimoto, K., Katsukawa, Y., et al. 2008, *Solar Physics*, 249, 167
- Underwood, J. H., Feldman, U., Dere, K. P., & Antiochos, S. K. 1978, *Astrophysical Journal*, 224, 1017
- Vernazza, J. E., Avrett, E. H., & Loeser, R. 1981, *Astrophysical Journal, Supplement*, 45, 635
- Vernazza, J. E. & Reeves, E. M. 1978, *Astrophysical Journal, Supplement*, 37, 485
- Walsh, R. W. & Ireland, J. 2003, *Astronomy and Astrophysics Reviews*, 12, 1
- Warren, H. P., Feldman, U., & Brown, C. M. 2008, *Astrophysical Journal*, 685, 1277

- Warren, H. P., Mariska, J. T., & Wilhelm, K. 1998, *Astrophysical Journal, Supplement*, 119, 105
- Watanabe, T., Hara, H., Sterling, A. C., & Harra, L. K. 2010, *Astrophysical Journal*, 719, 213
- Weber, M. A., Deluca, E. E., Golub, L., & Sette, A. L. 2004, in *IAU Symposium, Vol. 223, Multi-Wavelength Investigations of Solar Activity*, ed. A. V. Stepanov, E. E. Benevolenskaya, & A. G. Kosovichev, 321–328
- Widing, K. & Hiei, E. 1984, *Astrophysical Journal*, 281, 426
- Widing, K. G. 1982, *Astrophysical Journal*, 258, 835
- Widing, K. G., Doyle, J. G., Dufton, P. L., & Kingston, E. A. 1982, *Astrophysical Journal*, 257, 913
- Widing, K. G. & Spicer, D. S. 1980, *Astrophysical Journal*, 242, 1243
- Wilhelm, K., Curdt, W., Marsch, E., et al. 1995, *Solar Physics*, 162, 189
- Wood, R. W. 1905, *Physical Optics*
- Woodgate, B. E., Brandt, J. C., Kalet, M. W., et al. 1980, *Solar Physics*, 65, 73
- Woods, T. N., Eparvier, F. G., Hock, R., et al. 2012, *Solar Physics*, 275, 115
- Woods, T. N., Kopp, G., & Chamberlin, P. C. 2006, *Journal of Geophysical Research (Space Physics)*, 111, 10
- Young, P. 2013a, *EIS Analysis Guide - Software Note 1*
- Young, P. 2013b, *EIS Analysis Guide - Software Note 16*
- Young, P. R., Del Zanna, G., Mason, H. E., et al. 2007a, *Publications of the ASJ*, 59, 857

Young, P. R., Del Zanna, G., Mason, H. E., et al. 2007b, *Publications of the ASJ*, 59, 727

Young, P. R., Doschek, G. A., Warren, H. P., & Hara, H. 2013, *Astrophysical Journal*, 766, 127

Young, P. R., Watanabe, T., Hara, H., & Mariska, J. T. 2009, *Astronomy and Astrophysics*, 495, 587

-